Melting and melt migration in heterogeneous mantle beneath mid-ocean ridges

Samuel Weatherley

University College

University of Oxford

A thesis submitted for the degree of

Doctor of Philosphy

Michaelmas Term 2012

Abstract

Evidence for chemical heterogeneity in the mantle is widespread in oceanic basalts, yet its consequences for basalt petrogenesis are little understood. A significant unknown is the effect that heterogeneity has on the dynamics of magma flow in the mantle. Observations of oceanic crust and the upper mantle suggest that magma migrates to the surface through a network of high porosity channels. In this thesis, I use computational models of coupled magma/mantle dynamics beneath mid-ocean ridges to question whether a physical connection exists between channelized flow and mantle heterogeneity.

The models are intialized with simple, hypothetical patterns of heterogeneity that cause the fusiblity of the model mantle to vary. The principal result is that channelized melt flow is a consequence of melting in a heterogeneous mantle. Magma from preferentially melted heterogeneities nucleates high porosity, high permeability channels that grow by a feedback between magma flux and dissolution. Using the models in various configurations, I explore the dynamics of channel formation and investigate how the topology of mantle heterogeneity affects melt segregation and focusing beneath ridge axes. Additionally, I use the models to predict the speed and time scale of melt migration. A simple model of equilibrium partitioning is used to cast the results in terms of ^{230}Th disequilibria. Comparisons of the modelled geochemistry against global measurements indicate that the models presented here provide a reasonable, first-order description of the dynamics of magma flow beneath ridges.

I also explore a systematic connection between plate kinematics and global patterns of mid-ocean ridge bathymetry with three dimensional models of solid mantle flow beneath transform faults. The results provide new constraints on the scale of melt focusing and melt redistribution at ridge axes, and pose questions for future 3D studies of melt migration beneath ridges.

Extended Abstract

Evidence for chemical heterogeneity in Earth's mantle is widely observed in oceanic basalts, yet its consequences for basalt petrogenesis are little understood. A significant unknown is the effect heterogeneity has on the dynamics of magma flow in the mantle. Observations of the oceanic crust and upper mantle indicate that magma migrates to the surface through a network of high porosity, high permeability channels. These observations further suggest that channelized flow is why oceanic basalts preserve evidence for mantle heterogeneity. The main objective of this thesis is to investigate whether a physical connection exists between channelized magmatic flow and mantle heterogeneity, with a specific focus on melt migration beneath mid-ocean ridges.

I address this challenge using computational models of coupled magma / mantle dynamics and thermochemistry. Chapter 2 sets out the model. It is founded on statements for conservation of mass, momentum, energy, and mass of individual chemical species in a system with up to two phases and two thermodynamic components. One component is more fusible than the other. Mantle rock is modelled as a porous, compactible solid that deforms by creeping flow, and magma is modelled as a low viscosity liquid. Local thermodynamic equilibrium is assumed to hold everywhere, and a simple petrological phase diagram is used to relate pressure and bulk composition to the phase compositions, temperature, and melt fraction. Analytical solutions to the model assuming one dimension and steady state are presented; they provide a useful reference for later chapters that explore more complex behaviour in two dimensions.

Digressing from the main theme of melt migration in a chemically heterogeneous mantle, chapter 3 investigates the behaviour of solid mantle flow and melt focusing beneath transform faults. Global observations of mid-ocean ridge bathymetry reveal a correlation between the difference in axial depth across ridge offsets and the direction of ridge migration in the fixed hot spot reference frame. If upwelling and melt production rates are asymmetric across a ridge axis, three dimensional melt focusing may cause variations in the crustal thicknesses across ridge offsets, and thus account for the observed differences in axial depth. In this chapter I use a 3D numerical model

to constrain the flow and thermal structure of a ridge–transform–ridge plate boundary. By coupling a model of melt focusing to our simulations I generate predictions of crustal thickness and axial depth change across offsets of different lengths. These predictions are consistent with the morphological changes observed along the global MOR system. These predictions offer new constraints on the scale of melt focusing at mid–ocean ridges and the extent of melt redistribution at the ridge axis. Results from the simulations also suggest that plate–induced mantle dynamics and melt focusing beneath a migrating MOR may produce global, systematic variations in the geochemistry of axial lavas.

Chapter 4 returns to the main theme of magma flow and mantle heterogeneity beneath ridges. Observations from ophiolites, mantle rocks, and oceanic basalts indicate that magma generated in the mantle rises to the surface through a network of high-porosity, high-permeability channels. The channels are understood to form by a feedback between melt flux and dissolution, and are thought to be instrumental in preserving evidence for mantle heterogeneity in oceanic basalts. Using the computational model outlined in chapter 2 I investigate the relationship between melting, mantle heterogeneity, and channelized magma flow. The model setup consists of an upwelling column of mantle rock, and mantle heterogeneity is modelled by spatially varying the proportions of the two thermodynamic components. Results suggest that preferentially melted heterogeneities can nucleate magmatic channels. For reasonable parameter values, channels do not form in the absence of mantle heterogeneity. Channels that are nucleated by heterogeneities are cooler than the surrounding mantle. Heat diffuses into the channels and powers continued melting, whilst suppressing melting on their flanks. This behaviour is investigated by considering an energetically consistent expression for the melting rate that is derived from conservation principles. Using this result, the relative importance of decompression melting, reactive magma flow, and thermal diffusion to the total melting rate is considered. The results indicate that the energetics and chemistry of melting has profound consequences for the dynamics of magma flow in the mantle, and underscore the need for energetically consistent models of melt migration and mantle deformation.

In chapter 5, the models are extended to consider melt migration, melt focusing, and mantle heterogeneity beneath mid-ocean ridges. The models are initialized using two hypothetical, contrasting patterns of mantle heterogeneity. In one case, heterogeneity is modelled as discrete, randomly shaped blobs of more fusible material that are embedded in an otherwise homogenous, less fusible mantle. In the other case, heterogeneity varies smoothly over all spatial wavelengths greater than a specified cut-off. Results indicate that the topology of mantle heterogeneity has important consequences for the configuration of melt channels and dynamics of melt focusing. Variation in the spreading rate has negligible effect on the arrangement of melt channels and flow focusing. The models predict that segregating melts can collect in off-axis pools. Away from the ridge axis these pools freeze and introduce new heterogeneity into the mantle. It is possible that the melt in these pools could be delivered via dykes to off-axis magma chambers in the crust.

The final results chapter focuses on the speed of melt migration predicted by the models and the time required for magma to travel from the base of the melting region to the ridge axis. To obtain this information, the model domain is seeded with lagrangian particles that track the motion of individual fluid parcels. The models are initialized using the hypothetical patterns described above. For reasonable parameter values, the models predict that magma migrates from the base of the melting region to the ridge axis on time scales between 20 kyr and 350 kyr, with a mean speed of around 1 m/yr. The predicted time scales are around 20% faster in models initialized with mantle heterogeneity than in those initialized with a homogeneous mantle; the results, however, show no significant variation with the topology of mantle heterogeneity. Spreading rate is also observed to have a strong influence on the speed of melt migration. Scaling arguments are employed to understand how the results would change under different parameter regimes. To offer some comparison between predictions from the models and observed data, a simple model of equilibrium partitioning is used to cast the results in terms of ^{230}Th disequilibria. The modelled disequilibria compare well against measurements from zero-age MORB. The comparison indicates that the models presented in this thesis constitute a reasonable first-order description of the dynamics of magma flow in the mantle, and furthermore, provide a new perspective on the consequences of channelized melt flow for the uranium-series geochemistry of oceanic basalts.

Acknowledgements

In researching for this thesis I have benefitted enormously from the help and encouragement offered by a large number of people. To all who follow, and to those who remain unmentioned, I owe a great deal of thanks:

For the guidance, ideas and advice offered by my supervisor, Richard Katz, and for all the intellectual challenges he has provided, I am immeasurably grateful. Especially, I thank Rich for being so generous with his time, for devoting it to every aspect of the project — and to my development as a scientist over the last four and a bit years.

The Natural Environment Research Council, who funded my studentship and made possible a very comfortable standard of living in Oxford.

The Department of Earth Sciences, for providing a stimulating and productive environment over the last seven years for both postgraduate and undergraduate degrees. The training it afforded me is second to none. This thesis would not be what it is without Oxford Supercomputing Centre, who provided compute time and tireless technical support.

Thanks to Tim Elliott for making available the U-series data used in chapter 6, and to David Pyle for helping so readily (and frequently) with my questions about igneous petrology.

Ian Hewitt and John Maclennan for examining my thesis.

To Per Kalvig, for his friendship and mentorship, and for helping to ensure that rocks are never too far away. Thanks also to Mike Searle for an inspirational trip to Oman and for sharing his endless enthusiasm for geology.

Steve Baugh, for instilling a sense of self-belief at an early stage of my education in the earth sciences, and for encouraging me to apply to Oxford in the first place. I often wonder how different things could have been…

My thanks to those who have shared their time, company and experience with me, particularly around the department. Especially, and in no particular order: Tom O'Toole, Mark Bourne, Andrew Valentine, Alistair White, Teresa Kyrke-Smith, Owen Weller, Forest, Cedric Twardzik, Andy Nowacki, Brendan Dyck, Ivana Barisin, Rob Rickman, Brendan McCormick, Jon Wade, Rich Walters, Laura Gregory.

To my friends and family, who remain steadfast and unrelenting in their patience, support and encouragement, I am forever grateful. Finally, my thanks to Helen, for her love and friendship, without which it all would have been much, much harder.

Contents

Chapter 1

Introduction

This thesis seeks to extend our understanding of melt migration in Earth's mantle. It is motivated by a wide range of geological, geochemical, and geophysical observations of the oceanic crust and upper mantle. These observations help to constrain the nature of magma flow and confirm the presence of compositional heterogeneities in the mantle. In existing studies of melt transport, heterogeneity receives scant attention. However, results and analyses presented in this thesis indicate that mantle heterogeneity has profound consequences for the dynamics of melt migration.

1.1 Background

The main focus throughout this thesis is the dynamics of melt migration beneath Earth's mid-ocean ridge system. Mid-ocean ridges (MORs) comprise long chains of volcanoes that are confined to constructive plate margins (figure 1.1). Magmatism along their length generates nearly all of the crust that underlies the world's oceans. Compared to other crust forming regions, the tectonics of the mid-ocean ridge system are relatively simple (figure 1.2a); rigid lithospheric plates riding atop a convecting mantle spread away from one another, and new crust forms in between. In these locations volcanic activity and the genesis of new oceanic crust are consequences of convective motion in the underlying mantle.

Beneath MORs, hot mantle rock upwells and spreads laterally at a similar rate to

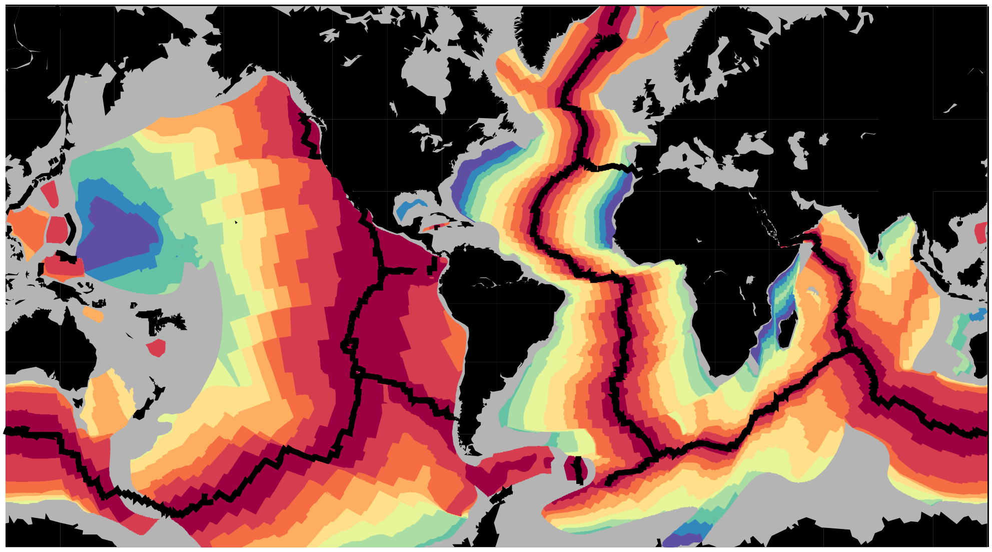

Figure 1.1: Map showing mid-ocean ridges (black lines) and the age of the oceanic crust. Dark red colours show the youngest crust (< 18 Ma) near the ridge, dark greens and purple colours show the oldest crust close to the continents.

the overlying lithospheric plates (figure 1.2a). The upwelling rock decompresses and cools adiabatically, resulting in a temperature gradient of about 0.6°C/km. Melting begins when the temperature of the upwelling rocks first equals or exceeds its solidus temperature (figure 1.2b). Since melting requires latent heat, the ambient temperature in the zone of partial melting drops below the adiabat. So long as the ambient temperature is greater than or equal to the solidus, energy carried by the upwelling mantle supplies the latent heat required to drive continued melting.

During melting, magma forms on boundaries between adjacent mineral grains and collects in pore spaces that form along grain edges. In three dimensions the pores connect to form a permeable network that enables magma to migrate through the porous mantle (Zhu et al., 2011). Generally, magma is less dense than the surrounding rock and buoyancy drives it towards the surface; this segregation of the magma from solid mantle rock causes the matrix to compact under its own weight. Compaction maintains small matrix porosities of around 1%, even in regions where melting converts several weight percent of the rock into magma (e.g McKenzie, 1985).

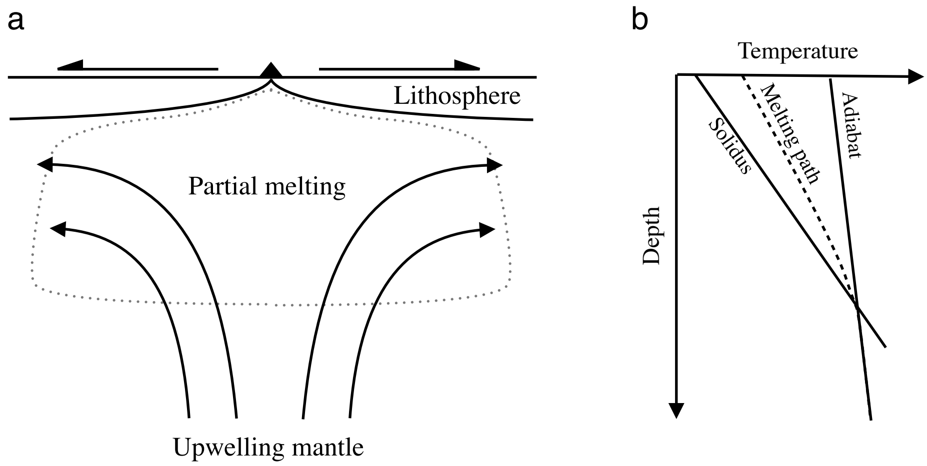

Figure 1.2: (a) The dynamical situation at mid-ocean ridges. Grey dotted line represents region of partial melting. (b) A schematic representation of the solidus, adiabatic temperature profile and temperature profile in the partially molten region directly beneath the ridge axis.

On the opposite side of ocean basins to MORs, the fate of oceanic crust is decided. In most instances, the oceanic crust is ultimately returned to the mantle through a subduction zone. Subducted oceanic crust is compositionally distinct from most other rocks in the mantle; it is an important source of chemical heterogeneity in the mantle, and is discussed in more detail in section 1.4. In exceptional circumstances, sections of the oceanic crust and upper mantle may be thrust onto continents during collisions between tectonic plates and preserved as ophiolites. The resulting slabs of oceanic lithosphere, known as ophiolites, provide remarkable natural laboratories for studying the processes involved in melt migration.

Whilst observations of mantle rocks and frozen magmas provide insights and constraints on melt migration and mantle deformation, efforts to understand the dynamics of the system appeal largely to mathematical theories of two phase flow. These theories model magma as a low viscosity liquid that migrates by porous flow, and consider mantle rock to be a compactible solid that deforms by creeping flow. Numerical models founded on these theories help us to understand the details of where magma originates, investigate how it migrates to the surface, and explore the necessary physical and chemical processes to satisfy constraints on melt migration from observations.

For this thesis, numerical models are the principal tool that I use to investigate melt migration beneath mid-ocean ridges. The aims of existing models are outlined below in section 1.3, and details of the approach and hypothesis explored in later chapters are set out in section 1.5. First, however, I outline existing observational constraints on magma flow in the mantle.

1.2 Constraints on magma flow

1.2.1 Magma flow is a chemically isolated process

Almost all rock formed at MORs is mid-ocean ridge basalt (MORB). Although MORB forms by decompression melting of the mantle, it is not in chemical equilibrium with the harzburgites and lherzolites that make up the residue of partial melting. For example, at Moho pressures MORB–forming magmas are undersaturated in the mineral orthopyroxene, whereas orthopyroxene is a major mineral phase in residual peridotites (harzburgite and lherzolite). This disequilibrium results from the effect of pressure on the relative stability of mineral phases in the mantle (Stolper, 1980). As pressure decreases, the stability of olivine increases at the expense of pyroxenes (figure 1.3). Thus magma formed at high pressure cannot crystallize pyroxene if it is moved to a low pressure environment. Analyses of primitive MORB compositions relative to the cotectics shown in figure 1.3 indicate that MORB-forming magmas last equilibrate with the mantle at depths of 30 km or more (Stolper, 1980). Consequently, for disequilibrium to occur at low pressures, the majority of MORB–forming magmas must migrate through the top 30 km of the mantle in chemical isolation from the residue of partial melting.

The trace element chemistries of MORB and residual mantle rocks provide further evidence for chemical disequilibrium during melt transport. Residual peridotites dredged and drilled from MORs are known as abyssal peridotites. Typically, clinopyroxene crystals in abyssal peridotites are strongly depleted in light rare earth elements (LREE) relative to heavy rare earth elements (HREE), and are far from trace element

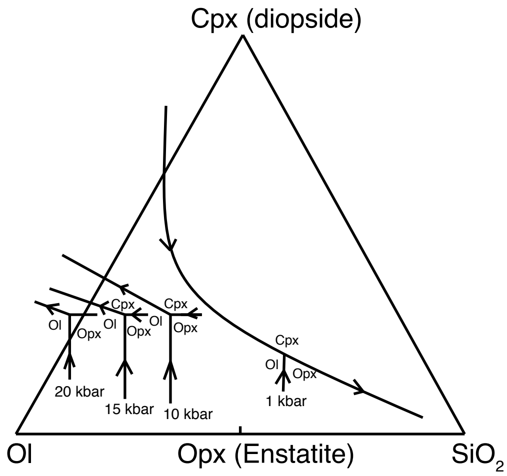

Figure 1.3: Projection of the basalt tetrahedron from plagioclase onto the plane olivine–diopside–silica. Black lines show experimentally determined cotectics for olivine (ol), clinopyroxene (cpx) and orthopyroxene (opx) taken from Stolper (1980).

equilibrium with MORB (figure 1.4, Johnson et al., 1990; Johnson and Dick, 1992; Ross and Elthon, 1997). This strong LREE depletion recorded by abyssal peridotites requires the porosity to be small at the locations where magma is generated. To satisfy this requirement and explain the observed geochemistry, Johnson et al. (1990) and Johnson and Dick (1992) developed a conceptual geochemical model for melting in which very small, but finite increments of melt are generated and then immediately extracted from the mantle. The increments of magma formed over all depths are then mixed to form MORB (Kinzler and Grove, 1992; Sobolev and Shimizu, 1993; Sobolev, 1996).

An important implication of trace element disequilibrium between MORB and residual peridotites is that melt cannot migrate from source to crust by diffuse porous flow through the peridotitic residue of partial melting (Spiegelman and Kenyon, 1992; Iwamori, 1993; Hart, 1993). If fractional melts did migrate mainly through porous residual peridotites, extensive chemical reaction would re-equilibrate the rock and magma. Evidence of trace element fractionation would decrease or vanish, and liquids would move close to low pressure orthopyroxene saturation (Stolper, 1980; Kelemen, 1990; Kelemen et al., 1995b). To preserve disequilibrium, therefore, a large amount of the magma generated in the mantle ($> 80\%$) must migrate to the ridge in chemical

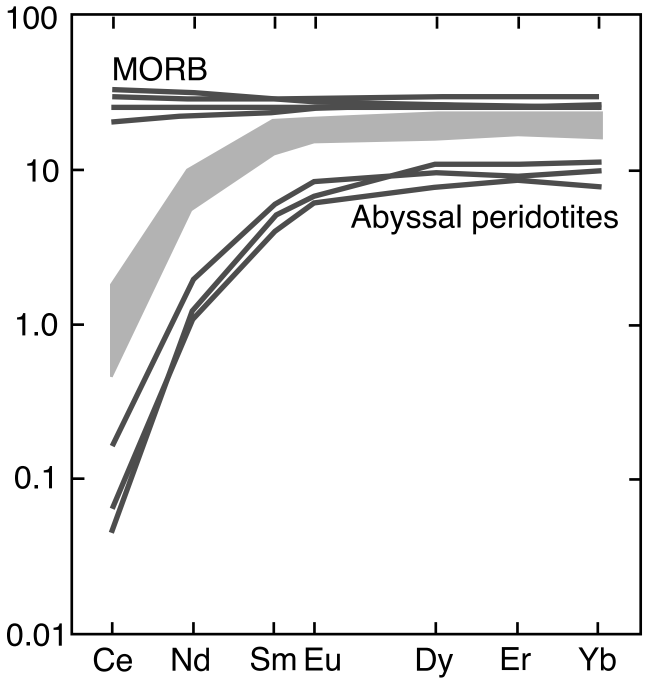

Figure 1.4: Chondrite normalized rare earth element patterns from clinopyroxene crystals hosted in abyssal peridotites and spatially associated basalts from the Atlantis II Fracture Zone, Southwest Indian Ridge. Grey region shows compositions of hypothetical melts in equilibrium with the abyssal peridotites. Modified from Johnson et al. (1990) by permission of American Geophysical Union.

isolation from mantle peridotites (Iwamori, 1993).

1.2.2 Chemical isolation by flow localization

Using simple numerical models and scaling arguments, Spiegelman and Kenyon (1992) investigate the consequences of a nonuniform distribution of magma flux for chemical disequilibrium between MORB and residual peridotites. In particular, they consider chemical equilibrium between rock and magma when flow is localized into vertically oriented channels. Spiegelman and Kenyon (1992) find that melt flow through channels can preserve chemical disequilibrium between MORB–forming magmas and the residue of partial melting if the time taken by magma to traverse the melting region is short compared to the time required for a chemical species to diffuse through the solid between adjacent channels.

1.2.3 Temporal constraints and flow focusing

Estimates of the speed and duration of melt migration beneath MORs derive from two types of observation. One is provided by the uranium–series geochemistry of oceanic basalts, the other is based on geological observations of erupted magmas and deglaciation in Iceland.

Several studies of uranium–series nuclides in zero–age MORB suggest that ^{238}U and ^{230}Th are fractionated in the presence of garnet, and that following fractionation, magma migrates to the surface within a few half-lives of ^{230}Th (75 kyr) (McKenzie, 1985; Williams and Gill, 1989; Beattie, 1993b,a; Spiegelman and Elliott, 1993; Iwamori, 1994; Richardson and McKenzie, 1994; Lundstrom et al., 1995; Stracke et al., 2006; Prytulak and Elliott, 2009). Since garnet is stable at depths greater than 75 km (Hirschmann and Stolper, 1996), the observed U/Th isotope ratios are thought to necessitate magma speeds of around 1 m/yr. Similar observations of ^{226}Ra and ^{230}Th require these isotopes to fractionate within the last 8000 years of melt migration. The implications of ^{226}Ra fractionation from ^{230}Th for the duration of melt migration are the subject of much debate (see Elliott and Spiegelman, 2003; Lundstrom, 2003, for reviews). To outline the end-member possibilities, Saal and Van Orman (2004) and Van Orman et al. (2006) suggest that Ra and Th isotopes are fractionated close to the surface, in which case they provide only weak constraints on the speed and duration of melt migration. On the other hand, if ^{226}Ra and ^{230}Th are fractionated with U and Th in the garnet stability field, the observations require that magma migrates to the surface within 8000 years, necessitating ascent velocities of around 50 m/yr.

Jull and McKenzie (1996) and Maclennan et al. (2002) infer similarly large ascent rates from outpourings of magma associated with deglaciation in Iceland. They propose that ice unloading accelerates decompression melting in the mantle, and note a 2000 year delay between the end of deglaciation and end of enhanced eruption rates. With melt production extending to depth of, perhaps, 100 km, the observations suggest that magma ascends to the surface at speeds of around 50 m/yr.

Kelemen et al. (1997) indicate that porous flow can support magma speeds of

50 m/yr, but suggest that porosities in excess of 6% would be needed to facilitate such great flow speeds beneath slow spreading ridges. However, efficient fractionation between LREE and HREE and uranium-series nuclides requires porosities of order 0.1%. The conceptual model of magma flow through channels by Spiegelman and Kenyon (1992) offers a resolution to this contradiction if the melt channels have a higher porosity ($> 1\%$) than the inter–channel regions (0.1%).

An additional requirement of the channel network beneath mid-ocean ridges is that it delivers magma from a wide region of partial melting to a narrow region at the ridge axis (Vera et al., 1990; Dunn et al., 2000). Observations of the East Pacific Rise by seismic and magnetotelluric techniques (Forsyth et al., 1998; Baba et al., 2006), and of the Mariana back–arc spreading ridge by electrical resistivity (Matsuno et al., 2012) show that the melting region is triangular-shaped, has an average porosity of $\lesssim 1\%$ and extends to several hundred kilometres either side of the ridge axis. However, observations of the East Pacific Rise between 9°N and 10°N by seismic reflection (Vera et al., 1990) and tomography (Dunn et al., 2000) reveal that the crust reaches its full thickness within a 2–5 km the ridge axis. These observations imply that melt is strongly focused to the ridge axis.

1.2.4 Field observations of channelized flow

Evidence for channelized melt migration is preserved at the outcrop and regional scale in ophiolite complexes. Ophiolites are sections of the oceanic crust and upper mantle that are emplaced onto continents during episodes of tectonic activity. One of the most complete and well studied examples is the Semail ophiolite, which outcrops along the northern coast of Oman and eastern seaboard of the United Arab Emirates. Combined structural, petrological and geochemical studies demonstrate that the Semail ophiolite formed at an oceanic spreading centre located above a subduction zone (Searle and Cox, 1999; MacLeod et al., 2012). The ophiolite is around 20 km thick, roughly comprising an 8 km thick layer of oceanic crust and 12 km of the upper mantle. Chemical analyses indicate that the basalts and gabbros in the crustal section derive from MORB–like parental magmas (Pearce et al., 1981; Pallister and Knight, 1981; Alabaster et al., 1982; Godard et al., 2003), and harzburgites and lherzolites in the $>$ 12 km thick mantle section are analogous to abyssal peridotites (Hanghøj et al., 2010). These similarities between rocks in Oman and samples from MORs indicate that ophiolites are formed by processes similar to those operating at mid-ocean ridges.

Evidence for localized flow takes the form of dunite ($>$ 90% olivine) bodies hosted in residual harzburgites and lherzolites. Dunites observed in ophiolites do not necessarily indicate localized magma flow; for instance, some are recognized as cumulates (Kelemen et al., 1997). However, those that do indicate localized magma flow are referred to exclusively as 'mantle dunites'. Kelemen et al. (1995a) first unravelled the full significance of mantle dunites for melt transport from outcrops in the Semail ophiolite. They are now also recognized in a number of ophiolites including the Trinity ophiolite, United States (Quick, 1981; Lundstrom et al., 2005), Josephine peridotite, United States (Kelemen et al., 1992; Sundberg et al., 2010), Bay of Islands ophiolite, Canada (Suhr, 1992; Suhr et al., 2003), Troodos, Cyprus (Batanova and Sobolev, 2000; Buchl et al., 2002), and Voykar, Polar Urals (Salevieva et al., 2008; Batanova and Savelieva, 2009).

Mantle dunites in these ophiolites exhibit common field relationships and structural features. They occupy $5-15\%$ of the exposed mantle section, forming networks of anastomosing bodies with tabular, cylindrical, and vein–like geometries (figure 1.5. See also Batanova and Savelieva, 2009). Mantle dunites vary in width from several centimetres to a few hundred metres and are continuous over length scales from metres to kilometres (Kelemen et al., 1997). Contacts between dunites and pyroxene–bearing peridotites are knife sharp.

Several key observations indicate that mantle dunites replace, rather than intrude, the host peridotites. Figure 1.6 illustrates some of the most important field relationships that indicate a replacive origin. Figure 1.6a shows that some dunites cross cut pyroxene–rich bands without incurring any displacement. In some location, relict trains of spinel within the dunites link pyroxene–rich bands on either side (grey rhombs in figure 1.6a). Dunites can selectively replace pyroxene–rich bands without

Figure 1.5: Field photo of mantle dunites (light brown) hosted in the residual harzburgites and lherzolites (dark brown) of the Oman ophiolite. Outcrop location: cliffs behind Muscat, Oman, 23.62°N, 58.56°E. Blue rucksack is 0.4 m long.

distorting the bands or surrounding foliation (figure 1.6b). Local widening features observed in the dunites do not dilate or deform the foliation in the host peridotites (figure 1.6c) and, furthermore, anastomosing dunites leave islands of unaltered residual peridotite that are not rotated or displaced relative to the surroundings (figure 1.6d). These field relationships strongly indicate that dunites are not intruded as dykes. If this were the case, intrusion would displace the wall rocks and preclude relict trains of spinel in dunite, distort the rock fabric surrounding widening features and intruded pyroxene–rich bands, and islands of unaltered mantle peridotite should be rotated relative to the wall rock.

Trace element analyses of rocks within the Semail ophiolite reveal that interstitial clinopyroxene crystals found within the dunites are in equilibrium with basalts in the crustal section, but are far from equilibrium with the harzburgites and lherzolites of the mantle section (Kelemen et al., 1995a). These observations provide further evidence that mantle dunites represent chemically isolated channels through which

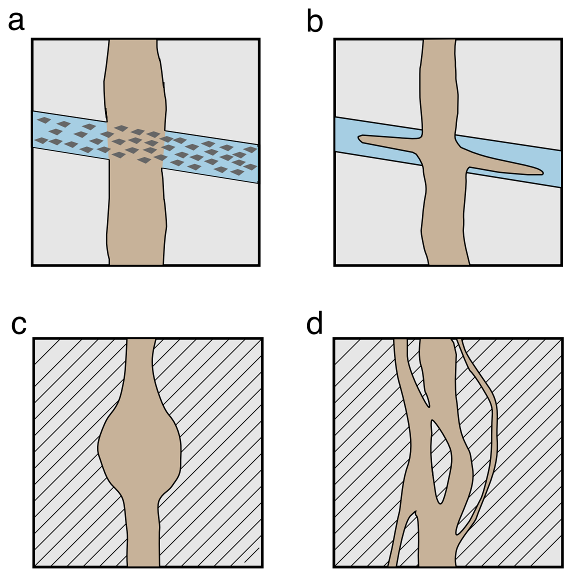

Figure 1.6: Schematic showing key field relationships between replacive dunites (dark brown), pyroxene–rich bands (blue) and residual peridotites (light brown). (a) Dunites cross-cut pyroxene rich bands without incurring any displacement. Relict spinel crystals (grey diamonds) present in the dunites form continuous trains with spinels in the pyroxene–rich bands to either side of the dunite. (b) Dunites that cross cut pyroxene–rich bands can laterally invade the bands without inducing any displacement. (c) Local widening features observed in the dunites do not dilate or deform the foliation in the host peridotite (black lines). (d) Blocks of peridotite hosted within the dunites show no signs of rotation relative to the surrounding peridotite. Adapted by permission from Macmillan Publishers Ltd: Nature, (Kelemen et al., 1995a), copyright 1995.

MOR–forming magmas flow to the surface.

Replacive dunites are understood to originate by a reaction that involves simultaneous dissolution of pyroxene and precipitation of olivine during melt migration by porous flow (Kelemen et al., 1995a). This combined process of melt migration and chemical reaction is known as reactive flow. Magmas generated from mantle peridotites will be above their liquidus temperature on rising adiabatically to lower pressures (Sleep, 1975). Kelemen et al. (1995b) showed that these magmas will react with and dissolve mantle peridotites as they rise through the mantle, until saturating in olivine. With further ascent the liquids continue to dissolve pyroxene and simultaneously precipitate olivine. At typical magmatic temperatures, the latent heat of fusion, per unit mass, of olivine is approximately 1.3 times that of pyroxenes. Therefore, reactions between olivine–saturated magmas and pyroxene–bearing rocks at constant pressure and enthalpy increase the mass of the liquid and porosity of the solid (Kelemen, 1990; Daines and Kohlstedt, 1993). During decompression, this reactive flow process will increase the liquid mass further still and result in the dunite dissolution channels having a higher porosity than the ambient peridotites. But what processes can cause flow to localize into channels?

1.3 Mechanisms of flow localization

1.3.1 Hydraulic fracture

One obvious possibility is that melt localizes into cracks and fractures (Nicolas, 1986; Sleep, 1988; Ito and Martel, 2002; Maalœ, 2003). Nicolas (1986) notes that sufficiently high fluid pressures could cause the matrix to fracture. Sleep (1988) suggests that once fractures are initiated, the low fluid pressure within them draws in melt from the surrounding matrix; the fractures can open and grow if the fluid pressure exceeds the minimum principal stress. In this context, mantle dunites could represent reaction zones around a melt–filled crack, with the crack having subsequently annealed (Nicolas, 1986; Takahashi, 1992). Melt localization by hydraulic fracture is a particularly appealing explanation for the tabular geometry of many mantle dunites. However, Kelemen and Dick (1995) questions whether magma can fracture mantle rock within the melting region, since plastic deformation may relieve the large stresses needed for fracture.

1.3.2 Mechanically driven instability

Another possibility is that melt localization is due to a fluid dynamical instability identified by Stevenson (1989) that results from a feedback between melt distribution and deformation. Of vital importance to this instability is the shear viscosity of partially molten rock, which is well understood to weaken with increasing melt fraction (Hirth and Kohlstedt, 1995a,b; Holtzman et al., 2003a,b). Stevenson (1989) shows that in a partially molten rock deformed under shear, melt is drawn into regions with enhanced porosity, since these regions are weaker and have a lower mean fluid pressure than those with a lower melt fraction. Subsequent laboratory experiments show that this positive feedback causes melt to organize into high porosity band oriented at 20° to the direction of maximum compressive stress (Holtzman et al., 2003a,b; King et al., 2010). In these laboratory experiments, however, partially molten aggregates are deformed at strain rates that are six to eight orders of magnitude larger than in the mantle (Kohlstedt and Holtzman, 2009). Understanding how this melt localizing mechanism behaves under mantle conditions requires further investigation with the aid of numerical models.

1.3.3 Reaction driven instability

A further mechanism that may account for channelized flow is a reaction–driven instability, first identified by Chadam et al. (1986), that relies on a feedback between liquid flux and dissolution. Beneath MORs and in other magma–producing regions in the mantle, the context for this instability is buoyantly rising magma that becomes increasingly undersaturated in pyroxene towards the surface (figure 1.3, Stolper, 1980; Kelemen et al., 1995b). Rising magmas react with and dissolve mantle rock, locally

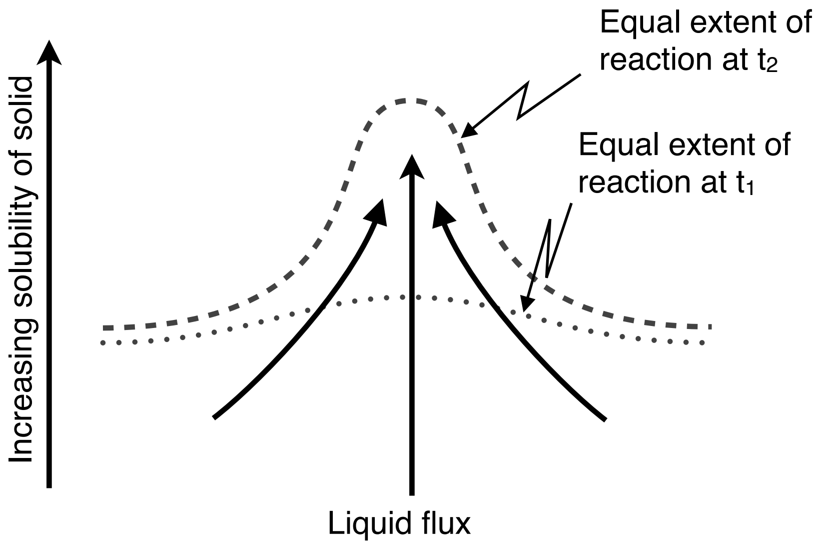

Figure 1.7: Schematic illustration of the reaction infiltration instability (Ortoleva et al., 1987). Solid black arrows indicate direction of melt flux. Dashed and dotted grey lines represent contours of constant dissolution at times t_1 and t_2 respectively.

increasing the porosity. In regions of larger than average porosity the melt flux and rate of dissolution will be greater, which further increases the porosity and establishes a positive feedback (figure 1.7). This is known as the reaction infiltration instability (Ortoleva et al., 1987) and is currently the favoured mechanism for flow localization and dunite formation (e.g Aharonov et al., 1995; Kelemen et al., 1995b, 1997; Spiegelman et al., 2001; Spiegelman and Kelemen, 2003; Batanova and Savelieva, 2009; Liang et al., 2010). The reactive infiltration instability and its consequences for magma flow and MORB are explored in chapters 4, 5 and 6 of this thesis.

If all three mechanisms described above occur under mantle conditions, it is possible that they reinforce each other to localize melt. Indeed, Kelemen and Dick (1995) find examples in the Josephine peridotite where replacive dunites coincide with ductile shear zones, suggesting that reaction– and shear–driven instabilities operated in synchrony.

1.3.4 Theoretical models and numerical experiments

General approach, previous studies

Theoretical models and numerical experiments are invaluable tools for understanding how the melt localizing mechanisms described above may behave under mantle conditions. The reactive infiltration instability is a specific focus of many numerical models, owing to its potential to explain a wide range of field and geochemical observations (Aharonov et al., 1995; Spiegelman et al., 2001; Spiegelman and Kelemen, 2003; Elliott and Spiegelman, 2003; Liang et al., 2010; Schiemenz et al., 2011; Hesse et al., 2011; Hewitt, 2010). With the exception of Hewitt (2010), the general approach of these models is to couple a formulation for reactive flow up a solubility gradient with equations that describe porous melt migration and deformation of the matrix (McKenzie, 1984; Fowler, 1985; Ribe, 1985; Scott and Stevenson, 1986; Bercovici et al., 2001). These numerical experiments use chemical kinetics to model melting and dissolution reactions and assume that the mantle is compositionally homogenous prior to the onset of melting.

Using this approach, numerical experiments by Aharonov et al. (1995) first showed that dissolution between upwelling magma and ambient mantle rock drives a reactive instability (section 1.3.3) that causes melt to localize into high porosity channels. Subsequent models verify this result and help to explore the geochemical consequences of channelized magma flow (Spiegelman and Kelemen, 2003; Elliott and Spiegelman, 2003; Morgan and Liang, 2003; Liang et al., 2010; Schiemenz et al., 2011). These models and their findings are discussed in more detail in chapters 4, 5 and 6.

Energetics of melting

A shortcoming of most existing numerical experiments that investigate reactive flow in the mantle is that they neglect the energetics of the system (Aharonov et al., 1995; Spiegelman et al., 2001; Spiegelman and Kelemen, 2003; Elliott and Spiegelman, 2003; Morgan and Liang, 2003; Liang et al., 2010; Schiemenz et al., 2011; Hesse et al., 2011). Melting, however, is an inherently thermodynamic process; theoretical experiments that predict melting rates without accounting for conservation of energy are inconsistent.

Recent studies by Katz (2008, 2010) and Hewitt (2010) address this deficiency with numerical experiments of melt migration and mantle deformation that incorporate conservation of energy. Their experiments allow for decompression melting and dissolution reactions between rock and magma in a thermodynamically consistent framework; they more accurately represent the natural system. But their results and accompanying stability analysis (Hewitt, 2010) predict that channels do not emerge within a homogenous mantle. However, Hewitt (2010) finds that flow is destabilized and localizes into channels if an additional melt flux is imposed at the base of, or at an arbitrary position within, the melting region.

A contradiction and a challenge

These results from the energy–conserving experiments by Katz (2008, 2010) and Hewitt (2010) challenge the earlier understanding of reactive flow and channelized melt transport developed by Aharonov et al. (1995); Spiegelman et al. (2001); Spiegelman and Kelemen (2003); Elliott and Spiegelman (2003); Morgan and Liang (2003); Liang et al. (2010); Schiemenz et al. (2011) and Hesse et al. (2011). What are the implications of these contradicting results? Is the reactive infiltration instability a physically and energetically plausible mechanism that localizes magma flow and forms mantle dunite? Are the current models of melt migration and mantle deformation adequate, or do they miss an important component of the natural system?

In this thesis I address these questions with energy-conserving numerical experiments in chapters 4, 5 and 6. I argue that conservation of energy is essential in theoretical models of melt migration and mantle deformation, that reactive instabilities are the primary mechanism by which melt localizes, and that existing numerical models miss from the natural system an ingredient of vital importance to reactive melt transport. That ingredient is mantle heterogeneity.

1.4 Mantle heterogeneity

Major element, trace element and isotopic variations in oceanic basalts prove that the mantle is chemically heterogeneous on a range of scales (e.g Schilling, 1973; Dupré and Allègre, 1983; Hofmann, 1997, 2003; Shorttle and Maclennan, 2011). Although heterogeneity is widely recognized and accepted, its implications for melt migration have received scant attention.

The largest scale of heterogeneity is evident in strontium, neodymium, hafnium and lead isotope ratios of MORB from different ocean basins (Dupré and Allègre, 1983; Hofmann, 1997, 2003). These variations reflect the differing degrees to which the mantle is depleted, mainly by formation of the continental crust. Geochemical evidence for shorter length scale heterogeneity is evident in lead isotope heterogeneity measured in individual phenocrysts of plagioclase in MORB samples (Bryce and DePaolo, 2004), and additionally in lead isotope heterogeneity in olivine–hosted melting inclusions in hand specimens collected from a single Icelandic lava flow (Maclennan, 2008).

An obvious source of metre to kilometre–scale heterogeneity is subducted oceanic crust. Allègre and Turcotte (1986) envisage a 'marble cake' mantle, in which convection stirs subducted oceanic crust into mantle peridotites. With the aid of scaling arguments, Allègre and Turcotte (1986) hypothesize that convection can shear kilometre–sized blocks of recycled oceanic crust into centimetre wide veins on timescales of 1 Ga. In the solid mantle, chemical diffusion is slow enough for such thin veins to survive as distinct compositional heterogeneities for 10^8 years (Hofmann and Hart, 1978; Allègre and Turcotte, 1986). In the presence of melt, diffusion is much more rapid, and the veins could be erased within $10^5 - 10^6$ years.

Recycled oceanic crust is widely recognized in the geochemistry of oceanic basalts (e.g. Hauri et al., 1996; Hirschmann and Stolper, 1996; Sobolev et al., 2005; Herzberg, 2006; Kokfelt et al., 2006; Prytulak and Elliott, 2007; Sobolev et al., 2007, 2008; Dasgupta et al., 2010; Herzberg, 2011; Shorttle and Maclennan, 2011). Under the pressure and temperature conditions of the mantle, oceanic basalts metamorphose into eclogite, a rock containing garnet, omphacite (high pressure sodic pyroxene), and accessory minerals such as quartz, kyanite, rutile and epidote. During adiabatic decompression, eclogite begins to melt at deeper depths than the host harzburgites and lherzolites (Yasuda et al., 1994). Melts derived from eclogites are far from equilibrium with mantle peridotites and will react with the ambient material. Then, following continued upwelling, the ensemble of reaction products, remnant eclogites, and ambient peridotites melt to produce the magmas that form oceanic basalts. Much debate surrounds the exact lithology of the reaction products. High pressure laboratory experiments by Yaxley and Green (1998) and Yaxley (2000) suggest that reaction between eclogite–derived melts and mantle peridotites produces an array of ‘refertilized’ lherzolites with different modal proportions of olivine, clinopyroxene, orthopyroxene, and garnet. Supported with analyses of Hawaiian basalts, Sobolev et al. (2005) argue that eclogitic melts and peridotites react in approximately equal proportions to produce an olivine–free pyroxenite, but an olivine–free lithology is not required to satisfy chemical signals of recycled oceanic crust in Icelandic basalts (Shorttle and Maclennan, 2011).

Despite these varied findings there is universal agreement that mantle rocks altered by recycled oceanic crust have a lower solidus temperature than the ambient, unaltered, harzburgites and lherzolites (Hirschmann and Stolper, 1996; Takahashi et al., 1998; Pertermann and Hirschmann, 2003). An important consequence is that the melting behaviour of the mantle depends on composition. More fusible and fertile compositions melt at deeper depths than the ambient peridotite and magmas derived from some of the most fusible heterogeneities are preserved in olivine–hosted melt inclusions (Maclennan, 2008). To explain these melt inclusion data and observations of osmium isotopes, Kogiso et al. (2004) and Maclennan (2008) suggest that high porosity melt channels are rooted in regions that are enriched by recycled oceanic crust.

1.5 Principal hypothesis

Motivated by

- the suggestions by Kogiso et al. (2004) and Maclennan (2008) that high porosity melt channels are rooted at enriched heterogeneities,
- energetically consistent numerical experiments by Hewitt (2010) that predict channelized flow when an additional flux of magma is imposed at some depth within the melting region,

I hypothesize that channelized reactive melt transport is a consequence of melting in compositionally heterogeneous mantle. In adiabatically upwelling mantle, heterogeneities enriched in recycled oceanic crust begin to melt at deeper depths than unaltered mantle peridotites. At slightly shallower depths, where the ambient mantle begins to melt, the enriched, partially molten heterogeneities will deliver an additional flux of magma to the background melting region. Chemical disequilibrium will exist between the partially melting peridotites and magma derived from the enriched heterogeneities. The disequilibrium will promote reactive melting and could lead to channel formation by a mechanism similar to the reaction infiltration instability (section 1.3.3). Furthermore, newly established and growing channels may coalesce with a preexisting channel network, enabling magmas generated deep in the mantle to travel to the surface in chemical isolation.

1.6 Outline of thesis

This hypothesis is tested and developed in the chapters that follow. Chapter 2 outlines a physically and energetically consistent mathematical model for the generation and deformation of partially molten rock. The approach is founded on fluid dynamical theories of two phase flow; the model rock is assumed to comprise two chemical components and coexisting rock and magma are assumed to be in thermodynamic equilibrium. Steady state, one dimensional solutions presented at the end of the chapter review the basic behaviour of the system.

Chapter 3 digresses from the main theme of reactive melt transport beneath mid-ocean ridges and instead focuses on large–scale solid mantle flow. Motivated by global observations of mid-ocean ridge bathymetry, it explores the effect that plate motion has on mantle flow and melting beneath transform faults with three dimensional numerical experiments. The findings promote a discussion on how melt is delivered to, and redistributed along individual ridge segments.

Returning to the topic of melt migration in chapter 4, I use the model outlined in chapter 2 to test the hypothesis that channelized melt transport is a consequence of melting in a heterogeneous mantle. The experimental setup comprises a two dimensional column of upwelling mantle rock in which is embedded a discrete, disk–shaped heterogeneity that is more fusible than the ambient mantle. Results from the experiments confirm the hypothesis, suggesting that preferentially melted heterogeneities can nucleate magmatic channels. The melting rate is analysed and the results highlight the importance of taking an energetically consistent approach to melting and mass transfer between the phases.

Chapter 5 has two main objectives. The first is to explore the dynamics of reactive melt transport in numerical experiments with boundary conditions appropriate for a mid-ocean ridge. These experiments are the first to consider the effects of plate spreading on channelized, reactive magma flow using a physically consistent numerical model. The models are initialized with contrasting hypothetical patterns of mantle heterogeneity. The second objective is to investigate the consequences of these patterns for the dynamics of melt migration. Results indicate that the distribution of mantle heterogeneity has important consequences for the configuration of melt channels and focusing of magma to the ridge axis. Furthermore, the results suggest that some segregating melts can pool away from the ridge axis and introduce new heterogeneities into the mantle.

In chapter 6 I investigate the consequences of mantle heterogeneity for the speed of melt migration beneath ridges and for the time taken for magma to travel from its source to the ridge axis. Numerical experiments suggest that the presence of mantle heterogeneity and spreading rate strongly affect the time scale of melt migration.

Scaling arguments are employed to understand how the results would change under different parameter regimes. For reasonable parameter values, the predicted durations of melt migration in a heterogeneous mantle vary over an order of magnitude between 10^4 and 10^5 years. To my knowledge, this is the first study that accurately determines the duration of melt migration predicted by a physically consistent model of reactive magma flow in the mantle. In addition, I use a simple model of equilibrium partitioning to cast the results in terms of ^{230}Th disequilibria and compare modelled excesses against measurements from zero–age MORB. The comparison indicates that models presented in this thesis constitute a reasonable first–order description of the dynamics of magma flow in the mantle, and provide a new perspective on the consequences of channelized melt flow for the uranium–series geochemistry of oceanic basalts.

Chapter 2

Generation and deformation of partially molten rock

2.1 Introduction

The dynamics of partially molten regions inside the Earth are routinely described using theories of two phase flow that account for physical and chemical interactions between solid rock and liquid magma. Of fundamental importance to these fluid dynamical models are geological and experimental observations that the solid mantle deforms by creeping flow and that magma resides in interstitial spaces between adjacent grains. Along three-grain boundaries the interstitial spaces interconnect, forming a three-dimensional porous network through which magma flows (Vaughan and Kohlstedt, 1982; Cooper and Kohlstedt, 1986; Zhu et al., 2011). In this context, deviations of the fluid pressure from the lithostatic cause the matrix of grains to compact or dilate, and thermodynamic and chemical processes result in mass transfer between the phases. Including these elements in a physically and energetically consistent model is crucial for a reasonable fluid dynamical perspective on the generation and deformation of partially molten rock.

Many authors have proposed equations to model partially molten rock (Sleep, 1974; Turcotte and Ahern, 1978; Ahern and Turcotte, 1979; McKenzie, 1984; Fowler, 1985; Ribe, 1985; Scott and Stevenson, 1986; Spiegelman, 1993a; Bercovici et al., 2001).

Most models are founded on statements of conservation for mass and momentum of liquid magma and solid rock. Depending on the aim of a particular study, conservation of energy and composition might also be included. Whilst particular details differ between derivations, they all share the same basic form.

Solutions to the models and experiments on physical analogues suggest that magma flow in the mantle is unstable. Some results suggest that fluid dynamical instabilities cause porosity variations to propagate through the partially molten medium as waves (e.g. Spiegelman, 1993c,b; Hesse et al., 2011); others indicate that melt localizes into high porosity features such as bands and channels (e.g. Stevenson, 1989; Aharonov et al., 1995, 1997; Zimmerman et al., 1999; Spiegelman et al., 2001; Holtzman et al., 2003a; Spiegelman, 2003; Spiegelman and Kelemen, 2003; Katz et al., 2006; Liang et al., 2010; King et al., 2010; Katz and Weatherley, 2012; Weatherley and Katz, 2012). Many of these investigations demonstrate that melting and mass transfer between the two phases by reaction can have important consequences for the dynamics of magma flow. Despite this general conclusion, few studies adopt a thermodynamically consistent approach to melting and reaction, or consider the full melting process.

The novel feature of Ribe (1985) and more recent studies by Katz (2008); Hewitt and Fowler (2008); Katz (2010); Hewitt (2010); Tirone et al. (2012); Weatherley and Katz (2012); Katz and Weatherley (2012) is their thermodynamically consistent approach to mass transfer between the phases, and thus to capturing the full melting process. These studies assume thermodynamic equilibrium and, with the exception of Hewitt and Fowler (2008) who neglected compositional variation, use a petrological phase diagram to relate bulk enthalpy, composition, and pressure to the phase compositions, temperature, and local melt fraction.

In this chapter I adopt this approach and set out a physically and thermodynamically consistent mathematical model for the generation and dynamics of partially molten rock. The equations that follow are based on the formulation by McKenzie (1984), but the form and approach is closest to Katz (2008). In common with the equivalent formulations by Fowler (1985); Ribe (1985); Scott and Stevenson (1986); Spiegelman (1993a); Bercovici et al. (2001), the equations apply to scales upwards of several grains where the physical properties of grains and interstitial magma are representative of the bulk asthenospheric mantle.

The remainder of this chapter is as follows. Section 2.2 sets out conservation statements for mass and momentum that govern the mechanical aspects of the system, and also outlines constitutive laws for permeability and rheology. Conservation statements for energy and mass of chemical components are described in section 2.3 and section 2.4 details how a simple petrological phase diagram is used to relate bulk enthalpy, composition and pressure to the phase compositions, temperature, and local melt fraction. Steady one-dimensional solutions are provided in section 2.5. Boundary conditions and details on the solution method are saved for subsequent chapters when the model is solved numerically in two dimensions. Finally, section 2.6 presents a nondimensionalization of the system of governing equations.

2.2 Governing equations: Mechanics

2.2.1 Conservation of mass

Conservation of mass for the liquid and solid phases can be written as

$$\frac{\partial \rho_f \phi}{\partial t} + \boldsymbol{\nabla} \cdot \rho_f \phi \mathbf{v}_f = \Gamma, \tag{2.1}$$

$$\frac{\partial \rho_m (1 - \phi)}{\partial t} + \boldsymbol{\nabla} \cdot \rho_m (1 - \phi) \mathbf{v}_m = -\Gamma, \tag{2.2}$$

where ρ_f and ρ_m are the densities of the liquid (magma) and matrix (solid rock), $\mathbf{v}_f$ and $\mathbf{v}_m$ are the velocities of the liquid and matrix, ϕ is porosity, t is time, and Γ is the rate of mass transfer from the solid to the liquid. Equation 2.1 states that the change in fluid mass at a point is caused by divergence of the fluid flux and rate of mass transfer from the solid to the liquid. Equation 2.2 is an equivalent expression for the solid mass.

2.2.2 Conservation of momentum

Conservation of momentum for the liquid phase closely resembles Darcy's law for flow through a porous medium. It is expressed as

$$\phi\left(\mathbf{v}_f - \mathbf{v}_m\right) = -\frac{K}{\mu}\left[\boldsymbol{\nabla} P_f - \rho_f g \mathbf{k}\right], \tag{2.3}$$

where K is permeability, defined in section 2.2.4, μ is the viscosity of the liquid, P_f is the fluid pressure, g is gravity and z is the depth. The z direction is defined to be parallel to and point in the same direction as gravity, hence $g = \mathbf{g} \cdot \hat{\mathbf{k}}$. Equation 2.3 states that the segregation of magma from the porous matrix is driven by gradients in the fluid pressure and body forces acting on the liquid. These driving forces are modulated by the viscosity of the liquid and permeability.

An important consequence of melt segregation is that pressure differences between the liquid and solid phases can drive compaction or dilation of the porous matrix. The resistance of the matrix to volume change is quantified by the bulk viscosity. Physically, one can expect the matrix to be more resistant to compaction or dilation when the amount of interstitial melt is small and for the bulk viscosity to become infinitely large when only infinitessimal amounts of melt are present. A constitutive relationship for the bulk viscosity that describes this behaviour is defined in section 2.2.4. Section 2.2.3 also provides a more comprehensive mathematical description of compaction in partially molten rock.

Considering, then, that the matrix is compressible when partially molten and also deforms in response to stresses by creeping flow, conservation of momentum for the matrix phase can be written as

$$\boldsymbol{\nabla} P_f = \boldsymbol{\nabla} \cdot \eta\left(\boldsymbol{\nabla}\mathbf{v}_m + \boldsymbol{\nabla}\mathbf{v}_m^{\mathrm{T}}\right) + \boldsymbol{\nabla}\left[\left(\zeta - \frac{2}{3}\eta\right)\boldsymbol{\nabla} \cdot \mathbf{v}_m\right] + \bar{\rho} g \hat{\mathbf{k}}, \tag{2.4}$$

where P_f is the fluid pressure, η is the shear viscosity, defined in section 2.2.4, ζ is the bulk visocisty, and $\bar{\rho} = \phi\rho_f + (1-\phi)\,\rho_m$ is the phase averaged density. Equation 2.4 states that pressure gradients in the liquid are balanced by the divergence of viscous stresses in the matrix, pressure gradients arising from divergence of the solid flux, and body forces acting on the mixture of fluids.

Important features of equations 2.3 and 2.4 are that they (i) consistently couple stresses arising from deformation of the matrix with fluid pressure and (ii) hold even when mass is transferred between the two phases.

2.2.3 Reformulation

Potential difficulties associated with numerical solution of equations 2.1–2.4 arise because the bulk viscosity can introduce a singularity in equation 2.4 when $\phi \to 0$. To avoid problems associated with this limit, two modifications are made to simplify and reformulate the mechanical model.

The first is to neglect density variations in all terms except for those associated with buoyancy. This simplification is an extension of the Boussinesq approximation. The aim of the second modification is to reformulate equations 2.1–2.4 so that the bulk viscosity appears as a denominator, thus avoiding a singularity when ζ is infinitely large. Following Katz et al. (2007), the fluid pressure is decomposed into three components

$$P_f = P_L + \mathcal{P} + P^*, \tag{2.5}$$

where

$$P_L = \rho g z \tag{2.6}$$

is the lithostatic pressure,

$$\mathcal{P} = \left(\zeta - \frac{2}{3}\eta\right) \boldsymbol{\nabla} \cdot \mathbf{v}_m \tag{2.7}$$

is the pressure exerted on the fluid by compaction or dilation of the matrix, otherwise known as the ‘compaction pressure’. In this relationship the term $-2\eta/3$ removes contributions to the stress tensor for the solid that arise from matrix shear. The remaining dynamic pressure

$$\boldsymbol{\nabla} P^* = \boldsymbol{\nabla} \cdot \eta \left(\boldsymbol{\nabla} \mathbf{v}_m + \boldsymbol{\nabla} \mathbf{v}_m^{\mathrm{T}}\right) - \phi \Delta\rho g \hat{\mathbf{k}}, \tag{2.8}$$

where $\Delta\rho = \rho_m - \rho_f$, results from viscous shear of the matrix and buoyancy forces. This is Stokes' equation and governs the large-scale shear flow of the solid. It states that dynamic pressure gradients arise from divergence of viscous shear stresses in the matrix and from the buoyant effect of magma in interstitial spaces.

To complete the reformulation, equations 2.1–2.2 are summed and combined with the divergence of 2.3 and equation 2.4 subject to the pressure decomposition (equations 2.6–2.8) to give

$$-\boldsymbol{\nabla}\cdot\frac{K}{\mu}\boldsymbol{\nabla}\mathcal{P} + \frac{\mathcal{P}}{\xi} = \boldsymbol{\nabla}\cdot\frac{K}{\mu}\boldsymbol{\nabla}\left(P^* + \Delta\rho g z\right), \tag{2.9}$$

where $\xi = \zeta - 2/3\eta$ is the compaction viscosity. Following this reformulation, equations 2.7-2.9 describe the mechanics of partially molten rock and are used to solve for $\mathcal{P}$, P^* and $\mathbf{v}_m$. To close these equations requires constitutive laws for permeability, shear viscosity and bulk viscosity, which are outlined below.

2.2.4 Constitutive relationships

Permeability

The permeability of partially molten rocks limits the rate at which magma can be transported through the aggregate. It is solely prescribed by the geometry and interconnectedness of melt-filled pores. At the grain scale under asthenospheric conditions, melt is understood to reside in interstitial spaces between three or more adjacent grains. The geometry of the spaces is a function of the relative interfacial energies between solid-solid (grain boundary) and solid-liquid (pore wall) joins (Herring, 1951). These energies are manifested as dihedral angles between adjacent grains. If the dihedral angle is greater than 60° melt collects in isolated pockets, but smaller angles result in an interconnected melt network along grain edges (von Bargen and Waff, 1986; Zhu et al., 2011). Dihedral angles of 10-50° are commonly observed in partially molten rock (Waff and Bulau, 1979; Riley Jr. and Kohlstedt, 1991; Cmiral et al., 1998; Faul, 1997; Holness, 2005) and indicate a well–connected network of pore spaces.

Mathematical models for permeability are commonly based on an array of cylindrical tubes (Bear, 1972; Turcotte and Schubert, 2002; Costa, 2006) that represent interstitial spaces along three-grain boundaries. Assuming that the cylinders act as capillary tubes, and that Poiseuille flow describes motion of the liquid through them, permeability and porosity are related by

$$K = k_0 \phi^n, \tag{2.10}$$

where $k_0 = d^2/C$ is the permeability coefficient, d is the diameter of grains in the matrix and the constants C and n depend on the specific geometry and arrangement of the cylinders. If the cylinders have a uniform diameter and are arranged in an isotropic manner, then $n = 2$ (Faul, 2001; Turcotte and Schubert, 2002). However, laboratory experiments (Wark and Watson, 1998; Connolly et al., 2009), geological observations (Wark, 2003), and theory (Faul, 1997, 2001) indicate that $n = 3$ is more appropriate for the asthenospheric mantle. Estimates for C range from 3-300, although recent experiments by Connolly et al. (2009) suggest $C \approx 30$. Using this recent estimate for C and $d = 10^{-3} - 10^{-2}$m, suitable values for k_0 lie between 10^{-4}m^2 and 10^{-8}m^2.

Some debate surrounds whether relationship 2.10 adequately describes the permeability of mantle rocks at melt fractions smaller than $\phi \approx 0.02$. Faul (1997) and Faul (2001) suggest that melt occupies disk–shaped pores, causing it to be effectively isolated from porous flow at small melt fractions. Consequently, Faul (1997) and Faul (2001) propose that K and ϕ are related by a noncontinuous function, whereby the permeability is very low when the melt fraction lies below a threshold value of $0.02 - 0.03$. At and above the threshold value, the disk-shaped pores interconnect, and the permeability rapidly increases. More recently, however, Wark (2003) reconsidered the microstructure of pore spaces and concluded that equation 2.10 describes the relationship between K and ϕ well even when the melt fraction is very small.

Shear viscosity

Experimental studies of rock deformation demonstrate that the shear viscosity of partially molten rocks η is a function of a large number of variables including pressure, temperature, grain size, water content and melt fraction. How these variables affect viscosity depends on whether the dominant creep mechanism is diffusion or dislocation and whether the viscosity is considered to be anisotropic, as suggested by Takei and Holtzman (2009a,b,c); Takei (2010). Although these dependencies can have significant implications for mantle dynamics, melt migration, and magma genesis (Karato and Wu, 1993; Hirth and Kohlstedt, 1996; Braun et al., 2000; Hirth and Kohlstedt, 2003; Katz et al., 2006), it is not practicable or useful to incorporate all of them into this model. Hence simplifying assumptions must be made. To capture the essence of behaviour observed in experiments, the shear viscosity is taken to be isotropic and to vary with temperature and porosity according to

$$\eta = \eta_0 \exp\left[\frac{E^*}{R}\left(\frac{1}{T} - \frac{1}{T_{\eta 0}}\right) - \lambda\phi\right], \tag{2.11}$$

where η_0 is a reference viscosity, E^* is the activation energy, R is the ideal gas constant, T is temperature, λ is a positive constant, and $T_{\eta 0}$ is a reference temperature. Equation 2.11 defines the shear viscosity to weaken with temperature and porosity. It represents a simplified parameterization of diffusion creep, thus strain rate increases linearly with stress. Although the dominant deformation mechanism in the upper mantle is probably dislocation creep (Karato and Wu, 1993), this mechanism is neglected, since it causes strain rate to increase nonlinearly with stress and adds considerable complexity to the system of equations. Constraints from laboratory experiments indicate the porosity weakening coefficient λ to lie in the range 25–30 for dunite and basaltic melt aggregates deforming by diffusion creep (Cooper and Kohlstedt, 1986; Beeman and Kohlstedt, 1993; Hirth and Kohlstedt, 1995a, 2003). In rocks containing pyroxene, however, estimated values of λ are slightly lower (Zimmerman, 2004). Typical values for the other parameters are provided in table 2.1.

Table 2.1: Typical parameter values.

Symbol	Meaning	Value	Notes
ρ	Reference density of matrix and magma	3000 kg m^{-3}	
$\Delta\rho$	Density difference between matrix and magma	500 kg m^{-3}	
g	Acceleration due to gravity	9.8 m s^{-2}	
k_0	Reference permeability	10^{-7}m^2	Assumes grain size of $\approx 2 \times 10^{-3} m$ and C from Connolly et al. (2009).
n	Permeability exponent	3	
$\mathcal{T}_0$	Potential temperature of the incoming mantle	1698 K	Similar to Putirka et al. (2007)
T_0	Solidus temperature for rock of composition C_0 at zero pressure	1605 K	
α	Coefficient of thermal expansion	3×10^{-5}K^{-1}	
c_P	Specific heat capacity	1200 J kg^{-1} K^{-1}	
L	Latent heat	0.55 MJ/kg	Similar to Kojitani and Akaogi (1997)
κ	Thermal diffusivity	1×10^{-6} m^2 s^{-1}	
$\mathcal{D}$	Chemical diffusivity in magma	1×10^{-8} m^2 s^{-1}	
C_0	Reference composition	0.5	
ΔC	Compositional difference between coexisting rock and magma	0.1	
M	Slope $\partial T/\partial C$ of the solidus and liquidus	200 K	
γ^{-1}	Clapeyron slope $\partial T/\partial P$	60 K GPa^{-1}	
η_0	Reference shear viscosity	10^{19} Pa·s	
ζ_0	Reference bulk viscosity	10^{19} Pa·s	
λ	Porosity weakening coefficient of shear viscosity	27	
μ	Magma viscosity	1 Pa·s	
E^*	Activation energy	2.99×10^5 J mol^{-1}	Similar to lower estimates from Hirth and Kohlstedt (1995a)
R	Molar gas constant	8.31 J mol^{-1} K^{-1}	

Bulk viscosity

Relative to interest in shear viscosity, a constitutive relationship for the bulk viscosity has received considerably less attention from experimentalists. However, measurements from physical experiments (Cooper, 1990), and theoretical studies (Batchelor, 1967; Fowler, 1985; Scott and Stevenson, 1986; Schemling, 2000; Bercovici et al., 2001; Hewitt and Fowler, 2008; Simpson et al., 2010) suggest the bulk viscosity varies with ϕ^{-1}. Based on these studies, the bulk viscosity is defined as

$$\zeta = \zeta_0 \exp\left[\frac{E^*}{R}\left(\frac{1}{T} - \frac{1}{T_{\eta 0}}\right)\right]\frac{1}{\phi}, \tag{2.12}$$

where ζ_0 is a reference value for the bulk viscosity that is approximately equal to, and of the same order of magnitude as η_0.

2.3 Governing equations: Thermochemistry

2.3.1 Conservation of energy

For a thermodynamically consistent approach to mass transfer between the phases, energy must be conserved. A frequent measure of the total energy of a thermodynamic system is enthalpy, thus the bulk enthalpy is defined as

$$\mathcal{H} = \rho\phi h_f + \rho\left(1 - \phi\right) h_m, \tag{2.13}$$

where h_f and h_m are the mass-specific enthalpies of the liquid and matrix. Standard thermodynamic relationships define the total differential for enthalpy to be

$$\mathrm{d}h = c_P \mathrm{d}T + \frac{1}{\rho}\left(1 - \alpha T\right)\mathrm{d}P, \tag{2.14}$$

where c_P is the bulk specific heat capacity, which is assumed to be equal for both phases, α is the coefficient of thermal expansion, and T is temperature. Assuming that variations in pressure at a point due to dynamics of the fluid are negligible, equation 2.14 can be substituted into equation 2.13 to return a more physically meaningful expression for the bulk enthalpy:

$$\mathcal{H} = \rho L\phi + c_P\left(T - T_0\right), \tag{2.15}$$

where $L = h_f - h_m$ is the latent heat of the liquid. The bulk enthalpy is defined to be zero at a reference temperature T_0, which is defined within the petrological context of the model (section 2.4).

Given this definition, conservation of energy, expressed in terms of $\mathcal{H}$ is given by

$$\frac{\partial \mathcal{H}}{\partial t} = \rho L \boldsymbol{\nabla} \cdot (1-\phi)\, \mathbf{v}_m - \rho c_P \bar{\mathbf{v}} \cdot \boldsymbol{\nabla} T - \rho \alpha T \mathbf{g} \cdot \bar{\mathbf{v}} + \kappa \nabla^2 T, \tag{2.16}$$

where $\bar{\mathbf{v}} = \phi \mathbf{v}_f + (1-\phi)\, \mathbf{v}_m$ is the phase averaged velocity and κ is the coefficient of thermal diffusion. Typical values for these constants are given in table 2.1. Equation 2.16 states that temporal changes in the bulk enthalpy are due to advection of latent heat, advection of sensible heat, conversion between potential energy and thermal energy by decompression, and diffusion of sensible heat. A more convenient form for problems concerning the asthenospheric mantle results from re-expressing equation 2.16 in terms of potential temperature $\mathcal{T}$, which is defined as

$$T = \mathcal{T} \exp \frac{\alpha g z}{c_P}. \tag{2.17}$$

Applying this definition and neglecting terms containing $(\alpha g z / cp)^2 \ll 1$ gives

$$\frac{\partial \mathcal{H}}{\partial t} = \rho L \boldsymbol{\nabla} \cdot (1-\phi)\, \mathbf{v}_m - \rho c_P \mathrm{e}^{-\mathcal{A}z} \bar{\mathbf{v}} \cdot \boldsymbol{\nabla} \mathcal{T} + \kappa \mathrm{e}^{-\mathcal{A}z} \nabla^2 \mathcal{T}, \tag{2.18}$$

where $\mathcal{A} = \alpha g / c_P$.

2.3.2 Conservation of mass for chemical components

Mass transfer between solid and liquid is a consequence of melting and also results from chemical reactions between the liquid and specific chemical components in the matrix. To account for mass transfer by reaction requires statements of conservation for individual chemical components in the liquid and solid. These statements are not included in the formulation by McKenzie (1984), but featured in Ribe (1985) and regularly thereafter.

Closely following the formulation by Spiegelman et al. (2001), in a system with N chemical components with J simultaneous reactions, conservation of mass for component i in the liquid is

$$\frac{\partial \phi C_{f,i}}{\partial t} + \boldsymbol{\nabla} \cdot \phi C_{f,i} \mathbf{v}_m = \boldsymbol{\nabla} \cdot \phi \mathcal{D}_i \boldsymbol{\nabla} C_{f,i} + \frac{1}{\rho} \sum_{j=1}^{J} C^*_{f,ij} X_j, \tag{2.19}$$

where $C_{f,i}$ is the mass fraction of component i in the liquid, $\mathcal{D}_i$ is the chemical diffusivity of component i in the liquid, $C^*_{f,ij}$ is the mass fraction of component i in the fluid that is involved in reaction j, and X_j is the rate of mass transfer for reaction j. Equation 2.19 states that temporal changes in the mass of component i are balanced by the flux of $C_{f,i}$ in the liquid, chemical diffusion of component i in the liquid and the total rate of mass transfer from all possible reactions. The equivalent expression for the solid matrix is

$$\frac{\partial (1-\phi)\, C_{m,i}}{\partial t} + \boldsymbol{\nabla} \cdot (1-\phi)\, C_{m,i} \mathbf{v}_m = -\frac{1}{\rho} \sum_{j=1}^{J} C^*_{m,ij} X_j, \tag{2.20}$$

where $C_{m,i}$ is the mass fraction of component i in the matrix, $C^*_{m,ij}$ is the mass fraction of component i in the matrix involved in reaction j. Chemical diffusion in the solid is reasonably assumed to be negligible, given the small diffusion coefficients of major elements in minerals. Experiments on Fe–Mg diffusion in olivine yield diffusion coefficients of the order 10^{-14}–10^{-22}m^2/s (Dohmen et al., 2007). In the melting region beneath mid-ocean ridges, where the residence time of solid mantle is of the order 100 Myr, length scales of $10^{-1} - 10^{-5}$m characterise chemical diffusion. For comparison, the grid spacing for numerical experiments presented in subsequent chapters is order 10^3m.

2.4 Petrology

To close the above equations requires knowledge of ϕ, T, and the mass fractions of chemical components throughout the system in both phases. To obtain this information, the model assumes thermodynamic equilibrium and uses a phase diagram to relate the unknown variables to the bulk enthalpy and composition of the system. Under this assumption, melting is rapid enough that the temperature and composition of rock and magma are confined to the solidus and liquidus surfaces of the phase diagram. Estimates of the Damköhler number for the mantle, which measure the relative importance of reaction and advection, are poorly constrained but sufficiently large that thermodynamic equilibrium is a judicious approximation for the mantle (Aharonov et al., 1995; Spiegelman et al., 2001; Spiegelman and Kelemen, 2003).

Much is known about the phase equilibria of rocks and magma in the mantle, and to fully integrate this knowledge into a dynamical model remains a substantial challenge. Thermodynamic models such as MELTS (Ghiorso and Sack, 1995; Asimow and Ghiorso, 1998) and pMELTS Ghiorso et al. (2002) currently provide some of the best descriptions of melt-rock phase equilibria in the mantle. A recent study by Tirone et al. (2012) uses the phase diagram and thermodynamic equilibrium approach outlined above and couples a thermodynamic database from the MELTS model to a two-phase fluid dynamical model of a mid-ocean ridge. Their approach offers a unique perspective on how magma flow influences the distribution of major elements in the upper mantle. The aim throughout this thesis, however, is to understand the dynamics of melt migration and flow localization, thus a simplified petrological model capturing the essence of melt-rock interaction in the mantle is more suitable.

One simple and reasonable description of melting in the asthenospheric mantle is offered by the system MgO–SiO_2 (Chen and Presnall, 1975). This system captures incongruent melting reaction orthpyroxene + melt A $\rightarrow$ olivine + melt B, which is understood to be fundamental to the generation of mantle dunites. In this system the solidus temperature at any given pressure is not dependent on composition. However, in the mantle, this is not the case; rocks of different composition have different fusibilities and melt at different depths. Thus even though the MgO–SiO_2 system may provide a convenient description of mantle melting, it does not lend itself well to investigating the effect that rocks of different fusibilities have on the dynamics of magma flow.

Asimow et al. (1997), however, note that major mineral phases in the asthenospheric mantle fall within the olivine, and pyroxene groups. Minerals in these groups form solid solutions. To the first order, then, a binary phase loop captures the essential behaviour of the natural system (Asimow et al., 1997). However, since it assumes perfect solid solution, it cannot caputure dunite formation by incongruent melting. Figure 2.1a provides an example of a binary loop. The solidus and liquidus surfaces relate phase compositions to temperature and pressure and can be expressed as

$$C_m = f_S\left(T_m, P_L\right), \tag{2.21}$$

$$C_f = f_L\left(T_f, P_L\right), \tag{2.22}$$

where C_m and C_f are the compositions of the matrix and liquid, f_S and f_L are functions that describe the solidus and liquidus, and T_m and T_f are the solidus and liquidus temperatures, which will be equal for coexisting rock and magma in thermodynamic equilibrium. Since the model applies a binary phase diagram to the entire asthenospheric mantle, the end-member compositions are hypothetical and are not intended to represent actual mineral phases.

In this simple two component system equation 2.19 and 2.20 reduce to a single equation for the bulk composition C

$$\frac{\partial C}{\partial t} + \boldsymbol{\nabla}\cdot\phi\mathbf{v}_f C_f + \boldsymbol{\nabla}\cdot\left(1-\phi\right)\mathbf{v}_m C_m = \mathcal{D}\boldsymbol{\nabla}\cdot\phi\boldsymbol{\nabla}C_f, \tag{2.23}$$

where

$$C = \phi C_f + \left(1-\phi\right)C_m. \tag{2.24}$$

Following this reduction, the system of governing equations comprises $4+D$ equations, where D is the number of dimensions, that are solved for $\mathcal{P}$, P^*, $\mathbf{v}_m$, $\mathcal{H}$ and C. These equations include four unknowns for ϕ, C_m, C_f and T. To solve for these unknowns, the definition of bulk enthalpy (equation 2.15) and composition (equation 2.24) are combined with expressions for the solidus and liquidus surfaces (equations 2.21 and

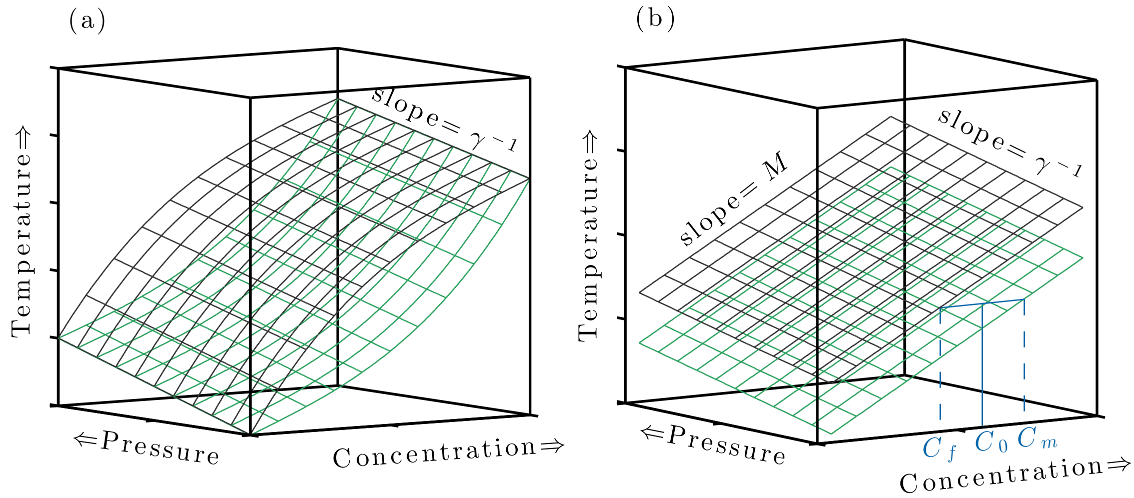

Figure 2.1: (a) Example binary phase loop relating the solidus (lower surface) and liquidus (upper surface) compositions to temperature and pressure. (b) Linearized version of a binary phase loop. C_f and C_m indicate the liquid and solid compositions in equilibrium with bulk composition C_0.

2.22) to give a quadratic equation for porosity:

$$\phi f_l \left(\frac{\mathcal{H} - \phi \rho L}{\rho c_P} + T_0, P_L \right) + (1 - \phi) f_m \left(\frac{\mathcal{H} - \phi \rho L}{\rho c_P} + T_0, P_L \right) - C = 0. \tag{2.25}$$

Using known values for $\mathcal{H}$, C, and P_L, this equation is solved numerically for ϕ; the result is used in equations 2.15, 2.21, 2.22 and 2.24 to find C_f, C_m and T. This general approach to closing the governing equations is known as the Enthalpy Method (Alexiades and Solomon, 1993).

2.5 Steady one dimensional analytical solutions

Analytical solutions to the governing equations can be found by restricting the system to one dimension and steady state. A further simplification is made by linearizing the solidus and liquidus surfaces of the phase diagram and assuming that they are parallel, as shown in figure 2.1b. In this simplified state, the equilibrium temperature is

$$T = T_0 + \frac{P_L}{\gamma} + M \left(C_m - C_0 \right), \tag{2.26}$$

where $\gamma = \partial P/\partial T$ is the Clapeyron slope and M is the slope $\partial T/\partial C$ of the surfaces. The composition of the liquid is related to the matrix composition through

$$C_f = C_m + \Delta C, \tag{2.27}$$

where ΔC is a positive constant. In this section $\gamma = 1/60$ GPa/K $M = 200$ K and $\Delta C = 0.1$. Appendix A outlines in full how the governing equations are reduced and solved (Ribe, 1985; Hewitt, 2010).

Ribe (1985) and Asimow and Stolper (1999) note that in this restricted case, melting is well understood to be equivalent to isentropic batch melting. The melting rate

$$\Gamma = \rho W_0 \frac{dF}{dz} \tag{2.28}$$

is a constant multiple of the productivity $\mathrm{d}F/\mathrm{d}z$, where W_0 is the upwelling rate of the matrix beneath the melting region. How the degree of melting F varies with depth is not known, but can be found using conservation of energy and constraints from the phase diagram.

Using the definition $F = (C_m - C_0)/(C_m - C_f)$ for batch melting and neglecting diffusion, the statement for conservation of energy (equation 2.16) can be integrated to give

$$c_P T = c_P \mathcal{T}_0 + \alpha g z \mathcal{T}_0 - LF. \tag{2.29}$$

Alongside constraints from the phase diagram, this provides a system of equations that is used to solve for F, T, C_m and C_f as functions of depth.

For the particular case of linearized phase surfaces (figure 2.1b), this equation can be combined with equations 2.26–2.27 to yield

$$F = \mathcal{G}\left(z_m - z\right), \tag{2.30}$$

where

$$z_m = \frac{\mathcal{T}_0 - T_0}{\rho g/\gamma - \alpha g \mathcal{T}_0/c_P} \tag{2.31}$$

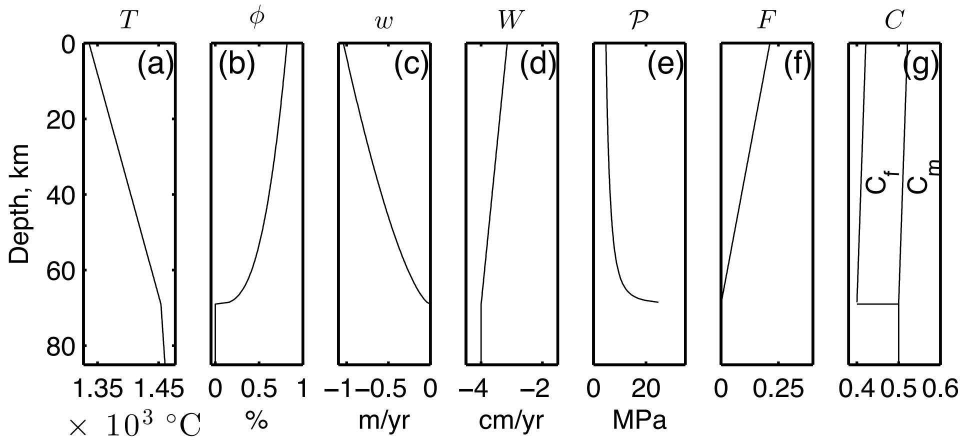

Figure 2.2: Steady one dimensional solutions to the equations provided in Appendix A for (a) temperature, (b) porosity, (c) magma speed (d) upwelling rate of the mantle (e) compaction pressure, (f) degree of melting (g) liquid (C_f) and solid (C_m) compositions, subject to the parameter values given in table 2.1.

is the depth of melting, which is found by equating equation 2.26 with the Taylor expansion of equation 2.17, and

$$\mathcal{G} = \frac{\rho g/\gamma - \alpha g \mathcal{T}_0/c_P}{L/c_P + M_S \Delta C}. \tag{2.32}$$

Thus for this particular case, the productivity $\mathrm{d}F/\mathrm{d}z$ is linear with depth. This will not necessarily hold for different phase diagrams and petrological systems. Indeed, results from the MELTS and pMELTS models, which are more realistic in terms of petrology, suggest a linear productivity is highly unlikely for peridotite under asthenospheric conditions (Asimow et al., 1997; Katz et al., 2003). Following this result, expressions for $\phi(z)$, $w(z)$, $W(z)$ and $\mathcal{P}(z)$ are then found in terms of F, as detailed in Appendix A.

Figure 2.2 shows analytical solutions to the model in this restricted state subject to the boundary conditions $T = \mathcal{T}_0$, $W = -4$ cm/yr, and $C = 0.5$ at the base of the domain ($z = 85$ km), and the parameter values in table 2.1. Under these conditions melting begins at a depth of 70 km, $F \approx 0.2$ at the surface and magma flow is stable throughout the melting column. Towards the surface the temperature, compaction pressure, and upwelling rate of the matrix decrease; the porosity, magma speed, degree of melting increase, and the matrix and magma have increasingly depleted compositions.

2.6 Nondimensionalization

The system of governing equations is nondimensionalized using the following characteristic scales

$$
\begin{aligned}
&\mathbf{x} = H\mathbf{x}', && \mathbf{v} = w_0\mathbf{v}', && t = \frac{H}{w_0}t' \\
&\mathcal{H} = \rho c_P \Delta T \mathcal{H}', && \boldsymbol{\nabla} = \frac{1}{H}\boldsymbol{\nabla}', && K = k_0 K', \\
&(\eta, \zeta, \xi) = \eta_0 (\eta', \zeta', \xi'), && \Gamma = \frac{w_0 \rho}{H}\Gamma', && w_0 = \frac{k_0 \Delta\rho g}{\mu}, \\
&(\mathcal{P}, P^*) = H\Delta\rho g \left(\mathcal{P}', P^{*\prime}\right),
\end{aligned}
\tag{2.33}
$$

where primes indicate nondimensional variables, H is the height of the domain and w_0 is the reference magma velocity. Temperature, potential temperature and composition are nondimensionalized as

$$
\theta = \frac{\mathcal{T} - T_0}{\Delta T}, \qquad \bar{\theta} = \frac{T - T_0}{\Delta T}, \qquad \Theta = \frac{C - C_0}{\Delta C}, \tag{2.34}
$$

where $\Delta T = \Delta C M$. Of the nondimensionalizing constants, H is freely chosen to capture the onset of melting for all model rock compositions within the computational domain. The choice of ΔC is arbitrary, but can be varied in conjunction with other thermodynamic parameters, including M, L, κ, c_P, γ, $\mathcal{T}_0$ and α so that $F \approx 0.2$ at the top of the melting column. Substituting these quantities into equations 2.7–2.9, 2.18 and 2.23, and dropping the primes yields

$$
-\boldsymbol{\nabla}\cdot K\boldsymbol{\nabla}\mathcal{P} + \frac{H^2}{\delta^2}\frac{\mathcal{P}}{\xi} = \boldsymbol{\nabla}\cdot K\boldsymbol{\nabla}P^*, \tag{2.35}
$$

$$
\frac{H^2}{\delta^2}\frac{\mathcal{P}}{\xi} = \boldsymbol{\nabla}\cdot \mathbf{v}_m, \tag{2.36}
$$

$$\nabla P^* = \frac{\delta^2}{H^2}\left[\nabla\cdot\eta\left(\nabla\mathbf{v}_m + \nabla\mathbf{v}_m^{\mathrm{T}}\right)\right] + \phi\hat{\mathbf{k}}, \tag{2.37}$$

$$\frac{\partial\mathcal{H}}{\partial t} + \mathrm{e}^{\mathcal{A}z}\bar{\mathbf{v}}\cdot\nabla\theta = \mathcal{S}\nabla\left(1-\phi\right)\mathbf{v}_m + \mathrm{Pe}_T{}^{-1}\mathrm{e}^{\mathcal{A}z}\nabla^2\theta, \tag{2.38}$$

$$\frac{\partial\Theta}{\partial t} + \nabla\cdot\phi\mathbf{v}_m\Theta_f + \nabla\cdot\left(1-\phi\right)\mathbf{v}_m\Theta_m = \mathrm{Pe}_C{}^{-1}\nabla\cdot\phi\nabla\Theta_f. \tag{2.39}$$

In these equations

$$\delta = \sqrt{\eta_0 k_0/\mu}$$

is the compaction length, which represents the mechanical properties of partially molten rock. Physically, the compaction length describes the length scale over which disturbances to the compaction pressure decay. Over this distance, flow of the magma and deformation of the matrix are coupled.

$$\mathcal{S} = L/c_P\Delta T,$$

is the Stefan number, which defines the ratio of sensible heat to latent heat, and

$$\mathrm{Pe}_T = Hw_0/\kappa$$

and

$$\mathrm{Pe}_C = Hw_0/\mathcal{D}$$

are the thermal and chemical Peclet numbers respectively. Pe_T and Pe_C compare the rates of advection for heat and composition respectively to the rate of diffusion of the same quantity. For the parameter values outlined in table 2.1, $\mathcal{S} \approx 20$, $\mathrm{Pe}_T \approx 6\times10^7$, and $\mathrm{Pe}_C \approx 6\times10^9$.

2.7 Summary

This chapter presents a mathematical model for the generation and deformation of mantle rock from a fluid dynamical perspective. The model comprises statements of conservation for mass, momentum, energy and composition in a system with two phases and two chemical components. Magma is defined to move by porous flow through solid rock that deforms very slowly by creeping flow and compacts or dilates in response to deviations of the fluid pressure from the lithostatic pressure. Thermodynamic equilibrium is assumed and a simplified petrological phase diagram is used to relate bulk enthalpy, bulk composition and pressure to temperature, local melt fraction and phase compositions. This energetically consistent approach to melting marks an important distinction between the model above and others used to investigate unstable magma flow in the mantle with mass transfer between the phases (Aharonov et al., 1995; Spiegelman et al., 2001; Spiegelman and Kelemen, 2003; Liang and Guo, 2003; Schiemenz et al., 2011; Hesse et al., 2011). The importance of this approach is evident in subsequent chapters. Analytical, steady one dimensional solutions to the governing equations summarise the fundamental behaviour of the system under conditions appropriate for the top 90 km of the mantle. These solutions serve as a useful reference state in future chapters, which explore the consequences of variation in C_m for the stability and dynamics of magma flow.

Chapter 3

Plate–driven mantle dynamics and global patterns of mid-ocean ridge bathymetry

This chapter is published as

Weatherley, S.M. and Katz, R.F., (2010) Plate–driven mantle dynamics and global patterns of mid-ocean ridge bathymetry, *Geochemistry, Geophysics, Geosystems*, vol. 11, Q10003.

3.1 Introduction

Earth's mid-ocean ridges (MORs) are a striking geological feature resulting from plate–mantle interaction. As oceanic plates spread apart, hot asthenospheric mantle upwells and melts adiabatically, supplying the spreading centre with material to generate new crust. On a global scale, the physical properties of the oceanic crust are approximately independent of spreading rate for slow to fast spreading ridges. Along the same ridges, the first–order petrological characteristics of the oceanic crust vary systematically with spreading rate. These similarities suggest that the fundamental processes governing plate–mantle interaction are uniform throughout the globe. On a regional scale, however, more subtle differences in the physical and chemical properties of oceanic crust become apparent. In this study we use these regional differences to investigate the details of plate–mantle interaction.

Global observations of MOR bathymetry by Carbotte et al. (2004) reveal a correlation between the difference in axial depth across ridge offsets and the direction of ridge migration relative to the fixed hotspot reference frame. At the majority of offsets, ridge segments leading with respect to the direction of ridge migration are shallower than trailing segments. The systematic connection between axial depth change across offsets and plate kinematics suggests that an explanation might be found in plate–motion–induced mantle dynamics. Differences in axial depth across offsets are thought to arise from differences in the volumes of melt being delivered to the leading and trailing ridge segments (Carbotte et al., 2004; Katz et al., 2004). However, the three dimensional nature of melt generation and focusing in the vicinity of MOR offsets requires further investigation.

Carbotte et al. (2004) suggest that the observed variations in MOR morphology are the result of melt focusing across ridge offsets from a broad, asymmetric zone of upwelling beneath a migrating ridge (figure 3.1). Kinematic models of asthenospheric flow beneath a migrating MOR (Davis and Karsten, 1986; Schouten et al., 1987) predict faster upwelling and greater melting beneath the leading plate. If the asymmetric melting behaviour is captured by melt focusing across offsets, the leading ridge segment is expected to have a thicker crust and shallower axial depth.

Geophysical studies of sub–MOR mantle support the conceptual model of Carbotte et al. (2004) and verify the kinematic models of Davis and Karsten (1986) and Schouten et al. (1987). Observations of migrating spreading centers show cross–axis asymmetry in mantle properties. Seismic (The MELT Seismic Team, 1998; Forsyth et al., 1998; Toomey et al., 1998) and electrical resistivity (Evans et al., 1999) studies of the MELT region of the East Pacific Rise reveal lower density, lower resistivity, lower seismic velocity, and higher seismic anisotropy beneath the leading plate (The MELT Seismic Team, 1998). Subsequent geodynamic models (Conder et al., 2002; Toomey, 2002) showed that ridge migration contributes to mantle asymmetry in the MELT region. In the MELT region, however, ridge migration alone does not com-

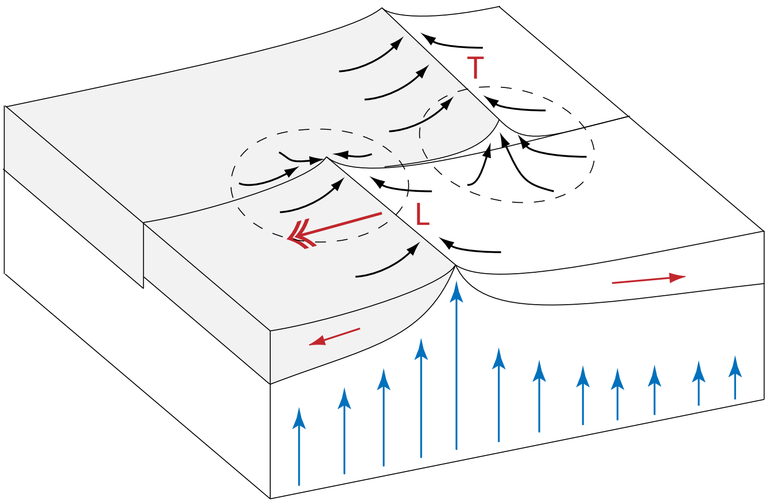

Figure 3.1: Schematic showing a ridge system consisting of a leading and trailing ridge segment separated by a discontinuity. (The leading and trailing ridge segments are marked L and T respectively.) Single headed red arrows show spreading component of plate motion whilst the double headed red arrow indicates the direction of ridge migration. The leading plate is shaded grey. Blue vertical arrows depict upwelling in the underlying mantle and black arrows show hypothetical melt focusing trajectories. The dashed circles represent idealized regions of melt focusing, which extend into the mantle beneath the adjacent plates. Melt tapped from these regions contributes to the morphological asymmetry of ridge segments separated by an offset.

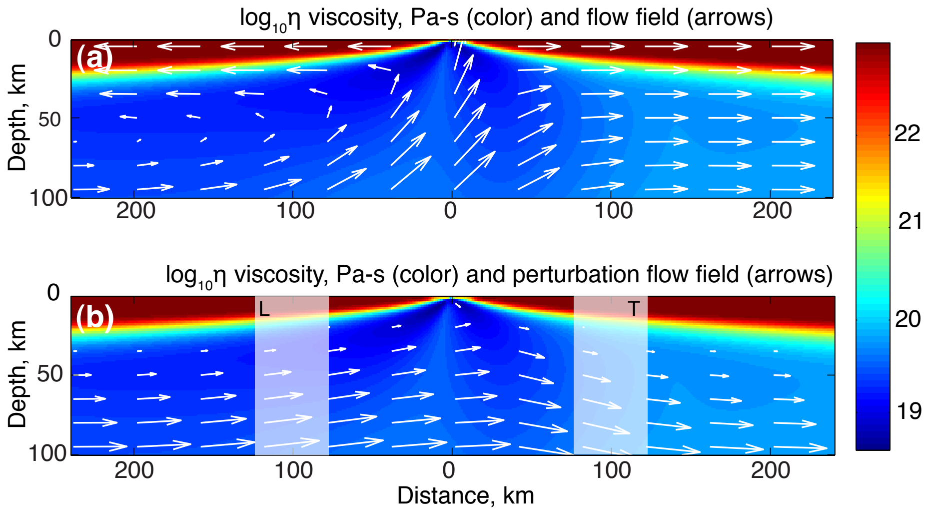

Figure 3.2: Example output from the 2D simulations by Katz et al. (2004). These figures compare the mantle flow pattern beneath a migrating ridge (a) and the component of mantle flow induced by ridge migration (b). (a) Solid mantle flow pattern (white arrows) from 2D simulation with half spreading rate U_o = 4cm/yr and ridge migration rate U_r = 4cm/yr. The ridge is migrating to the left. Coloured background shows viscosity in Pa s. (b) Component of mantle flow caused by ridge migration. White boxes show the regions within the leading (L) and trailing (T) minor focusing regions.

pletely account for the observed magnitude of asymmetry. Conder et al. (2002) and Toomey (2002) infer an additional component of asymmetry from hotspots in the nearby Pacific superswell region to completely account for the observed asymmetry. In this respect, the mantle dynamics of the MELT region are a special case. More generally, however, an asymmetric mantle structure is seen beneath migrating MORs across the globe (Panza et al., 2010).

Katz et al. (2004) used a 2D numerical model to simulate asymmetric mantle flow beneath a migrating ridge. These simulations quantified the conceptual model proposed by Carbotte et al. (2004). Figure 3.2 shows example output from a 2D simulation after Katz et al. (2004). The mantle flow pattern beneath a migrating MOR is shown in figure 3.2a; figure 3.2b shows the component of flow induced by ridge migration. To generate predictions of axial depth changes across offsets of different lengths, the authors coupled a simple parametric model of melt focusing to their simulations.

The parametric melt focusing model used by these authors assumes that melt focusing regions are rectangular–shaped in map view and are located at the end of ridge segments. For their experiments, the dimensions of the focusing regions were fixed for all offsets and spreading rates. Melt from these focusing regions was distributed evenly over the first 1 km of the ridge segments, in keeping with the distance over which Carbotte et al. (2004) make their observations. Predictions of axial depth asymmetry generated by the 2D model are consistent with the observations made by Carbotte et al. (2004).

Although Katz et al. (2004) generate reasonable predictions of axial depth differences across offsets, their model does not consider the fundamentally 3D nature of transform faults. The mantle flow pattern and thermal structure is two dimensional and constant along the entire length of each ridge segment. In nature, ridge offsets such as transform faults juxtapose cold, thick lithosphere against warm ridge segments. This temperature difference modifies the thermal structure of the lithosphere and mantle surrounding the offset. Because the thermal structure of the lithosphere and upper mantle close to offsets is three dimensional, mantle flow and melt focusing cannot be fully investigated with a 2D model. Close to offsets, changes in the temperature structure of the mantle with offset length and spreading rate will affect the shape and dimensions of the focusing regions. Furthermore, at the ridge axis, processes such as melt flow through the porous mantle and cracks are likely to redistribute melt over a substantial section of the ridge axis. These deficiencies of the 2D simulations can be overcome by extending the model into three spatial dimensions.

In this paper we use 3D, steady–state numerical simulations to investigate the dynamics of the mantle and melt focusing beneath a migrating MOR. We confirm that the magnitude of asymmetry generated solely by ridge migration is sufficient to explain the observations made by Carbotte et al. (2004). However, the behaviour of our predictions of axial depth asymmetry across offsets is different to that predicted by the 2D simulations of Katz et al. (2004). We show that the difference in bathymetry between two adjacent ridge segments depends on the difference in melt volume generated in the focusing regions and the distance over which melt is redistributed at the ridge.

The remainder of this paper is divided into three sections. In the first section we describe the construction of the numerical model that solves for passively driven, incompressible, creeping mantle flow. The same section details the parameterization of mantle melting, melt focusing, and melt redistribution that we couple to the numerical model. The next section shows how predictions of axial depth differences generated by our simulations compare against global MOR data for a range of offsets and spreading rates. In the final section we discuss how the spreading rate, rate of ridge migration, and geometry of a MOR system influence asthenospheric flow, and to what extent they control differences in axial depth across an offset. Further to this we examine the influence of a viscoplastic rheology on mantle flow and melting beneath a migrating MOR. We also consider how additional geophysical, geochemical, petrological, and numerical studies can better constrain the melt focusing and redistribution processes at MORs.

3.2 Model construction

The model is based on a set of coupled partial differential equations to describe incompressible, steady–state, passively driven solid mantle flow. We expect that these equations capture the upwelling behaviour of mantle beneath migrating MORs. By coupling the computed solid mantle flow field to an existing parameterization of mantle melting (Katz et al., 2003) we determine the melting rate throughout the simulation domain. In the final step of the computation, we apply a model of 3D melt focusing to the simulations to generate predictions of the difference in crustal thickness and axial depth across an offset. Each of these steps is described in more detail below.

3.2.1 Solid mantle flow

The following system of coupled partial differential equations governs passive solid mantle flow.

$$\nabla \cdot \mathbf{v} = 0, \tag{3.1}$$

$$\nabla P = \nabla \cdot \left[\eta \left(\nabla \mathbf{v} + \nabla \mathbf{v}^T \right) \right], \tag{3.2}$$

$$\mathbf{v} \cdot \nabla \mathcal{T} = \kappa \nabla^2 \mathcal{T}. \tag{3.3}$$

Here, $\mathbf{v}$ is the three dimensional mantle velocity, P is the dynamic pressure arising from viscous stresses, η is the dynamic viscosity, $\mathcal{T}$ is the potential temperature, and κ is the thermal diffusivity of mantle rock. Equation (3.1) is a statement of incompressibility, equation (3.2) enforces conservation of momentum for an incompressible fluid in the limit of zero Reynolds number and zero buoyancy forces, and equation (3.3) balances advection and diffusion of heat in steady state.

This system of equations is closed with a constitutive relation for mantle viscosity. The mantle flows by diffusion and dislocation creep; the creep mechanism giving rise to the highest strain rate controls the local viscosity of the mantle. We define the viscosity, η, as

$$\eta = \left(\frac{1}{\eta_{difn}} + \frac{1}{\eta_{disl}} \right)^{-1} \tag{3.4}$$

where η_{difn} is the viscosity due to pressure and temperature–dependent diffusion creep and η_{disl} is the viscosity due to pressure, temperature, and strain rate–dependent dislocation creep. η_{difn} and η_{disl} are combined in this way to capture transitions in the dominant creep mechanism within the simulation domain. The definitions of η_{difn} and η_{disl} are as follows:

$$\eta_{difn} = A_{difn} \exp\left(\frac{E^*_{difn} + PV^*_{difn}}{RT} \right) \tag{3.5}$$

$$\eta_{disl} = A_{disl} \exp\left(\frac{E^*_{disl} + PV^*_{disl}}{nRT} \right) \dot{\epsilon}_{II}^{\frac{(1-n)}{n}} \tag{3.6}$$

where η_{disl} is the viscosity due to pressure and temperature dependent diffusion creep, and η_{difn} is the viscosity due to pressure, temperature, and strain rate dependent dislocation creep. A is a proportionality constant, E^* is activation energy, V^* is an activation volume, R is the gas constant, T is temperature, and n is the power law exponent (Karato and Wu, 1993; Hirth and Kohlstedt, 1996). $\dot{\epsilon}_{II}$ is the second

Table 3.1: Boundary Conditions

Boundary	Variable	Boundary Condition
$z = 0$	u	$u(x, y, 0) = U_0(x, y)$ where U_0 is the prescribed plate motion
	v	$v = 0$
	w	$w = 0$
	P	BC does not influence the interior of the domain
	T	$T = 0$
$z = Z$	u	$u = U_r$ where U_r is the x-component of ridge migration
	v	$v = 0$
	w	$\partial w/\partial z = 0$
	P	$P = 0$
	T	Dimensionless T set equal to dimensionless mantle potential temperature
$x = 0, X$	u	Satisfies discretized form of Eq. (3.1)
	v	$v = 0$
	w	$w = 0$
	P	BC does not influence the interior of the domain
	T	$\partial T/\partial x = 0$
$y = 0, Y$	u	No shear stress
	v	No normal stress
	w	No shear stress
	P	BC does not influence the interior of the domain
	T	$\partial T/\partial y = 0$

The domain size is $x \in [0, X]$, $y \in [0, Y]$, $z \in [0, Z]$. The x dimension is parallel to the spreading rate vector,y dimension is parallel to the ridge axes and the z dimension is depth.

invariant of the strain rate tensor, providing a measure of the intensity of strain rate.

In the model, the lithosphere consists of material with sufficiently high viscosity to be considered rigid. For the purpose of this paper, in each vertical column of grid cells, the base of the lithosphere is defined where $|\partial\eta/\partial z|$ is maximum.

3.2.2 Boundary conditions

The governing equations are solved in a reference frame fixed to the migrating ridge. Table 3.1 provides a summary of the five boundary conditions for P, T, and $\mathbf{v}$ that are specified on each face of the computational domain.

In a study of current plate motions in the fixed hotspot reference frame, Small and Danyushevsky (2003) investigate the global relationship between the half spreading rate U_0 of MORs and the rate of ridge migration in a direction perpendicular to the ridge axis U_r. They show that the mean ratio of U_r to U_0 is 0.95 with a standard deviation of 0.33. For simplicity, we take U_r to equal U_0. Because the equations are solved in a reference frame fixed to the migrating ridge, the velocity field on the top boundary is set to that of symmetrically spreading plates, and U_r is imposed on the bottom boundary.

The bottom boundary of the domain is intended to correspond to the base of the asthenosphere. For this investigation we take the base of the asthenosphere to be rigid. A large drop in horizontal mantle velocity with increasing depth is expected across the base of the asthenosphere (Richards et al., 2003; Panza et al., 2010). This indicates that the component of mantle flow induced by ridge migration will be concentrated below the top of the lithosphere–asthenosphere boundary and above the base of the asthenosphere. The radially anisotropic shear velocity structure of sub–MOR mantle may indicate that the depth of the base of the asthenosphere is 200 km (Nettles and Dziewonski, 2008). However, large variations in the thickness of the asthenosphere occur across the globe. For our simulations we use an asthenospheric depth of 300 km. Katz et al. (2004) show that the difference in axial depth predicted by the 2D simulations scales inversely with the asthenospheric thickness.

3.2.3 Computational methods

A finite-volume discretization of equations (3.1)–(3.3) and the complete set of boundary conditions is iteratively solved using a Newton-Krylov solver provided by the Portable, Extensible Toolkit for Scientific Computing (PETSc) (Balay et al., 1997; Katz et al., 2007; Balay et al., 2009). The dislocation creep term in equation 3.4 introduces strong nonlinearity into the system, and presents an additional challenge in generating numerical solutions to the governing equations.

To handle the nonlinearity in equation 3.4 we adopt a continuation method, forcing the variation in viscosity to go from zero to the full predicted variance over a set of iterations of the nonlinear solve (Knepley et al., 2006; Katz et al., 2007). To smoothly control the variation in viscosity, we set an upper limit of 10^{23} Pa s and use this limit to normalize η to a range between zero and one. The viscosity field η^* used on the m^{th} iteration of the continuation loop is given by

$$\eta^* = \eta^{\alpha_m} \qquad \alpha_m \in [0, 1] \tag{3.7}$$

where $m = 1, 2, ..., M$. In the first iteration $\alpha_1 = 0$. This yields the solution to the isoviscous case, which is then used as the starting guess for the next step, where $\alpha_2 > \alpha_1$. The continuation loop ends at $\alpha_M = 1$ which corresponds to the full predicted variance in viscosity.

3.2.4 Melting and melt migration

We compute the rate of melt production using a parameterization of mantle melting by Katz et al. (2003). This parameterization expresses melt fraction as a function of pressure, temperature, water content, and modal clinopyroxene. For a given mantle potential temperature, the parameterization predicts that the adiabatic productivity $\mathrm{d}F/\mathrm{d}z|_S$ is approximately constant. The adiabatic melting rate Γ kg/m^3/yr is then calculated as

$$\Gamma = \rho_m W \left.\frac{\mathrm{d}F}{\mathrm{d}z}\right|_S \tag{3.8}$$

where ρ_m is the density of the mantle, W is the vertical velocity from the solution of equations (3.1)–(3.3), and S is entropy. We use equation (3.8), the solidus of Katz et al. (2003), a mantle potential temperature of 1300°C for consistency with Katz et al. (2004), and an adiabatic productivity of 0.4%/km to calculate the melting rate at each grid cell in the domain. If ridge migration causes any perturbation of W, the melting rate will be asymmetric across the ridge axis.

Melt from each grid cell is assumed to percolate vertically through the mantle to the top of the melting region. The upper surface of the melting region is an impermeable boundary that slopes upwards towards the ridge axis. Melt migrates uphill along this boundary on streamlines that follow the steepest local slope of the surface, that is

$$\left(\mathbf{i}\frac{\partial h}{\partial x} + \mathbf{j}\frac{\partial h}{\partial y}\right) \times \mathrm{d}\mathbf{s} = 0 \tag{3.9}$$

where h is the depth to the top of the melting region and d**s** is an element of arc length along the streamline. This model of melt migration was first proposed by Sparks and Parmentier (1991) and has been used in subsequent studies of 3D melt migration (Sparks et al., 1993; Magde and Sparks, 1997; Magde et al., 1997; Gregg et al., 2009). To determine where along the ridge axis melt is extracted we define a narrow, 2 km wide box, that surrounds the ridge axis and project it onto the top of the melting region. At the point where a streamline crosses into this box, the melt carried along that trajectory is extracted and accumulated at that position on the ridge.

Although melt focusing is thought to be an efficient process, complete extraction of melt from the mantle is unlikely. Petrological studies of abyssal and mantle peridotites (Warren and Shimizu, 2010; Dick et al., 2010; Seyler et al., 2007, 2001; Niu, 1997), active near–ridge seamounts (Niu and Batiza, 1991; Batiza et al., 1990), numerical simulations of mantle dynamics (Chen, 1996; Ghods and Arkani-Hamed, 2000; Katz, 2008) , geophysical experiments Lizarralde et al. (2004), and integration of geophysical and geochemical observations (Faul, 2001) all indicate that between 1% and 40% of the melt generated within the melting region is retained in the mantle.

In our models, all of the melt extracted at a ridge segment originates from inside a focusing region. The maximum horizontal extent of the focusing regions from the ridge axis, and hence the fraction of melt extracted at the ridge, is limited by a specified focusing distance. The focusing distance is assumed to increase with spreading rate in order to maintain a constant crustal thickness of 6 km at an on-axis point 70 km away from the transform fault.

Figure 3.3a shows predicted melt migration trajectories for a simulation with $U_r =$ 2cm/yr and an offset of 40 km; colours and contours show the solidus depth. The solidus depth increases close to the transform fault, deflecting melt away from the end of the ridge segment. This leads to on-axis bunching of melt trajectories 10–30 km away from the transform fault.

Along–axis profiles of melt-accumulation rate resulting from the melt focusing process described in figure 3.3a are shown in figure 3.3b. At sufficiently large distances from the transform fault, the crust has a constant thickness of 6 km. Close to the transform fault, deflection of melt trajectories causes large variation in crustal thickness. In nature, such large variations are not seen; for intermediate to fast spreading rates crustal thickness is nearly constant along the length of ridge segments. Investigations into the constancy of oceanic crustal thickness by Korenga and Kelemen (1997); Magde et al. (2000); Kelemen et al. (2000) and Singh et al. (2006b) suggest that along–axis redistribution of melt through cracks and porous mantle works to smooth the initial distribution of melt caused by focusing.

Thus to smooth the predicted distributions of melt shown in figure 3.3b, we assume that crustal and uppermost mantle processes evenly redistribute melt along the ridge axis between the transform fault and the solid dots in figure 3.3b, which indicate where the graident of the crustal thickness departs significantly from zero. The distance over which the melt is redistributed is termed the 'redistribution length' ζ, and figure 3.3c shows that ζ varies linearly with offset length.

3.2.5 Compensation of mid–ocean ridge crest topography

To compare the simulation results against data from the global MOR system, the difference in crustal thickness computed by the melting and melt migration parameterization is converted into a difference in axial depth. Spectral studies of MOR topography and gravity suggest that MOR topography is supported by flexure of the oceanic lithosphere (Cochran, 1979; McNutt, 1979; Bowin and Milligan, 1985). In the flexure model of isostasy the oceanic lithosphere is assumed to behave as a perfectly elastic material. The rigidity of the plate is given by the flexural rigidity, D,

$$D = \frac{ET_e}{12\left(1-\nu^2\right)}, \tag{3.10}$$

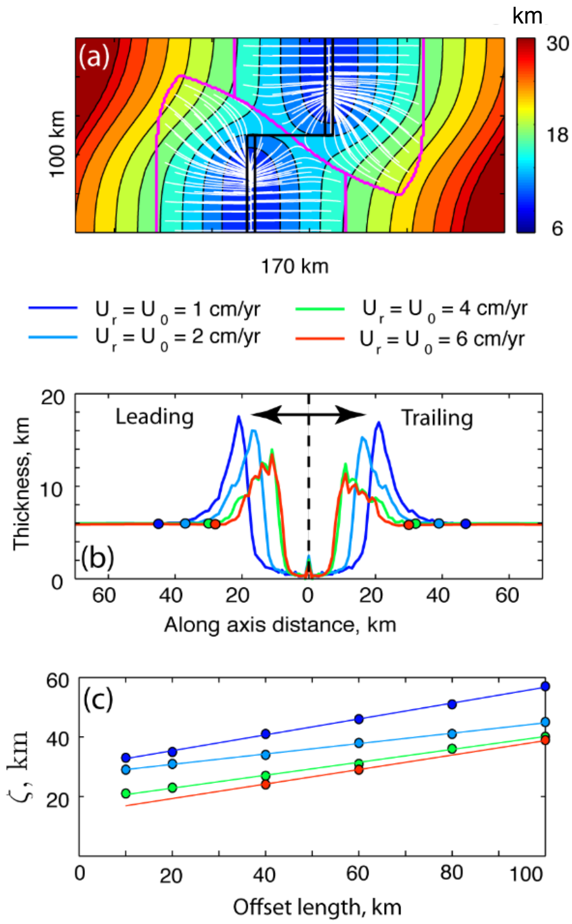

Figure 3.3: Summary of steps needed to focus melt to the ridge and redistribute it along the ridge axis. (a) Map showing the relationship between solidus depth, focusing region shape and melt focusing trajectories. White streamlines show melt focusing trajectories. Black lines outline the geometry of the ridge system. Magenta lines mark the perimeters of the focusing regions. Coloured contours show depth to the top of the melting region. Simulation has $U_r = 2$cm/yr and an offset of 40 km. The ridge is migrating to the left. (b) Profiles showing along–axis variation in crustal thickness for simulations with $U_r = 1, 2, 4, 6$cm/yr and an offset of 40 km. Solid dots show the positions at which the gradient of the crustal thickness profiles first departs significantly from zero. The distance between these points and the offset for each simulation is the redistribution distance ζ. (c) Variation in ζ as a function of transform fault length.

where E is Young's modulus, T_e is the elastic thickness of the plate, and ν is Poisson's ratio. In the limit $T_e \to 0$ the lithosphere has no elastic strength and the flexural model reduces to Airy isostasy. In the limit $T_e \to \infty$ the plate becomes rigid and does not flex. For dynamic processes, however, T_e approximately corresponds to the depth of the 600°C isotherm (Watts, 2007). The flexure $(t - d)$ generated by periodic loading of an elastic plate is

$$t - d = d \cos(ky)\, \mathcal{A}\phi_e, \tag{3.11}$$

where $\mathcal{A}$ is the Airy isostatic response,

$$\mathcal{A} = \frac{\rho_c - \rho_w}{\rho_m - \rho_c}, \tag{3.12}$$

and ϕ_e is the flexural response function,

$$\phi_e = \left[\frac{Dk^4}{(\rho_m - \rho_c)\, g} + 1\right]^{-1}. \tag{3.13}$$

Here, t is the crustal thickness, d is topography, y is the distance along the ridge axis, $k = \pi/\zeta$ is the wavenumber of the load in the along–ridge direction, and ρ_m, ρ_c, ρ_w are the densities of the mantle, oceanic crust, and seawater respectively. The flexural response function ϕ_e modifies the Airy isostatic response $\mathcal{A}$ so as to represent flexure.

From Equation 3.11, the difference in axial depth, Δd, between two adjacent ridge segments supported by flexure is related to the difference in crustal thickness, Δt, by

$$\Delta d = \mathcal{C}\Delta t, \tag{3.14}$$

where

$$\Delta t = \frac{\displaystyle\int_{y_0-\zeta}^{y_0} \gamma_l \,\mathrm{d}y - \int_{y_0}^{y_0+\zeta} \gamma_t \,\mathrm{d}y}{2\rho_c U_0 \zeta}, \tag{3.15}$$

the isostatic compensation function $\mathcal{C}$ is

$$\mathcal{C} = \left[1 + \mathcal{A}\phi_e\right]^{-1}, \tag{3.16}$$

y is the direction parallel to the ridge axis, γ_l and γ_t are the mass of melt accumulated per unit time at the leading and trailing segments of the ridge axis, and y_0 is the position of the transform fault. Watts (2001) shows that oceanic lithosphere can support topography by flexure over distances of 50 km. Therefore, in applying Equation (3.14) we use a single elastic thickness calculated at a point 50 km off–axis on the leading side of the ridge and 50 km away from the fracture zone, and assume $E = 100$ GPa, $\nu = 0.25$, $g = 9.81$ m/s^2, $\rho_w = 1030$ kg/m^3, $\rho_c = 2900$ kg/m^3, and $\rho_m = 3300$ kg/m^3.

3.3 Results

Figure 3.4 shows representative output from a simulation for which the offset is 80 km and $U_0 = 4$cm/yr. The grid resolution is 3 km in each direction and, for this simulation only, the base of the asthenosphere is 100 km. Figure 3.4a shows surfaces of constant upwelling beneath the ridge. Upwelling is uniform in the y–direction beneath most of each ridge segment but diminishes within 50 km of the transform fault. There, mantle is drawn across the offset into the region beneath the spreading centre. Because the melting rate Γ depends only on the upwelling rate, the vertically integrated melting rate $\int_0^Z \Gamma \mathrm{d}z$ gives a more compact perspective of upwelling; it is shown in figure 3.4b. In figure 3.4, upwelling is fastest, and approximately equal to U_0, at shallow depths immediately beneath the ridge axis. In the region of fastest upwelling our simulations, using experimentally calibrated viscosity laws, predict that the mantle viscosity can be as low as 5×10^{18} Pa s.

The white solid lines in figure 3.4b mark the perimeter of the focusing regions. A dashed white line divides each of these focusing regions into a major and minor subregion that are distal and proximal to the transform fault respectively. Minor subregions terminate at a distance of one redistribution length ζ from the transform fault. If the total melting rate in each of the minor focusing regions is different, then there is a difference in crustal production and $|\Delta d| > 0$. Because the minor focusing regions do not terminate at the transform fault and instead extend some way beyond the ridge axis, they are different to those proposed by Carbotte et al. (2004) and Katz

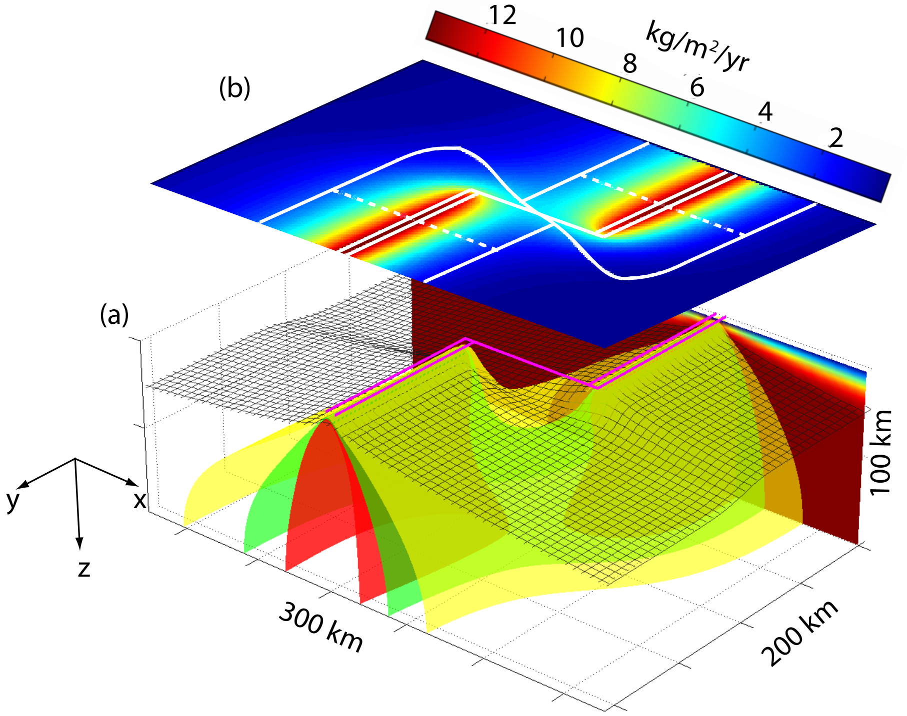

Figure 3.4: Example output from a 3D simulation with $U_r = 4$cm/yr and an offset of 80 km. The ridge is migrating to the left. (a) 3D image of the upwelling geometry beneath the ridge system. Magenta lines indicate the position of the transform fault and ridge segments. Red, green and yellow surfaces show constant upwelling rates of 1, 2 and 2.75 cm/yr respectively. Upwelling is asymmetric about the ridge axis. Wire mesh marks the base of the lithosphere, defined by the locus of the maximum rate of change in viscosity in the z-direction. The back wall shows a 2D slice through the potential temperature field. Dark red represents the mantle potential temperature (1300°C) and dark blue indicates 0°C. (b) Map of the vertically integrated melting rate, $\int_0^Z \Gamma \, \mathrm{d}z$. White lines show the location of the ridge segments, transform fault, and the focusing regions. The focusing regions are divided by a white, dashed line into major and minor sub–regions that are distal and proximal to the transform fault respectively. The vertically integrated melting rate is the melt production rate beneath any point on the surface of the solidus that can be focused to a ridge segment.

et al. (2004).

To calculate the behaviour of Δd as a function of transform fault length and U_0 when $U_0 = U_r$, we use suites of simulations that maintain constant U_0 and vary offset length. Figure 3.5 shows predictions of the difference in axial depth Δd generated from four suites of simulations using equation (3.8). Also shown in this figure are data from the global MOR system (Carbotte et al., 2004) for transform offsets only. These measurements are made by comparing the axial depth of leading and trailing ridge segments. The data are averaged over a 1 km window. Predictions and observations of Δd are for a range of half–spreading rates between 1 and 7cm/yr and offsets between 0 and 170 km. The focusing distance is 35 km for the suite of simulations with $U_r = 1$cm/yr, 48 km for the suite with $U_r = 2$cm/yr, 64 km when $U_r = 4$cm/yr, and 73 km when $U_r = 6$cm/yr. In each case the focusing distance is less than the width of the melting region, hence peripheral melts are not extracted. We find that the simulations using an asthenospheric thickness of 300 km best fit global ridge data. The amplitude of the difference in crustal thickness predicted by our simulations results scales approximately inversely with the asthenospheric thickness.

For fast spreading rates ($U_0 > 4$cm/yr), the model predicts that peak asymmetry in axial depth occurs at offsets of less than 20 km. This distance increases as U_0 decreases. For slow spreading rates ($U_0 < 1$cm/yr), Δd reaches a peak at offset lengths greater than 60 km. In general, the MOR data show two broad trends. First, the amplitude of the data increases with spreading rate. Second, the amplitude of the data decreases with increasing offset. The simulations results are consistent with these trends.

3.4 Discussion

3.4.1 3D melt generation, focusing and redistribution

The simulation results can be understood by considering the component of mantle flow induced by ridge migration. From here onwards we refer to this component as the

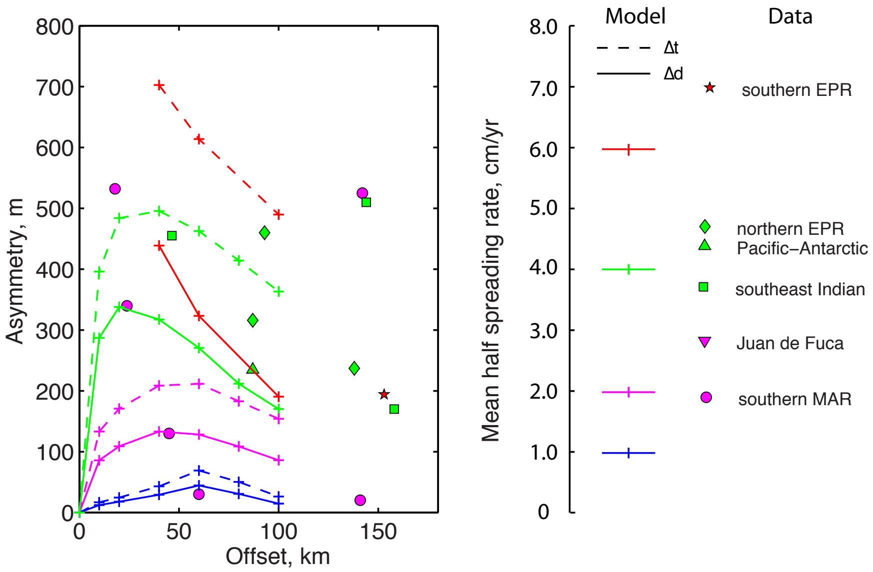

Figure 3.5: Left panel: Model results and global data showing the difference in axial depth of two ridge segments separated by an offset, as a function of offset length. Right panel shows legend. All simulations have a grid resolution of 3 km in each direction, an asthenospheric depth of 300 km. Data for transform faults on intermediate and fast spreading ridges (Juan de Fuca, JDF, south east Indian Rise, SEIR, Pacific Antarctic Rise, PACANT, north east Pacific Rise, NEPR, south east Pacific Rise, SEPR) are from Carbotte et al. (2004), and for the southern Mid-Atlantic Ridge (SMAR) from Katz et al. (2004). The data set covers some 11,000 km of MOR along which 76% of the leading ridge segments have a shallower bathymetry than the trailing ridge segment for all offsets in excess of 5 km. Any data not fitting this trend is excluded from the figure. Simulations for U_r = 6cm/yr with offsets of 10 km, 20 km, and 80 km did not converge to a solution.

perturbation flow. The vertical component of the perturbation flow W' is of particular importance. As implied by equation (3.8), the behaviour of W' in the minor focusing regions controls the magnitude of the bathymetric asymmetry, Δd.

At sufficiently large distances from the transform fault, the geometry of the lithosphere–asthenosphere boundary (LAB) and behaviour of mantle flow is two dimensional. Here, the LAB curves upwards beneath the ridge segments and the perturbation flow has a vertical component of velocity with upwelling on the leading side of the ridge and downwelling on the trailing side. With increasing depth, the loci of maximum $|W'|$ for each horizontal row of grid cells moves away from the ridge along the bold lines shown in figure 3.6a. Katz et al. (2004) show that the slope of these extremal lines of $|W'|$ varies with spreading rate. This indicates that far from the transform fault, where mantle flow is two dimensional, the shape of the LAB controls the upwelling behaviour of the perturbation flow.

Close to the transform fault the shape of the LAB is three–dimensional. Mantle flow in this vicinity has three components of velocity and the control exerted by the LAB on the perturbation flow is not clear. To determine the influence of the LAB on the perturbation flow, we extend the concept of the extremal lines shown in figure 3.6a into three dimensions and consider the relationship between the depth to the LAB and the depth to extremal surfaces of $|W'|$. If the LAB controls the perturbation flow, the depth to these extremal surfaces should show a clear relationship to the depth to the LAB.

Figure 3.6b shows that the depth to the extremal surfaces is correlated with the depth to the LAB. This indicates that the three–dimensional shape of the LAB controls the asymmetric, passive, plate-driven upwelling and melting beneath a migrating MOR system.

The offset length and spreading rate principally control the shape of the LAB and melting region. Consequently, these two parameters also influence the shape of the focusing regions. Figure 3.7 shows how the shape of the focusing regions and melting behaviour varies for a suite of simulations with $U_r = 1$cm/yr and different values of offset. Also shown are the traces of the extremal surfaces where they intersect the

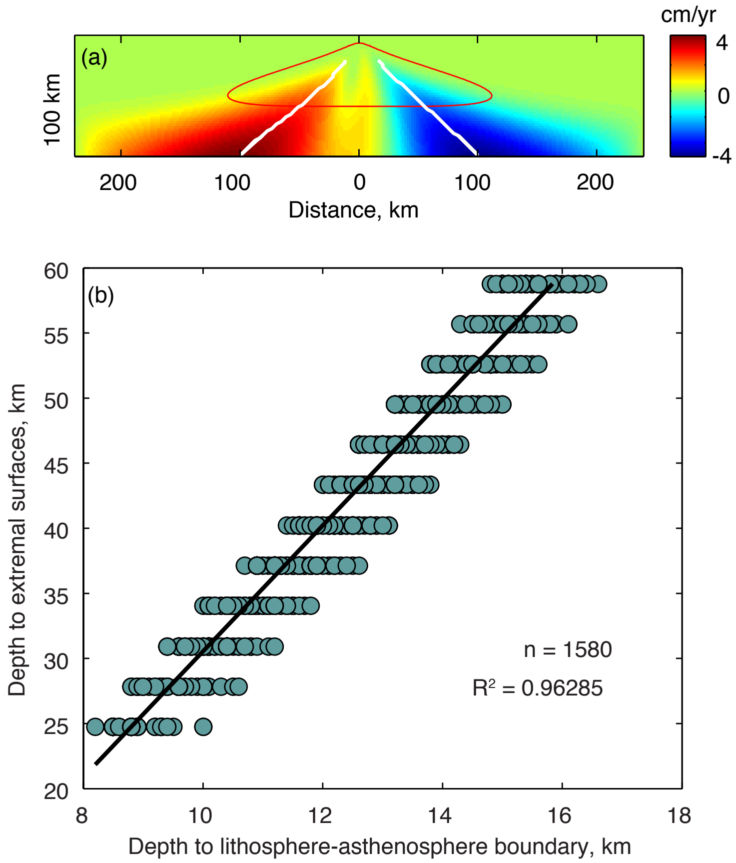

Figure 3.6: Results from analogous 2D and 3D calculations with $U_r = 1$cm/yr and an asthenospheric depth of 100 km. (a) Figure shows, for a 2D simulation, the locations of extremal values of W' and the shape of the melting region. Coloured field is the component of upwelling induced by ridge migration, W'. White bold lines mark the extremal values of W' as a function of depth. The red contour outlines the melting region. (b) This figure shows, for the analogous 3D simulation, the relationship between the depth to the extremal surfaces of W' and the depth to the lithosphere–asthenosphere boundary (LAB). The black line is least squares best fit line taken through all data points.

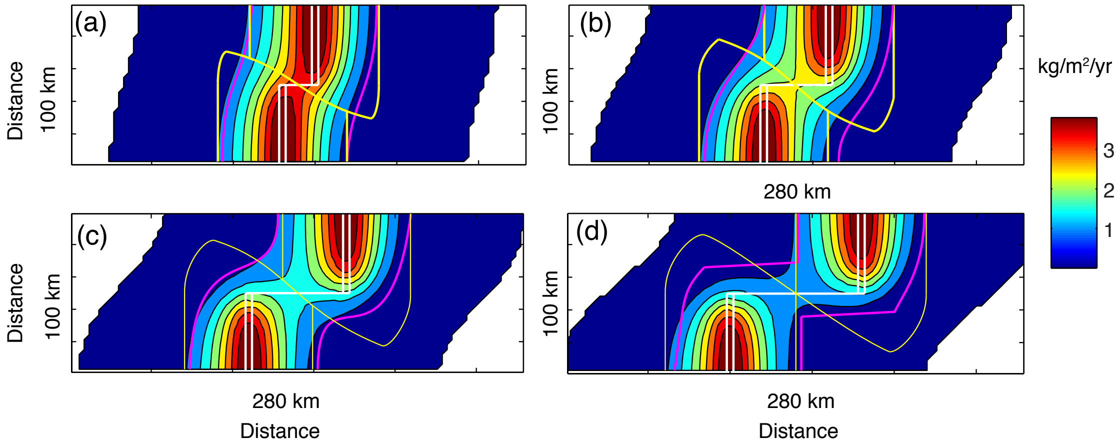

Figure 3.7: Maps contoured for the melting rate integrated over the depth of the domain. White lines show the trace of the ridge system, yellow lines show the outlines of the focusing regions, and magenta lines show the trace of the extremal surfaces on the base of the melting region. Results taken from simulations with U_r = 1cm/yr and offsets of (a) 20 km, (b) 40 km, (c) 60 km, (d) 80 km.

bottom of the melting region. The relative spatial positions of the extremal surfaces and minor focusing sub–regions lends itself to a more detailed explanation of the simulation results.

In the 2D study by Katz et al. (2004), melt is distributed over a constant along–axis distance at the ridge. Consequently, Δd is a maximum when the difference in excess melt production in the focusing regions ΔV is also a maximum. The magnitude of Δd depends on the ratio of ΔV to the volume of space created at the ridge by seafloor spreading. Katz et al. (2004) found the offset of maximum excess melt production to be approximately constant at 50 km. For 2D simulations, the offset of maximum excess melt production corresponds to the offset at which the extremal lines intersect the base of the melting region. In other words, when the excess melt production is a maximum, the minor focusing regions are centered above the locus of largest $|W'|$ within the melting region.

Results from our 3D simulations (figure 3.5) predict that the offset of peak Δt is dependent on spreading rate. Figure 3.5 shows that the offset of peak Δt decreases with increasing spreading rate. In contrast to Katz et al. (2004), the distance over which melt is distributed at the ridge axis, ζ, varies with spreading rate and offset length (figure 3.3). The offset of peak Δt, therefore, does not necessarily coincide with the offset of maximum excess melt production but depends on the ratio $\Delta V/\zeta$. When $\Delta V/\zeta$ is greatest, the difference in crustal thickness between two adjacent ridge segments is a maximum. The isostatic compensation function $\mathcal{C}$ given in Equation (3.16) converts Δt into a difference in axial depth, Δd. When $\mathcal{C}V/\zeta$ is greatest, Δd is a maximum. Figure 3.5 shows that, for a given spreading rate, there is little difference between the offset of peak Δt and peak Δd.

The results in figure 3.5 show significant asymmetry about their peak. The component of melting induced by ridge migration is a maximum on the extremal surfaces. It changes most rapidly with horizontal distance on the ridge–side of the surfaces. Therefore, ΔV, and thus Δt and Δd, changes most rapidly with offset for offsets less than that of peak Δd.

Figure 3.5 shows that Δd increases with spreading rate. In plate-driven flow, faster spreading rates drive faster upwelling. In our simulations U_r is equal to U_0, and thus the difference in melt production rate between the two minor focusing regions increases with U_0, causing Δd to increase with U_0.

Although the simulation results shown in figure 3.5 describe the general trends of the global MOR data, the data are distributed widely about the simulation results. With such a small number of data points it is difficult to assess how well our simulations and choice of parameters explain axial depth differences along the global mid–ocean ridge system. Furthermore, local, idiosyncratic, geological processes may induce large scatter in the data.

3.4.2 Constraining melt redistribution processes

Along mid ocean ridge systems, melt must be focused from a wide, partially molten region to a narrow zone approximately 5 km wide immediately beneath a ridge segment (Kelemen et al., 2000). To generate new crust, this melt must be tapped and redistributed on the scale of a ridge segment.

Geophysical observations of the MOR system offer an insight to the physical processes involved in melt redistribution. Seismic studies of fast spreading mid–ocean ridge systems suggest that melt is redistributed in the narrow zone beneath ridge segments to form axial magma chambers (Collier and Singh, 1998; Kent et al., 2000; Nedimovic et al., 2005; Singh et al., 2006b,a). These studies indicate that axial magma chambers for some fast and intermediate spreading rate ridges have a thickness of a few hundred meters and extend nearly continuously along the length of the ridge segment. Seismic reflections (Singh et al., 2006b) from the axial magma chamber beneath the 09°N overlapping spreading centre of the East Pacific Rise suggest that melt supply is enhanced beneath the ends of ridge segments. To form such magma chambers, melt must be supplied locally, rather than by large scale crustal redistribution (Macdonald et al., 1988; Wang et al., 1996). Field studies suggest that local melt redistribution processes include melt flow through cracks (Singh et al., 2006a), pipe-like features (Magde et al., 2000), and the porous mantle (Kelemen et al., 2000).

Seismic and gravity studies of slow-spreading centers show that crustal thickness varies along the length of MOR segments. The amplitude of inferred along–axis variation in crustal thickness decreases with increasing spreading rate (Lin and Phipps Morgan, 1992). For slow-spreading ridges, the crust is usually thickest at the centre of the segment and thins towards the ends (Kuo and Forsyth, 1988; Lin et al., 1990; Lin and Phipps Morgan, 1992; Tolstoy et al., 1993; Detrick et al., 1995; Escartin and Lin, 1995; Hooft et al., 2000; Canales et al., 2003; Planert et al., 2009). This feature has been attributed to enhanced melt delivery at segment centers. Figure 3.3a shows that the shape of the melting region deflects melt away from the end of the ridge segments. The simulations predict that the variation in crustal thickness prior to melt redistribution decreases with increasing spreading rate. This behaviour is common to other numerical studies of melt focusing that use the melt migration model of Sparks and Parmentier (1991) (Magde and Sparks, 1997; Magde et al., 1997; Gregg et al., 2009). For ridge segments that are tens of kilometers long, this behaviour may lead to enhanced melt supply and thicker crust at segment centers. Bell and Buck (1992) note that slow spreading ridges with thick crust do not show large crustal thickness variation on a segment scale, suggesting that melt redistribution may be a function of crustal thermal structure.

Although geophysical investigations can constrain melt redistribution processes on a large scale, the scale and extent of these processes may be studied more intimately using geochemical and petrological techniques. Geochemical variations in ridge–axis lavas can yield information about the source region and geological history of the parent magma. Petrological mapping of oceanic basalts at MORs indicates that igneous rocks formed close to ridge offsets have a deeper source region and lower extent of melting than those elsewhere along the ridge segment (Langmuir and Bender, 1984; Langmuir et al., 1986; Reynolds and Langmuir, 1997). In samples taken along the axis of the North East Pacific Rise, the most enriched geochemical signals are found consistently at the ends of leading ridge segments (Carbotte et al., 2004). These excursions peak very close to the offset and typically decay rapidly with distance along the ridge axis.

Results to the models presented here suggest that geochemical variations can exist between the melt focused from the leading and trailing focusing regions. Unless the direction of ridge migration is parallel to the ridge trace, the leading focusing region samples relatively deep mantle in advance of the trailing focusing region. Consequently, melts produced in the leading minor melt focusing region will be among the most enriched and compositionally diverse. In contrast, because the trailing minor focusing region lies in the wake of the leading ridge segment, melt generated in this trailing sub–region will have smaller variations in trace element geochemistry. The amplitude of these variations will be greatest when the direction of ridge migration is perpendicular to the ridge axis. The amplitude will decrease with the angle between the direction of ridge migration and the ridge axis. Hence the models appear to be compatible with the geochemical observations made by Carbotte et al. (2004).

3.4.3 Mantle rheology

Predictions of mantle dynamics and thermal structure generated by our simulations depend largely on the assumed mantle rheology. For this study we assume that the mantle is a non-Newtonian fluid that deforms by combined diffusion and dislocation creep. Katz et al. (2004) show that this choice of rheology improves the fit between simulation results and global MOR data over diffusion creep alone. Other numerical experiments of mantle flow near transform faults by Behn et al. (2007) and Gregg et al. (2009) explore the importance of using a viscoplastic rheology. They show that simulations with a viscoplastic rheology, over those with a constant or temperature–dependent viscosity, better fit geophysical and geochemical observables.

Figure 3.3 demonstrates the importance of the mantle thermal structure to melt focusing. The experiments by Behn et al. (2007) Gregg et al. (2009) predict that a viscoplastic rheology tends to localize deformation around the ridge segments and transform faults. This causes the mantle around the transform fault to be warmer and reduces the along–axis distance over which melt is focused away from the offset.

To examine the influence of a viscoplastic rheology on our simulations we define a viscoplastic rheology:

$$\eta = \left(\frac{1}{\eta_{difn}} + \frac{1}{\eta_{disl}} + \frac{1}{\eta_{bsa}} \right)^{-1}, \tag{3.17}$$

where η_{bsa} is a brittle strength approximation using Byerlee's law. The viscosity associated with brittle failure η_{bsa} is given by (Chen and Morgan, 1990)

$$\eta_{bsa} = \frac{\tau}{\sqrt{2}\dot{\epsilon}_{II}}, \tag{3.18}$$

in which brittle strength is approximated by a friction law:

$$\tau = \mu \rho g z + c_0. \tag{3.19}$$

Here, μ is the frictional coefficient (0.6), g is the acceleration due to gravity, and c_0 is the cohesion (10 MPa).

Figure 3.8 compares two identical suites of simulations with U_r = 2cm/yr, except that one (shown in pink) uses the non–Newtonian viscosity defined in equation (3.4), and the other (shown in blue) assumes the viscoplastic rheology given in equation (3.17). For the viscoplastic simulations, the focusing distance is 48 km. This returns a crustal thickness of 6 km at an on–axis point 70 km from the transform fault. Comparison of figures 3.8a with 3.3a demonstrates that the morphology of the melting

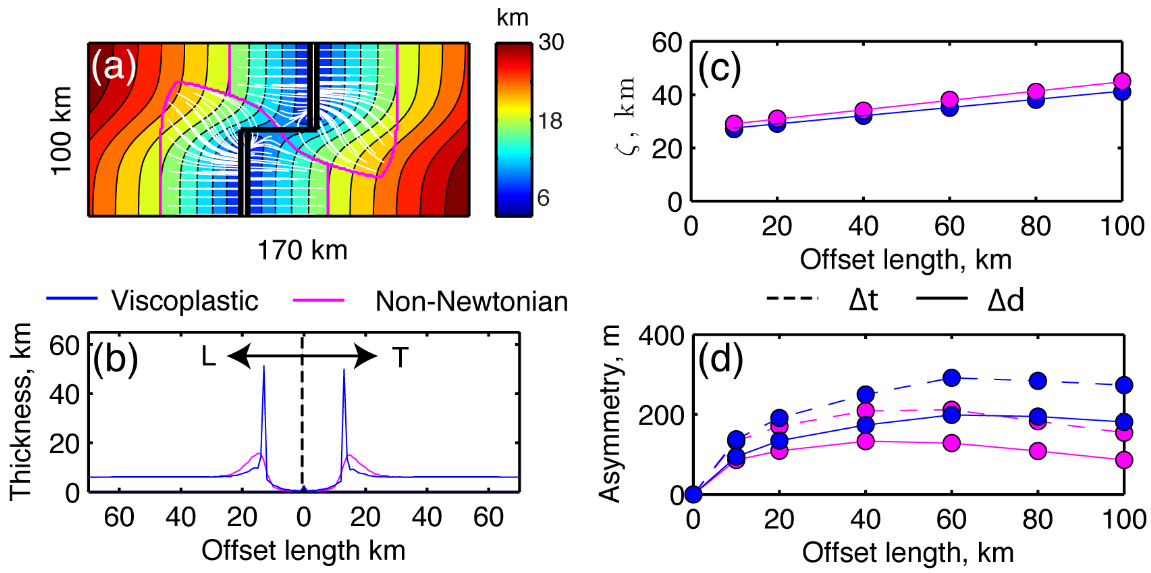

Figure 3.8: Comparison of results from a two suites of simulations, one having a non–Newtonian rheology (magenta lines) and the other using a viscoplastic rheology (blue lines). All simulations have U_r = 2cm/yr and a domain depth of 300 km. (a) Map showing the relationship between solidus depth, focusing region shape and melt focusing trajectories. White streamlines show melt focusing trajectories. Black lines outline the geometry of the ridge system. Magenta lines mark the perimeters of the focusing regions. Coloured contours show depth to the top of the melting region. The transform fault length is 40 km. Ridge is migrating to the left. This figure can be compared directly with its non–Newtonian analogue in figure 3.3a. (b) Profiles showing the along–axis crustal thickness prior to redistribution of the melt. The offset length for these simulations is 40 km. L and T denote the leading and trailing ridge segments respectively. (c) Variation in the redistribution length ζ as a function of transform fault length. (d) Comparison of the difference in crustal thickness (Δt, dashed) and axial depth (Δd, solid) for the two suites of simulations as a function of offset length.

region differs between analogous simulations. The viscoplastic rheology enhances the upwelling and thermal regime around the ridge segments and transform fault. This increases the amount of melt focused across offsets and, around the transform fault, decreases the depth to the melting region.

Figures 3.8a and b show that the change in morphology of the melting region alters the delivery of melt to the ridge axis. In the case of a viscoplastic rheology melt is delivered to a point close to the transform fault. However, figures 3.8b and c show that the neither the position of maximum melt delivery, or the redistribution distance ζ are changed much.

Figure 3.8d shows the effect of a viscoplastic rheology on axial depth differences for a range of transform fault lengths. The dashed curves show the difference in crustal thickness as a function of offset length. Assuming flexural support of ridge topography, these are converted into a difference in axial depth. For all nonzero offsets viscoplastic simulations predict greater asymmetry in crustal thickness and axial depth. This difference in asymmetry arises because the viscoplastic rheology increases the amount of melt focused across offsets (figures 3.8a and 3.3a). The significance of this effect increases with offset, resulting in increasingly greater differences in predicted crustal thickness and axial depth.

3.5 Conclusions

Results from 3D models of asthenospheric flow suggest that plate–induced mantle dynamics can account for morphological changes observed along the global MOR system. The models assume that the mantle viscosity is high enough for asthenospheric flow to be effectively plate–driven. Ridge migration perturbs asthenospheric flow, causing faster upwelling and enhanced melting beneath the plate that is leading with respect to the direction of ridge migration in the hotspot reference frame. Under reasonable assumptions of 3D melt focusing, this melting asymmetry causes a difference in axial depth and crustal thickness of ridge segments separated by an offset. The sense of mantle asymmetry predicted by our model is consistent with that seen in geophysical observations of MORs (The MELT Seismic Team, 1998; Panza et al., 2010). Predictions of differences in axial depth across ridge offsets generated by the models describe the general trend and amplitude of global MOR data. The amplitude of the data can be fit with a widely used model of 3D melt focusing (Sparks and Parmentier, 1991) and an asthenospheric thickness of 300 km. To smooth variations in crustal thickness close to transform faults, we assume that melt is redistributed along the ridge segment axis by melt flow through the porous mantle and cracks. Additional experiments that include a viscoplastic rheology predict enhanced mantle temperatures and upwelling rates around the ridge segments and transform fault. This leads to an increase in the predicted asymmetry in axial depth. Future models can further constrain shallow mantle and lithospheric processes that distribute melt at the ridge axis by using a parameterization of mantle melting and incompatible element behaviour.

Chapter 4

Melting and channelized magmatic flow in chemically heterogeneous, upwelling mantle

A version of this chapter is published as

Weatherley, S.M. and Katz, R.F., (2012) Melting and channelized magmatic flow in chemically heterogeneous, upwelling mantle, *Geochemistry, Geophysics, Geosystems*, vol. 13, Q0AC18.

4.1 Introduction

Partial melting and melt extraction in the mantle beneath mid-ocean ridges are often described as near-fractional processes (Langmuir et al., 1977; Johnson et al., 1990; Spiegelman and Kenyon, 1992; Hart, 1993; Iwamori, 1993; Kelemen et al., 1997; Spiegelman and Kelemen, 2003). In the simplest case of near-fractional melting, small amounts of melt form over a range of pressures and without further chemical interaction with the mantle, get transported to the surface and mixed (Klein and Langmuir, 1987; McKenzie and O'Nions, 1991). Once at the surface, these melts erupt and preserve in the oceanic crust a chemical record of melting, crystallization, and any reactions that they undergo while travelling through the mantle.

Geochemical analysis of the oceanic crust shows that the composition of erupted magmas varies across the globe. Some of the variation is systematic, and depends on properties of the spreading ridge. Klein and Langmuir (1987), for example, showed that the geochemistry of mid-ocean ridge basalts varies systematically with axial depth and the proximity of hotspots. But much of the chemical variation is unstructured and depends on the composition of the source rock (e.g., Wood, 1979; Allègre et al., 1984; Ben Othman and Allegre, 1990; Salters and Dick, 2002; Seyler et al., 2011). Processes subsequent to melting, such as mixing (Hirschmann and Stolper, 1996; Maclennan et al., 2003; Stracke and Bourdon, 2009), reaction between magma and the ambient mantle rock (Yaxley and Green, 1998), and crystal fractionation (Grove et al., 1992) may disguise the geochemical signal of the source rock; yet the isotopic variability of mid-ocean ridge basalts (MORB) is sufficient to prove that the mantle source is compositionally heterogenous. Recently Shorttle and Maclennan (2011) found that heterogeneity in the form of more and less fusible peridotite is sufficient to generate the observed chemical variability of Icelandic basalts. They showed that depleted basalts can result from melting of a depleted peridotite (similar to KLB-1 of Walter (1998)), while enriched basalts are likely to derive from a peridotite refertilized by up to 40% MORB. Shorttle and Maclennan (2011) also presented a bilithologic melting model that, in conjunction with geochemical observations, indicates that no more than 10% recycled MORB is present in the bulk mantle. This result is in broad agreement with other suggestions that the mantle source comprises small amounts ($\approx 10\%$) of eclogite or pyroxenite ($> 90\%$ pyroxene) hosted in the ambient peridotitic mantle (Wood, 1979; Zindler et al., 1979; Langmuir and Bender, 1984; Allègre and Turcotte, 1986; Prinzhofer et al., 1989; Langmuir et al., 1992; Chabaux and Allègre, 1994; Lassiter and Hauri, 1998; Phipps Morgan and Morgan, 1999; Pertermann and Hirschmann, 2003; Stracke et al., 2003; Ito and Mahoney, 2005; Stracke et al., 2005; Kokfelt et al., 2006; Prytulak and Elliott, 2007; Jackson et al., 2008; Gale et al., 2011).

For the geochemical identity of the source rock to be preserved in the erupted magma, melt transport must occur, to a large extent, without chemical re-equilibration or reaction with the ambient mantle. Chemically isolated flow is also required by observations of disequilibrium between MORB-forming magmas and residual mantle peridotites (rocks containing >40% olivine and >10% pyroxene). For example, residual peridotites (harzburgite and lherzolite) are saturated in orthopyroxene whereas mid-ocean ridge basalts are not. It follows that MORB-forming magmas are undersaturated in orthopyroxene at Moho pressures. But at pressures greater than 8 kbar the same magmas are saturated in orthopyroxene (O'Hara, 1965; Stolper, 1980). This pressure-dependent change in saturation indicates that basalt-forming liquids are chemically isolated from the solid, orthopyroxene-bearing mantle at pressures less than 8 kbar.

Uranium series disequilibria measured in oceanic basalts adds the further, challenging constraint that melt transport in the mantle must be rapid (Jull et al., 2002; Stracke et al., 2006). To generate the observed disequilibria, magma must be able to flow from its point of genesis to the surface on a timescale similar to, or shorter than, the half-life of ^{230}Th (75 kyr) (Turner and Bourdon, 2011).

In general, then, global observations of MORBs require that magmatic flow in the mantle is rapid and chemically isolated, and that magma forms by melting of a chemically heterogeneous mantle. What, if any, is the relationship between these two aspects of magmatism? Is chemically isolated magmatic flow a consequence of mantle heterogeneity? Or can this style of melt transport occur independently of chemical heterogeneities in the source region?

One currently popular model for rapid, chemically isolated melt transport invokes reactive porous flow of magma through a network of high porosity channels. This idea grew around field observations of the Oman ophiolite, which is thought to preserve the crust and uppermost mantle from a spreading ridge (Tilton et al., 1981; Alabaster et al., 1982; Nicolas, 1989; Kelemen et al., 1997). The mantle section of the ophiolite contains a suite of anastomosing, tabular-shaped dunites (>90% olivine) (Kelemen et al., 2000). The dunites replace mantle peridotites, rather than intrude then, and form when magma migrating by porous flow dissolves pyroxene out of the ambient peridotite (Kelemen et al., 1995a). In addition, the erupted melts preserved by the ophiolite are in chemical equilibrium with the dunites. The implication, therefore, is that dunites in the Oman ophiolite represent fossilized conduits, or channels, through which magma was transported to the surface. Similar conclusions are drawn from an increasing number of ophiolites and mantle peridotites around the globe, including the Ligurian ophiolites (Renna and Tribuzio, 2011), Polar Urals (Savelieva et al., 2008), the Bay Islands Ophiolite (Suhr et al., 2003), and Troodos (Batanova and Sobolev, 2000; Buchl et al., 2002).

The reactive infiltration instability (Chadam et al., 1986; Ortoleva et al., 1987) is thought to provide a mathematical description of how magmatic channels form (Aharonov et al., 1995, 1997; Kelemen et al., 1997; Spiegelman et al., 2001; Spiegelman and Kelemen, 2003; Liang and Guo, 2003; Hewitt, 2010; Liang et al., 2010; Schiemenz et al., 2011; Liang et al., 2011; Hesse et al., 2011). In this instability, a feedback between melt transport and corrosive dissolution causes magmatic flow to organize into a network of high porosity channels. To generate channels, magma rises buoyantly and dissolves pyroxene out of the ambient peridotite. Regions of larger melt flux accommodate greater dissolution, which increases the local permeability and causes magma to be focused to where it is already concentrated. This is the channel-forming instability.

To understand the implications of the reactive infiltration instability for magmatic flow, Aharonov et al. (1995) developed a numerical model of reactive melt transport in a column of chemically homogeneous mantle rock. Their model is based on canonical equations for porous flow and compaction (McKenzie, 1984) and emulates the behaviour of orthopyroxene in the mantle by assuming that mantle rock becomes more soluble towards the surface. Magma rising through the domain reacts with and removes mass from the solid. Provided that the solubility gradient is great enough, these experiments predict that magma flow is unstable and localizes into a network of high porosity channels.

Subsequent models of channel formation (Spiegelman et al., 2001; Spiegelman and Kelemen, 2003; Liang et al., 2010; Schiemenz et al., 2011; Liang et al., 2011) followed the same approach as Aharonov et al. (1995), but considered only magma flow and channelization in a chemically homogenous mantle. The specific details between the experimental setups varies. For example, Aharonov et al. (1995); Spiegelman et al. (2001), and Spiegelman and Kelemen (2003) modified the composition of the mantle with vanishingly small random perturbations and, in addition to Liang et al. (2010) and Schiemenz et al. (2011), considered the consequences of incongruent melting. To generate channelized flow, Liang et al. (2010) and Schiemenz et al. (2011) prescribed a sustained perturbation of porosity to a section of the inflow (bottom) boundary. To some extent this boundary condition could be interpreted to capture the behaviour of the mantle above an anomalously fusible heterogeneity that is melting. Such an interpretation, however, is inconsistent with the compositional variation of the magma that would be associated with the heterogeneous source.

An important shortcoming of most existing numerical investigations of reactive melt transport and channelized flow is that they neglect the energetics of the system (Aharonov et al., 1995; Spiegelman et al., 2001; Spiegelman and Kelemen, 2003; Liang et al., 2010; Schiemenz et al., 2011; Liang et al., 2011). Melting is an inherently thermodynamic process, and models that predict the melting rate without accounting for conservation of energy are inconsistent. Relatively few studies consider melting and magmatic flow in a thermodynamically consistent system (McKenzie, 1984; Fowler, 1985; Ribe, 1985; Katz, 2008, 2010; Hewitt, 2010; Katz and Weatherley, 2012), and of these only Hewitt (2010) and Katz and Weatherley (2012) investigate channelized flow. These models share the same theoretical framework for porous flow and compaction as models that don't conserve energy, but use the Enthalpy Method (Alexiades and Solomon, 1993) to close a system of equations that includes conservation of energy. This approach assumes local thermodynamic equilibrium and uses a phase diagram to relate bulk composition, enthalpy, and pressure to the phase compositions, temperature and melt fraction. Since reaction of major elements in the mantle is rapid relative to timescales of melt transport, the assumption of thermodynamic equilibrium is not unreasonable.

An interesting result from the energy-conserving studies of Katz (2010) and Hewitt (2010) is that channels do not form in an upwelling mantle that has a uniform composition prior to melting. This result is contrary to the previous studies that did not account for conservation of energy (Aharonov et al., 1995; Spiegelman et al., 2001; Spiegelman and Kelemen, 2003).

What, then, gives rise to magmatic channels? Hewitt (2010) showed that channels only form if the melting region is supplied with a sufficient, additional flux of magma. We hypothesise that this additional flux of magma is supplied by partially melting regions of more fusible rock. Provided that these regions are sufficiently fusible, this flux will nucleate and support high-porosity channels via a mechanism similar to the reactive infiltration instability.

This chapter examines the effect that chemical heterogeneities have on melting and melt extraction in an upwelling mantle. Specifically, the effect that a single, isolated heterogeneity has on melting and magma flow is investigated using the theory and approach outlined in Chapter 2. Attributes of the mantle and heterogeneity are systematically varied with the aim of elucidating the fundamental dynamics of the system.

In Section 4.2 we outline our numerical model. We describe the results of the model in section 4.3, and investigate its sensitivity to parameters that are either geologically or theoretically important. We explore the response of the system to the fertility, size, and shape of compositional heterogeneities, the upwelling rate of the mantle, latent heat of fusion and the thermal diffusivity. The results emphasise that the relationships between melting processes, compositional heterogeneities, and magma flow in the mantle are complex, and they underscore the importance of thermal diffusion to magmatic flow and melting in the presence of chemical heterogeneities.

Section 4.4 presents a derivation of the thermodynamically consistent melting rate, which accounts for thermal and chemical diffusion. The result of the derivation offers a structured framework in which to interpret the results. Using this derivation, we explore how different processes contribute to the melting rate and conclude with a discussion of the limitations of our model.

4.2 Methods

4.2.1 Domain, petrology, and initial condition

The situation considered is a two-dimensional column of upwelling mantle rock that contains a compositional heterogeneity (figure 4.1). The size and position of the domain are fixed: the top of the domain is aligned with the surface, where the lithostatic pressure is zero, and it extends 120 km into the mantle. Solid rock flows into the domain through the bottom boundary at a rate W_0, where it has a known potential temperature $\mathcal{T}$ and composition C_m.

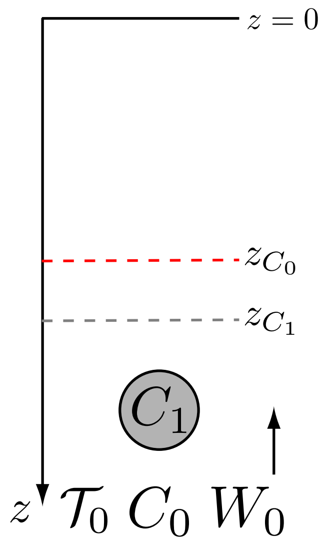

Figure 4.1: Schematic showing the general setup of our experiments. Solid rock flows into the base of the column at a rate W_0. It has a known potential temperature $\mathcal{T}_0$, and known composition C_0. The initial composition field contains a lithological heterogeneity (grey circle) of composition $C_1 < C_0$ that is enriched in the more fusible chemical component. The ambient mantle begins to melt at a depth z_{C_0}. Since the lithological heterogeneity is more fusible, it begins to melt at the deeper depth of z_{C_1}.

Following the general approach outlined in Chapter 2, thermodynamic equilibrium is assumed and a binary phase diagram (figure 4.2) is adopted to model the petrological system. To simplify the results, the solidus and liquidus surfaces are approximated to be linear and are given by

$$T_S = T_0 + \frac{P_L}{\gamma} + M_S \left(C_m - C_0\right), \tag{4.1}$$

$$T_L = T_0 + \frac{P_L}{\gamma} + M_L\,(C_f - C_0 + \Delta C)\,, \tag{4.2}$$

where T_S and T_L are the solidus and liquidus temperatures, P_L is the lithostatic pressure and γ is the Clapeyron slope, which is assumed constant. M_S and M_L define the slopes $\partial T/\partial C$ of the solidus and liquidus. C_0 is the composition of the ambient mantle at the onset of melting, and at zero pressure, melts at the reference temperature T_0. ΔC is the difference in composition between coexisting rock and magma in equilibrium at T_0. Figure 4.2 shows that one of the components melts at a lower temperature than the other; regions enriched in this component are referred to equivalently as 'enriched', or 'more fusible'. Conversely, regions enriched in the other component are referred to as 'depleted' or 'less fusible'.

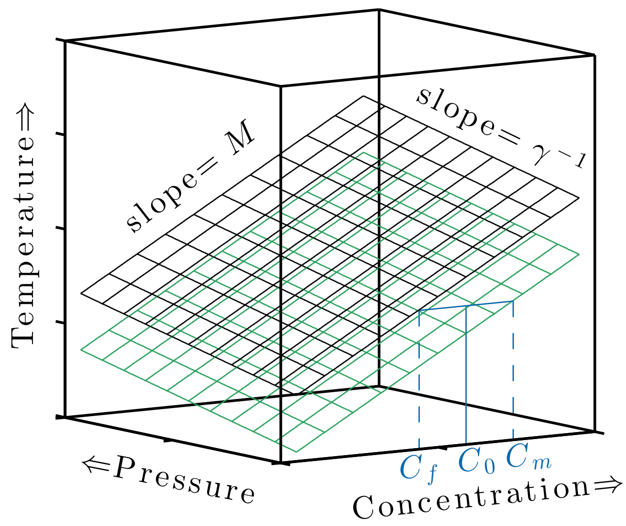

Figure 4.2: Linearized surfaces for the solidus (lower surface) and liquidus (upper surface). C_0 marks the bulk composition at zero pressure. C_f and C_m show the compositions of coexisting magma and solid rock. The mass fraction of the liquid is given by $(C_0 - C_f)/(C_m - C_f)$.

The initial condition incorporates a circular chemical anomaly, or enclave, that is enriched in the more fusible component (figure 4.1). The anomaly is defined as $C_{\mathrm{IN}} + \mathcal{C}\,[1/2 + \tanh(R - R_0)/2\lambda]$, where C_{IN} is the composition of ambient mantle rock on the bottom boundary, $\mathcal{C}$ specifies the amplitude of the anomaly, R_0 is the radius of the heterogeneity and R is the distance of a point from its centre, and λ is a parameter that determines the sharpness of the edges of the heterogeneity. Combining equation 4.1 with the linearized adiabatic temperature gradient $T = \mathcal{T} + \alpha g z \mathcal{T}/c_P$ shows the depth of melting to be

$$z_m \approx \frac{\mathcal{T} - T_0 - M_S\left(C_m - C_0\right)}{\rho g/\gamma - \alpha g \mathcal{T}/c_P}. \tag{4.3}$$

Hence the heterogeneity, enriched in the more fusible component, begins to melt at a greater depth than the surrounding ambient mantle. Above this depth the system contains two phases. As described in chapter 2, the rock is modeled as a porous, compactible solid that behaves as a fluid on geological timescales and the magma is considered to be a buoyant liquid. At the surface these interpenetrating fluids flow unrestrictedly out of the top of the domain. The boundary conditions are described in more detail in section 4.2.2.

Although our ultimate goal is to gain an insight into processes that might operate beneath a mid-ocean ridge, we do not attempt to model the physical setting of a mid-ocean ridge. At a spreading ridge the motion of the lithosphere introduces a horizontal component of motion into the solid mantle flow field. Since we aim only to understand how mantle heterogeneity influences melt transport in the mantle, we neglect the complicating factors introduced by plate motion. Furthermore, in this paper we will not attempt to infer whether our model can account for geochemistry of erupted magmas. To do so would require similar experiments to be run in a model configured to simulate a mid-ocean ridge. Examples of computations run with boundary conditions corresponding to a mid-ocean ridge are provided in Katz and Weatherley (2012) and the following chapters.

4.2.2 Governing equations

In restricting the situation to a two-dimensional upwelling column, large scale shear of the matrix governed by Stokes' equation (equation 2.8) is neglected. Consequently, the solid velocity $\mathbf{v}_m$ can be written as $\mathbf{v}_m = \boldsymbol{\nabla}\mathcal{U}$, where $\mathcal{U}$ is a velocity potential that is related to the compaction pressure (Spiegelman, 1993a). The equations governing the mechanical aspects of the model (equations 2.7–2.9) are then recast as

$$-\boldsymbol{\nabla}\cdot\frac{K}{\mu}\boldsymbol{\nabla}\mathcal{P}+\frac{\mathcal{P}}{\xi}=\boldsymbol{\nabla}\cdot\frac{K}{\mu}\left(1-\phi\right)\Delta\rho g\mathbf{k}, \tag{4.4}$$

$$\frac{\mathcal{P}}{\xi}=\nabla^2\mathcal{U}, \tag{4.5}$$

where $\xi=\zeta+4/3\eta$ is the compaction viscosity modified for the upwelling column. Equations 2.18 and 2.23, which govern the thermochemical aspect of the model remain unchanged from chapter 2 and are represented here for completeness.

$$\frac{\partial\mathcal{H}}{\partial t}=\rho L\boldsymbol{\nabla}\cdot\left(1-\phi\right)\mathbf{v}_m-\rho c_P\mathrm{e}^{-\mathcal{A}z}\bar{\mathbf{v}}\cdot\boldsymbol{\nabla}\mathcal{T}+\kappa\mathrm{e}^{-\mathcal{A}z}\nabla^2\mathcal{T}, \tag{4.6}$$

$$\frac{\partial C}{\partial t}+\boldsymbol{\nabla}\cdot\phi\mathbf{v}_fC_f+\boldsymbol{\nabla}\cdot\left(1-\phi\right)\mathbf{v}_mC_m=\mathcal{D}\boldsymbol{\nabla}\cdot\phi\boldsymbol{\nabla}C_f. \tag{4.7}$$

where $\mathcal{H}=\rho L\phi+\rho c_P(T-T_0)$ and $C=\phi C_f+\left(1-\phi\right)C_m$. These equations are closed using the approach described in section 2.4, where the equilibrium phase diagram is used to find values for ϕ, T, C_m and C_f.

The boundary conditions for the four primary variables $\mathcal{H}$, C, $\mathcal{P}$ and $\mathcal{U}$, on the top and bottom boundaries are specified in table 4.1. Rock flowing into the domain across the bottom boundary upwells at a rate W_0, has potential temperature $\mathcal{T}$, composition C_0 and, since it is completely solid, $\mathcal{P}=0$. The outflow boundary conditions correspond to the top boundary being open and $\partial\phi/\partial z=\partial\mathcal{T}/\partial z=0$. In the x-direction the domain is defined to be periodic.

4.2.3 Numerical methods

The system of governing equations and boundary conditions is discretized onto a staggered mesh using a semi-implicit, finite volume scheme with a grid resolution of 0.5×0.5 km. The mesh is illustrated in figure 4.3. To assist with numerical solution the equations are split into two groups that are solved iteratively at each time step. The first group comprises equations 4.4 and 4.5 that govern the mechanics, and the second comprises equations 4.6 and 4.7 for the time dependent variables $\mathcal{H}$ and C. At

Table 4.1: Boundary conditions for the upwelling column model.

Boundary	Variable	Boundary condition[a]
$z = 0$	$\mathcal{U}$	$\mathcal{U} = 0$
	$\mathcal{P}$	$\partial\mathcal{P}/\partial z = 0$
	$\mathcal{H}$	$\mathcal{H} = \rho L\phi + \rho c_P \exp(\alpha g z/c_P)(\mathcal{T} + T_0) - \rho c_P T_0$, where $\phi = \phi_{j+1,i}$ is the porosity in the grid cell underlying cell j, i and $\mathcal{T}$ is given by equation 2.17.
	C	$\partial C/\partial z = 0$
$z = D$	$\mathcal{U}$	$\partial U/\partial z = W_0$
	$\mathcal{P}$	$\mathcal{P} = 0$
	$\mathcal{H}$	$\mathcal{H} = \rho c_P \exp(\alpha g D/c_P)(\mathcal{T} + T_0) - \rho c_P T_0$
	C	$C = C_0$

[a] The domain size is $z \in [0, D]$.

every time step each group of equations is solved iteratively using an incomplete LU preconditioned Newton-Krylov method provided by the Portable, Extensible Toolkit for Scientific Computing (PETSc) (Balay et al., 1997, 2009). At each iteration the variables ϕ, T, C_f and C_m are also updated. For reasons of numerical efficiency, permeability is limited by an upper bound at $\phi = 15\%$ to avoid excessively large velocities when the porosity is large. This has a negligible effect on the dynamics of the system. No lower bound is set.

To preserve gradients in the system we use a total variation diminishing (TVD) flux limiting advection scheme that is outlined in Appendix B. TVD schemes are conservative and non-oscillatory. Normally, they are second order in space, but near sharp gradients, their order is reduced. Appendix B shows that the superbee flux limiter is the best for minimising dispersion and diffusion, hence it is used for the numerical experiments presented in this chapter.

4.3 Results

4.3.1 General behaviour

Figure 4.4 shows a time series of solutions from a single, representative experiment in terms of different variables. Figures 4.4a1–f1 show porosity and figures 4.4a2–f2 show

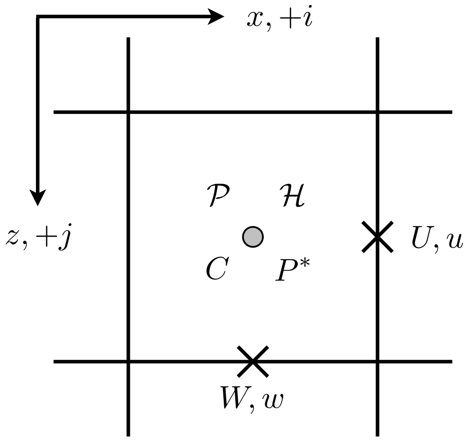

Figure 4.3: Schematic showing there the variables are located in each grid cell. $\mathcal{H}$, $\mathcal{P}$, $\mathcal{U}$, C, in addition to C_m and C_f (not shown) are located at the centre. The horizontal and vertical components of velocity for the matrix ($U = \mathbf{v}_m \cdot \mathbf{x}$, $W = \mathbf{v}_m \cdot \mathbf{k}$) and magma ($u = \mathbf{v}_f \cdot \mathbf{x}$, $w = \mathbf{v}_f \cdot \mathbf{k}$) are placed on the $+i$ and $+j$ faces respectively.

the solid composition. Since the petrological system is hypothetical, compositional variations are expressed as $\Delta T_C = M_S (C_m - C_0)$, which is the difference in solidus temperature due to deviation of the local composition from the reference composition C_0. Figures 4.4a3–f3 show the temperature and figures 4.4a4–f4 show the melting rate. Γ is computed diagnostically by rearranging equation 2.1 for conservation of the fluid's mass to give $\Gamma = \rho \left(\frac{\partial \phi}{\partial t} + \nabla \cdot \phi \mathbf{v}_f \right)$. Figures 4.4 a5–f5 show the the magma speed $|\mathbf{v}_f|$, which is computed diagnostically using equation 2.1 and figures 4.4 a6–f6 show the compaction pressure. Negative compaction pressures indicate that the matrix is compacting, and that the magmatic pressure is less than the lithostatic pressure.

The experiment in figure 4.4 is initialized with a disk of material that is enriched in the more fusible component, with $\Delta T_C = -30°\text{C}$. The radius of the disk is 4 km and the initial depth of its centre point is 100 km. All other parameters are assigned reference values that are listed in table 4.2.

The complete time series of results in figure 4.4 shows that an enclave of fertile rock, which is embedded into the upwelling mantle, partially melts and supplies the ambient melting region with an additional flux of magma. The additional flux of magma initiates reactive channelization.

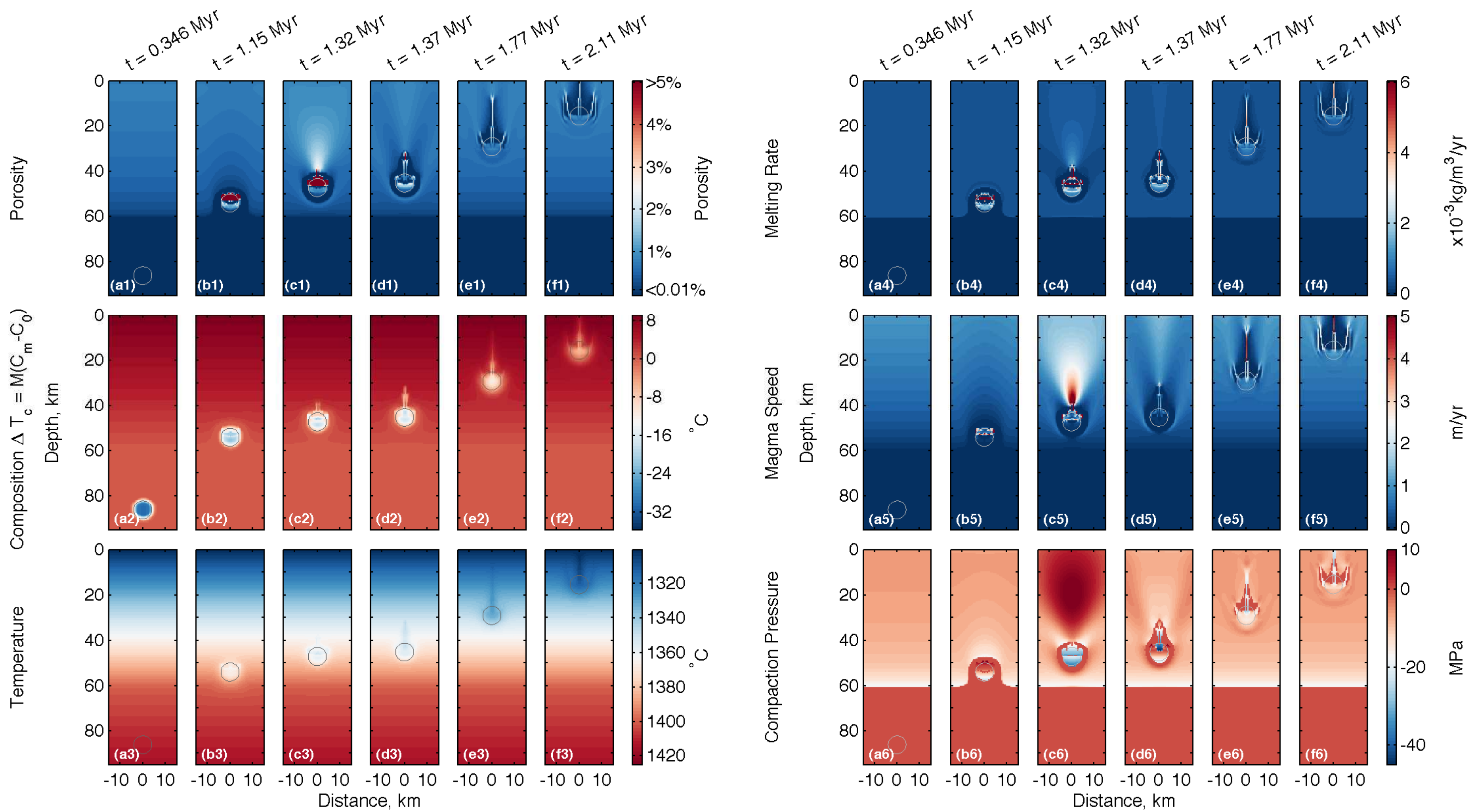

Figure 4.4: A series of snapshots charting the time evolution of a representative experiment. Columns show the solution at constant time steps. All parameters take the preferred values listed in table 4.2. Yellow circles show what would be the perimeter of the unmolten heterogeneity.

Table 4.2: List of parameters and preferred values.

Symbol	Meaning	Value
R	Enclave radius	4 km
ΔT_C	$M_S(C - C_0)$	-30°C
κ	Thermal diffusivity	1×10^{-6} m/s^2
W_0	Upwelling rate for the matrix	4 cm/yr
L	Latent heat of fusion	4×10^5J/kg
M_S	Slope $\partial T/\partial C$ of the solidus	400 K
M_L	Slope $\partial T/\partial C$ of the liquidus	400 K
$\mathcal{T}$	Potential temperature	1648 K
T_0	Solidus temperature for reference mantle at 0 kbar	1565 K
C_0	Reference mantle composition	0.85
ΔC	Difference in composition between rock and magma in thermodynamic equilibrium	0.1
ΔT	Temperature scale	$M\Delta C$
ρ	Density	3000 kg/m^3
α	Coefficient of thermal expansion	3×10^{-5} K^{-1}
c_P	Specific heat capacity	1200 J/kg/K
γ^{-1}	Clapeyron slope	60 K/GPa
$\mathcal{D}$	Chemical diffusivity	1×10^{-8} m/s^2
g	Acceleration due to gravity	9.8 m/s^2
k_0	Reference permeability	1×10^{-7} m^2
η_0	Reference shear viscosity	1×10^{19}Pa·s

The left most column of figure 4.4 (figures 4.4a1–a5) shows numerical solutions after a model time of 0.35 Myr. Throughout this paper a model time of zero is equal to the time at which the centre point of the anomaly crosses the 100 km depth contour. At this time, the enclave is not partially molten and the ambient melting region is in steady state. Melting of the ambient mantle begins at a depth of 60 km. Above this depth the porosity (figure 4.4a1), melting rate (figure 4.4a4), magma speed (figure 4.4a5), and ΔT_C (figure 4.4a2) increase towards the surface; the temperature (figure 4.4a3) and magnitude of the compaction pressure decrease (figure 4.4a6). These steady state results agree with the one-dimensional solutions found by McKenzie (1984); Ribe (1985); Katz (2008) and Hewitt (2010).

In figure 4.4, the second column from the left shows results from our experiment after a model time of 1.15 Myr. Figure 4.4b1 shows that the enriched enclave has started to melt, and that encasing it is an annulus of unmolten mantle rock. The solidus temperature of rock within the enclave is approximately 20°C cooler than the reference mantle (figure 4.4b2). Accordingly, the temperature of rock within the enclave is also lower than the surroundings. Heat diffuses into the enclave and powers melting. But diffusion removes heat from the surrounding mantle and suppresses melting, and so it gives rise to the annulus of subsolidus, impermeable rock that encases the enclave. This cool diffusion halo prevents magma flowing from the enclave into the ambient melting region.

As the enclave and annulus continue to upwell, rock within the annulus melts by decompression and establishes a permeable pathway that connects the enclave with the ambient melting region. Figures 4.4c1–c5 show the system at an instant after the completion of the pathway. The figures show that magma flowing from the enclave has invaded a balloon-shaped region in the overlying mantle. Within this region the porosity (figure 4.4c1) and melting rate (figure 4.4c4) are larger than the ambient values. Two effects give rise to the larger porosities and melting rates. First, the fluid pressure of the initial magma that leaves the enclave is greater than the lithostatic pressure, and so $\mathcal{P} > 0$ (figure 4.4c6). Thus the infiltrating magma mechanically increases the porosity in the overlying mantle. However, $\mathcal{P}$ remains positive only for a relatively short period of time (approximately 50 kyr, figure 4.4). Second, the flux of the infiltrating magma is greater than the ambient upwards flux of magma. Since the infiltrating magma is enriched, it must react with the ambient mantle rock to maintain thermodynamic equilibrium. By this reaction and the increased magma flux, the melting rate and porosity in the overlying mantle are increased.

Figures 4.4d1–d5 show that 50 kyr after the magmatic pathway is established, a channel emerges from the enclave. The channel grows by the same feedback that is fundamental to the reactive infiltration instability: enriched magma flows into the channel, the porosity increases by reaction, and so the channel can accommodate an even greater flux of magma. Within the channel, however, the matrix compacts and works to stabilize the flow, but the rate of porosity generation by melting outstrips the rate of porosity destruction by compaction, and so the channel grows. The channel itself accommodates a higher porosity (figure 4.4d1), melting rate (figure 4.4d4), and magma speed (figure 4.4d5) than the ambient mantle. It is enriched in the more fusible chemical component (figure 4.4d2) and, as a consequence, the temperature within the channel is a minimum for a given depth (figure 4.4d3). Heat, therefore, diffuses laterally into the channel, cooling the surrounding mantle and preventing it from melting. In this way, thermal diffusion encourages magmatic channelization at the expense of diffuse porous flow.

Over the remainder of the experiment (figures 4.4e1–f5) the channel grows and delivers magma to the surface. Initially, channels grow at a rapid rate, but the growth rate slows with time. Figures 4.4d2, 4.4e2, and 4.4f2 show that the fusibilities of the residual mantle within the enclave and channel gradually decrease with time, but the porosity, magma speed, and melting rate remain significantly larger than the ambient values. The elevated melting rate within the channel is associated with strong compaction (figure 4.4e6). Figures 4.4e1–f1 show that new channels begin to form on the flanks of the existing channel. The mechanisms that control the location of these channels remain unclear.

One feature of this and subsequent experiments is that the porosity generated within enclaves can exceed 20%. At porosities greater than 20% the matrix is likely to disaggregate (McKenzie, 1984) and the bulk material will behave as a slurry. Whether the governing equations and constitutive relationships accurately describe the mechanics of the system in this state is unclear. The aim, however, is not to fully capture the dynamics of magma flow within enclaves, nor to fully capture the process of magma leaving the heterogeneity. To do so would widen the scope of the models to include, amongst other processes, brittle fracture (Nicolas, 1986) and open fracture channels (Hewitt and Fowler, 2009). Instead, the study focuses on the dynamics that arise when a partially molten enclave supplements the ambient melting regions with an additional flux of magma. Since the porosity within enclaves drops to reasonable background values immediately after the onset of channelization, the large porosities generated within the enclaves do not adversely affect the trajectory of our experiments.

The results in figure 4.4 show that the flux of magma from a heterogeneity with $R = 4$ km and $\Delta T_C = -30°$C is sufficient to cause magma to localize. But for the same parameter values, what is the minimum size or fusibility required for a heterogeneity to nucleate channels? Figure 4.5 shows an array of computations for which the radius and fusibility of the heterogeneity is varied and separates the heterogeneities that give rise to channels from those that don't with the grey region. Clearly, magma channelizes when the heterogeneity is larger and more enriched. Both of these cases correspond to the heterogeneity delivering a greater flux of magma to the ambient melting region. However, the boundary does not depend simply on the excess volume of melt that a heterogeneity could supply. If this were the case, the boundary separating experiments that predict channels from those that do not might scale with $-T \propto R^{-2}$. This scaling assumes that the heterogeneity melts by decompression and all of the melt is directed into a single channel. Neither of these assumptions applies here and the results in figure 4.4 suggest that dynamics are more complex that assumed in this reasoning. Thus it is not surprising for the boundary to be more complex. Furthermore, the grid spacing may have some effect on the emergence and growth of channels, since channels resolve to the grid scale; this is discussed and explored in more detail in section 4.4.2. The sections that follow set out to explore how variations in important thermodynamical and geophysical parameters affect the dynamics of magma flow and

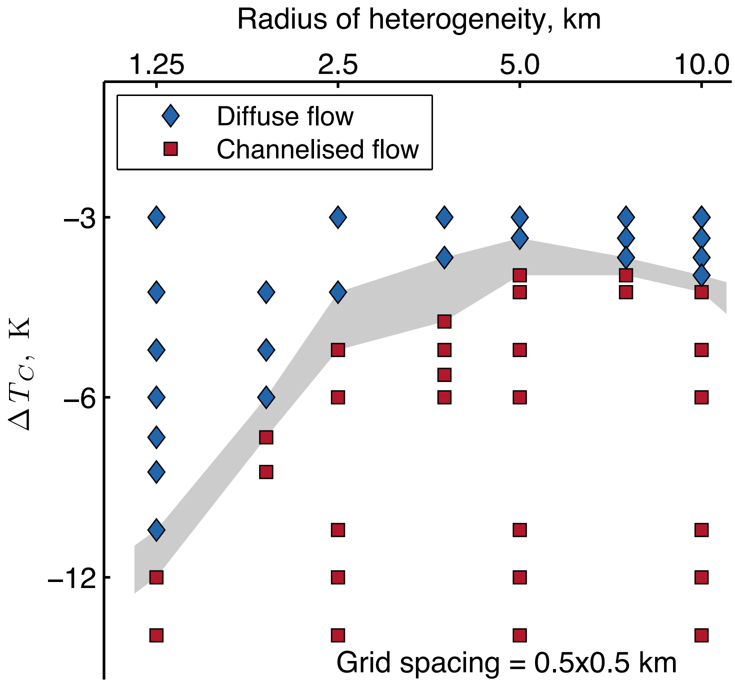

Figure 4.5: Diagram showing the boundary between diffuse porous flow and channelized flow for simulations run with heterogeneities of different size R and fusibility ΔT_C. Each point represents a single simulation with $W_0 = 3.5$ cm/yr. Red squares indicate that the additional flux of magma supplied by the heterogeneity is sufficient to cause melt localization. Blue diamonds indicate that the heterogeneity did not induce channelization. Figure adapted from (Katz and Weatherley, 2012).

melt localization.

4.3.2 Thermodynamic controls

Latent heat

The latent heat of fusion is an important control on melting, since it couples the rate of melt production to the energetic budget. We explore how L affects melting, and its subsequent influence on channelization, with an ensemble of five experiments (figure 4.6). For these experiments we varied L over an order of magnitude between $L = 9 \times 10^4$ J/kg and $L = 9 \times 10^5$ J/kg. Experimental work by Kojitani and Akaogi (1997) suggests that a reasonable value for the latent heat of fusion of mantle peridotite is 5×10^5 J/kg. All remaining parameters take their values from table 4.2. In figure

4.6 and each subsequent figure, the centre column shows results from an experiment run with our preferred parameter values from table 4.2.

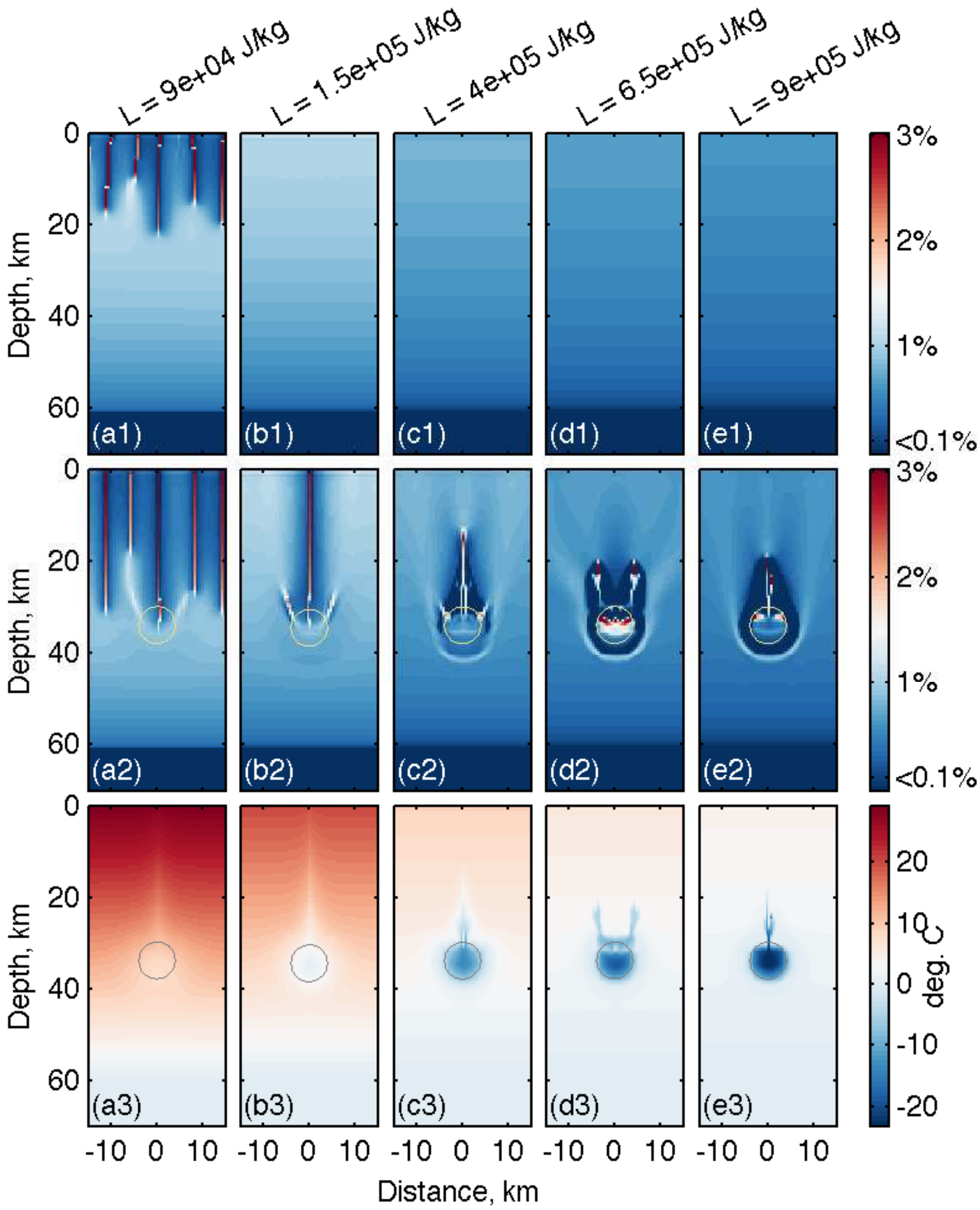

Figure 4.6: Solutions to a suite of experiments for which the latent heat of fusion L is varied. All other parameters are assigned the values listed in table 4.2. Panels a1–e1 show solutions, in terms of porosity for experiments that are not initialized with an enriched heterogeneity. Panels a2–e2 and a3–e3 show solutions from the similar experiments that were initialized with an enriched heterogeneity. Snapshots a2–e2 and a3–e3 show the solutions after a model time of 1.65 Myr in terms of porosity and ΔT_C respectively. Circles show what would be the perimeter of the unmolten heterogeneity.

Figures 4.6a1–e1 show the results from the experiments in terms of porosity after a model time of 600 kyr. In each experiment, magma from the enriched enclave has not yet infiltrated the ambient melting region. Figures 4.6b1–e1, which are taken from experiments where $L \geq 1.5 \times 10^5$ J/kg, show that the style of magmatic flow in the ambient melting region prior to the addition of melt from the more fusible enclave is stable, diffuse porous flow (figures 4.6b1–e1). When $L < 1.5 \times 10^5$ J/kg, however, magmatic flow in the ambient melting regime is unstable; channels form independently of mantle heterogeneity (figure 4.6a1). In this simulation, channels grow downwards over time, and stop growing at a depth of approximately 30 km. Figures 4.6a2–e3 show results from the same suite of experiments in terms of porosity and ΔT_C at the later model time of 1.65 Myr. They show that when L is large, the fertility of enclaves decreases more slowly (figures 4.6a3–e3), and channels grow more slowly (figures 4.6a2–e2).

Analysis of the results shows that the melting rate varies inversely with the latent heat. When L is small, enclaves melt more rapidly and supply a greater flux of enriched magma to their network of channels. Consequently, channels grow more rapidly when L is small. The inverse relationship between L and the melting rate also manifests itself in the properties of the ambient melting region. For example, when L is small and the melting rate is high, the porosity of the ambient mantle is large. The large porosity accommodates a greater upwards flux of magma. In the experiment where $L = 9 \times 10^4$ J/kg the upwards flux of magma is sufficient to generate channels without requiring and additional flux of magma from a more fusible heterogeneity.

Thermal diffusion

To determine how the thermal diffusivity affects the dynamics of the system, we vary the thermal diffusivity between 10^{-7} m^2/s and 10^{-5} m^2/s within a suite of five different simulations. Every other parameter uses the default value given in table 4.2.

Figure 4.7 shows results to these experiments after a model time of 0.91 Myr in terms of porosity (figures 4.7a1–e1) and ΔT_C (figures 4.7a2–e2). For each experiment the same amount of time has elapsed, yet figures 4.7a2–e2 show that the enclaves in

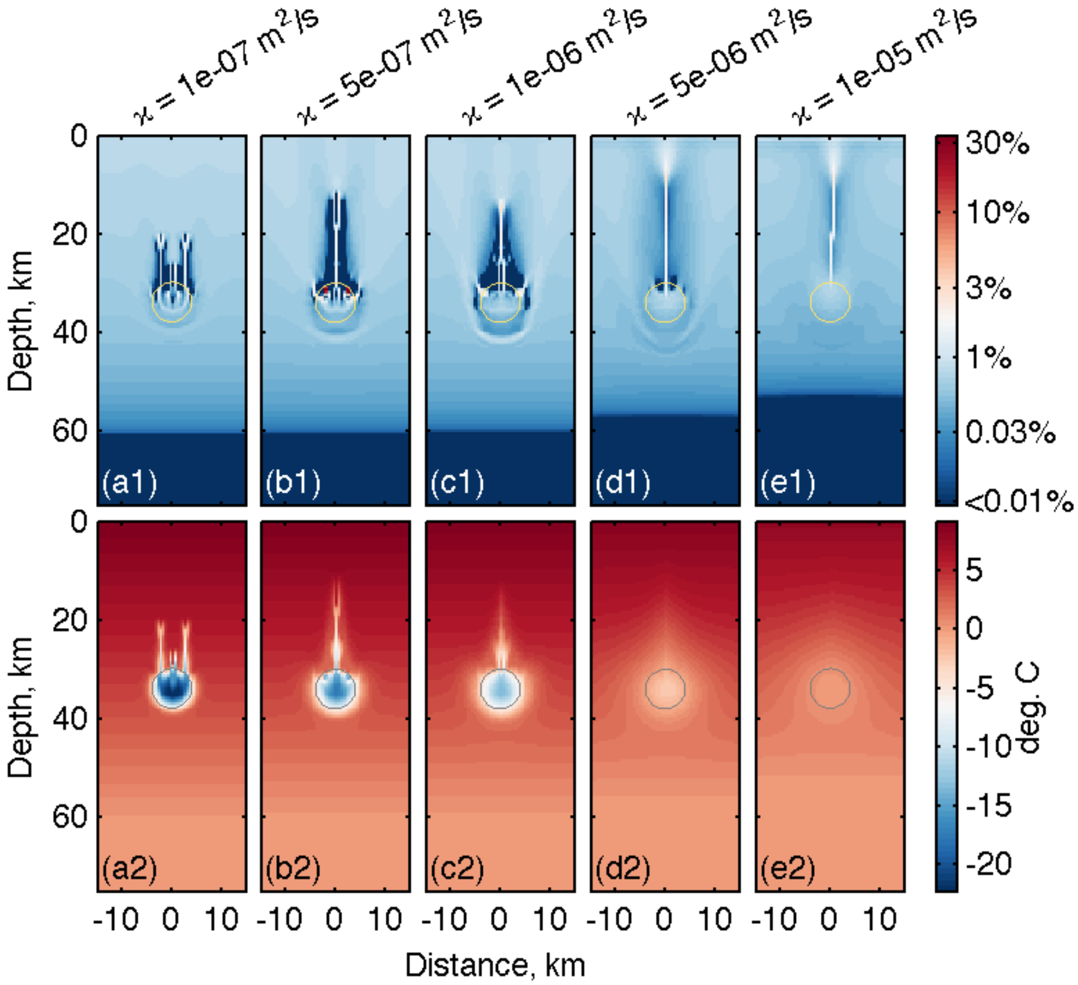

Figure 4.7: Solutions to a suite of five different experiment for which the thermal diffusivity is varied. All other parameters are assigned the default values given in table 4.2. The figures show results from the experiments in terms of porosity (panels a1–e1) and ΔT_C (panels a2–e2) after a model time of 0.91 Myr. Panels referenced by the same letter are taken from the same experiment. Circles show what would be the perimeter of the unmolten enclave.

the most diffusive experiments are the least fertile (figures 4.7a2–e2). This implies that melting rates are higher in more thermally diffusive experiments. Consequently, partial melting of enclaves in more diffusive systems can supply their network of channels with magma at a faster rate. In such systems, channels tend to grow more quickly, have a higher porosity, and accommodate faster melting rates and magma speeds.

A cool diffusion halo also forms around magmatic channels. Figure 4.7 shows that the permeability of the rock within the diffusion-halo varies with the enrichment of the rock and magma within a channel. When rock within a channel is more fertile, and therefore cooler, the surrounding mantle is less permeable. This is because a greater amount of heat diffuses into more fertile channels to maintain thermodynamic equilibrium. Since thermal diffusion toward channels removes heat from the surrounding rock, material within the diffusion-halo has less enthalpy available for melting, and its porosity is lower.

4.3.3 Geophysical controls

Size

We explore the effect that the enclave's size has on channelization using a suite of five different experiments (figure 4.8). For these experiments the initial radius of the enriched enclave ranges between 2 km and 6 km. This range agrees with Helffrich (2002), who estimated the characteristic size of mantle heterogeneity to be approximately 8km. All other parameters take the values listed in table 4.2. Figure 4.8 shows results from these experiments after a model time of 1.65 Myr. The top row shows the porosity, and the bottom row shows the composition, expressed in terms of ΔT_C. At the time of the snapshots, the larger enclaves remain more fusible and support channels that have a longer total length.

Figure 4.8 shows that the larger enclaves, which initially contained a larger mass of the more fusible component, remain more fertile after the same model time has elapsed. It is difficult to assess, from the results presented in this paper, how the melting rate within an enclave varies with its size. However, Katz and Rudge (2011) relate the degree of melting to a Peclet number for the enclave, which represents the balance between diffusion-driven and adiabatic melting, and show that the melting rate decreases with increasing radius of the enclave. Since larger enclaves also contain a greater mass of the more fusible component, they can supply channels with enriched magma for a longer period of time. In consequence, their channels are more enriched and grow to greater lengths via reactive flow (figure 4.8). Characteristics of more fertile channels include a higher melting rate, larger porosity, and a greater flux of

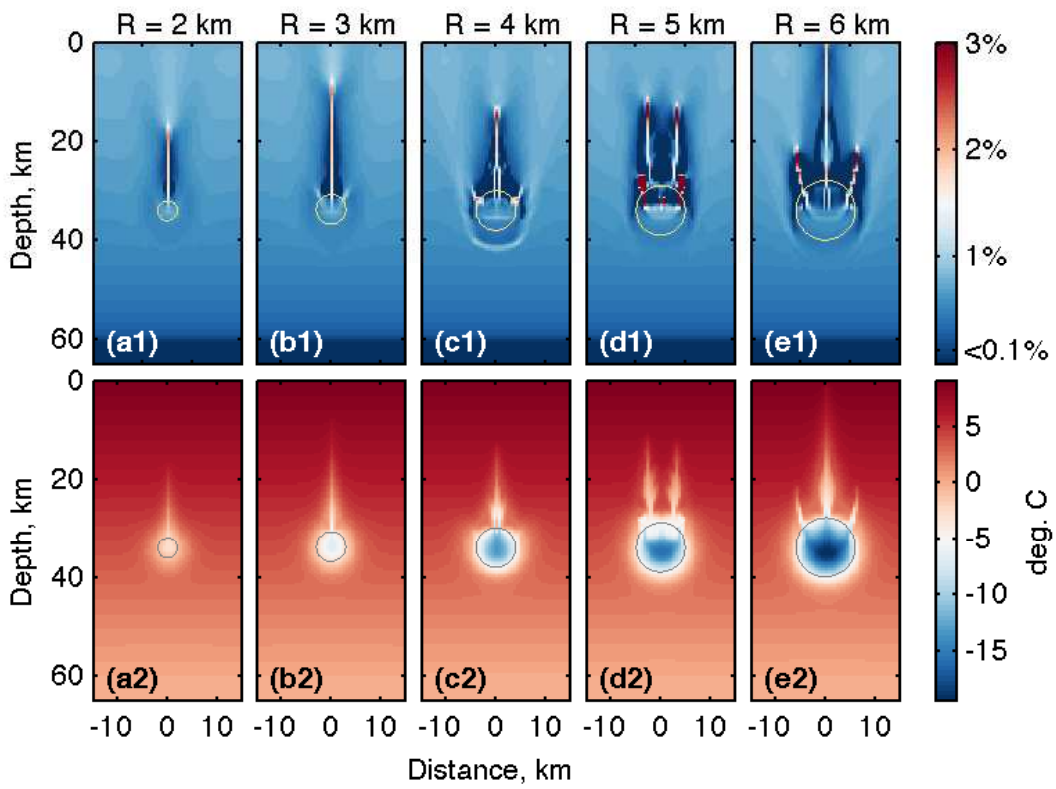

Figure 4.8: Solutions from a suite of five different experiments at $t = 1.65$ Myr for which the radius R is varied. All other parameters use the default values given in table 4.2. Snapshots referenced by the same letter are taken from the same experiment. Panels a1–e1 show the solutions in terms of porosity, whilst panels a2–e2 show ΔT_C. Circles show the perimeter of what would be the unmolten enclave.

magma.

Fusibility

Figure 4.9 examines the effect of the enclave's fertility on channelization through another suite of five experiments. The enclave in each experiment takes a different initial ΔT_C, and the values of all other parameters are held constant at the values listed in table 4.2.

Figure 4.9a illustrates the principal trend that emerges from this suite of experiments. It shows that the difference in time between the onset of channelization and the onset of melting within the enclave, Δt, is negatively correlated with ΔT_C. Rather than describe the data with a single line, we tentatively suggest that the data lie on two branches. The first branch describes the data for $\Delta T_C \geq -30$ K, and the second

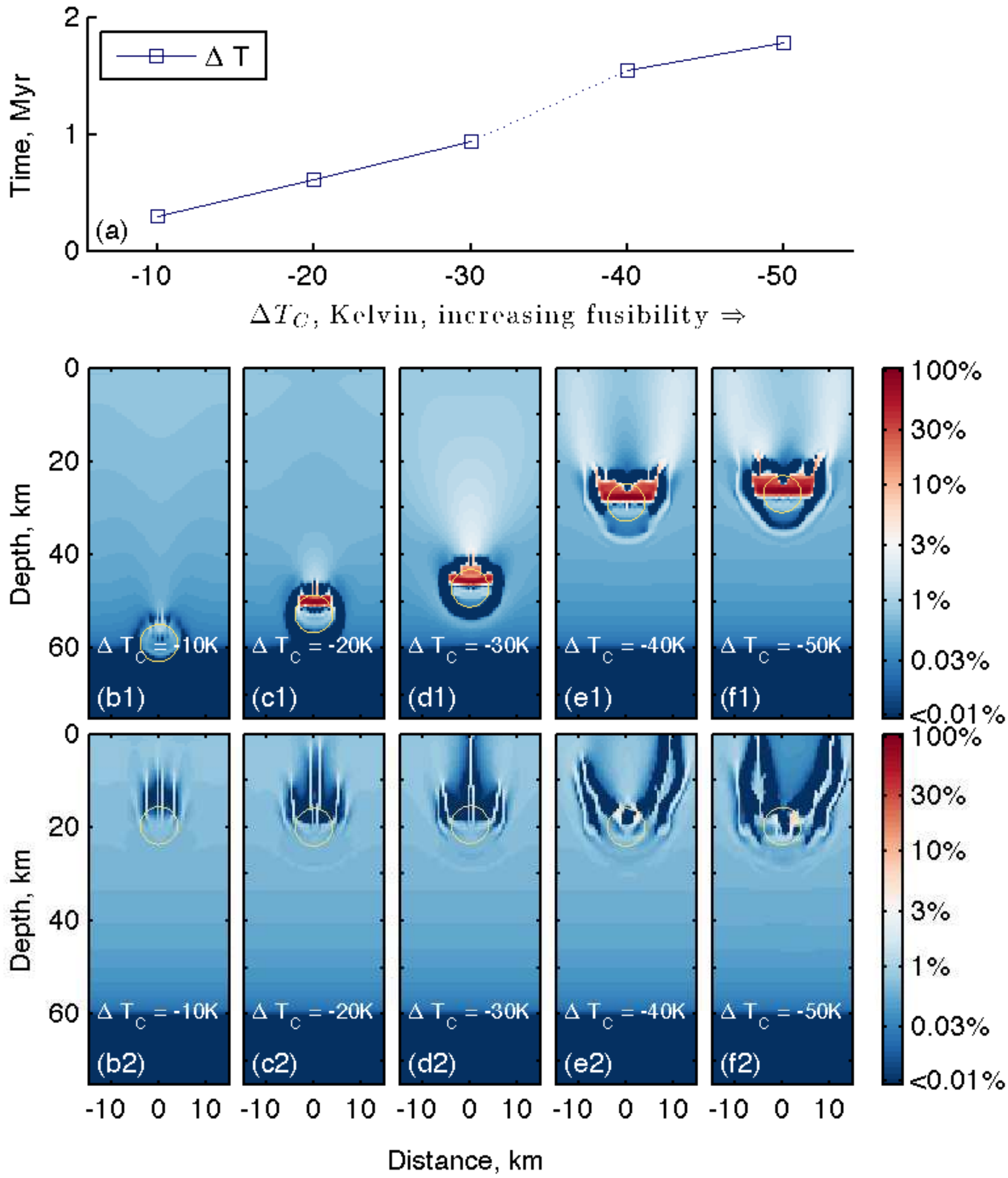

Figure 4.9: Solutions to a suite of five different experiments for which the enrichment of the heterogeneity ΔT_C is varied. All other parameters use the default values given in table 4.2. Panel a shows how the time Δt between the onset of channelization and the onset of melting within the enclave varies with ΔT_C. The dotted line indicates where the relationship between Δt and ΔT_C is uncertain. Panels b1–f2 show solutions from each experiment, in terms of porosity at the instant preceding channelization. Panels b2–f2 show the solutions in terms of porosity at $t = 2.01$ Myr. Snapshots referenced by the same letter are taken from the same experiment. Yellow circles show what would be the perimeter of the unmolten enclave.

branch spans the data for $\Delta T_C \leq -40$K. To better understand this trend we refer to the snapshots from each experiment that are shown in figures 4.9b1–f2.

Figures 4.9b1–f1 show porosity fields at the onset of channelization. These figures show that more fusible heterogeneities begin to channelize at shallower depths. The figures also show a cool diffusion halo surrounding each enclave. The temperature gradient across the diffusion halos is steeper for more fusible enclaves. For material within the halo to melt, the more fusible enclaves need to upwell to shallower depths. It is only when a permeable pathway connects the enclave to the ambient melting region that a channel can begin to form.

Branching of the data shown in figure 4.9a is a consequence of the partially molten enclave's morphology. The heterogeneities shown in figures 4.9e1 and 4.9f1 are each associated with two large pockets of melt. These pockets lie outside the perimeter of the original heterogeneity and are formed by partial melting of the surrounding mantle rock. This consumes latent heat and establishes a diffusive heat flux into the pocket, further chilling the surrounding mantle and delaying the onset of channelization.

From figures 4.9b1–f1 it is clear that more fusible enclaves produce a larger volume of magma prior to channelization. In figures 4.9b2–f2, we show the same experiments at a later model time of 2 Myr to illustrate how these different volumes of magma affect channelization. They show that the enclaves for which the initial $\Delta T_C \geq -30°\text{C}$ give rise to channels with a relatively simple geometry (figures 4.9b2–d2) that is symmetrical about the midline, whereas the channels in figures 4.9e2–f2 are considerably more complex and lack symmetry about the midline. The absence of symmetry in these two experiments results in part from (i) the unusually large flux of magma within the channels that is driven by the very large $\mathcal{P}$ in the enclave, and (ii) that the channels are rooted at separate pockets of magma, rather than a single partially molten heterogeneity. By analysing the full time-series of results for each of the experiments, more trends emerge: channels rooted at more fertile enclaves are more enriched, accommodate higher porosities and faster fluid velocities, grow more quickly, and melt at a greater rate. However, our results suggest that no simple relationship exists between the melting rate within channels and the initial composition of the heterogeneity.

Upwelling rate

Figure 4.10 shows results from a suite of five experiments that investigate the effect of the upwelling rate W_0 on the system. For these experiments W_0 ranges from 2 cm/yr to 6 cm/yr, and all other parameters take their values from table 4.2.

Figure 4.10 shows results from the ensemble of experiments at 0.5 Myr after the onset of channelization. In general, the figures show a subtle increase in the melting rate with W_0 for the ambient melting region. Correspondingly, the magma speed and porosity in the ambient melting region also increases with W_0. Figure 4.10 shows that spatial variations in the melting rate correlate with spatial variations in the porosity and magma speed (figures 4.10a2–e3). This is an important result that we wish to emphasise. The melting rate is large in regions where the porosity and magma speed are also large. A similar result was found by Hewitt (2010), who showed that the melting rate depends on the average upwelling rate $[\phi \mathbf{v}_f + (1 - \phi)\, \mathbf{v}_m] \cdot \hat{\mathbf{k}}$.

In general, the results in figure 4.10 show that the upwelling rate affects the dynamics of the system principally through the melting rate. They suggest that when W_0 is large, channels evolve more quickly to develop large porosities and melting rates. However, our experiments show no clear relationship between the upwelling rate and the geometry of channels.

4.3.4 Shape

The sections above explore the relationship between channelization and heterogeneity by considering only circular shaped compositional anomalies. Since the aim is to understand the most fundamental ways in which mantle heterogeneity influences magmatic flow, this simplified approach is justified. However, there is little doubt that heterogeneities in the real mantle have a geometry that is much more complex. In the real Earth, mantle flow will fold, stretch, and thin enclaves of recycled oceanic crust (Allègre et al., 1984). Some of the enclaves will be boudinaged, and dissolution will blur the edges of enclaves.

To consider whether the general behaviour of our experiments holds for enclaves

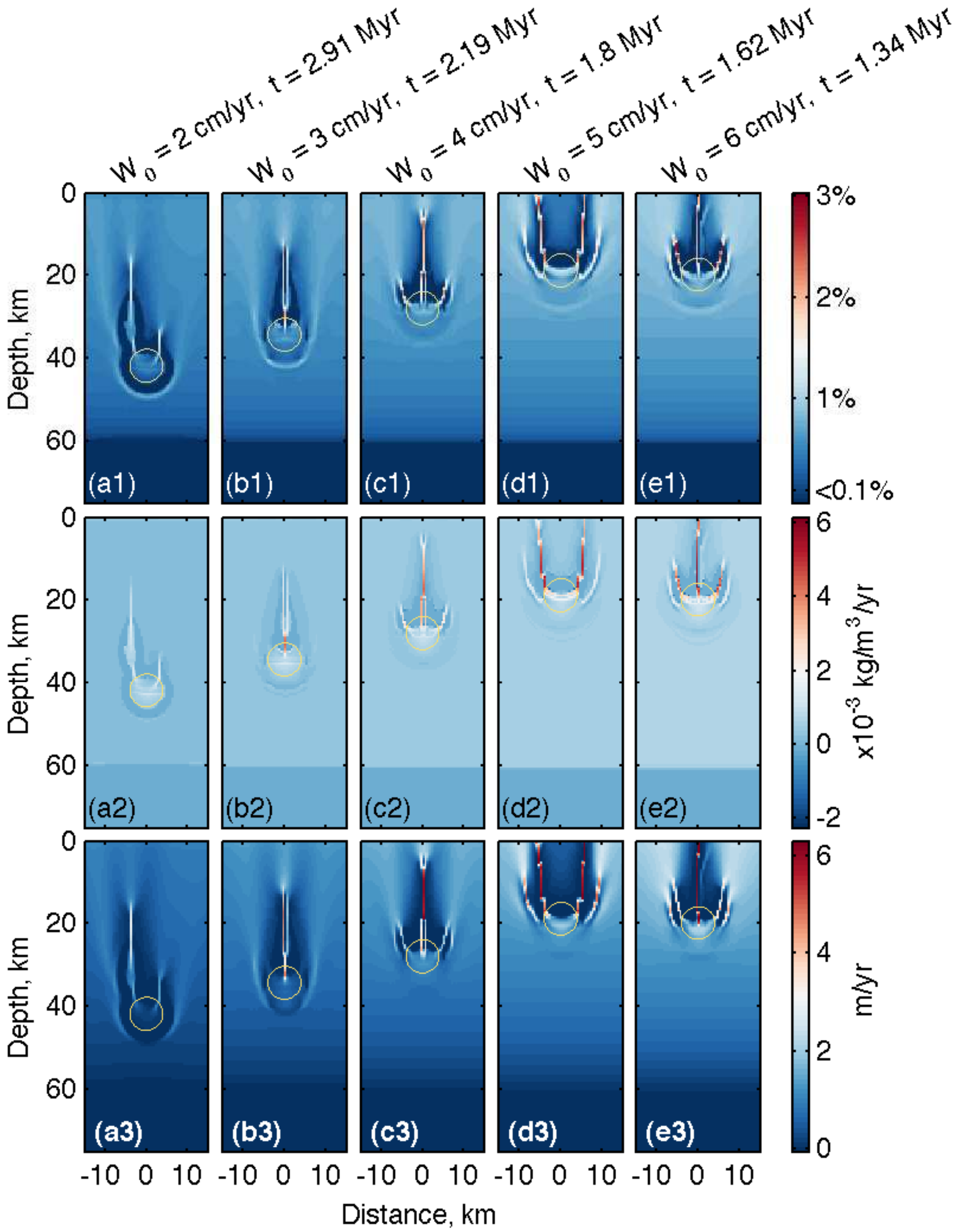

Figure 4.10: Solutions to a suite of five different experiments for which the upwelling rate is varied. All other parameters take the values given in table 4.2. Figures show snapshots from the experiment at 0.5 Myr after the onset of channelization. Snapshots referenced by the same letter are taken from the same experiment. Panels a1–e1 show the solutions in terms of porosity, and panels a2–e2 show them in terms of the melting rate, and panels a3–e3 show the solutions in terms of the magma speed. Yellow circles show what would be the perimeter of the unmolten enclave.

of different shapes, figure 4.11 shows results from two further experiments, each initialized with an ellipse-shaped enclave. In one of the experiments (figures 4.11a1,

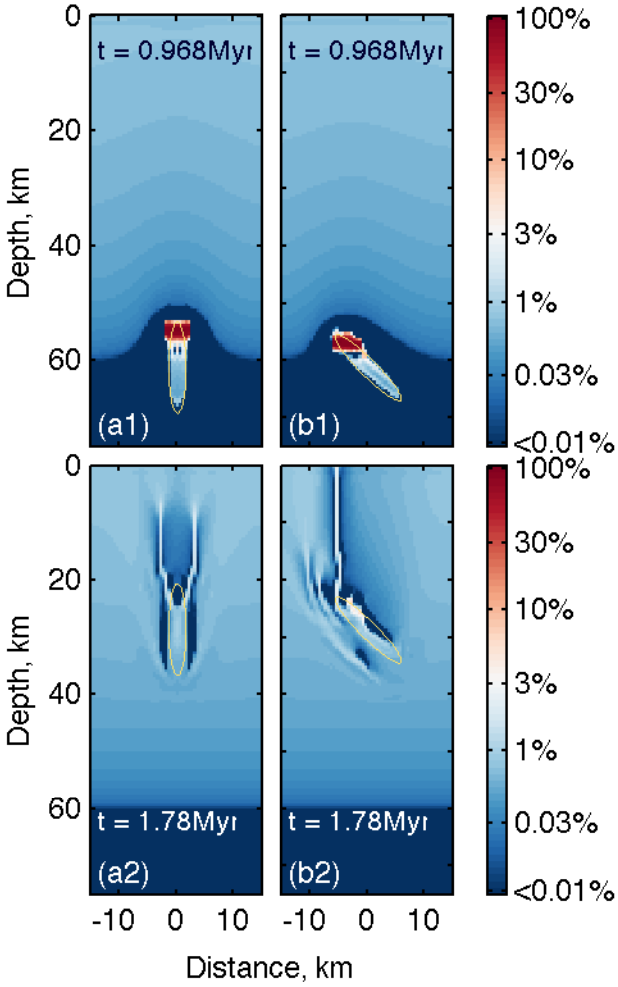

Figure 4.11: Solutions to two different experiments shown in terms of porosity. The original shape of the enclave for both experiments is an ellipse. The ellipse shown in panels b1 and b2 has been rotated by 45°. The long and short axes of the ellipse are 16 km and 4 km respectively. All other parameters take the default values given in table 4.2. Snapshots referenced by the same letter are taken from the same experiment. Yellow ellipses show what would be the perimeter of the unmolten enclaves.

4.11a2), the ellipse is aligned with its long axis parallel to the vertical; in the other, the long axis is rotated anticlockwise from the vertical by 45°.

Figures 4.11a1, 4.11b1 show that, in contrast to the previous experiments, for which the initial shape of the enclave was circular, the pocket of magma can be wider than the enclave. Figures 4.11a2, 4.11b2 show that the ellipse-shaped enclaves also produce channels. The geometry of these channels is arguably more complex than in the previous simulations. To illustrate, the enclave in figure 4.11a2 hosts two widely spaced channels that are growing in synchrony, and in figure 4.11b2, the large channel incorporates lateral deviations along its length. Nevertheless, the basic behaviour of the channels and their relationship with the surrounding mantle is consistent with the experiments described in the previous sections.

4.3.5 Summary of numerical results

The sections above investigate how the dynamics of magmatic channelization varies in response to changes in latent heat L, thermal diffusivity κ, the size R, shape, the fusibility of the heterogeneity, and the upwelling rate of the mantle W_0. Results from the numerical experiments indicate that the evolution of high-porosity channels is coupled to composition, heat flow, and fluid dynamics of the system. To summarise, channels grow faster, and are depleted more rapidly when L is small and κ is large. Fast-growing channels tend to have higher porosities, faster magma speeds, and greater melting rates. These properties are also apparent in channels that evolve in systems where the heterogeneities are larger and more fusible (ΔT_C is more negative), and the upwelling rate is faster.

Many of the trends apparent in each of the suites of experiments above are best understood in terms of the melting rate. The melting rate Γ depends on a range of thermodynamic and geophysical parameters. Specifically, Γ increases with the upwelling rate (figure 4.10), magma speed (figures 4.4 and 4.10), porosity (figures 4.4 and 4.10), and the thermal diffusivity (figure 4.7). They also show, in figure 4.6, that Γ scales inversely with L. The next section quantifies the effect that the upwelling rate, thermal diffusivity, latent heat and composition have on the melting rate, and explores the processes that give rise to spatial variations of Γ.

4.4 Discussion

4.4.1 Melting rate

The governing equations (4.4–4.7) can be combined to give a thermodynamically consistent expression for the melting rate. The derivation is presented in Appendix C; here we emphasise the most important findings. For a diffusive system that is not necessarily in steady state, and for which $M_S = M_L = M$, the melting rate is

$$\Gamma = \mathcal{G}\left[\mathcal{A}\bar{\mathbf{v}} \cdot \mathbf{k} + \kappa\nabla^2 T - M\mathcal{D}\nabla \cdot \phi\nabla C_f\right], \tag{4.8}$$

where $\mathcal{G}$ and $\mathcal{A}$ are dimensional constants

$$\mathcal{G} = \frac{\rho}{L/c_P + \Delta CM}, \tag{4.9}$$

$$\mathcal{A} = \left(\frac{\rho g}{\gamma} - \frac{\alpha\mathcal{T}g}{c_P}\right). \tag{4.10}$$

Equation 4.8 shows that the melting rate is a constant multiple of contributions from the phase averaged upwelling rate, thermal diffusion, and chemical diffusion in the liquid phase. The multiplying constant $\mathcal{G}$ (equation 4.9) depends on the reference density ρ, the ratio of the latent heat of fusion and the specific heat capacity, and ΔCM, which is the temperature difference between the solidus and liquidus at a fixed composition. Using values from table 4.2, $(L/c_P)/(\Delta CM) \approx 10$. As such, the multiplying constant $\mathcal{G}$ depends more strongly on the ratio of the latent heat of fusion and the specific heat capacity than on properties of the phase diagram. Furthermore, L determines how strongly the melting rate is coupled to the energetics of the system. Taking $L \to 0$ removes the principal coupling between the melting rate and the energetics of the system. In this case, our expression for the melting rate is similar to that for the reactive flow models of Liang et al. (2010) and Schiemenz et al. (2011), who neglect conservation of energy.

The first term in equation 4.8 shows that Γ depends on a constant multiple of the phase averaged upwelling rate. Because Γ depends on, and increases with, the upwelling rate of the magma, our expression for the melting rate (equation 4.8) models reactive flow. Unlike the other two terms in equation 4.8, $\bar{\mathbf{v}}$ is prefactored by an additional constant $\mathcal{A}$. The constant $\mathcal{A}$ depends on the Clapeyron slope and incorporates a small correction for adiabatic cooling. The product of these constants is closely related to standard expressions for the productivity $\mathcal{G}\mathcal{A} = -\frac{\partial F}{\partial p}$ (Asimow et al., 1997; McKenzie, 1984). The first term in equation 4.8 is identical to the melting rate derived by Hewitt (2010), who solved similar governing equations but neglected diffusion. He derived an approximate stability condition for the melting rate and found that the thermodynamically consistent mechanism that drives the reactive infiltration instability is a melting rate that increases with the melt flux. The increase in porosity caused by the melt flux is countered by compaction, but the rate of compaction also increases with the melt fraction. For this reason, compaction tends to stabilize small perturbations. In the non-diffusive case Hewitt (2010) found that the system is unstable only if the rate of porosity generation by melting exceeds the rate of destruction by compaction.

The second and third terms in equation 4.8 demonstrate that the melting rate depends on thermal and chemical diffusion in the magma. They show that heat diffuses into partially molten, enriched heterogeneities and increases the melting rate, whereas chemical diffusion blurs compositional gradients and reduces the melting rate. Using the nondimensional quantities outlined in section 2.6, the second term in equation 4.8 for thermal diffusion scales as $\kappa\delta T/l^2$, where l is a diffusive length scale and δT is a temperature difference, and the third term in equation 4.8 for chemical diffusion scales as $\mathcal{D}M\phi_0\delta C/l^2$, where ϕ_0 is a reference porosity. Since $\delta T = M\delta C$, the relative size of these scales is $\kappa \gg \mathcal{D}$. In other words, the contribution to the melting rate from chemical diffusion relative to that from thermal diffusion is negligible.

In light of this scaling, chemical diffusion is assumed to be negligible and the melting rate re-written as

$$\Gamma \approx \mathcal{G}\left[\mathcal{A}\bar{\mathbf{v}}\cdot\mathbf{k}+\kappa\nabla^2 T\right]. \tag{4.11}$$

Equation 4.11 emphasises that thermal diffusion powers melting in cooler regions. Since the assumption of thermodynamic equilibrium explicitly relates temperature and composition, the melting rate can be re-expressed in terms of C_f by combining equations 4.2 for the linearized liquidus and 4.11 to give

$$\Gamma = \mathcal{G}\left[\mathcal{A}\bar{\mathbf{v}}\cdot\mathbf{k}+\kappa M\nabla^2 C_f\right]. \tag{4.12}$$

Equation 4.12 shows that compositional variation gives rise to spatial variations in the melting rate. Importantly, though, the dependency of the melting rate on the second derivative of composition is through the thermal diffusivity. Equation 4.12 also implies that the melting rate within channels is related to the composition of the heterogeneity at which it is rooted. However, this relationship is not straightforward, since the prior reaction history will have modified the composition of magma and rock at any point in a channel. The composition of the magma will be further modified by melts that are drawn into the channel from the ambient mantle.

From equations 4.11 and 4.12 it is clear that the melting rate depends on several different variables. To better understand these dependencies we decompose the melting rate into three terms:

$$\Gamma = \Gamma_W + \Gamma_R + \Gamma_T. \tag{4.13}$$

Here, $\Gamma_W = \mathcal{G}\mathcal{A}\mathbf{v}_m\cdot\mathbf{k}$ is the contribution from the matrix velocity, $\Gamma_R = \mathcal{G}\mathcal{A}\phi\left(\mathbf{v}_f-\mathbf{v}_m\right)\cdot\mathbf{k}$ is the contribution to the melting rate from reactive flow, and $\Gamma_T = \mathcal{G}\kappa\nabla^2 T$ is the contribution from thermal diffusion.

To determine the relative importance of each of the terms in equation 4.13, we applied the decomposition to the representative calculation presented in figure 4.4. Figure 4.12 shows the contributions from Γ_W, Γ_R, and Γ_T, expressed as a fraction of

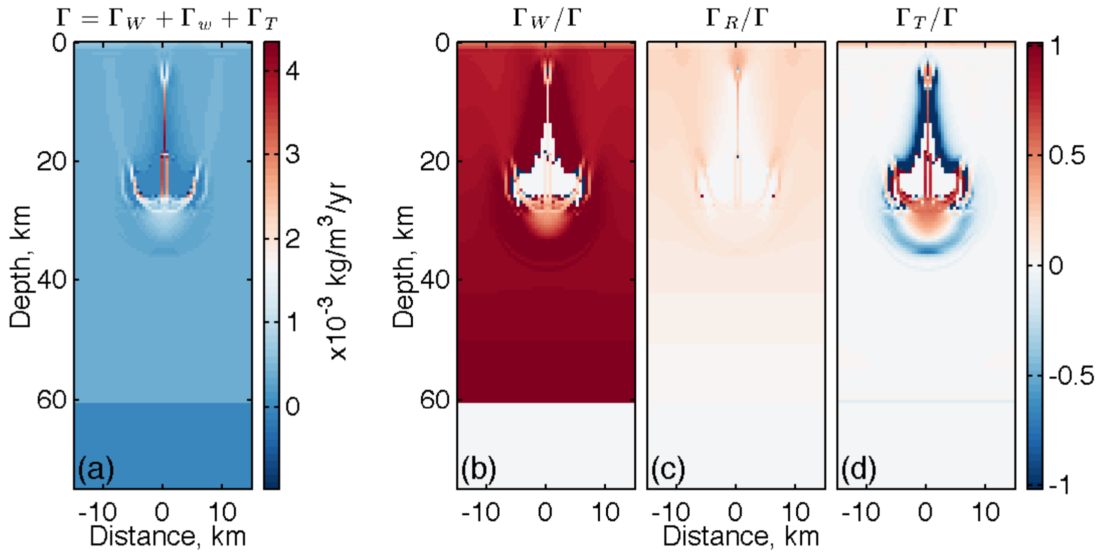

Figure 4.12: Panel a shows the melting rate from an experiment run with the default parameter values (table 4.2) after a model time of 1.81 Myr. The melting rate is the sum of contributions from the upwelling rate of the matrix Γ_W, the upwelling rate of the magma Γ_R, and thermal diffusion Γ_T. Panels b–d show each of these contributions as a fraction of the total melting rate.

Γ. Figures 4.12b–d show that in the ambient melting region, at distances far from the enclave and channel network, decompression accounts for the majority of the total melting rate. At the base of the ambient melting region, Γ_W accounts for over 95% of the total melting rate. The ambient porosity and the magma speed increase towards the surface. Consequently Γ_W/Γ decreases and the contribution from reactive flow, Γ_R, becomes more important. Close to the top of the ambient melting region, Γ_W accounts for approximately 80% of the total ambient melting rate, Γ_R supplies the remaining 20%, and the contribution from thermal diffusion is negligible.

Within the fertile enclave Γ_W and Γ_T each account for approximately 45% of the total melting rate, while Γ_R supplies the remaining 10%. These results show that diffusion of heat into a fertile enclave increases melting by a factor of 2 over that from adiabatic upwelling. Figure 4.12d shows that thermal diffusion suppresses melting in the mantle that surrounds the heterogeneity to values lower than that for the ambient mantle at equal depths. The positive contributions to melting, therefore, are decompression and reactive flow in the approximate ratio 10:1.

Figure 4.12a shows that the greatest melting rates occur within the channel. The characteristic features of channels that give rise to large melting rates are large porosities, fast magma speeds, and a discrete, steep-sided composition anomaly across which the $\nabla^2 C_f$ is large and positive. Figures 4.12b–d show that thermal diffusion provides the most significant contribution to the melting rate within channels. In this case, Γ_T accounts for approximately 60% of the total melting rate within the channel, Γ_R accounts for approximately 30%, and Γ_W supplies the remaining 10%. Thermal diffusion, therefore, powers much of the melting within channels. But in the surrounding mantle, it suppresses melting to such an extent that the $\Gamma < 0.2\Gamma_W$.

The results in figure 4.12 show that the relative importance of Γ_W, Γ_R, and Γ_T to the melting rate varies with the flow regime. In the ambient melting region where magmatic flow is in steady state, the decompression rate of the matrix provides the most important contribution to the melting rate. In regions where magmatic flow is channelized, thermal diffusion provides the greatest contribution to the melting rate; reactive flow accounts for much of the remainder.

4.4.2 Limitations of the model

Results presented in this paper indicate that magmatic channelization is a consequence of melting in a chemically heterogeneous mantle. The model is necessarily simplified in order to address the fundamental dynamics of the system. An important assumption made by the model is that local thermodynamic equilibrium holds everywhere. Estimates for the Damköhler number of the mantle, which measures the relative importance of advection and reaction, are, in general, poorly constrained (Aharonov et al., 1995; Spiegelman et al., 2001; Spiegelman and Kelemen, 2003), but are large enough for thermodynamic equilibrium to be a judicious approximation.

The most important simplification in the general approach is the phase diagram (figure 4.2). As outlined in section 2.4, the aim is to capture the essence of the natural system; the solid-solution chemistry of major mineral phases in the mantle motivates the binary loop. Nevertheless, this simple phase diagram is used at the expense of some important aspects of mantle petrology including nonlinear productivity in the ambient melting region, phase changes and exhaustions, the effect of volatiles on melting and rheology. Importantly, the petrological model assumes that melting is congruent throughout the upper mantle. Chen and Presnall (1975), however, shows that in the pressure range spanned by the melting region beneath mid-ocean ridges, the mode of orthopyroxene melting switches from congruent at high pressure to incongruent at low pressure. Since incongruent melting replaces fusible orthopyroxene with inert olivine, the melting rate in dunite channels will be lower than congruently melting channels under similar conditions. Numerical experiments by Liang et al. (2010), which allow for incongruent melting of orthopyroxene confirm this. Their simulations also predict that reactive melting occurs on the edges of dunite channels, causing the channel to widen. If this phenomenon persists in experiments that conserve energy, then it is likely that dunite channels in this petrological context will continue to represent a local thermal minimum.

Exploration of the effects of incongruent melting in numerical experiments that conserve energy should constitute a core aim of future work. Results here underscore the importance of thermal diffusion to melting and the dynamics of magma flow in a hypothetical mantle where melting is congruent and the heat of fusion is equal for all phases. Kelemen (1990) notes that the heat of olivine crystallization is ~ 1.3 times that of pyroxene dissolution; thus the reaction responsible for the formation of dunite channels is exothermic. One possible consequence of this is that the extra heat from olivine crystallization enhances melting on the flanks of the channel, leading to wider dunites and higher fluxes of localized melt.

In general, the nature of mantle heterogeneity is poorly constrained. Almost certainly, heterogeneities occur across a range of length-scales with a variety of fusibilities and complex topologies; the effect topology on magma flow is explored in the next chapter in the context of a mid-ocean ridge. Figure 4.5 suggests that kilometer-scale heterogeneities of relatively low fusibility ($\Delta T_C \approx -5$K) are capable of nucleating magmatic channels. In these experiments, the smallest heterogeneities are defined by only a few grid cells. However, figure 4.13 shows the basic behaviour of the system

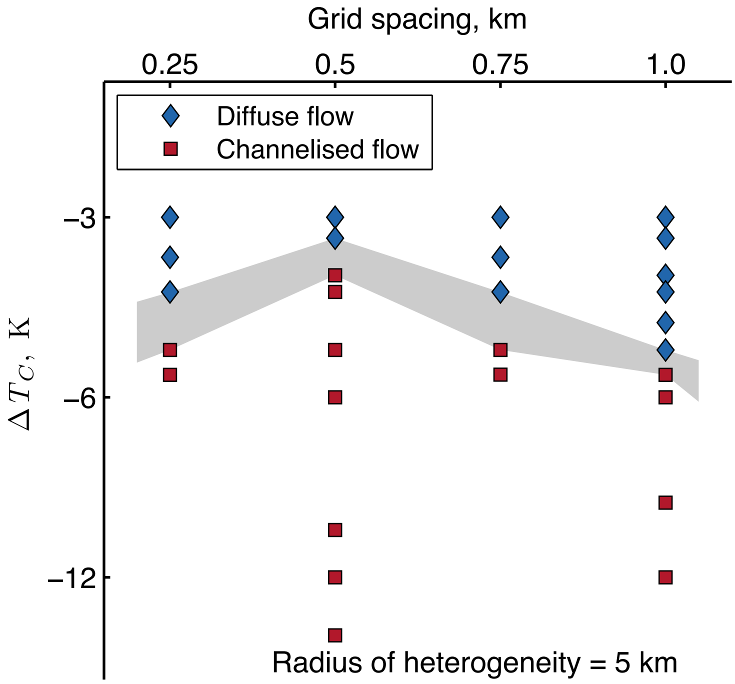

Figure 4.13: Array of simulations showing the effect that grid spacing and fusibility of the heterogeneity have on the mode of magma flow. Each point represents a single simulation. Blue diamonds indications for which magma migrates by diffuse porous flow, red squares denote those for which magma localizes into a channel. The radius of the heterogeneity is fixed at 5 km. All other parameter values are listed in table 4.2.

does not depend strongly on the grid spacing. To investigate how the system responds to heterogeneities on scales smaller than 100 m requires more challenging simulations at higher resolution.

A persistent feature of the experiments reported here is that magmatic channels evolve to be just one grid cell wide. Grid scale features seem to be a hallmark of existing numerical experiments that use the Enthalpy Method. Hewitt (2010) found similar behaviour in his calculations of magma flow in the mantle, as did Katz and Worster (2008) in their calculations of chimney formation in mushy layers. These features may stem from the numerical methods adopted by these studies. Given this, the reason for grid scale channels may be that the fluid pressure, at any constant depth, is lowest in the centre of a channel, and melt consequently moves towards the grid cell that corresponds to the centre of the channel. Irrespective of the resolution, magma always appears to localize to this central cell. Only if the porosity there reached 100% would we expect the channel to occupy a wider space. In this limit, however, magma flow cannot be described by Darcy's law, and the study would require a different parameterization, such as that used by Hewitt and Fowler (2009).

Alternatively, higher-order numerical methods, such as those used by Liang et al. (2011) and Hesse et al. (2011), may improve the resolution of channels, and resolve further instabilities in the system. For example, Richter and Daly (1989) suggested that melting in a heterogeneous mantle will give rise to porosity waves. Liang et al. (2011) and Hesse et al. (2011), verified this and showed that nonlinear interactions between compaction and dissolution give rise to porosity waves and magmatic channels. Their results offer an additional mode of channel formation, but it remains to be shown that these additional instabilities feature in systems that conserve energy.

4.5 Conclusions

Results from energetically consistent models of magma flow and congruent melting indicate that channelized melt transport is a consequence of melting in a heterogeneous mantle. Channels arise when magma from partially molten heterogeneities supplies the ambient mantle with an additional, and sufficient, flux of magma. The results are best understood in light of the melting rate, which is derived from conservation principles. The melting rate is coupled to the energetic budget dominantly through the latent heat. For values close to the estimated latent heat of the mantle, the mode of melt transport in the absence of heterogeneities is diffuse porous flow. Selecting a small value for the latent heat decouples the melting rate from the energetic budget; under these conditions, the mode of melt transport in a chemically homogeneous mantle is channelized flow.

The melting rate is a linear combination of contributions from decompression, reactive flow, and thermal diffusion. In the ambient melting region (i.e. not within, or in the vicinity of, high-porosity channels), melting is largely the response of adiabatic decompression. Within channels, however, thermal diffusion provides the most significant contribution to the melting rate. Since heat diffuses into channels, the adjacent mantle is starved of energy for melting. The permeability of these rocks is low, or sometimes even zero, and magma upwelling from deeper depths is focused into high-porosity regions. Consequently, thermal diffusion provides a positive feedback on channelization, and could discourage mixing between magmas flowing through channels and magmas in the adjacent mantle. Our results predict, for the first time, that thermal diffusion is important to the genesis and dynamics of magmatic channels, and underscore the need to use energetically consistent models in studies of coupled magma/mantle dynamics.

Chapter 5

Consequences of mantle heterogeneity for melt transport and focusing beneath mid-ocean ridges

A version of this chapter is published as

Katz, R.F. and Weatherley, S.M., (2012) Consequences of mantle heterogeneity for melt extraction at mid-ocean ridges. *Earth and Planetary Science Letters*, **335**, 226-237.

5.1 Introduction

Magma formed beneath mid-ocean ridges is strongly focused from a broad region of upwelling to a narrow zone at the ridge axis. Despite conclusive evidence for mantle heterogeneity (e.g. Ringwood, 1982; Sun and McDonough, 1989; Hofmann, 1997, 2003) and mounting evidence that magma flow is channelized (e.g. Kelemen et al., 1995a; Kelemen and Dick, 1995; Aharonov et al., 1995; Suhr, 1999; Lundstrom, 2000; Spiegelman and Kelemen, 2003; Savelieva et al., 2008; Batanova and Savelieva, 2009), existing theories for melt focusing appeal almost exclusively to diffuse porous flow in a chemically homogenous mantle (e.g. Spiegelman and McKenzie, 1987; Buck and Su, 1989; Yinting et al., 1991; Sparks and Parmentier, 1991). Results from the previous chapter and several studies by Kogiso and Hirschmann (2004); Maclennan (2008); Weatherley and Katz (2012); Katz and Weatherley (2012) suggest that mantle heterogeneities have significant consequences for the dynamics of magma flow. However, the effect that the topology of mantle heterogeneity might have on magma flow, and its implications for melt focusing remain largely enigmatic.

Some insight to the role of magmatic channels in focusing magma to ridge axes is provided by statistical analysis of mantle dunites in the Oman ophiolite. Kelemen et al. (2000) and Braun and Kelemen (2002) show that a power law relates the spatial frequency and width of dunites, suggesting they form a fractal, upwards coalescing melt transport network that focuses magma to the ridge axis. Supporting these observations are some numerical models that predict channels to coalesce upwards (Aharonov et al., 1995; Spiegelman et al., 2001; Spiegelman and Kelemen, 2003), although none consider the consequences of plate spreading and the thermal regime of a mid-ocean ridge. Kelemen et al. (2000) and Braun and Kelemen (2002), however, did consider the consequences of plate spreading, and drew conceptual sketches of the melt channel network beneath mid-ocean ridges. Their suggestions bear resemblance to tree roots, with individual channels (roots) feeding magma into successively larger channels and eventually to the ridge axis.

Melt focusing is typically investigated from a dynamical perspective with simple mathematical model of magma flow and mantle deformation similar to that presented in chapter 2. In one model by Spiegelman and McKenzie (1987) with constant porosity and no melting, pressure gradients arising from large scale convection of the matrix drive melt focusing. Yinting et al. (1991) included the effects of melting and suggested that the resulting upwards increase in porosity also plays an important part in focusing magma to the ridge axis. Buck and Su (1989) argue that mantle upwelling and magma is focused beneath the ridge axis due to a feedback between melting and viscosity. However, this model is difficult to reconcile with geochemical and petrographic analyses of mantle rocks and mid-ocean ridge basalts that require the porosity to be small. A widely referenced model by Sparks and Parmentier (1991) pays particular attention to the consequences of the thermal structure of the lithosphere. In this model, compaction of the porous, melting mantle results in a high porosity channel aligned subparallel to the lithosphere–asthenosphere boundary. Magma rises vertically and buoyantly to this impermeable barrier, then flows “uphill” through the channel to the ridge axis. More recent approaches combine the effects of melting, compaction, mantle convection, and porosity weakening viscosity into physically consistent numerical models (Katz, 2008, 2010; Tirone et al., 2012) and suggest that melt focusing occurs through a combination of the mechanisms offered by Yinting et al. (1991) and Sparks and Parmentier (1991).

Many of these models predict melt focusing to be incomplete. For example, Katz (2008) predicts that magma originating at lateral distances from the ridge axis greater than 60 km does not reach the spreading centre, but instead freezes into the lithosphere. Supporting observations include seismic images of residual mantle formed beneath slow and ultraslow spreading ridges (Lizarralde et al., 2004), and the geochemistry of seamount lavas, which are understood to tap the melting region beneath MORs (Batiza et al., 1990). Hellebrand et al. (2002) observed in abyssal peridotites the geochemical consequences of magma refreezing into the lithosphere, and Van der Wal and Bodinier (1996) and Bedini et al. (1997) recognized the effects of refertilization in xenoliths of mantle rock, and find that the volumes of refertilizing magmas vary on a kilometre scale.

To investigate how melt focusing may differ in the presence of mantle heterogeneity, constraints are needed on the size, shape, topology, and chemistry of heterogeneous domains in the mantle. Recycled oceanic crust is understood to be an important component of mantle heterogeneity and is thought to be present on a wide range of scales. Analyses of scattered seismic waves indicate chemically distinct heterogeneities with length scales of around 10 km occur throughout the mantle (Kaneshima and Helffrich, 1999, 2003). Some of the scatterers are clearly related to Cenozoic subduction zones and occur as uniformly dispersed bodies; others, however, are not and have a more tabular form. A finer resolution perspective of mantle heterogeneity is offered by the geochemistry of oceanic basalts. Basalts reveal mantle heterogeneity on scales smaller than one kilometre (e.g. Gast, 1968; Hanson, 1977; Hofmann and Hart, 1978; Wood, 1979; Hauri et al., 1996; Hanyu and Kaneoka, 1997), and field observations from peridotite massifs demonstrate that heterogeneities also exist as elongate, decimetre-wide veins (Reisberg et al., 1991; Blichert-Toft et al., 1999).

Whilst these observations constrain the expected size of mantle heterogeneity, they provide little insight to its topology on scales significant for melt transport. However, Allègre and Turcotte (1986) and Kellogg and Turcotte (1990) considered the fate of subducted oceanic crust from a mechanical perspective and found that the stirring effect of mantle convection stretches individual segments out into veins and schlierin. Their analysis shows that stretching by convection reduces the vein–widths exponentially with time, suggesting that in less than 1Ga, segments several kilometres wide can be stretched into veins a few centimetres thick. van Keken and Zhong (1999) consider a similar problem in three-dimensions and du Vignaux and Fleitout (2001) account for the higher viscosity of oceanic crust relative to mantle peridotite. Both of these studies argue that longer timescales, compared to those suggested by Allègre and Turcotte (1986) and Kellogg and Turcotte (1990), are needed to stretch subducted oceanic crust into such thin veins. Chemical diffusion in the solid mantle is low enough to preserve decimetre sized heterogeneities for billions of years (Hofmann and Hart, 1978). But in the presence of melt, diffusion is enhanced and can completely erase metre-scale heterogeneities in $10^5 - 10^6$ years.

A possible consequence of partial melting is that it redistributes and changes the topology of mantle heterogeneity. Recycled oceanic crust is usually present in the mantle as eclogite, which melts at significantly lower temperatures than the host peridotite (Yasuda et al., 1994). Magmas derived from eclogites will segregate from their parent body, perhaps by compaction, reactive and shear instabilities, and by percolation along shear zones, and infiltrate the surrounding peridotites. The eclogitic melts react with the ambient mantle to yield refertilized lherzolites or pyroxenites that are more fusible than the pyrolitic mantle (Yaxley and Green, 1998; Yaxley, 2000; Pertermann and Hirschmann, 2003; Sobolev et al., 2005; Herzberg, 2006; Sobolev et al., 2007, 2008; Herzberg, 2011).

This step of eclogite melting, melt segregation, and reaction conditions the mantle for subsequent melting at shallower depths beneath mid-ocean ridges and helps to define the topology of mantle heterogeneity. One end-member situation may be that melt segregation and reaction connect adjacent heterogeneities with a bridge of reaction products. On melting, these interconnected, more fusible heterogeneities might act as preferential pathways for melt extraction. Conversely, if fertile heterogeneities are spaced far apart, or melt migration is inhibited, heterogeneities may remain as discrete bodies. Results from the previous chapter suggest that heterogeneities of this form nucleate vertical channels on melting. Thus the topology of mantle heterogeneity could have severe consequences for the dynamics of melt extraction and focusing beneath mid-ocean ridges. Investigating these consequences is the focus of this study.

The aim of the present chapter is to investigate these consequences using an energetically and physically consistent model of mantle melting, deformation, and magma flow. In the next section, the model from the previous chapter is extended to include the effects of plate spreading and boundary conditions suitable for a mid-ocean ridge. Section 5.2 also outlines the algorithms used to model mantle heterogeneity. Results from experiments with and without mantle heterogeneity are described in section 5.3 and discussed in section 5.4. Limitations of the model in addition to those outlined in the previous chapter are described in section 5.5 and the chapter is concluded in section 5.6.

5.2 Methods

5.2.1 Domain, governing equations, boundary conditions

The situation we consider is that of a mid-ocean ridge (figure 5.1). A velocity field imposed on the top boundary drives lithospheric plates apart, resulting in large scale convection and melting in the underlying mantle. The domain extends to a depth greater than the depth of melting for the most fusible material in the domain and is wide enough to fully capture the region from which melt is focused to the ridge axis. The model is a direct extension of that used in the previous chapter: the system contains a maximum of two phases and two thermodynamic components in local thermodynamic equilibrium. The components form a solid solution series and the phase compositions are related to pressure, temperature and bulk composition through the linearized phase diagram given by figure 4.2 and equations 4.1 and 4.2.

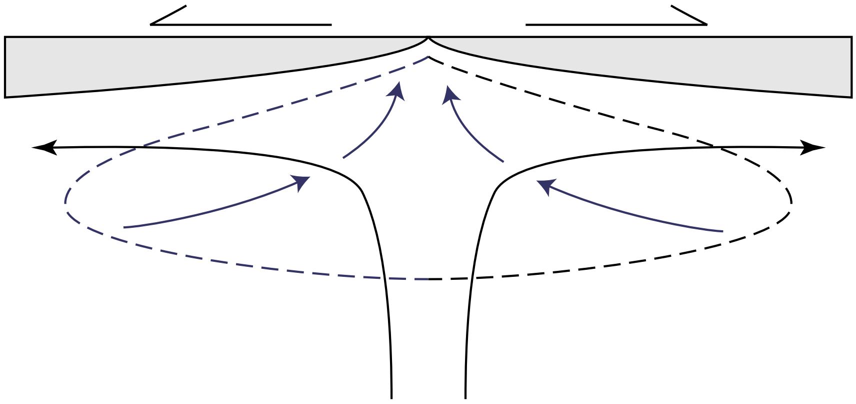

Figure 5.1: Schematic illustrating the model setup. Lithospheric plate (grey regions) diverge at a known rate, driving large scale convection in the solid mantle (black arrows). Decompression causes the mantle to melt within an unknown region indicated by the dashed line. Within this region solid rock and magma coexist and the melt is able to move by porous flow (blue arrows).

The governing equations and constitutive relationships are comprehensively described in chapter 2. To summarize, the governing equations are

$$\boldsymbol{\nabla} P^* = \boldsymbol{\nabla}\cdot \eta \left(\boldsymbol{\nabla}\mathbf{v}_m + \boldsymbol{\nabla}\mathbf{v}_m^{\mathrm{T}}\right) - \phi\Delta\rho g\hat{\mathbf{k}}, \tag{5.1}$$

$$-\boldsymbol{\nabla}\cdot \frac{K}{\mu}\boldsymbol{\nabla}\mathcal{P} + \frac{\mathcal{P}}{\xi} = \boldsymbol{\nabla}\cdot \frac{K}{\mu}\boldsymbol{\nabla}\left(P^* + \Delta\rho g z\right), \tag{5.2}$$

$$\mathcal{P} = \xi\boldsymbol{\nabla}\cdot \mathbf{v}_m \tag{5.3}$$

$$\frac{\partial\mathcal{H}}{\partial t} = \rho L\boldsymbol{\nabla}\cdot \left(1-\phi\right)\mathbf{v}_m - \rho c_P \mathrm{e}^{-\mathcal{A}z}\bar{\mathbf{v}}\cdot\boldsymbol{\nabla}\mathcal{T} + \kappa\mathrm{e}^{-\mathcal{A}z}\nabla^2\mathcal{T}, \tag{5.4}$$

$$\frac{\partial C}{\partial t} + \boldsymbol{\nabla}\cdot \phi\mathbf{v}_f C_f + \boldsymbol{\nabla}\cdot \left(1-\phi\right)\mathbf{v}_m C_m = \mathcal{D}\boldsymbol{\nabla}\cdot \phi\boldsymbol{\nabla} C_f, \tag{5.5}$$

where $\xi = \zeta - 2/3\eta$ is the compaction viscosity. Definitions for $\mathcal{H}$, C, K, ζ, and η are unchanged from those presented in chapter 2. Solutions to C_f, C_m, T, and ϕ are found using the Enthalpy Method, detailed in section 2.4. To simplify the behaviour of the system, the buoyant effect that melt in pore spaces has on large scale convection (equation 2.8) is neglected from the Stokes equation here (equation 5.1).

Table 5.1 summarises the boundary conditions on the principal variables P^*, $\mathcal{P}$, $U = \mathbf{v}_m \cdot \hat{\mathbf{x}}$, $W = \mathbf{v}_m \cdot \hat{\mathbf{k}}$, $\mathcal{H}$ and C. The top boundary is made impermeable to mantle flow and a velocity field in the horizontal is imposed upon it. The temperature is set to 0°C; consequently, a high viscosity, essentially rigid lithosphere forms by conductive cooling. For numerical efficiency the shear viscosity is limited by an upper bound of 10^{25} Pa·s and a lower bound of 10^{15} Pa·s. These bounds have negligible effect on the mantle flow field. Conditions on the bottom boundary allow solid mantle to flow into the domain at a rate determined by motion of the lithosphere and the internal dynamics of the system. The bottom boundary on C depends on the initial condition and is expanded on in section 5.2.3. Open boundary conditions are prescribed on the side walls, allowing material to flow passively out of the domain.

5.2.2 Melt extraction

A novel feature of the model is that it allows for melt extraction at the ridge axis. This feature is also necessary for the numerical experiments presented in chapter 6. At mid-ocean ridges, magma is extracted from the mantle through a complex system of melt lenses, dykes, faults, and fractures. Capturing the dynamics of ridge axis processes in a numerical model remains a significant challenge. Consequently, a greatly simplified approach is adopted here; the system is reduced to an internal boundary between adjacent grid cells beneath the ridge axis. The boundary is invisible to the solid, but any magma that crosses the boundary is immediately extracted from the domain.

The boundary begins beneath the ridge axis in the shallowest cell with non-zero porosity and extends j cells down into the melting region. Cells on either side of the boundary experience a fluid pressure gradient that is proportional to the difference between the lithostatic pressure and fluid pressure within features through which magma is extracted. The pressure gradient acts over half a grid cell either side of the

Table 5.1: Boundary conditions for the mid-ocean ridge configuration[a].

Boundary	Variable	Boundary Condition
$z = 0$	P^*	$\partial P^*/\partial z = 0$
	$\mathcal{P}$	$\partial \mathcal{P}/\partial z = 0$
	U	$U(x, 0) = U_0(x)$, where U_0 is the prescribed plate motion.
	W	$W = 0$
	$\mathcal{H}$	$\mathcal{H} = \rho c_P \exp(\alpha g z/c_P)(T + T_0) - \rho c_P T_0$, where $T = 273$K.
	C	$\partial C/\partial z = 0$
$z = D$	P^*	$P^* = 0$
	$\mathcal{P}$	$\mathcal{P} = 0$
	U	Satisfies discrete form of equation 5.1.
	W	$\partial W/\partial z = 0$
	$\mathcal{H}$	$\mathcal{H} = \rho c_P \exp(\alpha g z/c_P)(\mathcal{T} + T_0) - \rho c_P T_0$
	C	Set from initial condition (described in section 5.2.3).
$x = 0, W$	P^*	$P^* = 0$
	$\mathcal{P}$	$\mathcal{P} = 0$
	U	$\partial U/\partial x = 0$
	W	$W = 0$
	$\mathcal{H}$	$\partial \mathcal{H}/\partial x = 0$
	C	$\partial C/\partial x = 0$

[a]The domain size is $z \in [0, D]$, $x \in [0, W]$.

boundary and is given by

$$\left.\frac{dP_f}{dx}\right|_{\text{dyke}} = \pm\mathcal{F}\frac{\Delta\rho g z}{\Delta x/2}, \tag{5.6}$$

where $\mathcal{F}$ is a fraction between zero and one and Δx is the distance in the x-direction between the centre of a cell and its edge. Setting $\mathcal{F} = 1$ corresponds to the features through which magma is extracted being continuously open to the surface. This limit provides an upper bound on the pressure gradient. Choosing a smaller value leads to larger porosities and lower magma speeds in the immediate vicinity of the boundary. All numerical experiments presented in this study take $\mathcal{F} = 5 \times 10^{-3}$. This value, determined through experimentation, maintains low porosities beneath the ridge axis whilst avoiding a suction effect beyond the immediate surroundings of the internal boundary. One consequence of melting in a heterogeneous mantle is that the apex of the melting region might not necessarily coincide with the central pair of grid cells in the computational domain. Thus the position of the internal boundary is allowed to relocate at each time step to the shallowest grid cell of non-zero porosity within a narrow window of 5 grid–cells on either side of the axis. Numerical experiments presented later in this chapter are conducted with a grid spacing of 1.25 km in each direction. Thus the physical size of the window (6.25 km) approximately equals the distance from the ridge axis within which oceanic crust is observed to reach its full thickness (Dunn et al., 2000).

5.2.3 Initial conditions for mantle heterogeneity

Two stochastic algorithms are employed to generate contrasting topological styles of compositional heterogeneity that may be generated by melting and reaction of eclogite-derived melts. One algorithm is intended to simulate isolated refertilized bodies in the mantle; it produces an array of discrete, randomly shaped blobs that perturb the solidus to the same degree (figure 5.2a) and is hereafter referred to as 'random blob' heterogeneity. The other is intended to simulate continuously variable, interconnected heterogeneities that are both more and less fusible than the pyrolitic mantle. This algorithm allows composition to vary smoothly over all spatial wavelengths greater than a specified cut-off. Example output is illustrated in figure 5.2b and is referred to as 'smoothed noise' heterogeneity. The length scale of heterogeneity in both cases is restricted to several grid cells or larger to avoid excessive damping by numerical diffusion. Given the grid resolution of 1.25 km, the length scale of simulated heterogeneity is comparable to that measured using seismic techniques (Kaneshima and Helffrich, 1999, 2003) and inferred from geochemical observations (e.g. Hanyu and Kaneoka, 1997). The dimensions of the field generated by the algorithm are longer in the z-direction than the computational domain so that mantle convection can advect new compositional heterogeneity into the domain and satisfy the bottom boundary condition on C.

To generate the smoothed noise heterogeneity, the algorithm first generates an

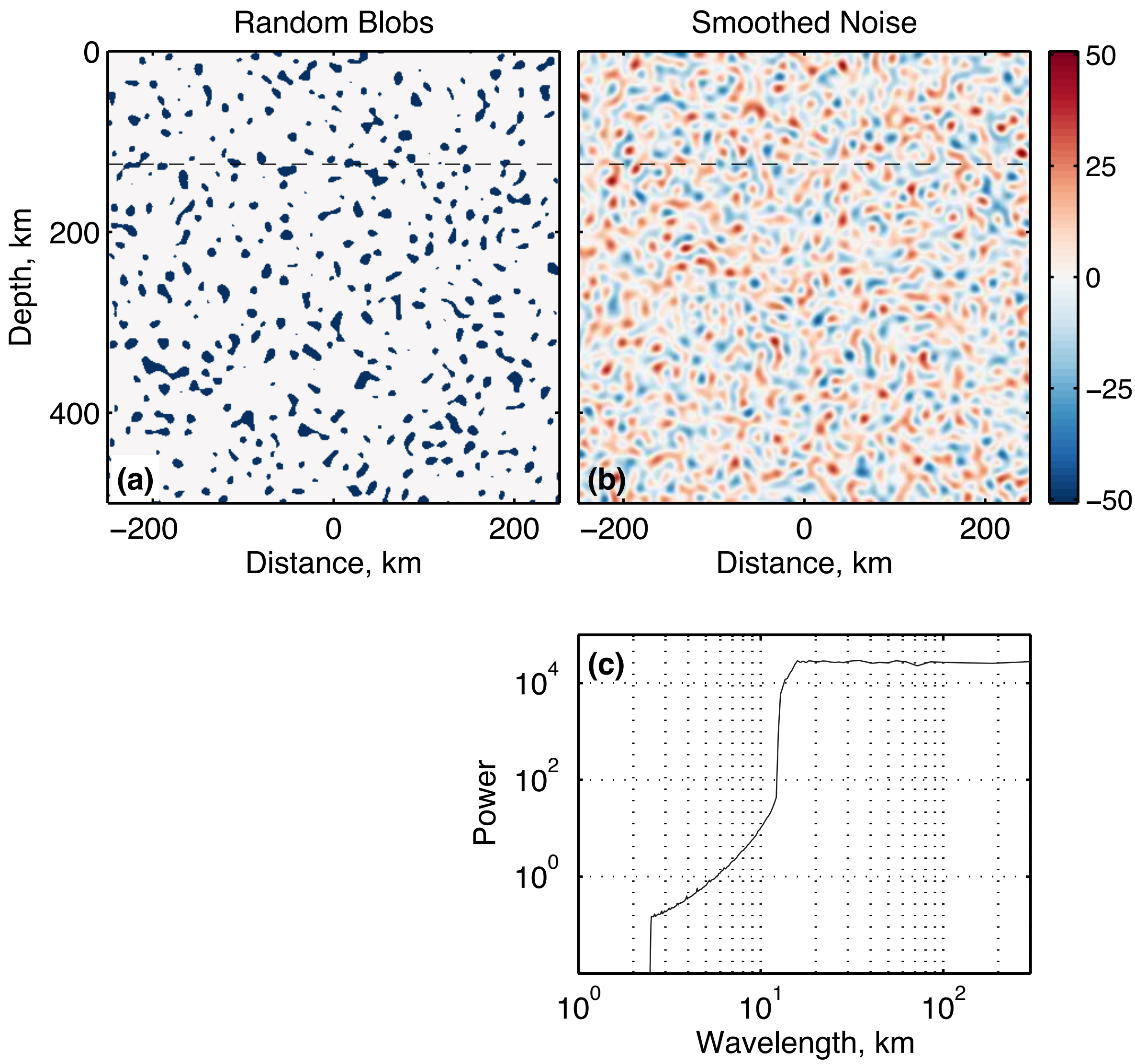

Figure 5.2: Results from the algorithms used to generate mantle heterogeneity, shown as a perturbation to the solidus temperature given by $\Delta T_C = M_S(C_m - C_0)$. The background composition C_0 is set to 0.5. Dashed lines in panels a and b indicate the size of the computational domain relative to the fields of heterogeneity; the heterogeneity fields are larger in the z-direction in order to satisfy the bottom boundary on C as material is advected into the domain. (a) Result from the random blob algorithm. 10% of the area is occupied by fertile heterogeneities. (b) Result from the smoothed noise algorithm. (c) Directionally averaged power spectrum for the heterogeneity field in panel b. It shows approximately uniform power above a wavelengths > 11 km and greatly reduced power for shorter wavelengths.

array of wave numbers given by

$$\mathcal{K}_{ij} = \sqrt{\left(\frac{2\pi n}{L_i}\right)^2 + \left(\frac{2\pi m}{L_j}\right)^2}, \tag{5.7}$$

where L_i and L_j are the maximum distances in the i and j directions, $n \in [-N_i/2, N_i/2]$ and $m \in [-N_j/2, N_j/2]$ are integers, and N_i and N_j are the number of grid cells in the i and j directions. Wave numbers are then converted into amplitudes by applying a band-pass filter to the magnitude of each element in the array. The amplitude for element ij is given by

$$\mathcal{A}_{ij} = \frac{1}{2}\left[1 - \tanh\left(\frac{|\mathcal{K}_{ij}| - |\mathcal{K}|_{\max}}{\sigma}\right)\right], \tag{5.8}$$

where $|K|_{\max}$ defines a cut-off for the maximum wavenumber and σ controls the sharpness of the cutoff. To remove wavelengths that numerical diffusion would damp, the wavenumber cut-off is set to $|\mathcal{K}|_{\max} = 2\pi/\lambda_{\min}$, where $\lambda_{\min}$ is a small multiple of the grid spacing. Figure 5.2 shows the initial heterogeneity field generated by this algorithm. At wavelengths greater than 10 km the spectrum has equal power (figure 5.2c) and negligible power for shorter wavelengths.

The random blob heterogeneity is generated in the same way, except that the continuously varying array of amplitudes produced by the smoothed noise algorithm above is converted into a binary field of more fusible blobs surrounded by more depleted, homogenous mantle. The blobs are defined by the elements of the amplitude array that are greater than a cut-off $\mathcal{A}_t$, which is set so that the number of elements exceeding $\mathcal{A}_t$ occupy a specified area fraction of the array. Entries with $\mathcal{A} > \mathcal{A}_t$ are set to one and the remainder are set to zero. Figure 5.2a shows the initial random blob heterogeneity field used for the simulations that follow. The size of the blobs is set with the same $\lambda_{\min}$ as the smoothed noise field in figure 5.2b and occupy an area fraction of 10%.

5.2.4 Numerical methods and initialization

The governing equations and boundary conditions are discretized using a finite volume scheme onto a staggered mesh with a grid resolution of 1.25 km in each direction. Using an approach similar to that outlined in the previous chapter, the equations are separated into two groups; the first comprising equations 5.4 and 5.5 for the time-dependent variables $\mathcal{H}$ and C; the second containing equations 5.1–5.3 for P^*, $\mathcal{P}$ and $\mathbf{v}_m$. These groups of equations are solved iteratively and explicitly at each time step using incomplete LU and complete LU preconditioned Newton–Krylov methods provided by PETSc (Balay et al., 1997, 2009).

Since the large scale mantle flow field evolves very slowly relative to porosity, composition, and melt flow, staggered time stepping is used to improve computational efficiency. At each time step the thermochemical variables $\mathcal{H}$ and C, along with ϕ, C_f, C_m, and T are updated and solved iteratively with equation 5.2 for the compaction pressure $\mathcal{P}$. The computationally more expensive Stokes equation (5.1) and associated continuity equation 5.3 are solved at larger time intervals. Provided that this time interval is no larger than small multiple of the time step, the loss of accuracy resulting from this staggered time stepping approach is insignificant. A TVD advection scheme (Appendix B) is again employed to preserve gradients in the system.

To initialize the compuational model the mechanical variables P^*, $\mathcal{P}$ and $\mathbf{v}_m$ are solved iteratively with the thermochemical variables $\mathcal{H}$ and C. The intial guess for $\mathcal{H}$ is derived from the solution to a half–space cooling model beneath a ridge axis, and the mantle is assumed to be compositionally homogenous. Next, the chosen model of mantle heterogeneity is added and the enthalpy method is employed to update the variables ϕ, T, C_f, and C_m. Finally, all porosity is removed from the melting region, completing the intialization.

5.3 Results

5.3.1 Homogenous mantle

Figure 5.3 shows results from a numerical experiment initialized with $U_0 = 4$ cm/yr and a compositionally homogenous mantle. The results are shown in terms of T (panel a), composition (panel b), ϕ (panel c), $|\mathbf{v}_f|$ (panel d), upwelling rate (panel e) and the melting rate Γ (panel f). At the model time shown (2 Ma) the experiment is effectively in steady state. Melting is confined to a triangular-shaped region that extends approximately 70 km into the mantle and over 200 km to either side of the axis of spreading.

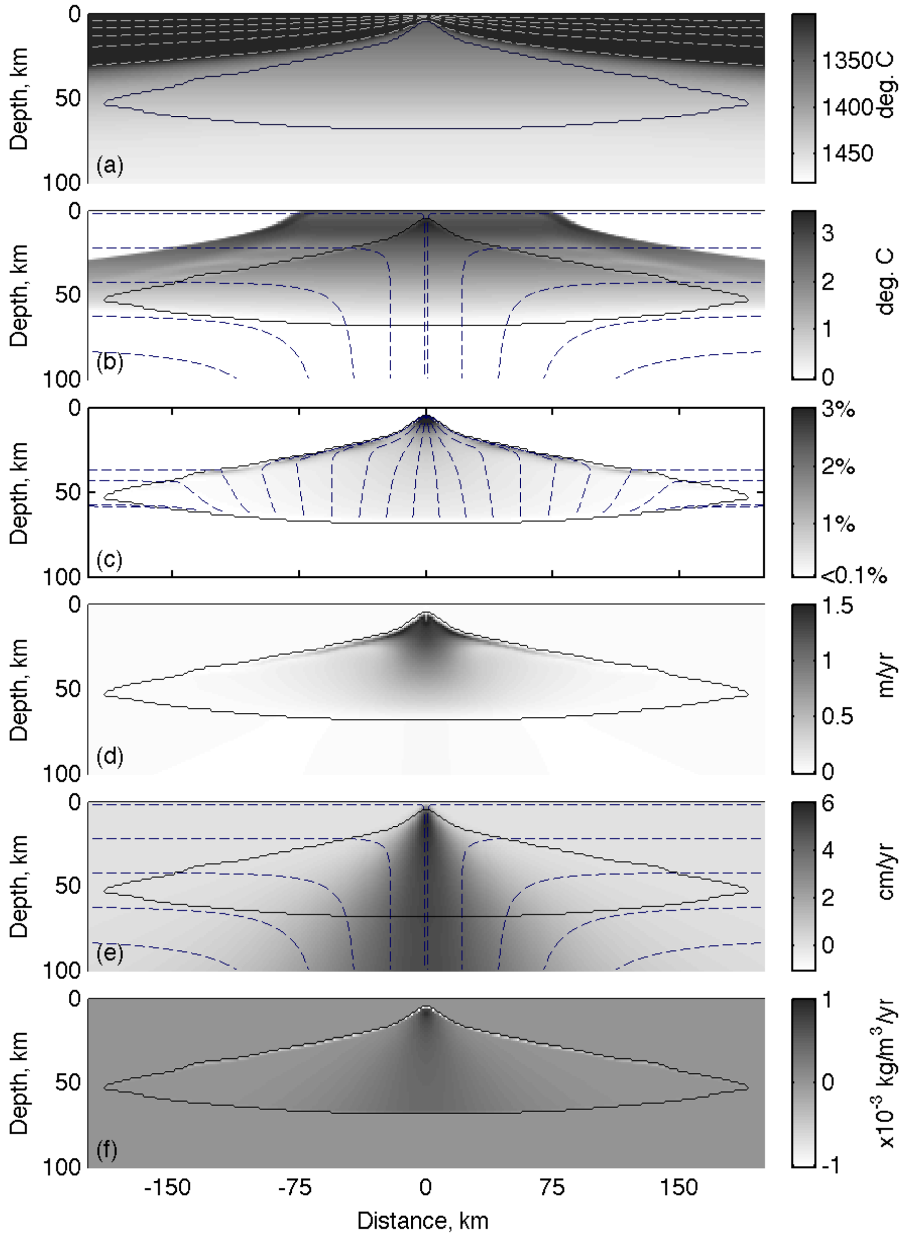

Figure 5.3: A snapshot from a simulation with no initial mantle heterogeneity and $U_0 = 4$ cm/yr after a model time of 2 Ma. Black solid lines in all panels contour the solidus. (a) Temperature with dashed grey lines contouring temperature in the lithosphere in intervals of approximately 200 K. (b) Composition of the solid mantle, expressed as a perturbation to the solidus temperature. Dashed blue lines show flow lines for the convecting mantle. (c) Porosity, with dashed blue lines representing flow lines for the magma. (d) Magma speed $|\mathbf{v}_f|$, (e) upwelling rate of the solid mantle $|\mathbf{v}_f \cdot \hat{\mathbf{k}}|$, (f) melting rate. Parameter values for this experiment are given in table 5.2.

Figure 5.3a shows the computed temperature structure of the mid-ocean ridge. Conductive cooling has established an essentially rigid, high viscosity lithosphere that thickens with distance from the ridge axis. In the subsolidus portion of the mantle, corresponding roughly to depths >70 km, the temperature profile is adiabatic. Because thermodynamic equilibrium is assumed, the temperature within the partially molten region is pinned to the local solidus temperature. Thus temperature varies with composition in regions where melt is present.

Figure 5.3b expresses the composition of the solid mantle in terms of a perturbation to the solidus temperature given by $\Delta T_C = M_S\,(C_m - C_0)$, where M_S is the slope $\partial T/\partial C$ of the solidus, C_m is the local composition of the matrix and C_0 is a reference composition. For this experiment material flowing into the domain across the bottom boundary defines the reference composition C_0. Other parameter values are defined in table 5.2. Figure 5.3b shows that the mantle becomes more depleted towards the surface. The crust is of approximately uniform composition. At the time slice shown in the figures, sufficient time has elapsed for the plates to spread around 50 km away from the ridge axis. At lateral distances greater than 50 km, remnants of the initial condition are evident in the lithosphere, shown by regions where $\Delta T_C = 0°\text{C}$. Dashed lines in this figure reveal that the large scale pattern of mantle convection is symmetrical about the ridge axis and approximates the corner flow solution of Batchelor (1967).

The porosity of the melting region is shown in figure 5.3c. Within the melting region, porosity is generally less than 2% and increases towards the ridge axis. Regions of large porosity > 2% are evident directly beneath the ridge axis, and also in high porosity channels, parallel to the base of the lithosphere, that result from compaction of the underlying mantle. The blue dashed lines illustrate the flow lines of magma beneath the ridge axis. Magma generated within approximately 50 km of the spreading axis flows to the ridge axis along gently curving paths. This mode of melt focusing corresponds closely to the findings of Spiegelman and McKenzie (1987) and Yinting et al. (1991). Between 50 km and 100 km from the ridge axis, the mode of melt focusing resembles the model by Sparks and Parmentier (1991): magma rises

Table 5.2: List of parameters and preferred values.

Symbol	Meaning	Value
κ	Thermal diffusivity	1×10^{-6} m/s^2
L	Latent heat of fusion	5.5×10^5J/kg
M_S	Slope $\partial T/\partial C$ of the solidus	200 K
M_L	Slope $\partial T/\partial C$ of the liquidus	200 K
$\mathcal{T}$	Potential temperature	1696 K
T_0	Solidus temperature for reference mantle at 0 kbar	1605 K
C_0	Reference mantle composition	0.5
ΔC	Difference in composition between rock and magma in thermodynamic equilibrium	0.1
ΔT	Temperature scale	$M\Delta C$
ρ	Density	3000 kg/m^3
α	Coefficient of thermal expansion	3×10^{-5} K^{-1}
c_P	Specific heat capacity	1200 J/kg/K
γ^{-1}	Clapeyron slope	60 K/GPa
$\mathcal{D}$	Chemical diffusivity	1×10^{-8} m/s^2
g	Acceleration due to gravity	9.8 m/s^2
k_0	Reference permeability	1×10^{-7} m^2
$\eta_{\max}$	Cut-off shear viscosity, maximum	10^{25}Pa·s
Δx	Grid spacing in x-direction	1.25 km
Δz	Grid spacing in z-direction	1.25 km

buoyantly to the decompaction channel, then flows uphill along the base of the lithosphere to the ridge axis. At still greater distances $\gtrsim$ 100 km, magma rises to base of the lithosphere, freezes, and is then advected laterally away from the ridge axis by mantle convection. Figure 5.3d shows that the magma speed $|\mathbf{v}_f|$ is no greater than 2 m/yr. Away from the base of the lithosphere where magma freezes, spatial variations in the magma speed correlate well with spatial variations of porosity, indicating that magma is driven largely by buoyancy.

The upwelling rate of the mantle, given by $-\mathbf{v}_m \cdot \hat{\mathbf{k}}$, is shown in figure 5.3e. Upwelling is fastest along the axis of spreading, reaching approximately 9 cm/yr, and decays with increasing lateral distance from the ridge. The upwelling rate provides the dominant contribution to the melting rate. The melting rate, shown in figure 5.3f is computed diagnostically from equation 2.1 as $\Gamma = \partial\phi/\partial t - \boldsymbol{\nabla} \cdot (1-\phi)\,\mathbf{v}_m$. Spatial variation of the melting rate corresponds closely to spatial variation of the upwelling rate. Strong freezing ($\Gamma = -2 \times 10^{-3}$ kg/m^3/yr – $\Gamma = -4 \times 10^{-3}$ kg/m^3/yr) occurs along the lithosphere–asthenosphere boundary in response to conductive cooling. These results provide a reference state against which the effects of compositional heterogeneity on melt migration can be compared.

5.3.2 Heterogeneous mantle

Figure 5.4 illustrates the effect of compositional heterogeneity on the dynamics of magma flow and mantle deformation. Panels a-c show results from an experiment initialized with the random blob heterogeneity model. Prior to melting the isolated blobs occupy an area fraction of 10% and perturb the solidus temperature by -50 K (figure 5.4a). Panels d-f show results from an experiment initialized with the smoothed noise heterogeneity model. The imposed heterogeneity (figure 5.4d) perturbs the solidus temperature by $\pm$50K and has equal power on wavelengths greater than 10 km. With the exception of the heterogeneity model, the experiments are identical and share the parameter regime detailed in table 5.2.

Panels b and e show the porosity distribution for the random blob and smoothed

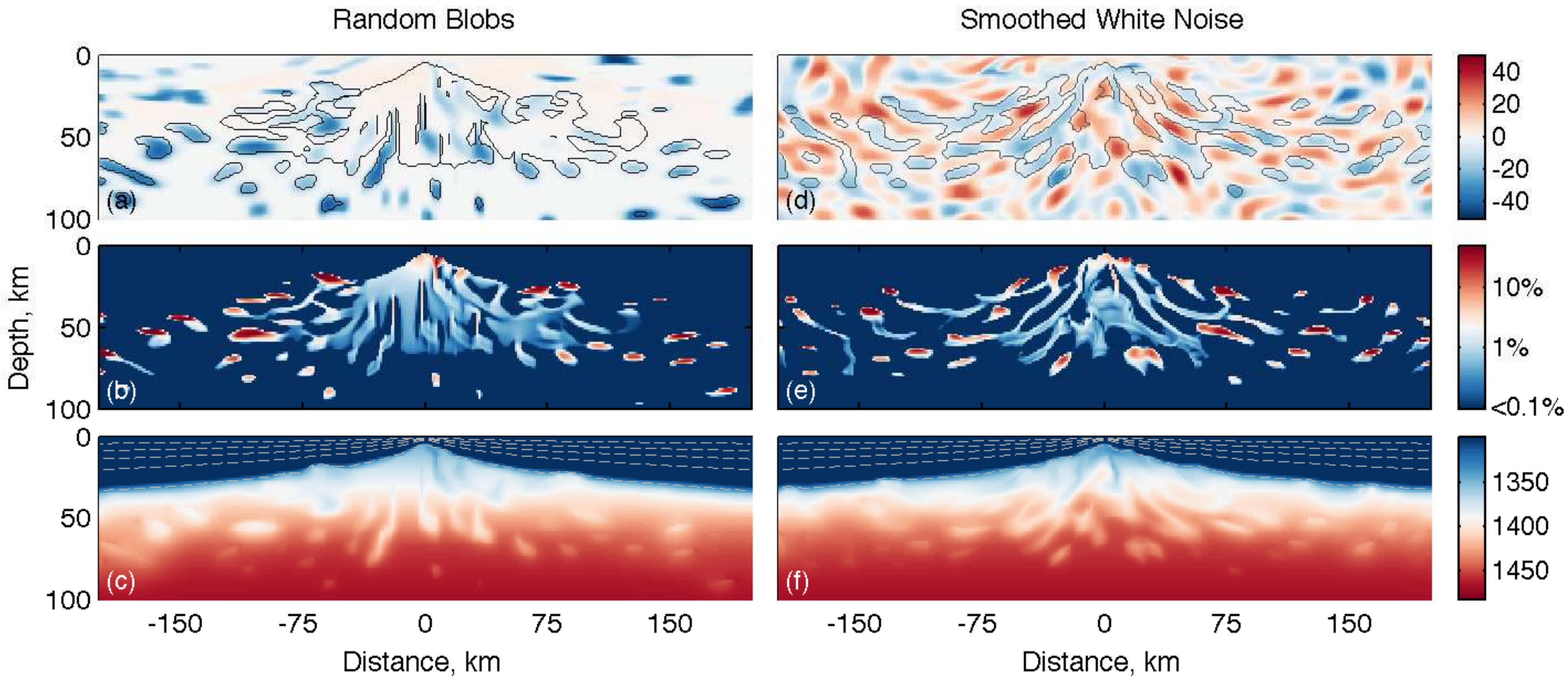

Figure 5.4: Snapshots from two representative simulations run with contrasting styles of mantle heterogeneity and $U_0 = 4$ cm/yr. Panels a–c show results from a simulation with the random blob style heterogeneity after a model time of 1.9 Ma; panels d–f show results from a simulation run with the smoothed white noise heterogeneity after a model time of 1.9 Ma. Panels a and d show mantle heterogeneity expressed as a perturbation to the solidus temperature, (b and e) show porosity, (c and f) show temperature.

noise experiments respectively. Heterogeneity has a striking effect on the distribution of porosity and dynamics of melt migration. In the random blob case (panel b) heterogeneities far from the ridge axis cause large ($10 - 20$ km), isolated blobs of magma to form. At large distances from the axis of spreading, mantle convection has sheared some of the heterogeneities into elongate shapes. Associated with these off-axis heterogeneities are large porosities in excess of 40%. Closer to the ridge axis, at lateral distances of 40–75 km, partially molten, fertile heterogeneities are connected by bridges of enriched mantle for which $\Delta T_C \approx -10$ K. The bridges form by reactive flow and typically have porosities in excess of 1%. Even closer to the ridge axis within distances of 40 km from the spreading axis, heterogeneities nucleate and support vertical, narrow reactive channels. These channels are hosted in compositionally homogenous mantle and form in the manner described in the previous chapter. Despite these complexities, some portions of the melting region in the random blob experiment are reminiscent of the homogenous case (figure 5.3c). For example, figure 5.3b shows the porosity to vary regularly close to the base of the lithosphere at lateral distances of -20 km to -75 km from the axis of spreading. In this region magma migrates by diffuse porous flow and is focused towards the ridge axis by a mechanism similar to that described by Sparks and Parmentier (1991). In the remainder of the melting region, however, melt focusing depends strongly on the topology of channels.

In the smoothed noise experiment a network of channels is established throughout the melting region. No portion of the melting region resembles the homogenous case (figure 5.4e). Channels are rooted at, and coincide with the more fusible heterogeneities; thus channels take a meandering route to the surface that depends on the local fusibility of mantle rock. Regions of less fusible, depleted mantle are frequently subsolidus and help to divide the melting region into discrete, but interconnected channels. In the flanks of the melting region, isolated ponds of magma and high porosity mantle coincide with more fusible heterogeneities. At depths greater than approximately 70 km, heterogeneities enriched to a similar degree are partially molten and isolated from the channel network.

In both experiments, some of the isolated ponds of magma are artefacts of the initial condition. At the time slices shown, these ponds are confined to distances in excess of 120 km from the axis of spreading and depths shallower than 60 km. Heterogeneities associated with these melt ponds were initialized within the melting region for the ambient mantle. Thermal diffusion prevented melt generated within them from escaping, thus they were not able to interact with the ambient melting region in the same way as heterogeneities initialized at greater depths. Numerical complexities associated with the extraction mechanism prevented most experiments from running for model times longer than 2–3 Ma. However, similar experiments by Katz and Weatherley (2012), which did not include the extraction mechanism, were stable for long enough that all traces of the initial condition were removed. Fusible off-axis heterogeneities in experiments presented by Katz and Weatherley (2012) behave in very similar ways to that evident in the present study. Therefore, artefacts of the initial condition do not adversely affect the results of experiments presented here.

Figures 5.4c and 5.4f show that mantle heterogeneity induces significant variability into the thermal structure of the mantle. Partially molten fertile heterogeneities coincide with local temperature minima; unmolten depleted heterogeneities correspond with local temperature maxima. Heat diffuses into the more fertile heterogeneities and powers melting over that from decompression alone. However, this leads to reduced melting rates and porosity in the surrounding mantle. At the base of the lithosphere, crystallizing melt ponds that coincide with fertile heterogeneities act as a heat source; heat released from these regions diffuses into the cooler lithosphere and locally modifies the thermal structure.

Figure 5.5 shows the same solutions as figure 5.4 in terms of the upwelling rate $W = -\mathbf{v}_m \cdot \hat{\mathbf{k}}$, magma speed, melting rate, and compaction pressure. Panels a and e show that corner flow remains a good approximation for the solid mantle flow field. Subtle differences from the homogenous case evident both experiments result from local effects of compaction and crystallization.

The magma speed, given by $|\mathbf{v}_f|$ for each experiment is shown in figures 5.5b and 5.5f. Channels accommodate faster magma speeds than regions of diffuse porous flow. Within channels, buoyancy is the dominant driving force. In these representative

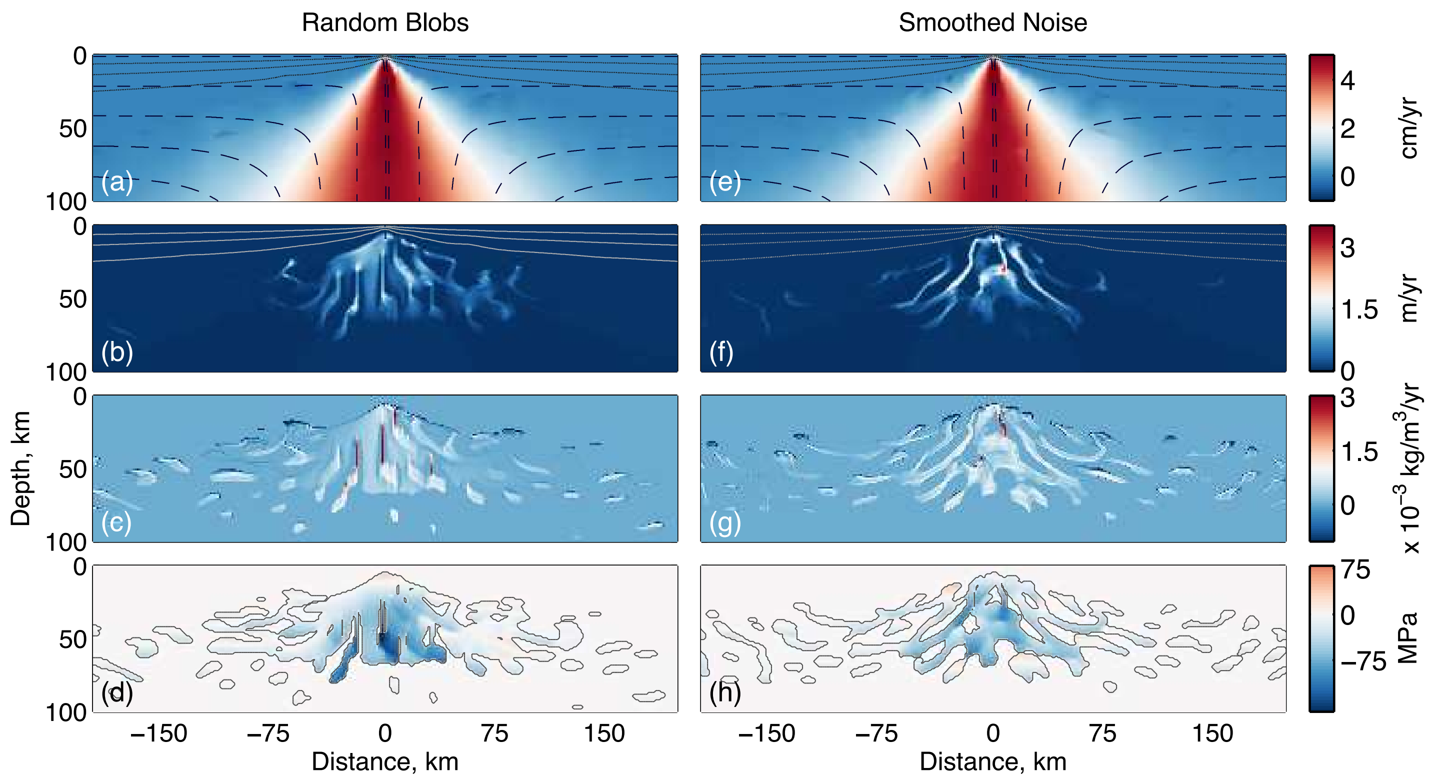

Figure 5.5: Extension of figure 5.4 showing (a, e) the upwelling rate of the matrix, (b, f) the magma speed $|\mathbf{v}_f|$, (c, h) the melting rate, (d, h) the compaction pressure.

experiments intrachannel magma speeds are approximately 1.5 m/yr. Speeds are highest in channels that feed melt directly to the ridge axis (figure 5.5f), rather than into a sub-axial region of more uniform porosity (figure 5.5b). In isolated melt ponds, the magma speed approximates the speed of the solid mantle, $|\mathbf{v}_m|$. Panels c and g shows that spatial variations in the melting rate correlate strongly with variations in magma speed where $|\mathbf{v}_f|$ is large. In regions were the magma speed is small, decompression and thermal diffusion drive melting. Crystallization is evident along the lithosphere–asthenosphere boundary and around the upper edges of isolated melt ponds in the flanks of the melting region.

Figures 5.5d and 5.5h show that most of the partially molten region is under compaction. Compaction pressures are of the order 10 MPa. Compaction is strongest (most negative) where the melting rate is fastest and generally decreases with distance from the axis of spreading. Small regions of $\mathcal{P} > 0$, indicating dilation, are confined to pools of melt that collect at the base of the lithosphere and isolated ponds deeper in the mantle.

Despite its crudeness, the melt extraction mechanism (section 5.2.2) successfully maintains low porosities beneath the ridge axis without a suction being felt by the surrounding grid cells. Katz and Weatherley (2012) present analogous experiments where melt is not extracted at the ridge axis. The dynamics and results of both sets of experiments are consistent, indicating that the mechanism outlined in section 5.2.2 removes melt from the system without adversely affecting the dynamics of the interior.

5.3.3 Variable spreading rate

Figure 5.6 shows snapshots of the porosity field from a suite of eight experiments to illustrate how the dynamics of magma flow in a heterogeneous mantle vary with spreading rate. Faster spreading rates drive faster upwelling over a broader area, which causes the melting rate to widen. For $U_0 > 4$ cm/yr (panels c–h) the region of melting stretches for more than 250 km either side of the spreading axis. Further analysis of these experiments reveal a general increase in the melting rate, porosity and magma speed with spreading rate.

Figures 5.6f and 5.6h show ponds magma forming adjacent to the lithosphere-asthenosphere boundary at lateral distances of −40 km to −80 km from the spreading axis. These pools are fed by channels and form because a region of depleted, subsolidus rock lies adjacent to the melt pool on the ridge side and prevents magma from flowing towards the ridge axis. This behaviour is not evident in experiments run with the random blob model of heterogeneity.

5.4 Discussion

Results presented in this chapter indicate that the spatial arrangement of mantle heterogeneity has significant consequences for the dynamics of melt migration and focusing. In this experimental framework, the arrangement of sufficiently fusible heterogeneities has little effect on the emergence of channels. However, the configuration of channels is strongly related to the topology of chemical heterogeneity. Figures 5.4 and 5.5 show that channels are narrow and vertical when heterogeneity is modelled as randomly shaped, fusible blobs that are hosted in less fusible and compositionally homogenous mantle. In this case the channels, which form by reactive instability, are straight because (i) buoyancy is the dominant force that drives magma and (ii) the structure of the surrounding mantle in terms of permeability, pressure, composition and enthalpy, has approximate bilateral symmetry about the mid-line of channel.

In contrast, when heterogeneity randomly varies, channels meander through the mantle in a general upwards direction (figures 5.4d–f). In this case the geometry of channels is defined by the combined effects of buoyancy and the energetics of melting. Equation 4.12 from the previous chapter shows that thermal diffusion drives melting and favours high porosities in regions relatively more fusible than their surroundings. Conversely, it suppresses melting and high permeabilities in less fusible regions. Figures 5.4d and 5.4e illustrate that in context of the smoothed noise heterogeneity model this causes channels to coincide with more fusible heterogeneities, and divert around

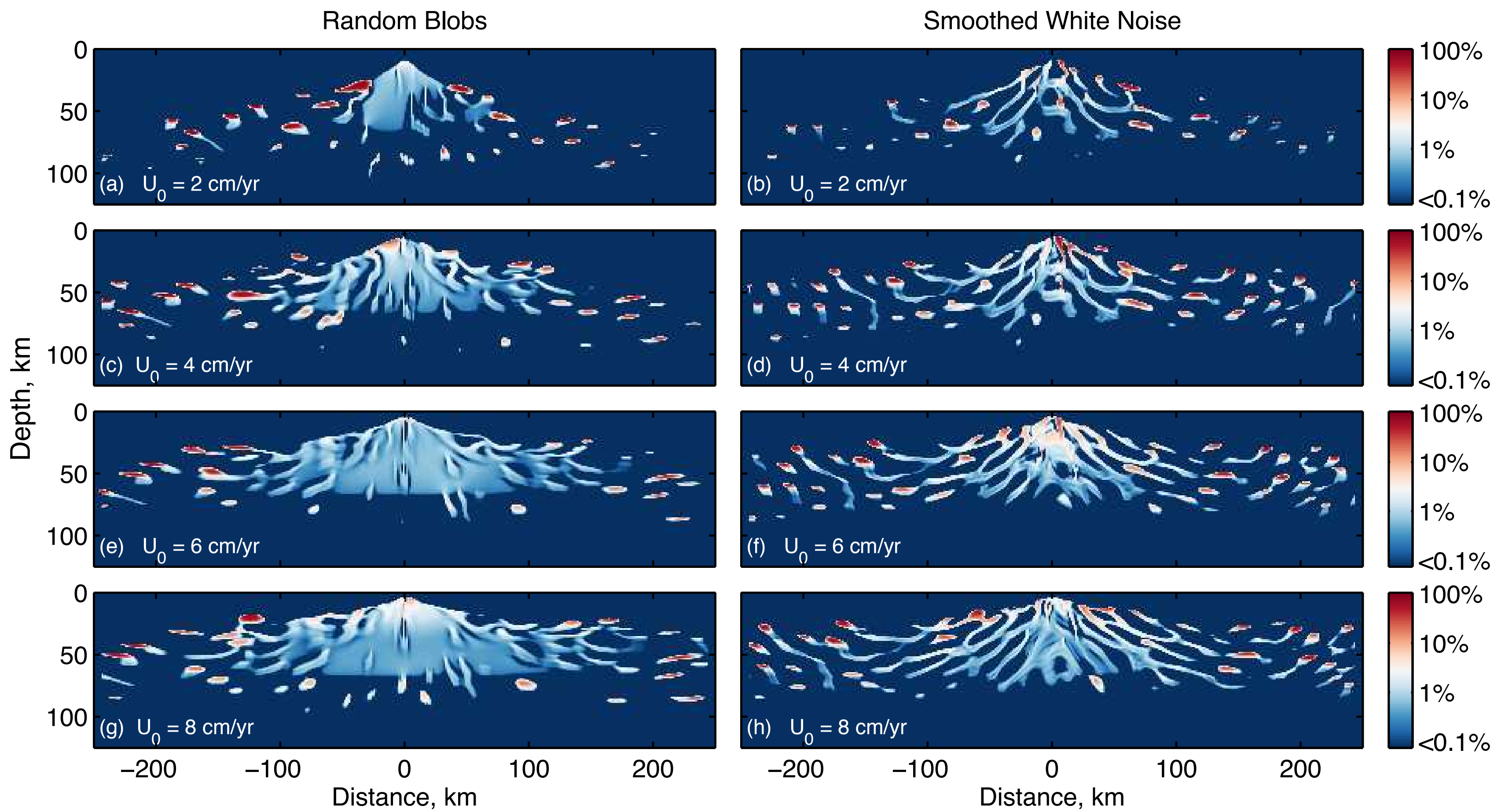

Figure 5.6: Representative snapshots of porosity from simulations run at different half spreading rates with the random blob (panels a–d) and smoothed white noise (panels e–h) heterogeneity models. The half spreading rates are indicated on each panel and the elapsed model times are as follows: (a) 2.1 Myr, (b) 2.6 Myr, (c) 1.9 Myr, (d) 1.3 Myr, (e) 2.9 Myr, (f) 1.5 Myr, (g) 1.5 Myr, (h) 1.4 Myr. Other parameter values are given in table 5.2 and are consistent for each experiment.

less fusible regions with lower permeability.

Since magma is directed away from less fusible regions, depleted heterogeneities are unlikely to be refertilized by migrating magma. Melting and melt segregation will further deplete them, and sufficiently depleted heterogeneities may be advected beneath the spreading ridge without melting. The simulations predict that depleted heterogeneities are under-represented in magma that crystallizes at mid-ocean ridge. Furthermore, they suggest that the most depleted heterogeneities will not be represented in oceanic basalts at all. Understanding the nature of severely depleted heterogeneities in the mantle is a significant challenge. Recent evidence from hafnium and neodymium isotopes in mid-ocean ridge basalts, however, reveal previously unrecognized domains of depleted mantle on scales of several hundred kilometres (Salters et al., 2011). Whether this depleted component is also present on smaller length scales is yet to be determined.

Results from the experiments above also suggest that mantle heterogeneity has important consequences for melt focusing to the ridge axis. In experiments with a homogenous mantle, melt focusing by flow along the lithosphere–asthenosphere boundary and by pressure gradients resulting from mantle convection represents a hybrid between early models by Yinting et al. (1991) and Sparks and Parmentier (1991) (figure 5.3c). In the random blob case a series of vertical channels and off-axis melt ponds complicate this focusing mechanism, and in the smoothed noise case, a network of interconnected channels focus magma to the ridge axis. The network of channels in the smoothed noise case bears some resemblance the mechanism proposed by Kelemen et al. (2000) and Braun and Kelemen (2002), whereby a web of upwards coalescing channels focus magma to the ridge axis. Off-axis melt ponds interrupt broader melt focusing along the lithosphere–asthenosphere boundary. Katz (2008) noted that similar features form in experiments with a homogenous mantle and low resistance to compaction. In the experiments presented here, however, the bulk viscosity is large (order 10^{19} Pa s), hence heterogeneity must be the controlling factor.

Melt focusing in the experiments is incomplete; magma that does not reach the ridge axis is frozen into the lithosphere and refertilizes the mantle (figures 5.3f, 5.5c and 5.5g). In general, less than 10% of the total melt produced in the experiments is frozen into the lithosphere. This is roughly equivalent to the volume of magma generated at distances greater than 50 km from the axis of spreading. In the heterogenous cases, the distribution of refertilized mantle rock is nonuniform. Some refertilization takes place at the base of the lithosphere; the rest occurs in off-axis melt localizations as they are advected laterally away from the spreading axis.

This result suggests that mid-ocean ridges are generators of mantle heterogeneity as well as consumers. Halliday et al. (1995) envisaged a similar situation and proposed that certain geochemical aspects of ocean island basalts are best explained if the source mantle is partly metasomatised by shallow, small–degree partial melts. Furthermore, observations of the Ronda peridotite by Bedini et al. (1997) provide evidence for kilometre-scale variation in the volume and composition of melts that infiltrate and refertilize the lithosphere. In the experiments above, melt pooling suggests one way in which spatial and chemical variability in refertilization might be generated.

Many of the melt pools evident in the results are represented by regions with porosities larger than 10%. Whether regions with such large porosities can exists in the mantle is unclear. Furthermore, large porosities predicted in numerical experiments may partly derive from an incomplete description of the dynamics in Earth's mantle. For instance, pervasive infiltration of magma into the host rock around enriched heterogeneities, for example, along grain boundaries, shear zones, and fractures, might be rapid enough to maintain low porosities ($< 10\%$) everywhere within the melting region. Another possibility is that brittle fractures might tap the shallow melt ponds and transport magma to the surface (e.g. Kelemen and Aharonov, 1998). Recent seismic observations of young oceanic crust indicate that melt pooling and brittle fracture are important processes in the shallow mantle. Reflection (Canales et al., 2009, 2012) and refraction (Durant and Toomey, 2009) surveys of intermediate to fast spreading ridge segments reveal crustal melt lenses located 4–20 km away from the ridge axis. Owing to the large distances separating these lenses from active volcanoes on the ridge axis, it is unlikely that melt migrates to them through the crust. Rather, the lenses may be supplied with magma directly from the underlying mantle. The smoothed noise experiments (figures 5.4d–f, 5.5e–h) predict how less fusible mantle heterogeneities close to the lithosphere–asthenosphere boundary can act as a permeability barrier, disrupt magma flow to the ridge axis, and focus it to an off-axis location. Networks of faults and fractures could tap this off-axis magma, leading to its emplacement in the crust.

5.5 Limitations

The results above are subject to a number of limitations that build on those outlined in the previous chapter. In order to explore the fundamental dynamics of the system, the model is necessarily simplified relative to our understanding of the Earth and knowledge of earth materials. It is based on a fluid dynamical description of magma flow and mantle deformation, and rheological properties are defined through a constitutive relationships (equations 2.11–2.12). For experiments presented in this chapter, the relationship for shear viscosity closely resembles experimentally derived laws for diffusion creep. Including dislocation creep and viscoplasticity in the models would provide a more comprehensive description of mantle rheology. In light of results from chapter 3, these additional deformation mechanisms would result in slight differences in the dynamics of mantle convection. Since the changes are small, the general behaviour is unlikely to be drastically different from the results above.

An important objective of future models should also be to explore the consequences of brittle fracture for the ponds of magma predicted in the experiments above. Pursuing this line of investigation may help to understand the formation of the off-axis melt bodies observed by Durant and Toomey (2009); Canales et al. (2009) and Canales et al. (2012), and their implications for crustal magmatism.

Further simplifications to the physical dynamics of the system are made by neglecting the buoyancy effects of interstitial magma and density variations associated with mantle heterogeneity. Katz (2010) and Katz and Weatherley (2012) show the buoyancy of interstitial magma can break the symmetry of mantle convection about the axis of spreading. However, the effect of melt and compositional buoyancy on the dynamics of channelization are not well understood and await exploration in future studies.

The most important simplification in this theoretical framework is the petrological model. Asimow et al. (1997) argue that a binary phase loop provides a reasonable first-order approximation of mantle petrology; furthermore, it is well-suited to exploring the dynamics of reactive flow. However, the model misses important aspects of mantle petrology including mass transfer from the liquid to the solid by reaction, multiple mineral phases, the presence of volatiles, variation in the productivity of mantle rocks, and phase-specific enthalpies of fusion. Whilst more complex petrological models will increase the complexity and dynamics of future models, the central theme of results presented here – that mantle heterogeneity has important consequences for the dynamics of melt migration – is unlikely to change. Overcoming these limitations, however, presents an significant challenge and will help to improve and clarify our interpretations of the geochemistry of oceanic basalt in terms of magma dynamics.

Additional limitations lie within the models of mantle heterogeneity and the grid resolution of numerical experiments. Two stochastic algorithms in this study generate end-member models of mantle heterogeneity. These models do not presume to capture the true topology, fusibility and scales of mantle heterogeneity; rather they are a means to hypothesise how variations in the solidus temperature and fusibility of mantle rock might affect the dynamics of magma flow. In the present simulations, the grid spacing limits the length scale of the hypothetical heterogeneity and width of melt localization features. For the experiments above, the grid spacing is 1.25 km in each direction. Observations from ophiolites and peridotite massifs, however, record such features on scales upwards of 10 cm (Reisberg et al., 1991; Blichert-Toft et al., 1999). At these small scales, attributes of the mantle such as grain size variations and minor shear zones are likely to have consequences for melt localization in addition to those from compositional heterogeneity. Our understanding of how these different variables influence the dynamics of magma flow will benefit from future studies that combine lithological and structure mapping of mantle peridotites on a range of scales with numerical models at higher resolution.

Between the models presented here and those by Katz and Weatherley (2012), the principal difference is the means to extract melt at the ridge axis. Implementing the mechanism outlined in section 5.2.2 successfully maintains low porosities at the ridge axis without adversely affecting the dynamics of the interior of the domain. However, the current mechanism of melt extraction violates conservation of mass at the locus of melt extraction and can hamper numerical solution when the compaction pressure fluctuates. In consequence it is difficult to maintain the stability of the experiments for long enough to remove all traces of the initial condition. With longer run times and complete removal of the initial condition, robust calculations can be made of the efficiency of melt extraction and extent of refertilization. To overcome these shortcomings requires a more advanced mechanism of melt extraction. Several options that do not violate conservation of mass exist. One is to incorporate into the governing equations a sink term that removes magma from within a specified region at the ridge axis; another is to adopt an approach similar to Tirone et al. (2012) and allow for crust to be produced by strong freezing at the ridge axis.

An additional concern is the dimensionality of the simulations. Modelling the system in two dimensions assumes that all features are infinite in extent perpendicular to the plane of the domain. In three dimensions melt channels can have tubular or tabular forms; these different geometries may have different consequences for the dynamics of melt flow on scales similar to that which characterise the heterogeneity. On larger scales, transform faults and ridge offsets perturb the thermal structure and dynamics of the mantle (Morency et al., 2005; Gregg et al., 2009; Weatherley and Katz, 2010). This probably affects the dynamics of melt transport beneath the lithosphere and may have unrecognised consequences for magma flow in a heterogeneous mantle.

5.6 Conclusions

Despite these limitations, the models presented in this study provide a physically consistent fluid dynamical perspective on the consequences of mantle heterogeneity for melt migration and focusing beneath mid-ocean ridges. In this theoretical framework, mantle heterogeneity is a prerequisite for channelized flow. Results show that the topology of heterogeneity strongly affects the spatial arrangement of channels; their arrangement is determined by the combined effects of buoyant magma flow and the energetics of melting. Variations in spreading rate have little effect on their geometry. These results suggest that a physical connection exists between mantle heterogeneity and melt transport beneath mid-ocean ridges, and consequently support inferences of such a connection from geochemical studies (Lundstrom, 2000; Kogiso and Hirschmann, 2004). Channels play an important role in focusing magma to the ridge axis. In regions of diffuse porous flow, however, existing theories by Yinting et al. (1991) and Sparks and Parmentier (1991) are adequate. Segregation of magma generated beneath mid-ocean ridges can generate fertile chemical heterogeneities by melt-pooling and freezing. Melt ponds may deliver magma to off-axis crustal magma chambers, and cause spatial variation in refertilization of the lithosphere. Channelized magma flow is considered a primary mechanism for generating lithological variability in mantle peridotites (e.g. Kelemen et al., 1995a; Braun and Kelemen, 2002), creating geochemical disequilibrium between MORB-forming magmas and the residue of partial melting (Kelemen et al., 1995a,b), and is thought to influence the uranium-series geochemistry of MORB (e.g. Elliott and Spiegelman, 2003). Reconciling the present models with these observations, and validating them against geological, geophysical, and geochemical data presents a major challenge for future work and is touched upon in the next chapter.

Chapter 6

The speed and duration of melt migration in a heterogeneous mantle

6.1 Introduction

Observations of uranium-series decay chains in oceanic basalts offer valuable insights to the speed and duration of magma flow in the mantle (e.g Lundstrom, 2003; Bourdon and Sims, 2003; Elliott and Spiegelman, 2003; Turner and Bourdon, 2011). Although much debate surrounds the interpretation of these observations, it is generally agreed that magma flow is too rapid to be consistent with diffuse porous flow in the mantle. Channelized flow, however, is thought to better fit the observations, but only one previous study by Elliott and Spiegelman (2003) investigates its consequences for U-series systems with a physically consistent model of melt migration and mantle deformation. The previous chapter builds on the model by Elliott and Spiegelman (2003) in that it conserves energy, considers the effects of spreading plates, and investigates the effect of mantle heterogeneity on melt migration. Results indicate that the dynamics of magma flow strongly depend on mantle heterogeneity, and suggest that compositional variation could have important, but previously unrecognized consequences for the speed and duration of melt migration, and for the U-series geochemistry of mid-ocean ridge basalts.

Efforts to constrain the speed and duration of melt migration focus largely on the radiogenic daughter products of ^{235}U and ^{238}U. These isotopes of uranium decay with half-lives of approximately 0.7 Gyr and 4.5 Gyr respectively and support long chains of intermediary nuclides. The intermediaries decay with shorter half-lives spanning a wide range of scales from 164 μs to 245 kyr. Thus not all intermediaries are of use to studies melt migration; the decay series for ^{238}U and ^{235}U can be reduced to

$$^{238}\mathrm{U} \rightarrow^{230} \mathrm{Th} \rightarrow^{226} \mathrm{Ra} \rightarrow^{206} \mathrm{Pb},$$

$$^{235}\mathrm{U} \rightarrow^{231} \mathrm{Pa} \rightarrow^{207} \mathrm{Pb}.$$

^{230}Th decays with a half-life of 75 kyr, ^{226}Ra decays on a time scale of 1.6 kyr, ^{231}Pa has a half-life of 33 kyr, and the lead isotopes are stable. If undisturbed for long periods of time, these decay chains enter a steady state known as secular equilibrium. Specifically, secular equilibrium occurs when all daughter nuclides in a system decay at the same rate. Decay rates are routinely expressed as activities; for the i-th nuclide in a decay series, the activity is given by $a_i = \lambda_i m_i$, where λ is its decay constant, and m is its concentration by weight. In perfect secular equilibrium, the activity ratio of a daughter–parent nuclide pair (a_i/a_{i-1}), is 1. Activity ratios different to 1 can be generated by chemical fractionation. Disturbed chains relax back to secular equilibrium by decay of the shorter-lived nuclides. As a general guide, secular equilibrium is reached in about five half-lives of the shorter-lived nuclide, after which $< 3\%$ of the initial excess remains.

First-order observations of young mid-ocean ridge basalts (MORB) show that erupted magmas are not in secular equilibrium. Figure 6.1 shows a global compilation of activity ratios from fresh, unaltered MORB glass measured by mass spectrometry. In general, observed ratios are greater than 1. Activity ratios greater than 1, otherwise known as excesses, reveal that the sample contains more daughter product than decay of the parent nuclide can support. The compilation in figure 6.1 exhibits ^{230}Th excesses between 1 and 1.4, ^{226}Ra excesses ranging from 1 to 4.5, and ^{231}Pa excesses spanning 1.5–3. ^{230}Th/^{238}U correlates negatively with ^{226}Ra/^{230}Th but positively with ^{231}Pa/^{235}U. To generate these excesses requires preferential addition of daughter nuclides to the magma. If it is know where in the magmatic system and by what process these excesses form, uranium-series disequilibria can be used to constrain the duration of melt migration.

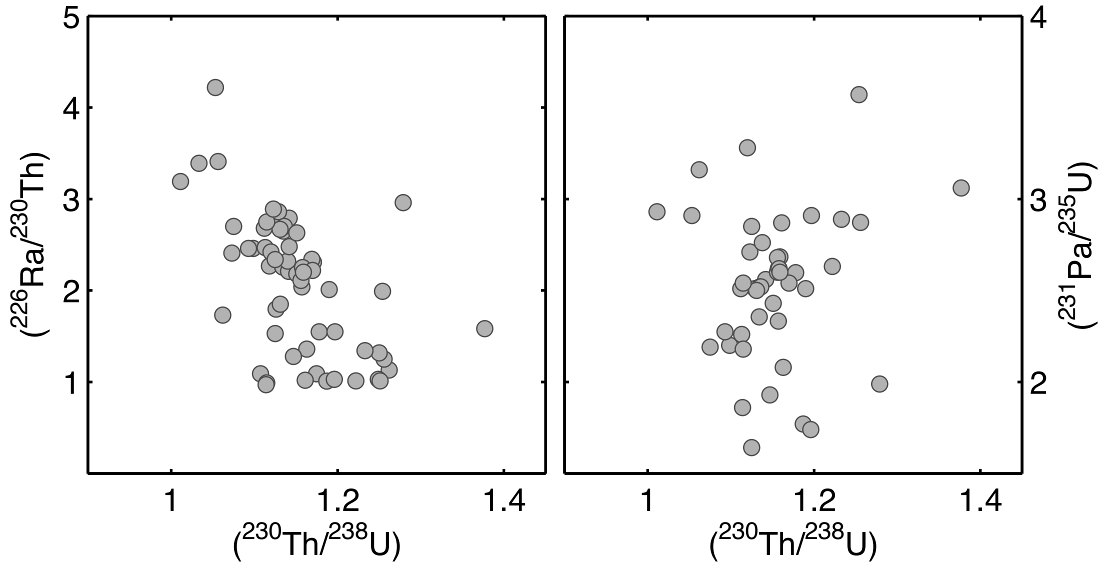

Figure 6.1: (a) Variation of ^{226}Ra/^{230}Th with ^{230}Th/^{238}U. Measurements from the Juan de Fuca ($U_0 = 3$ cm/yr) and Gorda ($U_0 = 2.75$ cm/yr) ridges (Goldstein et al., 1991; Volpe and Goldstein, 1993; Lundstrom et al., 1995; Cooper et al., 2003), East Pacific Rise 9–10°N ($U_0 = 5.5$ cm/yr) (Volpe and Goldstein, 1993; Lundstrom et al., 1999; Sims et al., 2002), Mid-Atlantic Ridge 33°S ($U_0 = 1.8$ cm/yr)(Lundstrom et al., 1998). (b) Variation of ^{231}Pa/^{235}U with ^{230}Th/^{238}U. Locations and references as above with additional data from (Goldstein et al., 1993). All measurements are made using mass spectrometry. Data compiled by Elliott and Spiegelman (2003).

One possible mechanism by which excesses form is mineral–melt partitioning of parent–daughter nuclide pairs; this is generally regarded as the principal mechanism by which excesses are generated. Partition coefficients for U, Th, Ra, and Pa in the mantle are uniformly small, and are comparable in size to estimates of mantle porosity (The MELT Seismic Team, 1998; Prytulak and Elliott, 2009). Daughter nuclides have consistently greater preference for the melt phase than parent nuclides. Thus in regions where the local melt fraction is smaller than the relevant partition coefficients, mineral–melt partitioning will strongly fractionate parent-daughter nuclide pairs. Partition coefficients also vary between mineral phases. For example, mineral–melt partitioning of U is stronger in garnet–facies rocks than spinel–facies lherzolite (Salters and Longhi, 1999; Salters and Stracke, 2004). Consequently, the partitioning behaviour of nuclides in the mantle varies with pressure and mantle heterogeneity.

Much uncertainty surrounds where in the melting region excesses are generated. The most rudimentary constraints on the duration and speed of melt migration can be made by assuming that excesses are generated at the base of the melting region (Condomines et al., 1988). If the source mantle is in secular equilibrium, and between the melt source and ridge axis the initial excess decays, but is otherwise unaltered, then observations of ^{230}Th/^{238}U > 1 in MORB require magma to transit the melting region in less than 350 kyr. For a melting region that stretches 70 km into the mantle, this equates to flow speeds of 0.2 m/yr or greater. To satisfy ^{231}Pa excesses would require melt migration in less than 165 kyr, needing speeds greater than a few decimetres per year. To satisfy ^{226}Ra excesses with this simple model is most demanding, requiring melt migration to occur in less than 8000 years and mean flow speeds greater than a few metres per year. Such great speeds over the whole of the melting region are difficult to reconcile with current theories of magma flow through channels and cracks in the mantle. However, results from models based on these theories are subject to significant uncertainty, which is explored in some detail in section 6.6.

Models that consider the dynamics of melt migration in more detail, however, show that mineral–melt partitioning can contribute to existing excesses between the melt source and the ridge axis (e.g. McKenzie, 1985; Williams and Gill, 1989; Qin, 1993; Spiegelman and Elliott, 1993; Iwamori, 1993, 1994; Richardson and McKenzie, 1994; Lundstrom, 2000; Jull et al., 2002). Elliott and Spiegelman (2003) present an exhaustive review of these models; a subset that illustrate the most important processes are noted below. One important process during melt migration is known as ingrowth, which occurs because the residence time of magma in the melting region is less than that of the solid. During the extra time spent by the solid in the melting region, U-series nuclides in the matrix continue to decay, and the daughters are fractionated into the magma. McKenzie (1985) and Williams and Gill (1989) consider the effects of ingrowth under conditions of diffuse porous flow and show that it can generate ^{230}Th excesses comparable to observed disequilibria. Using a one-dimensional model of magma flow and mantle deformation, Spiegelman and Elliott (1993) further show that nuclides have different residence times, owing to the relative sizes of partition coefficients and mantle porosity. This chromatographic effect can generate significant ^{230}Th excesses in erupted basalts, and enable disequilibria to form in the shallow mantle. Even with this mechanism, however, Spiegelman and Elliott (1993) find it difficult to reconcile ^{226}Ra disequilibria with reasonable flow speeds and mantle structure.

Models that consider the effect of channelized flow on U-series disequilibria generally have more success in satisfying observed ^{226}Ra disequilibria (Iwamori, 1994; Lundstrom, 2000; Jull et al., 2002; Elliott and Spiegelman, 2003). These models suggest that flow speeds within channels are too slow to preserve ^{226}Ra excesses generated at the base of the mantle. However, they generate the observed ^{226}Ra disequilibria by considering the effects of mixing and chromatographic fractionation in the uppermost mantle. Jull et al. (2002) had notable success in predicting the inverse correlation between ^{230}Th and ^{226}Ra excesses. Their model setup simulates of a set of vertically oriented, high porosity channels (with porosity $\phi \approx 1\%$) that are separated by regions of low porosity ($\phi \lesssim 0.1\%$). Magma fed to the top of the model domain through conduits has high ^{230}Th/^{238}U that is generated by partitioning at the base of the melting region and ingrowth. This magma also has negligible ^{226}Ra/^{230}Th because ^{226}Ra excesses decay to secular equilibrium over the time scale of melt migration. Conversely, magma generated at shallow depths in the low porosity, inter-channel regions has negligible ^{230}Th/^{238}U but significant ^{226}Ra/^{230}Th that are maintained by chromatographic fractionation. These magmas form end-members of a mixing array and mix to produce the negative correlation between ^{230}Th and ^{226}Ra excesses.

An alternative explanation of the inverse relationship between ^{226}Ra and ^{230}Th is offered by Stracke et al. (2006), who consider melt–mineral paritioning, melt migration and mixing in the melting region beneath mid-ocean ridges. They suggest that the negative correlation is readily explained by mixing between melts produced at varying lateral distances from the ridge axis, so long as the melts produced closer to the ridge axis are extracted more rapidly. More rapid melt extraction within small lateral distances of the ridge axis may reflect shorter distances between the point of magmagenesis and the ridge axis, or faster magma speeds associated with larger upwelling rates and porosities.

Another process that can fractionate parent–daughter nuclide pairs is diffusive equilibration between rock and magma. Saal and Van Orman (2004) and Van Orman et al. (2006) suggest this process is particularly important in generating large ^{226}Ra disequilibria. They argue that diffusive interaction between magma and plagioclase–bearing cumulates in axial magma chambers will modify the activities and ratios of ^{226}Ra and ^{230}Th in the magma. Van Orman et al. (2006) note that protactinium is tentatively inferred to have a higher diffusivity than U and Th and propose that diffusive interaction in the shallow mantle could have significant consequences for interpretation ^{231}Pa excesses. In a recent contribution to the debate on whether excesses represented by short-lived nuclides originate deep in the melting region, Rubin et al. (2005) suggest that ^{210}Pb excesses observed in MORB, with a 22 year half-life, provide the most demanding constraints on the duration of melt migration. However, Van Orman and Saal (2009) argue that diffusion in crustal cumulates can affect ^{210}Pb excesses, thus they too suffer from the possibility of a shallow origin.

At present, then, ^{230}Th excesses observed in MORB provide the most reliable constraints on the duration and speed of melt migration. Existing theories of melt migration predict magma speeds capable of preserving ^{230}Th excesses generated deep within the melting region (Spiegelman et al., 2001; Spiegelman and Kelemen, 2003; Liang et al., 2010; Hewitt, 2010; Hesse et al., 2011; Weatherley and Katz, 2012; Katz and Weatherley, 2012), but none of the existing studies are quantified in terms of the duration of melt migration. Only one study by Elliott and Spiegelman (2003), who use an extension of the model by Spiegelman et al. (2001), attempt to quantify these models in terms of U-series disequilibria. With the exception of Weatherley and Katz (2012) and Katz and Weatherley (2012) these models consider magma flow in an upwelling column of chemically homogenous mantle. The previous chapters show that mantle heterogeneity and plate spreading have drastic consequences for the dynamics of magma flow, but their implications for the speed and duration of melt migration remain unquantified.

In this study I use the model presented in the previous chapter to explore the consequences of mantle heterogeneity for the speed and duration of melt migration beneath mid-ocean ridges. Experiments are conducted with the random blob and smoothed noise heterogeneity models outlined in chapter 5, with no mantle heterogeneity, and with various spreading rates. To assess whether the model provides a plausible description of the time scales of melt migration, the results are then cast in terms of ^{230}Th disequilibria. For the first time, modelled excesses are directly compared with the speed and duration of melt migration predicted by a physically consistent model of magma flow.

The remainder of this chapter is as follows. Section 6.2 outlines modifications made to the model described in chapter 5 that are necessary to determine the predicted durations and speeds of melt migration. Section 6.3 presents results from the numerical experiments. In section 6.4 the results are interpreted in the context of the dynamics of melt migration. Section 6.5 outlines a simple model to convert the results into ^{230}Th disequilibria and compares the model results against observed ^{230}Th excesses. The chapter is concluded in section 6.7.

6.2 Model setup

The situation considered is that of melt migration and mantle deformation beneath diverging lithospheric plates figure 5.1. The dynamics of coupled magma flow and mantle deformation in this setting are investigated using the model and approach set out in section 5.2 of the previous chapter. Several enhancements to the model are made to meet the aims of this study; these are outlined below.

To determine the speed and duration of melt migration predicted by the model, the domain is seeded with lagrangian particles that track the motion of individual fluid parcels. In subsolidus portions of the domain, the motion of the tracer particles is defined by the velocity field of the matrix ($\mathbf{v}_m$); in partially molten regions it is defined by the velocity field of the liquid magma ($\mathbf{v}_f$). The fluid velocity is computed diagnostically from equation 2.3 and is given by

$$\mathbf{v}_f = \mathbf{v}_m - \frac{K}{\mu} \left[\boldsymbol{\nabla} \left(\mathcal{P} + P^* \right) + \Delta\rho \mathbf{g} \right], \tag{6.1}$$

where K is permeability, μ is the viscosity of the magma and ϕ is porosity, $\Delta\rho = \rho_m - \rho_f$ is the density difference between the matrix and magma, g is the acceleration due to gravity and z is depth. Equation 6.1 states that the velocity of the magma depends on the matrix velocity, dynamic pressure gradients, and buoyancy forces that are modulated by permeability and the viscosity of the magma. The tracer particles are defined to be perfectly incompatible. They are released from the solid at the onset of melting, can be re-incorporated into the solid by freezing, and can exit the domain at the ridge axis. Accuracy in determining the motion of the tracers is ensured by updating their position at each time step in a two stage process. For each particle the velocity field is first recomputed at the corners of the host grid cell, and is then linearly interpolated to the particle's position. Using the interpolated velocity, the position of the particle is updated over one half of a time step. The process is then repeated and the tracer particles are moved over the remaining half of the time step.

The tracer particles are initialized by placing one in the centre of every grid cell. As the particles move through the domain they build a detailed history of their motion; they record at every time step: their velocity, position, the porosity and composition of the matrix within their host grid cell, and the model time. Those that exit the domain at the ridge axis are filtered to exclude any that (i) are not initialized in subsolidus mantle for which the degree of melting is zero, and (ii) are refrozen into the matrix between the melt source and the ridge axis. Data from particles that pass through this filter are used to compute the duration and speed of melt migration. The suite of tracer particles is reinitialized approximately every 350 kyr to maintain even sampling across the entire width of the melting region.

6.3 Results

6.3.1 Duration and distance of melt migration

Three suites of numerical experiments are used to investigate the duration of melt migration and to constrain the distance tracer particles travel between the melt source and ridge axis. Each suite of experiments comprises four simulations. Each simulation within a suite is run with a half spreading rate U_0 of 2, 4, 6, or 8 cm/yr and an identical of mantle heterogeneity. The mantle for one suite of experiments is homogenous, another is initialized with the random blob heterogeneity model described in section 5.2.3 (figure 5.2a), and the other is initialized with the smoothed noise heterogeneity model (figure 5.2b). Compositional variation perturbs the solidus temperature by -50°C in the random blob case, and up to ± 50°C in the smoothed noise cases. The experimental setup and initial conditions are identical to experiments in the previous chapter. Parameter values are specified in table 5.2, and these values are maintained for all experiments presented in this chapter.

Figure 6.2 plots the time taken for tracer particles to travel from the base of the melting region to the ridge axis as a function of the distance that they travel. The duration of melt migration for any tracer particle is also referred to hereafter as the travel time, τ, and the distance travelled by tracer particles is also referred to as the path length d. They are defined as

$$\tau = t_{\mathrm{exit}} - t_{\mathrm{release}}, \tag{6.2}$$

$$d = \int_{t_{\mathrm{release}}}^{t_{\mathrm{exit}}} \left[u\left(t\right)^2 + w\left(t\right)^2\right]^{1/2} \mathrm{d}t, \tag{6.3}$$

where t_{release} is the time at which a particle is released from the solid by melting, t_{exit} is the time at which the same particle exits the melting region at the ridge axis, and u and w are the horizontal and vertical components of the magma velocity.

Figure 6.2a shows results from experiments run with a homogeneous mantle. In these experiments magma flow is not channelized; the dynamical behaviour is illus-

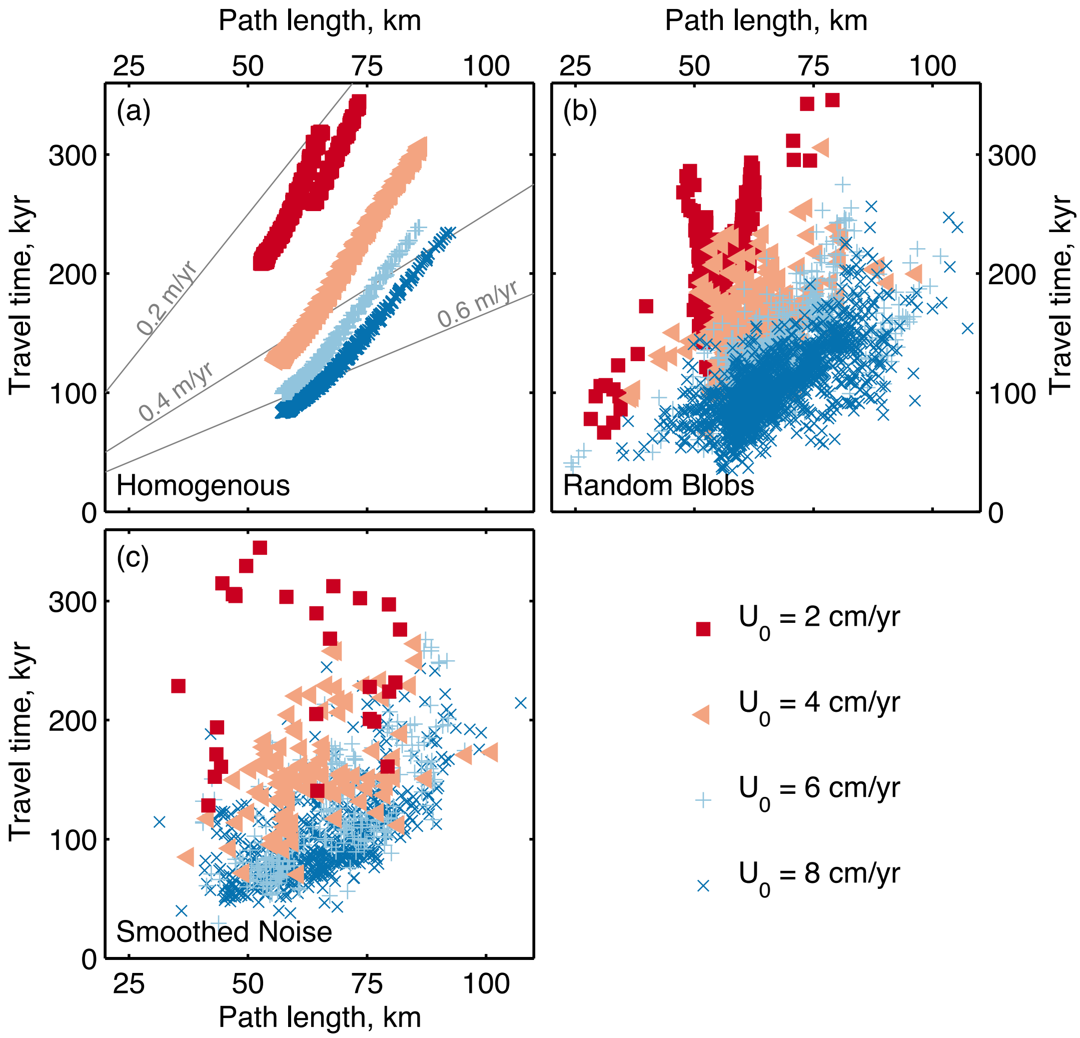

Figure 6.2: Travel time for individual particles plotted as a function of path length for half-spreading rates of 2, 4, 6, and 8 cm/yr. Figure (a) shows data from experiments run in a homogenous mantle. Grey lines correspond to the magma flow speeds indicated. (b) shows data from simulations where the heterogeneity is manifested as random blobs, and (c) plots data from simulations run with smoothed noise heterogeneity.

trated in figure 5.3 and detailed in section 5.3. Results in figure 6.2a show that the travel time increases linearly with the path length and is shorter when the spreading rate is fast. Path lengths range from $50 - 75$ km when $U_0 = 2$ cm/yr to $55 - 95$ km when $U_0 = 8$ cm/yr. For each experiment the range of travel times is approximately 150 kyr, and decreases from $200 - 350$ kyr when $U_0 = 2$ cm/yr to $90 - 240$ kyr when $U_0 = 8$ cm/yr. The arrays of data are more densely populated with tracer particles representing shorter path lengths and travel times.

Figures 6.2b and 6.2c show results from experiments run with the random blob and smoothed noise heterogeneity models. Magma flow in these experiments is channelized, and the dynamical behaviour is illustrated in figures 5.4 and 5.5. To first order these data show the same trends as experiments conducted with a homogenous mantle (figure 6.2a); the travel time increases with path length and decreases with spreading rate. However, the data in figures 6.2b–c exhibit much scatter and the degree of correlation between path length and travel time is poorer. Compared to results from the homogenous case, the data span a wider range of travel times and path lengths. For a half spreading rate of 2 cm/yr, travel times range from approximately $50-350$ kyr and path lengths span $25-80$ km; for $U_0 = 8$ cm/yr travel times span $25-300$ kyr and path lengths range between 25 km and 110 km. The arrays of data in figures 6.2b–c are more densely populated for intermediate path lengths and travel times. Compared to magma flow in a homogenous mantle, the duration of melt migration for a given path length and spreading rate is approximately $10-20\%$ shorter in the heterogeneous cases.

6.3.2 Speed

Figure 6.3 shows normalized histograms of the mean particle speed for each of the numerical experiments presented in figure 6.2. The mean speed for particle p is defined as $\langle v_p \rangle = \tau_p/d_p$, where τ_p and d_p are the travel time and path length defined in equations 6.2 and 6.3. Figures 6.3a–d show data from experiments run with a homogenous mantle and spreading rates U_0 of 2, 4, 6, and 8 cm/yr respectively. These histograms have a strong negative skew, showing that particles with the fastest speeds are most abundant. Reference to figure 6.2a demonstrates that the fastest particles are generally associated with shorter travel times and path lengths. The mode of the binned data increases with spreading rate from $0.20-0.25$ m/yr at $U_0 = 2$ cm/yr to $0.65-0.70$ m/yr when $U_0 = 8$ cm/yr. The range of mean particle speeds also increases with spreading rate from 10 cm/yr when $U_0 = 2$ cm/yr to 35 cm/yr when $U_0 = 8$ cm/yr.

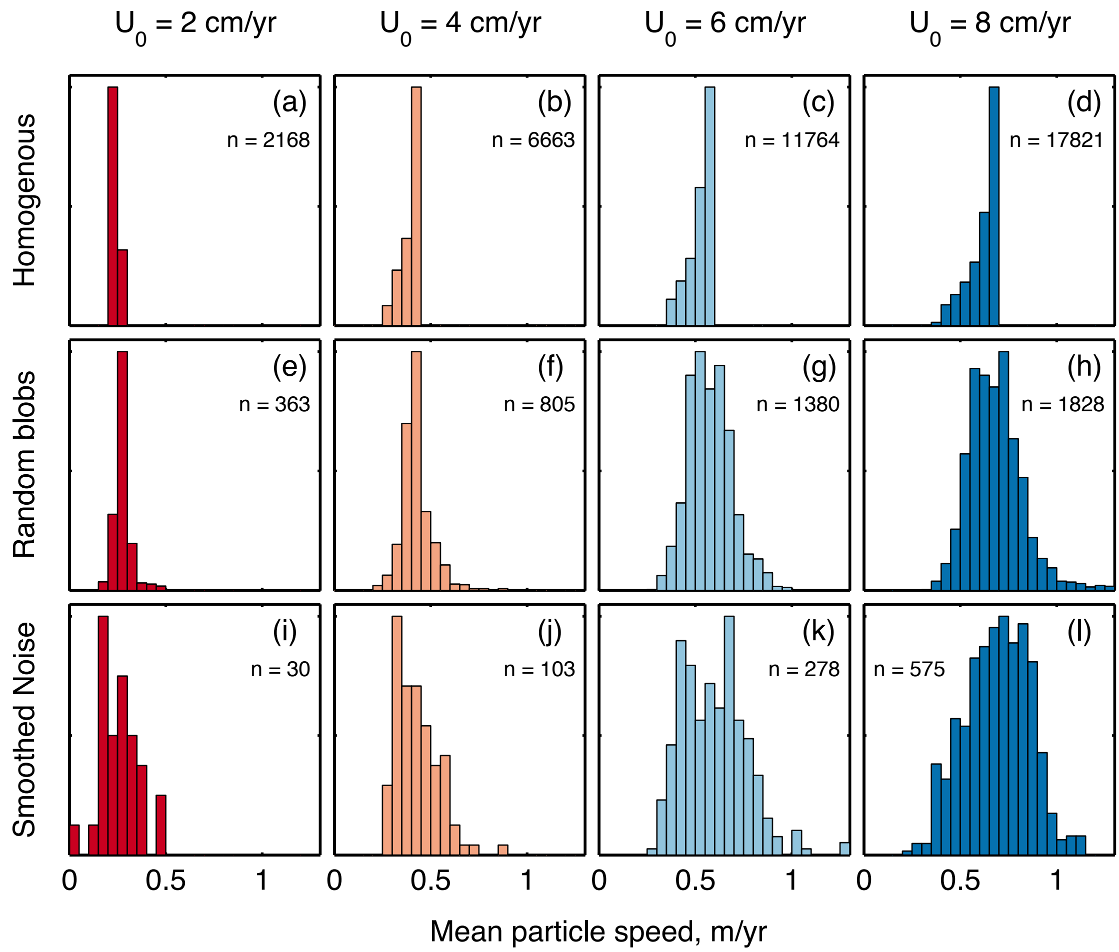

Figure 6.3: Normalized histograms showing the local mean speeds of particles. Each column shows results from simulations with the same half-spreading rate and each row presents data from simulations with different styles of heterogeneity as the initial condition. Bin widths are 5 cm/yr.

Results in figures 6.3e–h and 6.3i–l correspond to experiments run with the random blob and smoothed noise heterogeneity models respectively. These histograms have roughly negligible skew and approximately show a factor of 2 increase on the range of mean particle speeds predicted by experiments run with no mantle heterogeneity. Figures 6.3e–l indicate that the mean particle speeds range from $0 - 0.6$ m/yr when $U_0 = 2$ cm/yr to $0.15 - 1.3$ m/yr when $U_0 = 8$ cm/yr. In general, histograms for the smoothed noise cases have a more irregular structure than for those corresponding to experiments run with the random blob heterogeneity model. However, the mode of the binned mean particle speeds is approximately independent of the presence or topology of mantle heterogeneity.

6.3.3 Effect of composition

Figure 6.4 illustrates the effect of composition on the duration and speed of melt migration. Data are taken from experiments run with the smoothed noise heterogeneity model only. Composition is expressed as a perturbation to the solidus temperature $\Delta T_C = M_S\,(C_m - C_0)$, where M_S is the slope $\partial T/\partial C$ of the solidus, C_m is the composition of the solid. In the smoothed noise cases, C_0 is the average composition of mantle rock. The source composition at the onset of melting is denoted $\Delta T_{C,0}$.

Figure 6.4a shows that the path length correlates negatively with $\Delta T_{C,0}$. This negative correlation is a consequence of more fusible rocks (more negative $\Delta T_{C,0}$) melting at deeper depths. However, the combined effects of the shape of the melting region, channelized flow, and mantle heterogeneity mean that a range of path lengths can be associated with any given source composition. Data are distributed relatively evenly across source compositions between $-20°\text{C} \leq \Delta T_C \leq 20°\text{C}$ but are less abundant for more extreme values. Figure 6.4b reveals that, to the first order, the travel time also negatively correlates with the source composition, although the degree of correlation is poor.

Figure 6.4c reveals a clustering of high mean speeds (> 0.5 m/yr) at intermediate compositions $-20°\text{C} \leq \Delta T_{C,0} \leq 20°\text{C}$. Mean speeds are generally slower and span a smaller range for more extreme values of $\Delta T_{C,0}$.

To complement these data, the instantaneous speed and composition for each particle were sampled at a frequency of about 1000 years. These results are shown in figure 6.4d and exhibit negligible correlation between speed and composition along trajectories of tracer particles. Instead, the greatest range and fastest speeds are observed in regions where mantle heterogeneity perturbs the solidus temperature between $-15°$C and $+10°$C. In these regions, instantaneous speeds can reach up to 30 m/yr, but are often as low as a few decimetres per year. For more extreme compositions the range and magnitude of instantaneous speeds is much reduced. In these regions the maximum magma speeds are around 2 m/yr, but the vast majority of tracers passing through more highly enriched and depleted regions have speeds of a

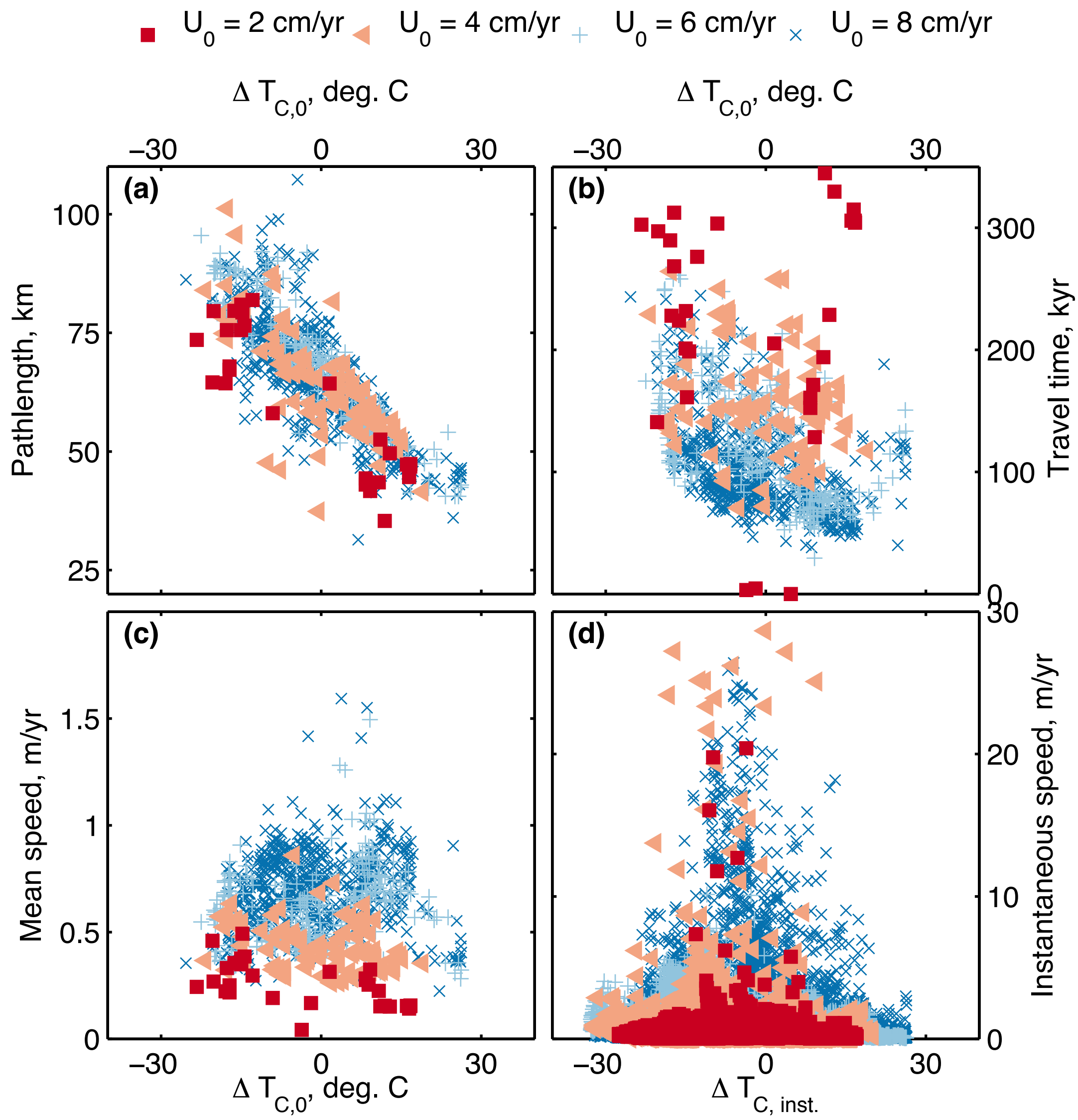

Figure 6.4: Effect of composition on the time scale and speed of melt migration for experiments run with the smoothed noise heterogeneity model. (a) Variation of travel time with source composition $\Delta T_{C,0}$, (b) path length as a function of source composition, (c) mean particle speed as a function of source composition, (d) variation of the instantaneous speed with instantaneous composition, $\Delta T_{C,\text{inst.}}$, expressed in terms of a perturbation in solidus temperature. The sampling frequency is approximately 1000 years.

few centimetres to a few tens of centimetres per year.

6.4 Interpretation

The fundamental behaviour of magma flow predicted by the experiments is defined by those conducted with no mantle heterogeneity. Figure 6.5, a condensed version of figure 5.3 from the previous chapter, illustrates certain aspects of the predicted structure and dynamics of the mantle beneath a ridge axis. Dashed lines in figure 6.5a show trajectories of representative tracer particles released at the base of the melting region. They show that the path length is shortest for particles released directly beneath the ridge and longest for those released farthest from the axis of spreading; the increase in path length with distance from the axis of spreading is regular and systematic. Figures 6.5a and 6.5b show that the tracer particles travelling to the ridge axis along the longest paths migrate with slower speeds through lower porosity mantle. Conversely, those released directly beneath the ridge axis travel with a high mean speed through more porous mantle. This relationship is manifested as the strong correlation between travel time and path length in figure 6.2.

In the present theoretical framework the pattern of porosity and magma speed beneath the ridge axis are ultimately a consequence of the thermal and upwelling regime (figure 6.5c) established by plate-spreading. Equation A.16 from Appendix A shows that in one dimension and steady state, the magma speed scales with $W^{1-1/n}$, where W is the upwelling rate of the matrix and n is the permeability exponent (equation 2.10). For mantle convection patterns that resemble corner flow, a useful scaling between the half spreading rate and a reference upwelling rate W_0 is $W_0 = 3/2U_0$ (Batchelor, 1967), thus $w \approx (3/2 \cdot U_0)^{1-1/n}$. Figure 6.6 shows that this approximation for w scales the results presented in figure 6.2a. The scaled data reveal that tracer particles associated with short path lengths ($\leq$ 65 km) in the experiment assigned $U_0 = 2$ cm/yr travel to the ridge with anomalously slow speeds. Results from the suite of experiments reveal that the slower magma speeds at $U_0 = 2$ cm/yr are caused by the cooler thermal regime, which suppresses melting and porosity generation in

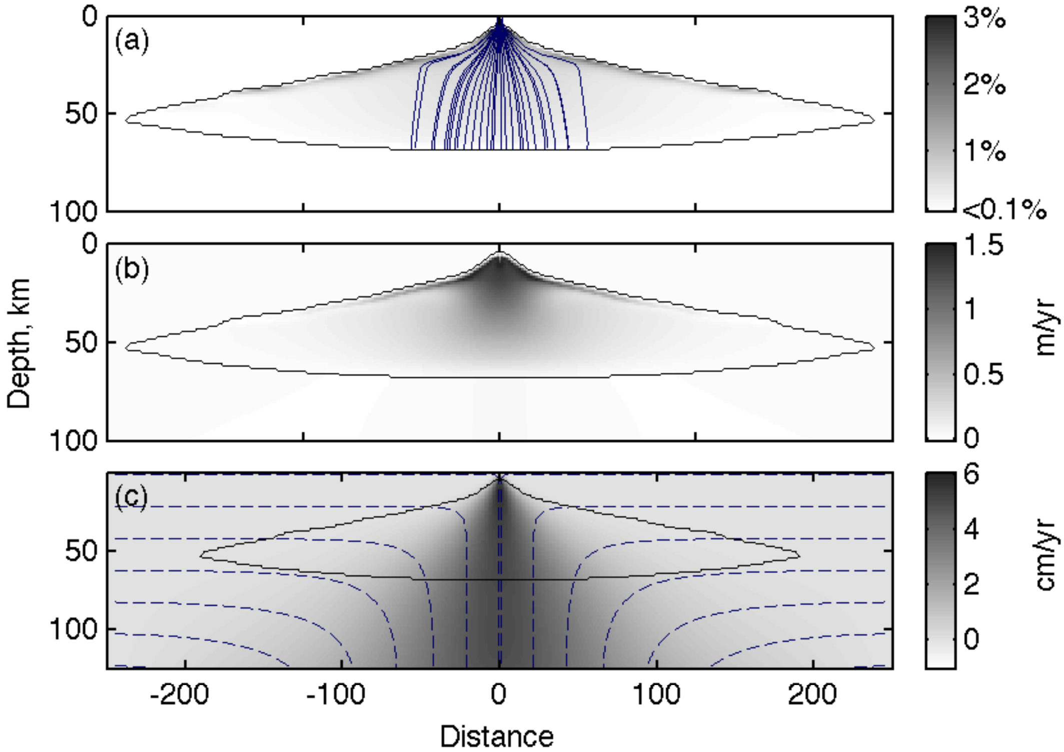

Figure 6.5: Snapshots from an experiment conducted with no mantle heterogeneity and $U_0 = 4$ cm/yr after a model time of 2 Ma. Black solid lines in all panels contour the solidus. (a) Color shows porosity, blue lines show trajectories of randomly selected tracers that migrate from the base of the melting region to the ridge axis. (b) Magma speed $|\mathbf{v}_f|$. (c) Upwelling rate of the matrix $-\mathbf{v}_m \cdot \hat{\mathbf{k}}$. Dashed lines show the flow pattern of the matrix.

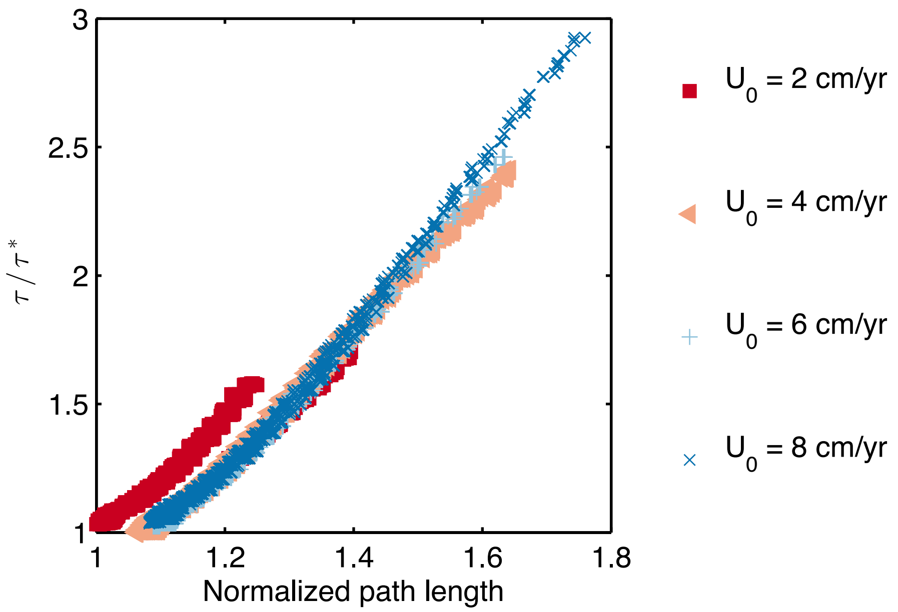

Figure 6.6: Scaled travel time versus nondimensional distance for the experiments conducted with no mantle heterogeneity. Travel time τ is scaled by $\tau^* = (3/2U_0)^{1-1/n}/l$, where l is a characteristic length scale.

the shallower portions of the melting region. The pattern of upwelling illustrated by figure 6.5c defines the rate at which tracers particles enter the melting region. Since the upwelling rate is greatest directly beneath the ridge axis, the tracers associated with the shortest path lengths and fastest speeds are most abundant in the population of erupted particles.

Results from the heterogeneous cases show that mantle heterogeneity has significant consequences for the dynamics of melt migration. In the melting region, heterogeneity continually changes in response to mantle deformation, melting, and magma flow; its effect on each tracer particle is unique.

To help elucidate how heterogeneity affects melt migration, figure 6.7 plots the spatial covariation of mantle heterogeneity with porosity for a representative experiment. The results shown are from an experiment run with the smoothed-noise heterogeneity and $U_0 = 6$ cm/yr. Black lines in panels a and c contour porosities greater than 1%. They roughly indicate the location of melt channels and magma ponds. In this experiment, channels are generally confined to distances within 100 km from the axis of spreading and depths shallower than 60 km. The channels accommodate the fastest magma speeds (figure 6.7d) and broadly coincide with heterogeneities of intermediate fusibility ($-15°\text{C} \leq \Delta T_C \leq +10°\text{C}$, figures 6.7b–c); in regions of more extreme composition, magma speeds are slower.

This complex relationship between composition and magma speed is a consequence of the energetics of melting. At any location within the melting region, heat diffuses away from the most depleted regions into the surrounding cooler and more fusible mantle. In the most depleted regions ($\Delta T_C \geq 10°\text{C}$), therefore, melting is suppressed, porosity is destroyed by compaction, and the resulting small permeabilities accommodate slow magma speeds. Flow speeds are slow in the most enriched regions ($\Delta T_C \leq -15°\text{C}$) for a different reason. The most fusible heterogeneities start to melt earlier than the surrounding mantle and are surrounded by a halo of impermeable rock. The halo prevents tracer particles from flowing into the channel network, and causes the magma speed $|\mathbf{v}_f|$ within the heterogeneity to approximate the speed of the matrix $|\mathbf{v}_m|$. Several examples of this situation are evident in figures 5.4 and 6.7. This relationship between thermodynamics and magma speed also causes tracers released from the most enriched and depleted rocks to have lower mean speeds relative to those released from rocks of intermediate composition.

A surprising feature of the results above is the apparent insensitivity of the duration, distance, and speed of melt migration to the topology of mantle heterogeneity (figures 6.2b–c, 6.3e–l). Figure 6.7 demonstrates that in the smoothed noise cases, tracer particles are released over all depths between those at which the most and least fusible compositions melt. In the random blob case, it might be expected that tracers are released from either the depth at which mantle of composition $\Delta T_{C,0} = 0°\text{C}$ melts, or the depth at which the most enriched compositions melt. However, assimilation of the ambient mantle by upwards-percolating magmas produced by melting of the enriched heterogeneities releases tracer particles over a wide range of depths. Similarly, heat diffusion into enriched heterogeneities can delay melting of the surrounding mantle to shallow depths, resulting in short path lengths. The consequence of these thermodynamic processes is a similar range of possible path lengths for both models

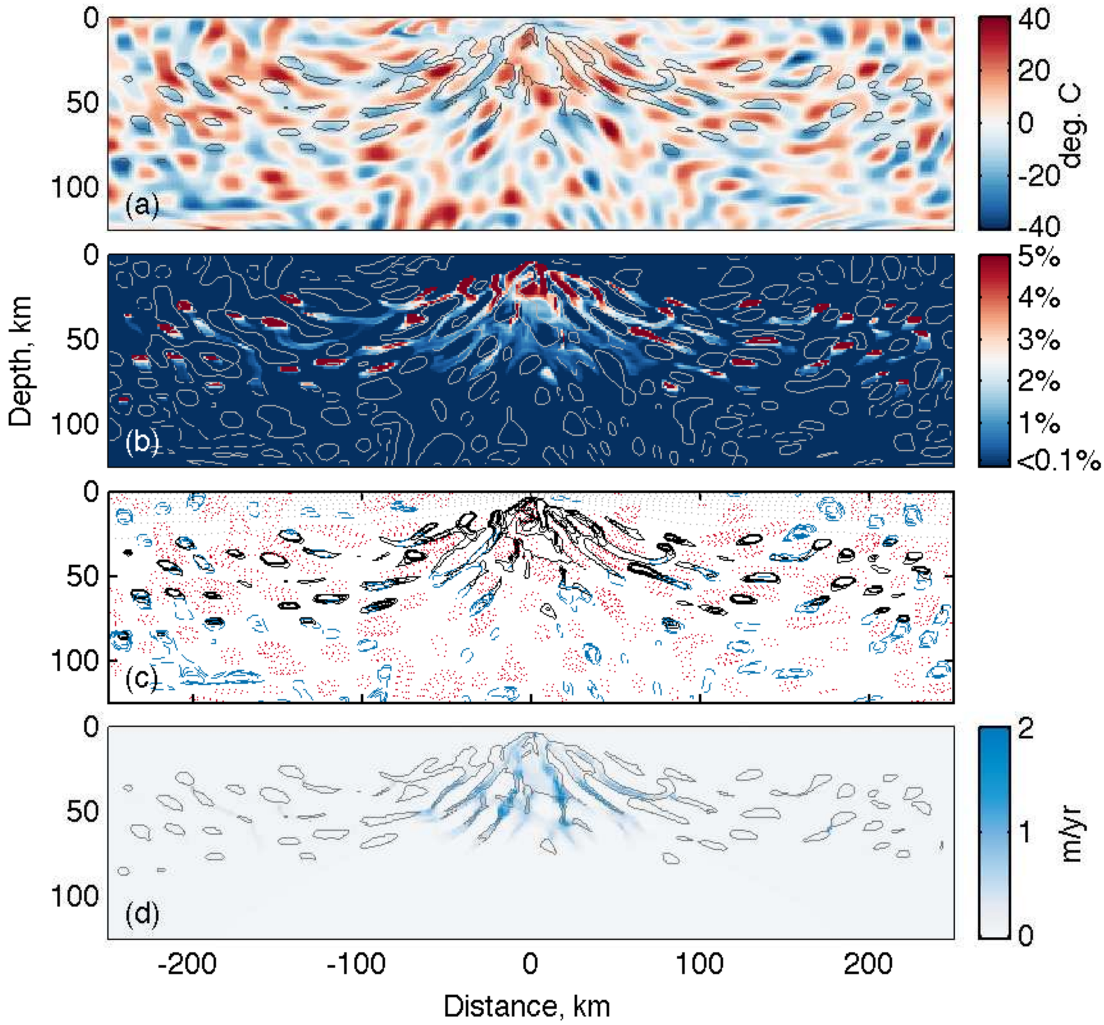

Figure 6.7: Covariation of porosity and composition from a representative experiment initialized with the smoothed noise heterogeneity model and $U_0 = 6$ cm/yr. (a) Colours show composition in terms of a perturbation to the solidus temperature, black lines contour $\phi = 1\%$. (b) Colour shows porosity, grey dashed lines contour $\Delta T_C = -15°$C, grey solid lines contour $\Delta T_C = +10°$C. (c) Covariation of large porosities and regions of enriched and depleted mantle. Black lines contour $\phi = 1\%$, blue solid lines contour $\Delta T_C \leq -15°$C in 5°C intervals, and red dashed lines contour $\Delta T_C \geq +10°$C in 5°C intervals. (d) Magma speed $|\mathbf{v}_f|$ with grey lines showing the 1% porosity contour.

of mantle heterogeneity.

6.5 Comparison with global ^{230}Th excesses

6.5.1 Model description

To assess whether the model constitutes a plausible description of the duration of melt migration beneath mid-ocean ridges, the results (section 6.3) are converted into ^{230}Th disequilibria and compared against global observations. ^{226}Ra and ^{231}Pa excesses are not considered because they suffer from the possibility of a shallow origin (Jull et al., 2002; Saal and Van Orman, 2004; Van Orman et al., 2006).

The approach of the model outlined here is not based on computing the concentrations of U-series nuclides within the melting region. Consequently, it is not possible to interpret the results in terms of the mean composition, or activity, of the mixed melts erupted at the ridge axis. Instead, the model computes ^{230}Th disequilibria, by assuming that equilibrium partitioning generates an initial excess for each tracer particle at the instant of its release from the solid by melting. Between the source and the ridge axis each particle behaves as a closed system: the excess decays and is not modified by any other process. At the ridge axis the activity ratios are not mixed, but could instead be interpreted as points that define a mixing array.

The unmolten source is defined to be in secular equilibrium prior to the onset of melting. In general, the model rock contains N mineral phases. Each phase occupies a mass fraction X_i and has an equilibrium mineral–melt partition coefficient D_i. In the time step that a given particle is released from the solid, the bulk activity ratio in its host grid cell is

$$\left(\frac{^{230}\mathrm{Th}}{^{238}\mathrm{U}}\right)_{\mathrm{bulk}} = 1 = \frac{\left(\sum_{i=1}^{N} X_i D_i^{\mathrm{Th}} + X_{\mathrm{f}}\right)(^{230}\mathrm{Th})_{\mathrm{f}}}{\left(\sum_{i=1}^{N} X_i D_i^{\mathrm{U}} + X_{\mathrm{f}}\right)(^{238}\mathrm{U})_{\mathrm{f}}}, \tag{6.4}$$

where X_f is the mass fraction of the melt present within the grid cell, D_i^{U} and D_i^{Th} are the partition coefficients for U and Th respectively within mineral phase i, and $(^{238}\mathrm{U})_{\mathrm{f}}$

and $(^{230}\mathrm{Th})_\mathrm{f}$ are their activities in the magma. Making the judicious approximation that $X_f = \phi$ and rearranging yields the initial activity ratio of the magma:

$$\left(\frac{^{230}\mathrm{Th}}{^{238}\mathrm{U}}\right)_\mathrm{f} = \frac{(1-\phi)\,D_\mathrm{U} + \phi}{(1-\phi)\,D_\mathrm{Th} + \phi}, \tag{6.5}$$

where D_Th and D_U are the bulk partition coefficients for Th and U. Equation 6.5 is used to assign an initial activity ratio to each tracer particle on its release from the solid. It shows that mineral–melt partitioning can generate activity ratios different to 1 if the melt fraction X_f is smaller than the partition coefficients. Debate exists whether magma can segregate from mantle rock at all porosities (Wark, 2003), or whether the porosity must reach a threshold value for pores to become interconnected (Faul, 2001). This model assumes the former, in keeping with geological observations by Wark (2003). Consequently the potential exists for large initial excesses to form if the porosity at the onset of melting is very small. Analysis of data from the tracers reveals no systematic dependence between the size of the time step and the porosity at the onset of melting.

Table 6.1 outlines the partition coefficient and mineralogical structure of the mantle used for this study. It defines the garnet–spinel transition to occur at a depth of 80 km. At shallower depths, calcium resulting from garnet breakdown is accommodated in high-Ca clinopyroxene, which has slightly different partition coefficients to the low-Ca clinopyroxene present in the garnet zone. In Earth's mantle, compositional heterogeneity is the result of changes in the relative proportions of mineral phases, and associated with it is variation of the bulk partition coefficients for the U-series nuclides. Specifically, the bulk partition coefficients will be higher for more fusible heteroegeneities. However, to aid interpretation of the model results presented here, the mineral proportions listed in Table 6.1 are assumed constant and do not vary with the fusibility of the model mantle rocks. As the tracers particles migrate to the ridge axis, the initial excesses decay in a closed system; ingrowth and diffusive effects are neglected entirely. For a decay chain of length n, the temporal evolution of activities

Table 6.1: Preferred partition coefficient values

	ol	opx	Low Ca cpx	High Ca cpx	grt	sp
U	3.8×10^{-4}	2×10^{-3}	1.13×10^{-2}	9.4×10^{-3}	2.8×10^{-2}	0
Th	5×10^{-5}	2×10^{-3}	5.7×10^{-3}	5.9×10^{-3}	9×10^{-3}	0
Modal Composition						
$z > 80$ km	0.53	0.08	0.34	0	0.05	0
$z \leq 80$ km	0.53	0.26	0	0.18	0	0.03
Bulk Partition Coefficients						
		U	Th			
$z > 80$ km		5.6×10^{-3}	2.6×10^{-3}			
$z \leq 80$ km		2.4×10^{-3}	1.6×10^{-3}			

Partition coefficients from Salters and Longhi (1999); Salters et al. (2002); Salters and Stracke (2004), modal compositions from Stracke et al. (2006). Mineral abbreviations: (ol) olivine, (opx) orthopyroxene, (cpx) clinopyroxene, (grt) garnet, (sp) spinel.

is

$$\frac{d}{dt}\begin{bmatrix} a_1 \\ a_2 \end{bmatrix} = \begin{bmatrix} - & \lambda_1 & & \\ & \lambda_2 & - & \lambda_2 \end{bmatrix}\begin{bmatrix} a_1 \\ a_2 \end{bmatrix}, \tag{6.6}$$

or, more compactly

$$\frac{d\mathbf{a}}{dt} = L\mathbf{a}. \tag{6.7}$$

Elliott and Spiegelman (2003) note that equation 6.7 can be solved analytically as

$$\mathbf{a}\,(t) = A \exp\left(\Lambda t\right) A^{-1}\mathbf{a}_0 \tag{6.8}$$

where A is the matrix of eigenvectors of L, Λ is a diagonal matrix of the eigenvalues of L.

6.5.2 Modelled and observed ^{230}Th excesses

Figure 6.8 compares the ^{230}Th disequilibria computed from results of the experiments against the global dataset of observations presented in figure 6.1. Excesses corresponding to experiments conducted with no mantle heterogeneity do not compare well against the observed data. The range of excesses modelled by the experiments run without mantle heterogeneity spans less than 50% of the range observed in MORB. The poor comparison shows that the magma speeds predicted by the models run without mantle heterogeneity are too slow to preserve the ^{230}Th disequilibria observed in MORB.

Figures 6.8b–c show that results from the heterogeneous cases compare better against the observed disequilibria. Excesses corresponding to experiments conducted with $U_0 \geq 4$ cm/yr approximately span the full range of observed disequilibria. Figure 6.9 demonstrates that very small source porosities do not generate any bias towards large erupted excesses. Hence the largest disequilibria correspond to tracers that migrate to the ridge axis quickly. That the observed and modelled excesses is comparable suggests that the models run with mantle heterogeneity predict a plausible range of magma flow speeds and durations of melt migration.

One discrepancy between the modelled and observed excesses is that the range of modelled disequilibria increases with spreading rate whilst the range of observed excesses shows no meaningful variation with spreading rate. The lack of correlation between observed excesses and spreading rate is, perhaps, one of the more surprising observations from studies of U-series disequilibria in MORB. Most theories of melt migration suggest that mantle permeabilities and magma speeds are higher beneath fast spreading ridges; the geochemical consequence being a positive correlation between ^{230}Th disequilibria and spreading rate. Indeed, this is true of the results presented here. However, the model used in this study does not consider the effect of ingrowth on U-series disequilibria. Elliott and Spiegelman (2003) note that the degree of disequilibrium produced during ingrowth depends inversely on the upwelling rate. It is reasonable to expect, therefore, that if the present model did consider the effects of ingrowth, the variation in the range of modelled excesses with spreading rate would be weaker than currently predicted.

An important point, however, is that the variation of the range of modelled excesses contains important information about how the dynamics of magma flow change with the spreading rate. This motivates the question whether variation in the range of observed excesses between spreading centres reflects local and regional differences in the dynamics of melt migration. For example, a narrow range of excesses could indicate similarity in the duration, speed and distance of melt migration, or efficient

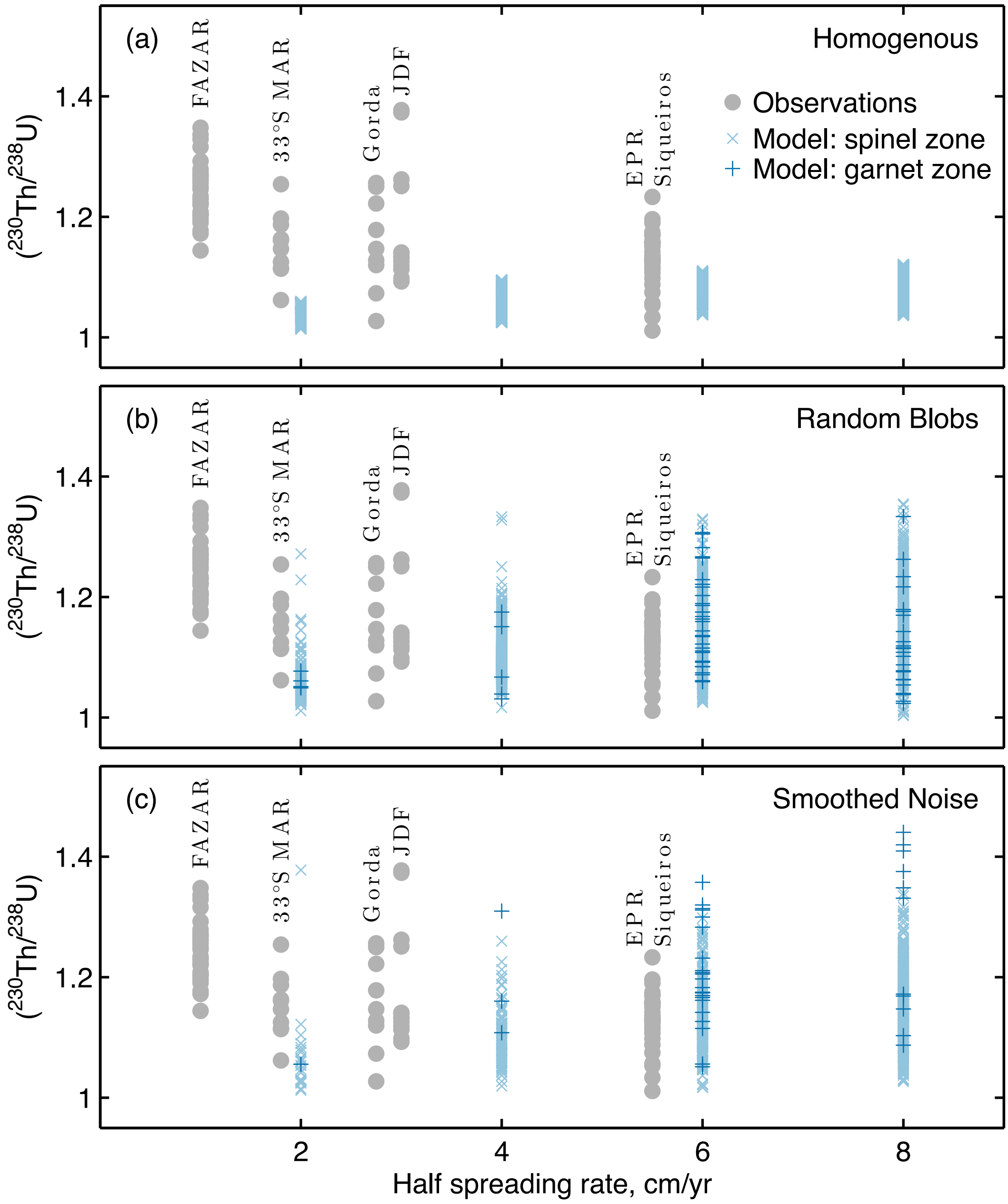

Figure 6.8: Variation in predicted and observed ^{230}Th excesses with spreading rate. (a) Results from experiments run with no mantle heterogeneity. (b) Results from experiments run with the random blob heterogeneity. (c) Results from experiments conducted with the smoothed noise heterogeneity. Grey circles show observations, light blue crosses show modelled excesses for tracers that originate in the spinel zone, dark blue plus signs show modelled excesses for tracers that originate in the garnet zone. Observed excesses are taken from the dataset plotted and referenced in figure 6.1. Abbreviations are as follows: FAZAR, Azores Platform; MAR, Mid-Atlantic Ridge; JDF, Juan de Fuca Ridge; EPR, East Pacific Rise $9 - 11$°N.

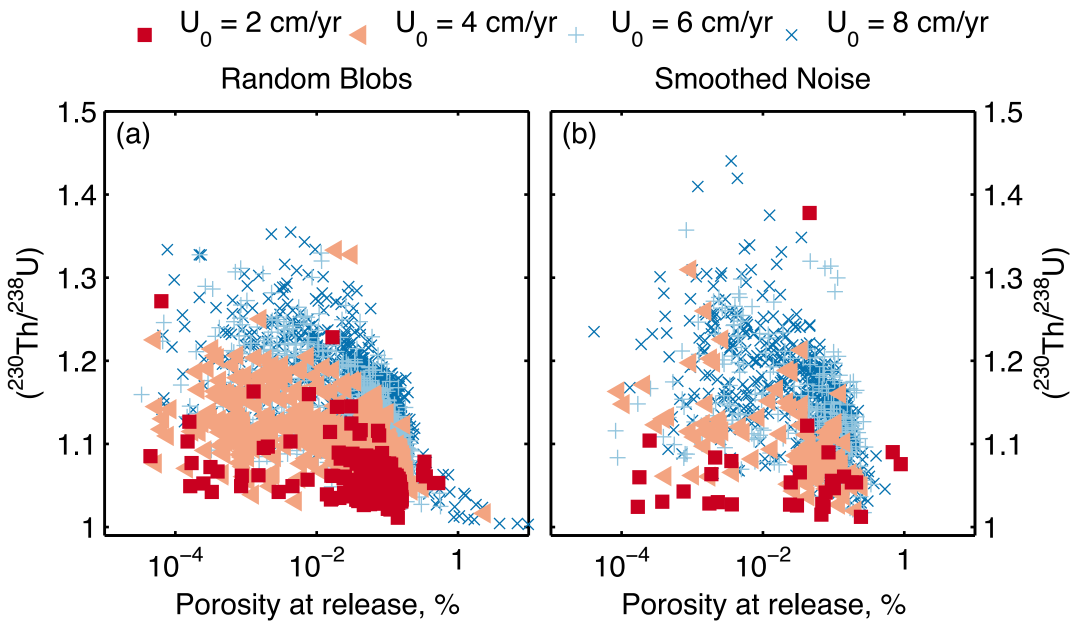

Figure 6.9: Variation of the decayed excesses for the erupted tracers with the porosity at the points from which the tracers are released. (a) Results from experiments run with the random blob heterogeneity. (b) Results from experiments run with the smoothed noise heterogeneity.

mixing beneath the ridge axis. Conversely, a wide range might point to less efficient mixing or large differences in the speed and duration of melt migration. A major challenge lies in distinguishing between the different processes that can generate and modify excesses and their effect on observed disequilibria. To address this challenge, future studies would benefit from interpretation of major and trace element geochemistry alongside U-series disequilibria.

6.6 Discussion and limitations

The results above show that the magma speeds predicted by experiments run with mantle heterogeneity are sufficiently fast to preserve in erupted magmas ^{230}Th excesses generated at the base of the melting region. Some tracer particles migrate to the ridge axis quickly enough to preserve ^{231}Pa disequilibria generated deep in the mantle; but without exception, the predicted travel times are too long to preserve ^{226}Ra excesses that form at the base of the melting region. These results are unique to the parameter regime that the models are run under. To determine how the results may differ under parameter regimes other than the preferred regime prescribed in table 5.2 requires a systematic study. However, a preliminary assessment can be made using scaling arguments.

Parameters of particular importance to the results above are those that directly affect the magma velocity (equation 6.1). Application of the scales presented in section 2.6 to equation 6.1 reveals that the magma velocity is nondimensionalized by the factor $\mathcal{R} = k_0 \Delta\rho g/\mu$, where k_0 is the reference permeability, $\Delta\rho$ is the density difference between the matrix and magma, g is the acceleration due to gravity, and μ is the viscosity of the magma. Of these parameters, g is accurately known, possible values for $\Delta\rho$ vary to within a few percent of the value assigned to the experiments, measurements of μ span one order of magnitude ($10-100$ Pa·s, Dingwell (1995)), and estimates of k_0 range over five orders of magnitude from 10^{-9} m^2 to 10^{-4} m^2 (section 2.2.4). Uncertainty in these parameters mean that the range of plausible values for $\mathcal{R}$ span some 6 orders of magnitude. In the middle of the range lies the $\mathcal{R}$ value for the parameters listed in table 5.2.

Figures 6.10a–b show how the mean particle speed and travel time vary with $\mathcal{R}$ in an upwelling column of compositionally homogenous mantle. These results are generated using the upwelling column model described in chapter 4 and the parameter regime given in table 5.2. The upwelling rate is 6 cm/yr and the grid resolution is 1 km in each direction. The scaling factor $\mathcal{R}$ is varied over five orders of magnitude by allowing k_0 to take values between 10^{-9} m^2 and 10^{-4} m^2. For comparison, the value of k_0 used in the experiments above is 10^{-7} m^2. This value is motivated by recent laboratory experiments (Connolly et al., 2009) and millimetre grain sizes in samples of mantle peridotite. The corresponding $\mathcal{R}$ value is denoted $\mathcal{R}^*$. Figure 6.10a shows that the mean particle speed varies with $\mathcal{R}^{1/n}$, where n is the permeability exponent; accordingly the travel time varies with $\mathcal{R}^{-1/n}$. This scaling is corroborated by the one-dimensional steady state solutions derived in appendix A (equation A.16). Consequently, change in $\mathcal{R}$ by a factor of 10^3 will produce an order of magnitude change in the mean particle speed and travel time.

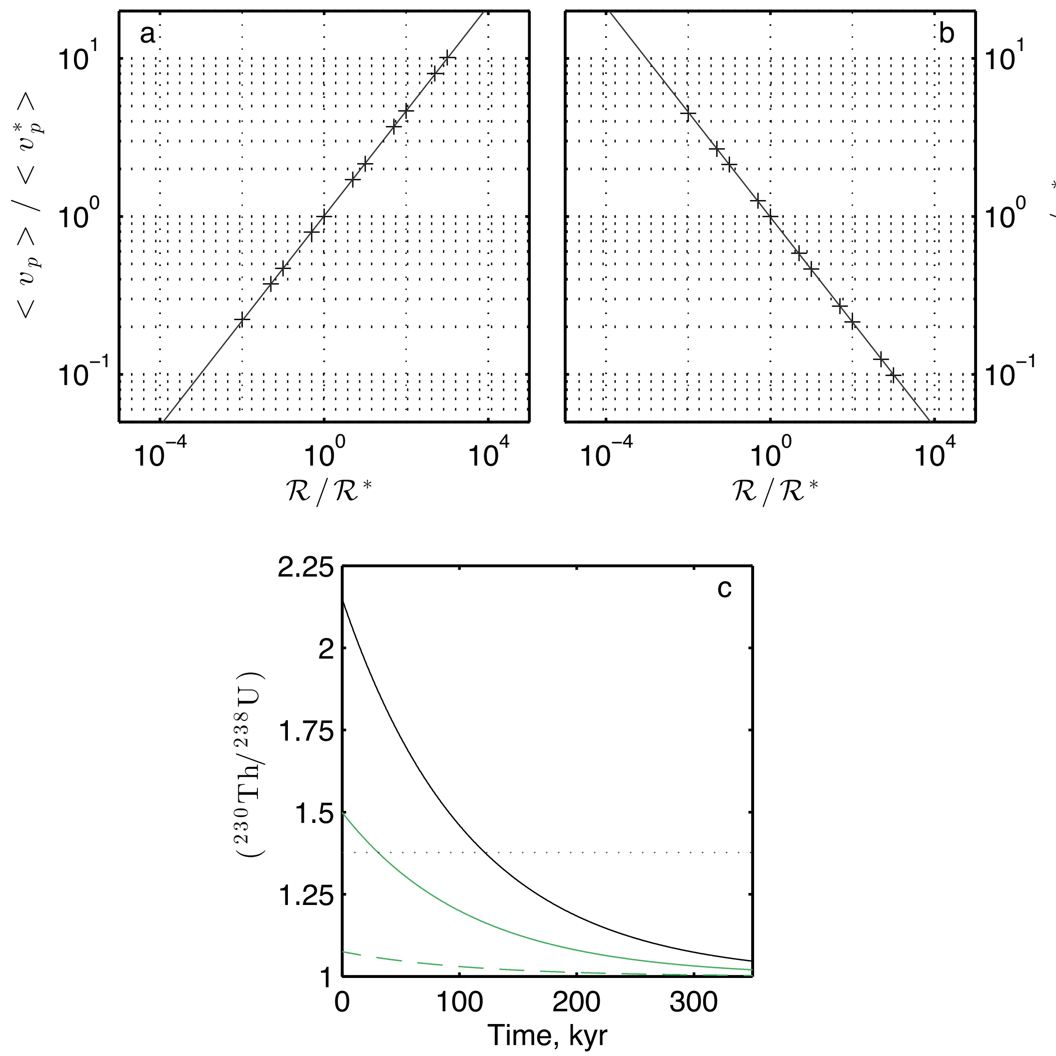

Figure 6.10: The effect of $\mathcal{R} = k_0 \Delta \rho g / \mu$ on melt migration computed using the upwelling column model outlined in chapter 4. The upwelling rate is 6 cm/yr and the grid spacing is 1 km in each direction. Other parameter values are given in table 5.2. (a) Effect of $\mathcal{R}$ on the mean particle speed $\langle v_p \rangle$. $\mathcal{R}^*$ and $\langle v_p \rangle^*$ indicate normalizing values computed from an experiment that shares the same $\mathcal{R}$ value as other experiments presented in this chapter. (b) Effect of $\mathcal{R}$ on the duration of melt migration τ, where τ^* is the duration associated with the $\mathcal{R}^*$ parameter regime. (c) Figure shows how the range of excesses computed by the numerical experiments run with mantle heterogeneity changes with time. Green dashed curve corresponds to the minimum initial excess predicted by the random blob and smoothed noise cases, solid green curve corresponds to the maximum initial excess generated in the spinel zone, black curve corresponds to the maximum initial excess generated in the garnet zone. Black dotted line shows the maximum observed ^{230}Th excess from the dataset presented in figure 6.1.

By assuming this scaling holds for magma flow in channels, figure 6.10c can be used to estimate the effect of different $\mathcal{R}$ on the modelled U-series disequilibria. The figure shows decay curves for the initial ^{230}Th excesses computed in the experiments conducted with mantle heterogeneity. The green curves correspond to the maximum and minimum excesses generated within the spinel zone and the black curve corresponds to the maximum excess generated within the garnet zone. The horizontal dashed line marks the maximum observed ^{230}Th excess in the global dataset presented in figure 6.1. Figure 6.10c suggests that the full range of observed excesses can be preserved by tracer particles that originate in the spinel zone and migrate to the ridge axis in 30 kyr or more. This situation corresponds well to the results from experiments run with a heterogeneous mantle and half spreading rates of 6 cm/yr and 8 cm/yr (figures 6.2b–c). In these experiments, the fastest tracer particles released in the garnet zone travel to the ridge in around 110 kyr. Figure 6.10c shows that excesses associated with these particles are also comparable to the maximum observed excess. For $\mathcal{R}/\mathcal{R}^* < 1$ the duration of melt migration would be longer. Figure 6.10c suggests that under this parameter regime the model would struggle to produce the range of observed excesses. Conversely, choosing values such that $\mathcal{R}/\mathcal{R}^* > 1$ would favour faster melt migration. Figures 6.10b and 6.2b–c indicate that $\mathcal{R} = 10^3\mathcal{R}^*$ would enable melt migration to occur in as little as 3000 years, a short enough time to preserve ^{226}Ra excesses generated deep in the mantle. However, figure 6.10c suggests that the maximum ^{230}Th excesses predicted by the model would be greater than the observed maximum.

Further improvements to the current model model may result from considering how the mineralogy of the mantle and bulk partition coefficient structure varies with mantle heterogeneity. More fusible regions of the mantle will be richer in garnet and clinopyroxene, and in mantle rocks of similar bulk composition to that of basalt (eclogite), garnet will be stable to shallower depths than in lherzolite. This variation corresponds to higher bulk partition coefficients in more fusible parts of the mantle, and will probably cause a greater number of tracer particles to have larger final ^{230}Th excesses.

To make additional advances in reconciling predictions of melt migration made by the present model with observations of U-series disequilibria, several notable deficiencies must be overcome. In the model above, mineral-melt partitioning generates ^{230}Th excesses at the base of the melting region only, and the excesses are assumed to migrate to the surface in chemical isolation from the mantle and other magmas. Existing theory and models, however, indicate that between the melt source and the ridge axis, excesses can be modified by additional mineral–melt partitioning, diffusive fractionation in the presence of plagioclase, and mixing (McKenzie, 1985; Williams and Gill, 1989; Qin, 1993; Spiegelman and Elliott, 1993; Iwamori, 1993, 1994; Richardson and McKenzie, 1994; Lundstrom, 2000; Jull et al., 2002; Saal and Van Orman, 2004; Van Orman et al., 2006; Van Orman and Saal, 2009).

Spiegelman and Elliott (1993) and Elliott and Spiegelman (2003) approach these complications by directly solving for the concentrations of U-series nuclides in the magma and matrix. They also solve for concentrations of stable elements to give information that is readily plotted on an equiline diagram, an important tool for interpreting the U-series geochemistry of MORB (e.g. Elliott and Spiegelman, 2003). Spiegelman and Kelemen (2003) use a similar approach to investigate the consequences of channelized flow for the trace element chemistry of erupted magmas. They predict that the full range of trace element variability observed in MORB occurs within a single channel, because channelized flow transposes the chemical variability produced throughout the melting column into chemical gradients across the width of each channel.

With the present model, a similar approach could be made to compute excesses and explore the consequences of melt migration for the trace element geochemistry of MORB. In its current state, however, the low spatial resolution, and near grid-spacing width of channels could introduce significant numerical errors into the results. Using a finer mesh size, higher-order numerical schemes, and a more accurate advection scheme, such as a Weighted Essentially Non-Oscillatory (WENO) scheme, to preserve sharp chemical gradients may help to overcome these challenges. Using the same advanced infrastructure, future models could be used to investigate the trace element variability of erupted magmas. Rubin et al. (2009) notes that mantle–derived compositional variations in erupted magmas appear to be better preserved when the magma supply rate is low. In contrast, higher spreading rates promote differentiation and loss of geochemical variability. Comparison between these observations and model results may help further understand how well current theories and numerical models describe the dynamics of magma flow in the mantle.

The previous chapters identify the petrological model as one of the most important simplifications made by the present theoretical framework. In the models above, compositional variation has fundamentally important consequences for the dynamics and duration of melt migration, and potentially important consequences for the U-series geochemistry of erupted magmas. Through making improvements to the current petrological model, future studies should aim to: explore the consequences of diffusive fractionation for the U-series geochemistry of magma that reaches the ridge axis, account for variation of bulk partition coefficients for U, Th, Pa, and Ra with mantle heterogeneity, and further address how magma migrates through the mantle in chemical isolation from the residue of partial melting.

6.7 Conclusions

This study represents the first attempt to use physically and energetically consistent models of magma flow and mantle deformation in a heterogeneous mantle to predict the duration of magma flow beneath mid-ocean ridges. The duration and speed of melt migration strongly depend on the upwelling and thermal regimes established by plate spreading. In general, the duration is shorter for magmas released directly beneath the ridge axis and longer for those released in the flanks of the melting region. Mantle heterogeneity has significant consequences for the duration and speed of melt migration. It perturbs the thermal structure of the mantle, forcing magma to localize into channels of high porosity. The net effect of heterogeneity is to speed up melt migration. However, its effect on individual parcels of magma is unique.

For the parameter regime investigated, the mean speed channelized flow in a heterogeneous mantle is approximately 20% faster than diffuse flow in a homogenous mantle. Individual packets of magma, however, may move quicker still, or ideed slower. The duration of melt migration ranges from $25 - 350$ kyr, and the typical mean speed of melt parcels travelling between the base of the melting region and the ridge axis are $0.2 - 1.3$ m/yr. These speeds are too slow to preserve in zero-age mid-ocean ridge basalts ^{226}Ra excesses that were generated deep in the mantle. Using a simple model of equilibrium partitioning, ^{230}Th disequilibria are computed from the results. The modelled excesses compare well against global observations of ^{230}Th disequilibria. Additional capability is needed to investigate the effects of in-growth, chromatographic fractionation, and diffusive fractionation in the presence of plagioclase. Whilst there are many avenues for future work and improvement, the results provide encouragement that the numerical models used throughout this thesis provide a plausible first-order description of magma flow in heterogeneous mantle beneath mid-ocean ridges.

Chapter 7

Conclusions

Below I review the conclusions to chapters 2, 3, 4, 5 and 6 and briefly outline avenues for future work.

7.1 Review of conclusions

Chapter 2 presents a mathematical model for the generation and deformation of mantle rock based on theories of two phase flow. The model comprises statements of conservation for mass, momentum, energy and composition in a system with up to two phases and two chemical components. Magma is defined to move by porous flow through solid rock, and solid rock is defined to deform very slowly by creeping flow, and compact or dilate in response to deviations of the fluid pressure from the lithostatic pressure. Thermodynamic equilibrium is assumed and a simplified petrological phase diagram is used to relate bulk enthalpy, bulk composition and pressure to temperature, local melt fraction and phase compositions. This energetically consistent approach to melting marks an important distinction between the model used in chapters 4, 5 and 6 and others used to investigate unstable magma flow in the mantle with mass transfer between the phases (Aharonov et al., 1995; Spiegelman et al., 2001; Spiegelman and Kelemen, 2003; Liang and Guo, 2003; Schiemenz et al., 2011; Hesse et al., 2011). Analytical, steady one dimensional solutions to the governing equations summarise the fundamental behaviour of the system under conditions appropriate for the top 90 km of the upwelling mantle in the absence of chemical heterogeneities.

Chapter 3 digresses from the main theme of reactive melt transport beneath mid-ocean ridges and instead focuses on large-scale solid mantle flow. Motivated by global observations of mid-ocean ridge bathymetry, it explores the consequences of ridge migration on mantle flow and melting beneath transform faults with three dimensional (3D) numerical experiments. The model mantle is assumed to deform by combined diffusion and dislocation creep. Results from the experiments suggest that ridge migration perturbs asthenospheric flow, driving faster upwelling and enhanced melting beneath the plate that is leading with respect to the direction of ridge migration in the hotspot reference frame. These predictions agree with the sense of mantle asymmetry observed in geophysical studies of mid-ocean ridges (The MELT Seismic Team, 1998; Panza et al., 2010). Under reasonable assumptions of 3D melt focusing across transform faults, the melting asymmetry causes differences in the axial depth and crustal thickness of ridge segments separated by an offset. Predictions of differences in axial depth across ridge offsets generated by the models under reasonable parameter values describe the general trend and amplitude of global observations of the MOR system. The models also predict severe variations in the crustal thickness close to segment ends, owing to the thermal effect of juxtaposing a hot ridge axis against older, cooler material across a transform fault. These variations are smoothed by assuming that magma is redistributed along the ridge segment axis in the shallow mantle by flow through cracks and the porous mantle. Additional experiments that include a viscoplastic rheology predict enhanced mantle temperatures and upwelling rates around transform faults and in the shallow mantle beneath ridge segments, which result in an increased predicted asymmetry in axial depth.

Chapter 4 returns to the main theme of reactive melt transport and uses the model outlined in chapter 2 to test the hypothesis that channelized melt transport is a consequence of melting in a chemically heterogeneous mantle. A suite of numerical experiments consider a column of upwelling mantle into which is embedded a chemical heterogeneity that is more fusible than the ambient mantle. Results from the experiments indicate that channels arise when magma from partially molten heterogeneities supplies the ambient mantle with an additional, and sufficient, flux of magma. Previous studies postulate a connection between mantle heterogeneities and channelized flow (Kogiso et al., 2004; Maclennan, 2008). However, to my knowledge, these results are the first to demonstrate that a physical connection may exist.

The results are best understood in light of the melting rate, which is derived from conservation principles. The melting rate is coupled to the energetic budget dominantly through the latent heat of fusion. Experiments conducted with latent heat values close to the estimated value for the mantle, the mode of melt transport in the absence of chemical heterogeneities is diffuse porous flow. Selecting a small value for the latent heat decouples the melting rate from the energetic budget and emulates the experimental setup used in many previous investigations that do not conserve energy (Aharonov et al., 1995; Spiegelman et al., 2001; Spiegelman and Kelemen, 2003; Liang et al., 2010; Schiemenz et al., 2011; Liang et al., 2011). Under these conditions the mode of melt transport in a chemically homogenous mantle is channelized flow.

The melting rate is a linear combination of contributions from decompression, reactive flow, and thermal diffusion. In the ambient melting region (i.e. not within, or in the vicinity of, high-porosity channels), melting is largely the response of adiabatic decompression. Within channels, however, thermal diffusion provides the most significant contribution to the melting rate. Since heat diffuses into channels, the adjacent mantle is starved of energy for melting. The permeability of these rocks is low, and magma upwelling from deeper depths is focused into high-porosity regions. Consequently, thermal diffusion provides a positive feedback on channelization, and could discourage mixing between magmas flowing through channels and magmas in the adjacent mantle. In addition to the main result that magma from chemical heterogeneities in the mantle can nucleate magmatic channels, results presented in chapter 4 predict for the first time that thermal diffusion is important to the genesis and dynamics of magmatic channels. Furthermore, they underscore the need to use energetically consistent models in studies of coupled magma/mantle dynamics.

Chapter 5 extends the models presented in chapter 4 to explore the consequences of mantle heterogeneity for melt migration and focusing beneath mid-ocean ridges.

Numerical experiments are run with two contrasting topological styles of mantle heterogeneity. For one suite of experiments, heterogeneity is simulated as discrete, randomly shaped blobs, approximately 10 km in size, that perturb the solidus to the same degree. For the second suite of experiments, composition is allowed to vary smoothly over all spatial wavelengths greater than a specified cut off. Both suites of experiments predict that channelized flow is a consequence of melting in a heterogeneous mantle. These results suggest that a physical connection exists between mantle heterogeneity and melt transport beneath mid-ocean ridges. Consequently, they support inferences of such a connection from geochemical studies (Lundstrom, 2000; Kogiso and Hirschmann, 2004).

The results also show that the topology of heterogeneity strongly affects the spatial arrangement of channels; their arrangement is determined by the combined effects of buoyant magma flow and the energetics of melting. In general, in regions where magma is rising buoyantly, the melt flux is greater in cooler, more fusible regions, and lower in warmer, less fusible regions. Variations in spreading rate have little effect on the geometry of melt channels. Channels play an important role in focusing magma to the ridge axis, but in regions of more diffuse flow, existing theories by Yinting et al. (1991) and Sparks and Parmentier (1991) are adequate.

An important result from the experiments is that segregation of magma produced beneath MORs can generate new chemical heterogeneities by melt-pooling and freezing. Ponds of melt that collect in the mantle may deliver magma to off-axis crustal magma chambers, and cause spatial variation in refertilization of the lithosphere. Supporting evidence for this result lies in geochemical observations of oceanic basalts and mantle peridotites by Halliday et al. (1995) and Bedini et al. (1997).

Chapter 6 investigates the consequences of mantle heterogeneity for the speed and duration of melt migration beneath ridges. This section of my thesis represents the first attempt to use physically and energetically consistent models of magma flow and mantle deformation in a heterogeneous mantle to predict the duration of magma flow beneath mid-ocean ridges. The duration and speed of melt migration strongly depend on the upwelling and thermal regimes established by plate spreading. In general, the duration is shorter for magmas released directly beneath the ridge axis and longer for those released in the flanks of the melting region. Mantle heterogeneity has significant consequences for the duration and speed of melt migration. It perturbs the thermal structure of the mantle, forcing magma to localize into channels of high porosity. The net effect of heterogeneity is to speed up melt migration. However, its effect on individual parcels of magma is unique.

For the parameter regime investigated, the mean speed of channelized flow in a heterogeneous mantle is approximately 20% faster than diffuse flow in a homogenous mantle. The duration of melt migration ranges from $25-350$ kyr, and the typical mean speed of melt parcels travelling between the base of the melting region and the ridge axis are $0.2 - 1.3$ m/yr. These speeds are too slow to preserve in zero-age mid-ocean ridge basalts ^{226}Ra excesses that were generated deep in the mantle. Using a simple model of equilibrium partitioning, ^{230}Th disequilibria are computed from the results. The modelled excesses compare well against global observations of ^{230}Th disequilibria. Although there exist many avenues for future work and improvement, the results provide encouragement that the numerical models used throughout this thesis provide a plausible first-order description of magma flow in heterogeneous mantle beneath mid-ocean ridges.

7.2 Future work

The results and discussion presented in chapters 4, 5 and 6 have helped to develop and test, using a theoretical approach, the hypothesis that channelized melt flow is a consequence of melting in a heterogeneous mantle. An important focus for future work is to further develop this hypothesis and test it against observations. Some important avenues to explore and consider in future work are outlined below.

Improve the petrological model

The petrological model is one of the most important simplifications made by the models of melt migration in chapters 2 and 4–6. It reduces the petrological system to two thermodynamic components and assumes that coexisting rock and magma are in local thermodynamic equilibrium. Extending the petrological model to include more thermodynamic components could yield greater insights to the fluid dynamical and thermodynamic consequences of melt–rock interaction in the presence of chemical heterogeneities. It would be especially interesting to consider incongruent melting, and investigate the consequences of mantle dunite formation for the dynamics of reactive melt transport in energetically consistent numerical experiments. Future experiments that relax the condition of thermodynamic equilibrium, and instead consider disequilibrium melting, could yield additional insights to the dynamics of reactive melt transport. With a more advanced petrological model, future studies will be able to explore the geochemical consequences of magma flow in greater detail than considered for this thesis.

Extend solutions to three dimensions

Field observations reveal that mantle dunites have a range of shapes and forms in three dimensional space, from tabular structures to cylindrical pipes. The reason for these different geometries is currently unknown, but insights to the physics and processes involved in their formation could result from extending the present numerical experiments of magma flow to three dimensions. For models to successfully predict the range of observed channel geometries it may be necessary to address anisotropy of viscosity and permeability, consider the effects of plate spreading, and address the three dimensional topology and geometry of mantle heterogeneity.

With three dimensional numerical models of melt flow it will be possible to improve on the study presented in chapter 3 and investigate the dynamics of channelized magma flow and melt focusing beneath ridge discontinuities. It will be particularly interesting to explore the consequences of mantle heterogeneity and melt pooling for the delivery of magma to the ends of ridge segments. Also, this avenue of future research may benefit from incorporating viscoplasticity into the constitutive relationships for rheology and considering the consequences of brittle fracture for melt pools.

Relate model results to observations

An important step in developing and testing the current theories of melt transport is to relate model results to observations of the natural system. The results presented in chapter 6, where the models are used to predict the ^{230}Th disequilibria of mid-ocean ridge basalts, represents the first step in this process. Many more opportunities exist, and several are outlined below:

- **Extend the work on U-series disequilibria** presented in chapter 6 to include ^{226}Ra and ^{231}Pa nuclides. Results may help to reconcile numerical predictions of the speed and duration of magma flow with the demanding constraints suggested by ^{226}Ra and ^{231}Pa disequilibria. In making this extension, the model must be adapted to (i) consider the effects of ingrowth and diffusive fractionation. To achieve this goal, the model must solve additional equations for conservation of mass for each parent–daughter nuclide pair, as suggested by Spiegelman and Elliott (1993), rather than compute disequilibria using the Lagrangian particle approach used in chapter 6. (ii) use higher order numerical schemes and a more accurate advection scheme to try and improve the resolution of melt channels on the computational grid.

- **Consider the seismic anisotropy of the global MOR system.** Shear wave splitting measurements at MORs made by Nowacki et al. (2012) reveal a pattern of increasing splitting with distance from the ridge axis, and greater splitting beneath fast spreading ridges. At distances greater than 50 km from a ridge axis, fast waves are polarized approximately parallel to the spreading direction (ridge perpendicular). Nearer the ridge axis the azimuth of fast waves is more scattered, and is often parallel to the ridge. Additional surface wave studies show that horizontally polarized surface waves travel faster than vertically polarized waves in the region 50-100 km beneath the ocean floor.

  These observations are not well explained by models that attribute seismic anisotropy solely to the lattice preferred orientation of minerals. However, melt channels are likely to have drastically different seismic properties to the surrounding mantle. Results from the models presented in chapter 5 predict that channels close to the ridge axis dip at $30° - 45°$ from the horizontal. These channels may explain the ridge–parallel polarization of fast waves. Further from the ridge axis, melt channels and lenses are subhorizontal and may explain the observation that horizontally polarized surface waves are faster than those polarized in the vertical. In the first instance, the present two dimensional results presented in chapter 5 can be used to generate predictions of the seismic anisotropy beneath MORs.

- **Conduct new field studies** to test the hypothesis that channelized melt transport is a consequence of melting in a heterogeneous mantle. Outcrops of mantle dunites in ophiolites provide an ideal laboratory to address this challenge. Useful insights may result from detailed geochemical and structural mapping of mantle dunites and the host peridotites across large regions. The results will guide future work, and lead to the formulation of new, testable hypotheses that concern the dynamics of melt migration.

- **Explore the geochemical consequences of reactive melt transport.** A fundamental observation of oceanic basalts is that they are in major and trace element disequilibrium with residual harzburgites and lherzolites. Reconciling this observation with the predictions of reactive melt transport presented in chapters 4–6 should be a principal goal of future work. One possible approach to address this challenge is to extend the present models to consider the behaviour of rare earth elements during melting and melt transport. Another interesting topic to consider is how the composition of erupted material relates to the distribution of heterogeneity and dynamics of melt flow beneath MORs.

Relate to volcanism in other tectonic settings

Although the experiments presented in this thesis consider melt migration beneath MORs only, it is likely that the findings translate to volcanism in other tectonic settings. In particular heterogeneity is likely to affect the dynamics of melting and magma flow beneath ocean island volcanoes and in the mantle wedge in subduction zones. Furthermore, the results presented here could shed new light on the formation of alkaline igneous provinces during episodes of intracontinental rifting.

Appendices

Appendix A

Governing equations in 1D and steady state

By restricting the governing equations to a steady state in one dimension most of the equations reduce to a form that can be solved analytically. These approximate forms of the governing equations are also derived by Ribe (1985) and Hewitt (2010). In one dimension and steady state, the equations for conservation of mass 2.1–2.2 reduce to

$$\rho\phi w = \Gamma \tag{A.1}$$

and

$$\rho\,(1-\phi)\,W = -\Gamma, \tag{A.2}$$

where $w = \mathbf{v}_f \cdot \mathbf{k}$ and $W = \mathbf{v}_m \cdot \mathbf{k}$ are the liquid and matrix velocities. Integrating equations A.1 and A.2 and applying the conditions $W = W_0$, $\phi = 0$ and $z = z_m$, where z_m is the depth of melting gives

$$\phi w + (1-\phi)\,W = W_0. \tag{A.3}$$

Under the same restrictions and neglecting the diffusion, equation 2.23 for conservation of composition becomes

$$\frac{d}{dz}\phi w C_f + \frac{d}{dz}\left(1-\phi\right) W C_m = 0. \tag{A.4}$$

Integrating with the extra condition $C_m = C_0$ at $z = z_m$ returns

$$\phi w C_f + \left(1-\phi\right) W C_m = W_o C_0. \tag{A.5}$$

Combining equations A.3 and A.5 relates magma speed to the degree of melting F

$$\phi w = W_0 F, \tag{A.6}$$

where

$$F = \frac{C_m - C_0}{C_m - C_f}. \tag{A.7}$$

Next, substituting in equation A.1 for conservation of mass for the liquid phase gives

$$\rho W_0 \frac{dF}{dz} = \Gamma, \tag{A.8}$$

which expresses the melting rate Γ in terms of $F(z)$.

To find $F(z)$, equations A.3 and A.6 are substituted into the statement for conservation of energy. Making these substitutions and neglecting the effects of thermal diffusion, the statement for conservation of energy can be cast in terms of temperature T as

$$c_P \frac{dT}{dz} = \alpha g \mathcal{T} - L\frac{dF}{dz}. \tag{A.9}$$

Integrating this equation with $T = \mathcal{T} + (\mathcal{T}\alpha g z)/c_P$ at $z = z_m$ yields

$$c_P T = c_P \mathcal{T} + \alpha g \mathcal{T} z - LF. \tag{A.10}$$

Equation A.10 is solved with the definition of F (equation A.7) and phase constraints from the phase diagram (figure 2.1) given by

$$T = f_M\left(P_L, C_m\right), \tag{A.11}$$

$$C_f = A\left(C_m\right), \tag{A.12}$$

where A is the relationship between solid and liquid compsitions to give T, C_m, C_f and F as functions of z.

Analytical solutions for ϕ, w, W and $\mathcal{P}$, are found by taking $w \gg W$ and the compaction length to be small. Under these approximations, the statement for conservation of momentum for the liquid,

$$\phi\left(w - W\right) = -\frac{k_0\phi^n}{\mu}\left(\frac{d\mathcal{P}}{dz} + \Delta\rho g z\right), \tag{A.13}$$

reduces to

$$\phi w \approx \frac{\phi g k_0 \phi^n}{\mu}. \tag{A.14}$$

Combining with equation A.6 returns functions for ϕ and w:

$$\phi \approx -\left(\frac{k_0\Delta\rho g}{\mu}\right)^{-\frac{1}{n}} W_0^{\frac{1}{n}} F^{\frac{1}{n}}, \tag{A.15}$$

$$w \approx -\left(\frac{k_0\Delta\rho g}{\mu}\right)^{\frac{1}{n}} W_0^{1-\frac{1}{n}} F^{1-\frac{1}{n}}, \tag{A.16}$$

and from equation A.3,

$$W \approx W_0\left(1 - F\right). \tag{A.17}$$

To find an expression for the compaction pressure, equation 2.9 is approximated in one dimension as

$$\mathcal{P} \approx \frac{\zeta_0}{\phi}\frac{dW}{dz}. \tag{A.18}$$

Substituting in equations A.15 and A.17 yields

$$\mathcal{P} \approx -\zeta_0\left(\frac{k_0\Delta\rho g}{\mu}\right)^{\frac{1}{n}} W_0^{1-\frac{1}{n}} F^{-\frac{1}{n}}\frac{dF}{dz}. \tag{A.19}$$

In the case where the solidus and liquidus temperatures are linear functions of composition (figure 2.1b), the solidus temperature is defined as

$$T = T_0 + \frac{\rho g z}{c_P} + M_S \left(C_m - C_0\right), \tag{A.20}$$

where M_S is the slope of the solidus, and

$$C_f = C_m + \Delta C, \tag{A.21}$$

where ΔC is the difference in composition between a coexisting liquid and solid in thermodynamic equilibrium. Combining equation A.20 with the linearized adiabatic temperature profile $T = \mathcal{T} + (\mathcal{T}\alpha g z)/c_P$ gives a relationship for the depth of melting

$$z_m = \frac{T_o + M_S \left(C_m - C_0\right) - \mathcal{T}}{\alpha g \mathcal{T}/c_P - \rho g/\gamma} \tag{A.22}$$

subject to the condition that $C_m = C_0$ at $z = z_m$. Substituting equations A.22 and A.21 into A.20 returns an equation for the solidus temperature in terms of z and F

$$T = \mathcal{T} + \frac{\alpha g \mathcal{T}}{c_P} z_m + \frac{\rho g}{\gamma}\left(z - z_m\right) + M_S \Delta C F. \tag{A.23}$$

Finally, substituting A.23 into A.10 gives a linear relationship for F in terms of z

$$F = \mathcal{G}\left(z_m - z\right) \tag{A.24}$$

where

$$\mathcal{G} = \frac{\rho g/\gamma - \alpha g \mathcal{T}/cp}{L/cp + M_S \Delta C}. \tag{A.25}$$

The temperature and matrix composition are then given by

$$T = \mathcal{T} + \frac{\alpha g \mathcal{T}}{c_P} z - \frac{L}{c_P}\mathcal{G}\left(z_m - z\right), \tag{A.26}$$

$$C_m = C_0 + \Delta C \mathcal{G}\left(z_m - z\right). \tag{A.27}$$

Solutions to these equations for T, C_m, C_f, F, ϕ, w, W and $\mathcal{P}$ and linear phase constraints are presented in section 2.5.

Appendix B

Advection schemes

Numerical experiments of mantle dynamics and melt migration require accurate advection schemes that are conservative, non–oscillatory, show negligible numerical diffusion, and preserve sharp gradients. Here I outline a total variation diminishing (TVD), flux limiting scheme that satisfies these requirements (e.g Harten, 1983; Sweby, 1984). The general approach of the scheme is to supplement a first order scheme with additional fluxes that are corrected, or limited, to ensure negligible numerical diffusion and oscillation–free advection. The result is an advection scheme that second order in time and space, except near sharp gradients where its order in space is reduced.

To illustrate the scheme, I consider here the one dimensional advection equation

$$\frac{\partial C}{\partial t} + \frac{\partial VC}{\partial x} = 0, \tag{B.1}$$

where t is time, V is velocity, and C is the quantity being advected.

Here, I discretize B.1 on to a staggered mesh with grid spacing Δx. V is located on the cell edges in the $+i$ direction, and C is located at the cell centre. To achieve second order accuracy in time, the partial derivative with respect to time is centred half way between the current time level t and the next time level $t + \Delta t$. Accordingly, the first term in equation B.1 can be written as

$$\left.\frac{\partial C}{\partial t}\right|_i^{t+\Delta t/2} \approx \frac{C_i^{t+\Delta t} - C_i^t}{\Delta t}, \tag{B.2}$$

and defining $\mathcal{F}_i = V_i C_i$, the second term can be approximated as

$$\left.\frac{\partial \mathcal{F}}{\partial x}\right|_i^{t+\Delta t/2} \approx \frac{1}{2}\left(\left.\frac{\partial \mathcal{F}}{\partial x}\right|_i^{t} + \left.\frac{\partial \mathcal{F}}{\partial x}\right|_i^{t+\Delta t}\right). \tag{B.3}$$

To avoid spurious growth of the cell averaged fluxes $\mathcal{F}$ the scheme must be TVD. That is, the total variation TV of cell averaged fluxes

$$TV\left(\mathcal{F}\right) = \sum_i \mathcal{F}_i - \mathcal{F}_{i-1}, \tag{B.4}$$

satisfies

$$TV\left(\mathcal{F}^{n+1}\right) \leq TV\left(\mathcal{F}^{n}\right), \tag{B.5}$$

where n is the time step. This condition for a TVD scheme is enforced by multiplying the flux $\mathcal{F}$ between cells by a limiting function $\lambda\left(\mathcal{R}\right)$, where $\mathcal{R}$ is a measure of the smoothness of the flux between the upwind cell and the local cell. Consequently, advection of $\mathcal{F}$ in the $+i$ direction at a single time level can be approximated as

$$\left.\frac{\partial \mathcal{F}}{\partial x}\right|_i^{+} \approx \frac{1}{\Delta x}\left[\lambda^+_{i+1/2}\mathcal{F}^+_{i+1/2} - \lambda^+_{i-1/2}\mathcal{F}^+_{i-1/2}\right], \tag{B.6}$$

and when advection is in the $i-$ direction

$$\left.\frac{\partial \mathcal{F}}{\partial x}\right|_i^{-} \approx \frac{1}{\Delta x}\left[\lambda^-_{i+1/2}\mathcal{F}^-_{i+1/2} - \lambda^+_{i-1/2}\mathcal{F}^-_{i-1/2}\right]. \tag{B.7}$$

Details of the flux limiting functions λ and smoothness indicators $\mathcal{R}$ are discussed below. Since the direction of advection is not necessarily known *a priori*, equations B.6 and B.7 are combined to give

$$\left.\frac{\partial \mathcal{F}}{\partial x}\right|_i \approx \left.\frac{\partial \mathcal{F}}{\partial x}\right|_i^{+} + \left.\frac{\partial \mathcal{F}}{\partial x}\right|_i^{-}, \tag{B.8}$$

where at least one of the quantities on the right hand side must be zero. Recalling that $\mathcal{F}^{+/-}_{i+1/2} = V^{+/-}_{i+1/2} C^{+}_{i+1/2}$, in equations B.7–B.8

$$V^{+}_{i+1/2} = \frac{1}{2}\left(V_{i+1/2} + |V_{i+1/2}|\right), \tag{B.9a}$$

$$V^{-}_{i+1/2} = \frac{1}{2}\left(V_{i+1/2} - |V_{i+1/2}|\right), \tag{B.9b}$$

and

$$C^{+}_{i+1/2} = C_i + \frac{\lambda^{+}_{i+1/2}}{2}\left[C_{i+1} - C_i\right], \tag{B.10a}$$

$$C^{-}_{i+1/2} = C_{i+1} + \frac{\lambda^{-}_{i+1/2}}{2}\left[C_i - C_{i+1}\right]. \tag{B.10b}$$

By combining equations B.6–B.10, the advection term (equation B.8) can be written as

$$\left.\frac{\partial \mathcal{F}}{\partial x}\right|_i \approx \frac{1}{\Delta x}\left(a_i C_{i-1} + b_i C_i + ciC_{i+1}\right), \tag{B.11}$$

where

$$a_i = -V_{i-1/2}\left(1 - \frac{\lambda^{+}_{i-1/2}}{2}\right) - \frac{V^{-}_{i-1/2}\lambda^{-}_{i-1/2}}{2}, \tag{B.12a}$$

$$b_i = V^{+}_{i+1/2}\left(1 - \frac{\lambda^{+}_{i+1/2}}{2}\right) + \frac{V^{-}_{i+1/2}\lambda^{-}_{i+1/2}}{2} - \frac{V^{+}_{i-1/2}\lambda^{+}_{i-1/2}}{2} - V^{-}_{i-1/2}\left(1 - \frac{\lambda -_{i-1/2}}{2}\right), \tag{B.12b}$$

$$c_i = V^{+}_{i+1/2}\left(1 - \frac{\lambda^{+}_{i+1/2}}{2}\right) + \frac{V^{-}_{i+1/2}\lambda^{-}_{i+1/2}}{2}. \tag{B.12c}$$

The smoothness indicators vary as functions of V and C according to

$$\mathcal{R}^{+}_{i+1/2} = \frac{V^{+}_{i-1/2}\left(C_i - C_{i-1}\right)}{V^{+}_{i+1/2}\left(C_{i+1} - C_i\right)}, \tag{B.13}$$

$$\mathcal{R}^{-}_{i+1/2} = \frac{V^{-}_{i+3/2}\left(C_{i+2} - C_{i+1}\right)}{V^{-}_{i+1/2}\left(C_{i+1} - C_i\right)}. \tag{B.14}$$

The coefficients a_i, b_i and c_i depend on velocities and, through λ, the advected quantity. These coefficients may be explicit, fully implicit, or semi-implicit in time, but are assumed constant over a single timestep. Accordingly, equation B.1 is solved as

$$C_i^{t+\Delta t} = C_i^t - \frac{\Delta t}{2\Delta x}\left[a_i\left(C_{i-1}^t + C_{i-1}^{t+\Delta t}\right) + b_i\left(C_i^t + C_i^{t+\Delta t}\right) + c_i\left(C_{i+1}^t + C_{i+1}^{t+\Delta t}\right)\right]. \tag{B.15}$$

The flux limiting functions λ use information about the smoothness of the flux between the upwind and local cells to make the advection scheme non-oscillatory and limit numerical diffusion. Setting $\lambda = 0$ everywhere reduces the advection scheme to the upwind difference scheme on a staggered mesh, and setting $\lambda = 1$ yields the centred difference scheme. These schemes are not fully TVD. However, there exist many different flux limiting schemes that are fully TVD. Fully TVD schemes allow λ to vary between 0 and 2. The smaller λ is, the more limiting that is applied to jumps in cell averages; when $\lambda > 1$, the flux limiter is used to steepen the advected gradient.

Out of the many TVD flux limiting schemes available, I investigated the suitability of the minmod (Roe, 1985), superbee (Roe, 1985) and MC limiters for the models presented in chapters 4–6. These flux limiting functions are defined as follows:

$$\lambda(\mathcal{R}) = \max\left[0, \min\left(1, \mathcal{R}\right)\right] \qquad \text{Minmod} \tag{B.16}$$

$$\lambda(\mathcal{R}) = \max\left[0, \min\left(1, 2\mathcal{R}\right), \min\left(2, \mathcal{R}\right)\right] \qquad \text{Superbee} \tag{B.17}$$

$$\lambda(\mathcal{R}) = \max\left[0, \min\left(\frac{1+\mathcal{R}}{2}, 2, 2\mathcal{R}\right)\right] \qquad \text{MC.} \tag{B.18}$$

I tested the performance of the advection scheme subject to these limiters by computing the advection of a profile by a two dimensional velocity field. Figure B.1a shows the initial profile prior to advection. The numerical experiments were conducted on a grid consisting of 200 evenly spaced grid cells in the i and j directions. In both directions the nondimensional velocity was equal, resulting in the profile being advected diagonally across the grid. The experiments used semi-implicit time stepping with a Courant number less than 1, and were stopped after the profile had made one full pass across the grid. Hence, a perfect advection scheme should result in an identical profile to that shown in figure B.1a.

Figures B.1 b–i show results from tests using the limiters described above. To

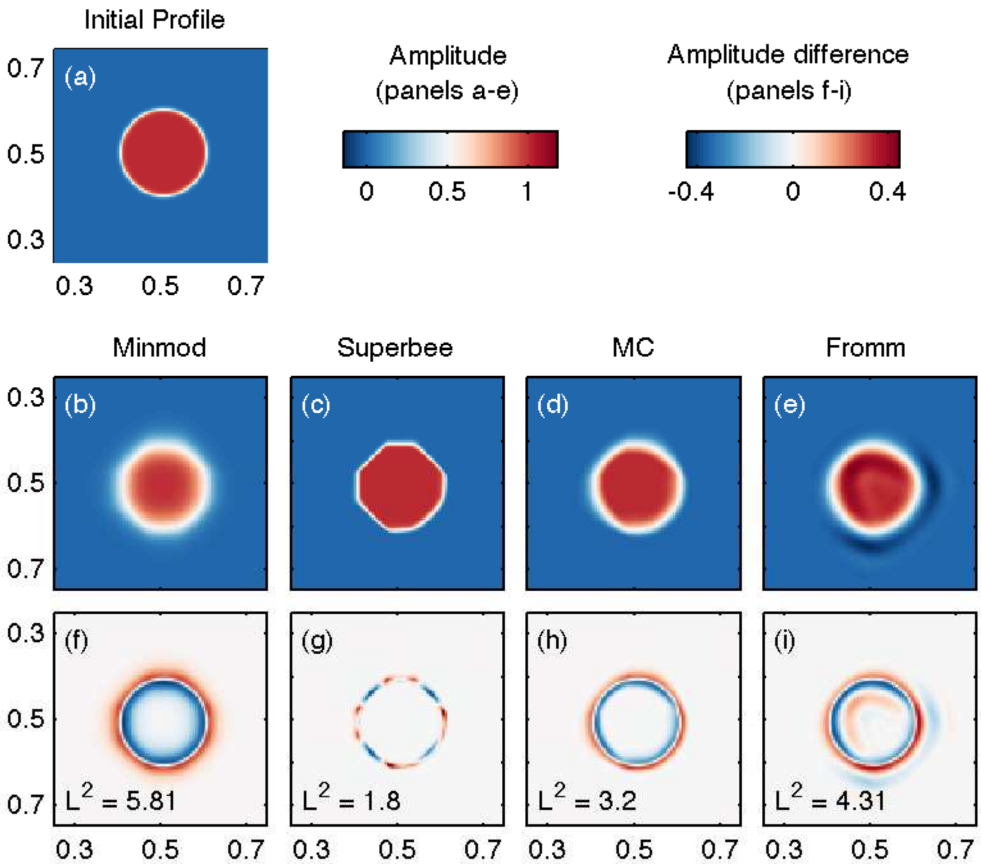

Figure B.1: Results from tests in which an initial profile is advected diagonally across the grid in a top left–to–bottom right direction using different advection schemes. (a) Initial profile. (b–e) Final solution after the initial profile has made one pass around the grid. (f–i) Plots of the difference between each final solution and the initial profile. The L^2 norm of the result is indicated on each panel.

illustrate the adventages of using an oscillation free, TVD advection scheme, figures B.1 e and i show results one additional test conducted using the Fromm advection scheme (not TVD) that is used for the models presented in chapter 3. The Fromm scheme is given by $\lambda = 1/2(1+\mathcal{R})$. Panels b–e show the final profiles, and panels f–i plots the difference between each of the final profiles and the initial profile shown in figure B.1a. The L^2–norm for the results plotted in figures B.1f–i is also given.

Figures B.1b–e show that the three TVD advection schemes (panels b–d) return oscillation free results. Spurious oscillations are present in the solution obtained using the Fromm advection scheme (figure B.1e). Panels b–d and f–h show that the minmod, superbee and MC flux limiters result in slight differences between the solutions. The superbee limiter returns the most accurate solution, as indicated by the smallest L^2 norm. In some places, the sides of the advected profile are oversteepened, and induce a slight distortion to the shape of the final profile (panel b). The minmod limiter is most diffusive but maintains the overall shape of the intial profile, and the MC limiter represents an intermediary between the superbee and minmod schemes. Owing to its ability to preserve steep gradients, the superbee limiter is used for all numerical experiments presented in chapter 4. However, it is more challenging to numerically solve the models of magma flow beneath a spreading rigde in chapters 5 and 6. Consequently, the minmod limiter is employed for these simulations to allow some numerical diffusion, which benefits the convergence of the solution.

Appendix C

Derivation of the melting rate

The melting rate is derived by combining conservation statements for energy (equation 4.6) and composition (equation 4.7) with equations that conserve mass for the liquid and solid phases. Respectively, the equations that conserve mass for the liquid and solid phase respectively are:

$$\frac{\partial \phi}{\partial t} + \boldsymbol{\nabla} \cdot \phi \mathbf{v}_f = \frac{\Gamma}{\rho}, \tag{C.1}$$

$$\frac{\partial (1-\phi)}{\partial t} + \boldsymbol{\nabla} \cdot (1-\phi)\, \mathbf{v}_m = -\frac{\Gamma}{\rho}. \tag{C.2}$$

For this derivation, the equation for conservation is expressed in terms of temperature, rather than potential temperature. With this modification the statement becomes

$$\frac{\partial \mathcal{H}}{\partial t} - \rho L \boldsymbol{\nabla} \cdot (1-\phi)\, \mathbf{v}_m + \rho c_P \bar{\mathbf{v}} \boldsymbol{\nabla} T - \rho \alpha T^* \mathbf{g} \cdot \bar{\mathbf{v}} = k \nabla^2 T, \tag{C.3}$$

where k is the thermal conductivity, and T^* is approximated as the mantle's potential temperature.

We combine equations 4.7 and C.3 with equations C.1 and C.2, and substitute in the definition $\mathcal{H} = \rho L \phi + \rho c_P (T - T_0)$ to express the statements conserving energy and composition in terms of the melting rate Γ:

$$L\Gamma + \rho c_P \frac{\partial T}{\partial t} + \rho c_P \bar{\mathbf{v}} \cdot \boldsymbol{\nabla} T - \rho \alpha \mathcal{T} \mathbf{g} \cdot \bar{\mathbf{v}} = k \nabla^2 T, \tag{C.4}$$

$$\frac{\Gamma}{\rho}\left(C_f - C_m\right) + \phi\frac{\partial C_f}{\partial t} + \phi\mathbf{v}_f\cdot\boldsymbol{\nabla}C_f + \left(1-\phi\right)\frac{\partial C_m}{\partial t} + \left(1-\phi\right)\mathbf{v}_m\cdot\boldsymbol{\nabla}C_m = \mathcal{D}\boldsymbol{\nabla}\cdot\phi\boldsymbol{\nabla}C_f. \tag{C.5}$$

Next, we use equations 4.1 and 4.2 to rewrite equation C.4 in terms of C_f, and to eliminate C_m from equation C.5. By making these modifications and combining the results, the melting rate is given by

$$\Gamma = \mathcal{G}\bar{\mathbf{v}}\cdot\mathbf{g}\left(\frac{\frac{\mathcal{B}\alpha\mathcal{T}}{c_P}-\rho}{\gamma}\right) - \mathcal{G}\bar{\mathbf{v}}\cdot\boldsymbol{\nabla}T\left(\mathcal{B}-1\right) + \mathcal{G}\mathcal{B}\kappa\nabla^2T - \mathcal{G}\mathcal{D}M_L\boldsymbol{\nabla}\cdot\phi\boldsymbol{\nabla}C_f, \tag{C.6}$$

where

$$\mathcal{B} = \frac{\phi\left(R-1\right)+1}{R}, \tag{C.7}$$

$$R = \frac{M_S}{M_L}, \tag{C.8}$$

and

$$\mathcal{G} = \frac{R\rho}{L/c_P\left[\phi\left(R-1\right)+1\right] + \Delta CM_L - \left(R-1\right)\left(C_f - C_0\right)M_L}. \tag{C.9}$$

To arrive at the expression for the melting rate given by equation 4.8, we take $R = 1$, which renders $\mathcal{B} = 1$, and $\mathcal{G} = \rho/(L/c_P + \Delta CM)$.

Bibliography

Aharonov, E., Spiegelman, M., Kelemen, P., 1997. Three–dimensional flow and reaction in porous media: Implication for the Earth's mantle and sedimentary basins. Journal of Geophysical Research 102, 14821–14883.

Aharonov, E., Whitehead, J., Kelemen, P., Spiegelman, M., 1995. Channeling instability of upwelling melt in the mantle. Journal of Geophysical Research 100, 20433–20450.

Ahern, J., Turcotte, D., 1979. Magma migration beneath an ocean ridge. Earth and Planetary Science Letters 45, 115–122.

Alabaster, T., Pearce, J., Malpas, J., 1982. The volcanic stratigraphy and petrogenesis of the Oman ophiolite complex. Contributions to Mineralogy and Petrology 81, 168–183.

Alexiades, V., Solomon, A., 1993. Mathematical Modeling of Melting and Freezing Processes. Hemisphere.

Allègre, C., Hamelin, B., Dupré, B., 1984. Statistical analysis of isotopic ratios in morb: the mantle blob cluster model and the convective regime of the mantle. Earth and Planetary Science Letters 71, 71—84.

Allègre, C., Turcotte, D., 1986. Implications of a 2-component marble-cake mantle. Nature 323, 123–127.

Asimow, P., Ghiorso, M., 1998. Algorithmic modifications extending MELTS to calculate subsolidus phase relations. American Mineralogist 83, 1127–1132.

Asimow, P., Hirschmann, M., Stolper, E., 1997. An analysis of variations in isentropic melt productivity. Philosophical Transactions of the Royal Society of London A 355, 255–281.

Asimow, P., Stolper, E., 1999. Steady-state mantle-melt interactions in one dimension I: Equilibrium transport and melt focusing. Journal of Petrology 40, 475–494.

Baba, K., Chave, A., Evans, R., Hirth, G., Mackie, R., 2006. Mantle dynamics beneath the East Pacific Rise at 17°S: Insights from the Mantle Electromagnetic and Tomography (MELT) experiments. Journal of Geophysical Research 111, B02101.

Balay, S., Buschelman, K., Eijkhout, V., Gropp, W., Kaushik, D., Knepley, M., Curfman McInnes, L., Smith, B., Zhang, H., 2009. PETSc Users Manual. anl-95/11 - revision 3.0.0 ed. Argonne National Laboratory. URL: http://www.mcs.anl.gov/petsc/docs.

Balay, S., Gropp, W., Curfman McInnes, L., Smith, B., 1997. Efficient management of parallelism in object oriented numerical software libraries, in: Arge, E., Bruaset, A.M., Langtangen, H.P. (Eds.), Modern Software Tools in Scientific Computing, Birkhauser Press. pp. 163–202.

Batanova, V., Savelieva, G., 2009. Melt migration in the mantle beneath spreading zones and formation of replacive dunites: a review. Russian Geology and Geophysics 50, 763–778.

Batanova, V., Sobolev, A., 2000. Compositional heterogeneity in subduction-related mantle peridotites, Troodos massif, Cyprus. Geology 28, 55–58.

Batchelor, G., 1967. An introduction to fluid dynamics. Cambridge University Press, Cambridge.

Batiza, R., Niu, Y., Zayac, W., 1990. Chemistry of seamounts near the East Pacific Rise: Implications for the geometry of subaxial mantle flow. Geology 18, 1122–1125.

Bear, J., 1972. Dynamics of fluids in porous media. Dover, New York.

Beattie, P., 1993a. The generation of uranium series disequilibria by partial melting of spinel peridotite: constraints from partitioning studies. Earth and Planetary Science Letters 117, 379–391.

Beattie, P., 1993b. Uranium–thorium disequilibria and partitioning on melting of garnet peridotite. Nature 363, 63–65.

Bedini, R., Bodinier, J.L., Dautria, J.M., Morten, L., 1997. Evolution of LILE-enriched small melt fractions in the lithospheric mantle: a case study from the East African Rift. Earth and Planetary Science Letters 153, 67–83.

Beeman, M., Kohlstedt, D., 1993. Deformation of fine-grained aggregates of olivine plus melt at high temperatures and pressures. Journal of Geophysical Research 98, 6443–6452.

Behn, M., M.S., B., Hirth, G., 2007. Thermal structure of oceanic transform faults. Geology 35, 307–310.

Bell, R., Buck, R., 1992. Crustal control of ridge segmentation inferred from observations of the Reykjanes Ridge. Nature 357, 583–586.

Ben Othman, D., Allegre, C., 1990. U-Th isotopic systematics at 13 °N east Pacific Ridge segment. Earth and Planetary Science Letters 98, 129–137.

Bercovici, D., Ricard, Y., Schubert, G., 2001. A two-phase model for compaction and damage 1. General Theory. Journal of Geophysical Research 106, 8887–8906.

Blichert-Toft, J., Albarède, F., Kornprobst, J., 1999. Lu-Hf isotope systematics of garnet pyroxenites from Beni Bousera, Morocco: Implications for basalt origin. Science 283, 1303–1306.

Bourdon, B., Sims, K., 2003. U-series constraints on intraplate basaltic magmatism, in: Bourdon, B., Henderson, G., Lundstrom, C., Turner, S. (Eds.), Uranium-series Geochemistry. Volume 52 of *Reviews in Mineralogy and Geochemistry*, pp. 215–254.

Bowin, C., Milligan, J., 1985. Negative gravity–anomaly over spreading rift valleys—Mid-Atlantic Ridge at 26°N. Tectonophysics 113, 223–256.

Braun, M., Hirth, G., Parmentier, E., 2000. The effects of deep damp melting on mantle flow and melt generation beneath mid-ocean ridges. Earth and Planetary Science Letters 176, 339–356.

Braun, M., Kelemen, P., 2002. Dunite distribution in the Oman ophiolite: Implications for melt flux through porous dunite conduits. Geochemistry, Geophysics, Geosystems 3, 8603.

Bryce, J., DePaolo, D., 2004. Pb isotopic heterogeneity in basaltic phenocrysts. Geochimica et Cosmochimica Acta 68, 4453–4468.

Buchl, A., Burgmann, G., Batanova, V., Munker, C., Hofmann, A., 2002. Melt percolation monitored by Os isotopes and HSE abundances: a case study from the mantle section of the Troodos Ophiolite. Earth and Planetary Science Letters 204, 384–402.

Buck, W., Su, W., 1989. Focused mantle upwelling below mid-ocean ridges due to feedback between viscosity and melting. Geophysical Research Letters 16, 641–644.

Canales, J., Carton, H., Carbotte, S., Mutter, J., Nedimović, M., Xu, M., Aghaei, O., Marjanović, M., Newman, K., 2012. Network fo off-axis melt bodies at the East Pacific Rise. Nature Geoscience 5, 279–283.

Canales, J., Detrick, R., Toomey, D., Wilcock, W., 2003. Segment-scale variations in the crustal structure of 150-300 kyr old fast spreading oceanic crust (East Pacific Rise, 8°15'N–10°5'N) from wide-angle seismic refraction profiles. Geophysical Journal International 152, 766–794.

Canales, J., Nedimović, M., Kent, G., Carbotte, S., Detrick, R., 2009. Seismic reflection images of a near-axis melt sill within the lower crust at the Juan de Fuca ridge. Nature 460, 89–94.

Carbotte, S., Small, C., Donnelly, K., 2004. The influence of ridge migration on the magmatic segmentation of mid-ocean ridges. Nature 429, 743–746.

Chabaux, F., Allègre, C., 1994. 238u–230th–226ra disequilibria in volcanics: A new insight into melting conditions. Earth and Planetary Science Letters 126, 61–74.

Chadam, J., Hoff, D., Merino, E., Ortoleva, P., Sen, A., 1986. Reactive Infiltration Instabilitites. IMA Journal of Applied Mathematics 36, 207–221.

Chen, C., Presnall, D., 1975. The system Mg_2SiO_4–SiO_2 at pressures up to 25 kilobars. American Mineralogist 60, 398–406.

Chen, Y., 1996. Constraints on melt production rate beneath the mid-ocean ridges based on passive flow models. Pure and Applied Geophysics 146, 589–620.

Chen, Y., Morgan, W., 1990. A nonlinear rheology model for mid-ocean ridge axis topography. Journal of Geophysical Research 95, 19583–17604.

Cmiral, M., Fitzgerald, J., Faul, U., Green, D., 1998. A close look at dihedral angles and melt geometry in olivine-basalt aggregates: a TEM study. Contributions to Mineralogy and Petrology 130, 336–345.

Cochran, J., 1979. Analysis of isostasy in the world's oceans: 2. Midocean ridge crests. Journal of Geophysical Research 84, 4173–4729.

Collier, J., Singh, S., 1998. A seismic inversion study of the axial magma chamber reflector beneath the East Pacific Rise near 10°N, in: Modern Ocean Floor Processes and the Geological Record. Geological Society of London. Volume 148 of *Geological Society of London Special Publications*, pp. 17–28.

Conder, J., Forsyth, D., Parmentier, E., 2002. Asthenospheric flow and asymmetry of the East Pacific Rise, MELT area. Journal of Geophysical Research 107, 2344.

Condomines, M., Hémond, C., Allègre, C., 1988. U-Th-Ra radioactive disequilibria and magmatic processes. Earth and Planetary Science Letters 90, 243–262.

Connolly, J., Schmidt, M., Solferino, G., Bagdassarov, N., 2009. Permeability of asthenospheric mantle and melt extraction rates at mid-ocean ridges. Nature 462, 209–212.

Cooper, K., Goldstein, S., Sims, K., Murrell, M., 2003. Uranium-series chronology of the Gorda Ridge volcanism: new evidence from the 1993 eruption. Earth and Planetary Science Letters 206, 459–479.

Cooper, R., 1990. Differential stress-induced melt migration: An experimental approach. Journal of Geophysical Research 95, 6979–6992.

Cooper, R., Kohlstedt, D., 1986. Rheology and structure of olivine-basalt partial melts. Journal of Geophysical Research 91, 9315–9323.

Costa, A., 2006. Permeability-porosity relationship: A reexamination of the Kozeny-Carman equation based on a fractal pore-space geometry assumption. Geophysical Research Letters 33, L02318.

Daines, M., Kohlstedt, D., 1993. The transition from porous to channelized flow due to melt/rock reaction during melt migration. Geophysical Research Letters 21, 145–148.

Dasgupta, R., Jackson, M., Lee, C., 2010. Major element chemistry of ocean island basalts — Conditions of mantle melt heterogeneity of mantle source. Earth and Planetary Science Letters 289, 377–392.

Davis, E., Karsten, J., 1986. On the cause of the asymmetric distribution of seamounts about the Juan de Fuca ridge: Ridge–crest migration over a heterogeneous asthenosphere. Earth and Planetary Science Letters 79, 385–396.

Detrick, R., Needham, H., Renard, V., 1995. Gravity anomalies and crustal thickness variations along the Mid-Atlantic ridge between 33°N and 40°N. Journal of Geophysical Research 100, 3767–3787.

Dick, H., Lissenberg, C., Warren, J., 2010. Mantle melting, melt transport, and delivery beneath a slow-spreading ridge: the Paleo-MAR from 23°14'N to 23°45'N. Journal of Petrology 51, 425–467.

Dingwell, D., 1995. Viscosity and anelasticity of melts, in: Ahrens, T. (Ed.), Mineral Physics and Crystallography: A Handbook of Physical Constants. AGU, Washington. Volume 2 of *AGU Reference Shelf*, pp. 209–217.

Dohmen, R., Becker, H., Chakraborty, S., 2007. Fe-Mg diffusion in olivine I: Experimental determination between 700 and 1,200° as a function of composition, crystal orientation and oxygen fugacity. Physics and Chemistry of Minerals 34, 389–407.

du Vignaux, N., Fleitout, L., 2001. Stretching and mixing of viscous blobs in Earth's mantle. Journal of Geophysical Research 106, 30893–30908.

Dunn, R., Toomey, D., Solomon, S., 2000. Three-dimensional seismic structure and physical properties of the crust and shallow mantle beneath the East Pacific Rise at 9°30'N. Journal of Geophysical Research 105, 23537–23555.

Dupré, B., Allègre, C., 1983. Pb-Sr isotope variation in Indian Ocean basalts and mixing phenomena. Nature 303, 142–146.

Durant, D., Toomey, D., 2009. Evidence and implications of crustal magmatism on the flanks of the East Pacific Rise. Earth and Planetary Science Letters 287, 130–136.

Elliott, T., Spiegelman, M., 2003. Melt Migration in Oceanic Crustal Production: A U-series Perspective, in: Editors-in Chief: Holland, H., Turekian, K. (Eds.), Treatise on Geochemistry. Pergamon, Oxford. Volume 3. Chapter 14, pp. 465–510.

Escartin, J., Lin, J., 1995. Ridge offsets, normal faulting, and gravity-anomalies of slow-spreading ridges. Journal of Geophysical Research 100, 6163–6177.

Evans, R., Tarits, P., Chave, A., White, A., Heinson, G., Filloux, J., Toh, H., Seama, N., Utada, H., Booker, J., Unsworth, M., 1999. Asymmetric electrical structure in the mantle beneath the East Pacific Rise at 17°S. Science 286, 752–756.

Faul, U., 1997. Permeability of partially molten upper mantle rocks from experiments and percolation theory. Journal of Geophysical Research 102, 10299–10311.

Faul, U., 2001. Melt retention and segregation beneath mid-ocean ridges. Nature 410, 920–923.

Forsyth, D., Webb, S., Dorman, L., Shen, Y., 1998. Phase velocities of Rayleigh waves in the MELT experiment on the East Pacific Rise. Science 280, 1235–1238.

Fowler, A., 1985. A mathematical model of magma transport in the asthenosphere. Geophysical and Astrophysical Fluid Dynamics 33, 63–96.

Gale, A., Escrig, S., Gier, E., Langmuir, C., Goldstein, S., 2011. Enriched basalts at segment centers: The lucky strike (37°17n) and menez gwen (37°50n) segments of the mid-atlantic ridge. Geochemistry Geophysics Geosystems 12, Q06016.

Gast, P., 1968. Trace element fractionation and the origin of tholeiitic and alkaline magma types. Geochimica et Cosmochimica Acta 32, 1057–1086.

Ghiorso, M., Hirschmann, M., Reiners, P., Kress III, V., 2002. The pMELTS: A revision of MELTS for improved calculation of phase relations and major element partitioning related to partial melting of the mantle to 3 GPa. Geochemistry, Geophysics, Geosystems 3, 5.

Ghiorso, M., Sack, R., 1995. Chemical mass transfer in magmatic processes IV: A revised and internally consistent thermodynamic model for the interpolation and extrapolation of liquid-solid equilibria in magmatic systems at elevated temperatures and pressures. Contributions to Mineralogy and Petrology 119, 192–212.

Ghods, A., Arkani-Hamed, J., 2000. Melt migration beneath mid-ocean ridge. Geophysical Journal International 140, 687–697.

Godard, M., Dautria, J., Perrin, M., 2003. Geochemical variability of the Oman ophiolite lavas: Relationship with spatial distribution and paleomagnetic directions. Geochemistry, Geophysics, Geosystems 4, 8609.

Goldstein, S., Murrell, M., Janecky, D., Delaney, J., Clague, D., 1991. Geochronology and petrogenesis of MORB from the Juan De Fuca and Gorda Ridges by ^{238}U–^{230}Th disequilibrium. Earth and Planetary Science Letters 107, 25–41.

Goldstein, S., Murrell, M., Williams, R., 1993. ^{231}Pa and ^{230}Th chronology of mid-ocean ridge basalts. Earth and Planetary Science Letters 115, 151–159.

Gregg, P., Behn, M., Lin, J., Grove, T., 2009. Melt generation, crystallization, and extraction beneath segmented oceanic transform faults. Journal of Geophysical Research 114, B11102.

Grove, T., Kinzler, R., Bryan, W., 1992. Fractionation of mid-ocean ridge basalt. Mantle Flow and Melt Generation at Mid- Ocean Ridges, Geophysical Monograph 71, 281–310.

Halliday, A., Lee, D.C., Tommasini, S., Davies, G., Paslick, C., Fitton, J., James, D., 1995. Incompatible trace elements in OIB and MORB and source enrichment in the sub-oceanic mantle. Earth and Planetary Science Letters 133, 379–395.

Hanghøj, K., Kelemen, P., Hassler, D., Godard, M., 2010. Composition and genesis of depleted mantle peridotites from the Wadi Tayin Massif, Oman Ophiolite; Major and trace element geochemistry, and Os isotope and PGE systematics. Journal of Petrology 51, 201–227.

Hanson, G., 1977. Geochemical evolution of the suboceanic mantle. Journal of the Geological Society of London 134, 235–253.

Hanyu, T., Kaneoka, I., 1997. The uniform and low ^{3}He/^{4}He ratios of HIMU basalts as evidence for their origin as recycled materials. Nature 390, 273–276.

Hart, S., 1993. Equilibration during mantle melting: A fractal tree model. Proceedings of the National Academy of Science 90, 11914–11918.

Harten, A., 1983. High resolution schemes for hyperbolic conservation laws. Journal of Computational Physics 49, 357–393.

Hauri, E., Lassiter, J., DePaolo, D., 1996. Osmium isotope systematics of drilled lavas from Mauna Loa, Hawaii. Journal of Geophysical Research 101, 11793–11806.

Helffrich, G., 2002. Chemical and seismological constraints on mantle heterogeneity. Philosophical Transactions of the Royal Society A 360, 2493–2505.

Hellebrand, E., Snow, J., Mühe, R., 2002. Garnet-field melting and late-stage refertilization in 'residual' abyssal peridotites from the Central Indian Ridge. Journal of Petrology 43, 2305–2338.

Herring, C., 1951. Surface tension as a motivation for sintering, in: Kingston, W. (Ed.), Physics of Powder Metallurgy. McGraw-Hill, New York, pp. 143–179.

Herzberg, C., 2006. Petrology and thermal structure of the Hawaiian plume from Mauna Kea volcano. Nature 444, 605–609.

Herzberg, C., 2011. Identification of source lithology in the Hawaiian and Canary Islands: Implications for origins. Journal of Petrology 52, 113–146.

Hesse, M., Schiemenz, A., Liang, Y., Parmentier, E., 2011. Compaction-dissolution waves in an upwelling mantle column. Geophysical Journal International 187, 1057–1075.

Hewitt, I., 2010. Modelling melting rates in upwelling mantle. Earth and Planetary Science Letters 300, 264–274.

Hewitt, I., Fowler, A., 2008. Partial melting in an upwelling mantle column. Proceedings of the Royal Society A 464, 2467–2491.

Hewitt, I., Fowler, A., 2009. Melt channelization in ascending mantle. Journal of Geophysical Research 114, B06210.

Hirschmann, M., Stolper, E., 1996. A possible role for garnet pyroxenite in the origin of the"garnet signature" in MORB. Contributions to Mineralogy and Petrology 124, 185–208.

Hirth, G., Kohlstedt, D., 1995a. Experimental constraints on the dynamics of the partially molten upper mantle: deformation in the diffusion creep regime. Journal of Geophysical Research 100, 1981–2001.

Hirth, G., Kohlstedt, D., 1995b. Experimental constraints on the dynamics of the partially molten upper mantle2. Deformation in the dislocation creep regime. Journal of Geophysical Research , 15441–15449.

Hirth, G., Kohlstedt, D., 1996. Water in the oceanic upper mantle: implications for rheology, melt extraction and the evolution of the lithosphere. Earth and Planetary Science Letters 144, 93–108.

Hirth, G., Kohlstedt, D., 2003. Rheology of the upper mantle and the mantle wedge: A view from the experimentalists, in: Eiler, J. (Ed.), Inside the Subduction Factory. AGU, Washington. Volume 138 of *Geophysical Monograph Series*, pp. 83–105.

Hofmann, A., 1997. Mantle geochemistry: the message from oceanic volcanism. Nature 385, 219–229.

Hofmann, A., 2003. Sampling mantle heterogeneity through oceanic basalts: Isotopes and trace elements, in: Editors-in Chief: Holland, H., Turekian, K. (Eds.), Treatise on Geochemistry. Pergamon, Oxford. Volume 2. Chapter 3, pp. 61–101.

Hofmann, A., Hart, S., 1978. An assessment of local and regional isotopic equilibrium in the mantle. Earth and Planetary Science Letters 38, 44–62.

Holness, M., 2005. Melt-solid dihedral angles of common minerals in natural rocks. Journal of Petrology 47, 791–800.

Holtzman, B., Groebner, N., Zimmerman, M., Ginsberg, S., Kohlstedt, D., 2003a. Stress-driven melt segregation in partially molten rocks. Geochemistry, Geophysics, Geosystems 4, 8607.

Holtzman, B., Kohlstedt, D., Zimmerman, M., Heidelbach, F., Hiraga, T., Hustoft, J., 2003b. Melt segregation and strain partitioning: Implications for seismic anisotropy and mantle flow. Science 301, 1227–1230.

Hooft, E., Detrick, S., Toomey, D., Collins, J., Lin, J., 2000. Crustal thickness and structure along three contrasting spreading segments of the Mid-Atlantic Ridge, 33.5°–35°N. Journal of Geophysical Research 105, 771–778.

Ito, G., Mahoney, J., 2005. Flow and melting of a heterogeneous mantle: 1. method and importance to the geochemistry of ocean island and mid–ocean ridge basalts. Earth and Planetary Science Letters 230, 29–46.

Ito, G., Martel, S., 2002. Focusing of magma in the upper mantle through dike interaction. Journal of Geophysical Research 107, 2223.

Iwamori, H., 1993. A model for disequilibrium mantle melting incorporating melt transport by porous and channel flows. Nature 366, 734–737.

Iwamori, H., 1994. ^{238}U–^{230}Th–^{226}Ra and ^{235}U–^{231}Pa disequilibria produced by mantle melting with porous and channel flows. Earth and Planetary Science Letters 125, 1–16.

Jackson, M., Hart, S., Saal, A., Shimizu, N., Jurz, M., Blusztajn, J., Skovgaard, A., 2008. Globally elevated titanium, tantalum, and niobium (TITAN) in ocean island basalts with high 3He/4He. Geochemistry, Geophysics, Geosystems 9, Q04027.

Johnson, K., Dick, H., 1992. Open system melting and temporal and spatial variation of peridotite and basalt at the Atlantis II fracture zone. Journal of Geophysical Research 97, 9219–9241.

Johnson, K., Dick, H., Shimizu, N., 1990. Melting in the oceanic upper mantle: an ion microprobe study of diopsides in abyssal peridotites. Journal of Geophysical Research 95, 2261–2678.

Jull, M., Kelemen, P., Sims, K., 2002. Consequences of diffuse and channelled porous melt migration on uranium series disequilibria. Geochimica and Cosmochimica Acta 66, 4133–4148.

Jull, M., McKenzie, D., 1996. The effect of deglaciation on mantle melting beneath Iceland. Journal of Geophysical Research 101, 21815–21828.

Kaneshima, S., Helffrich, G., 1999. Dipping low-velocity layer in the mid-lower mantle: Evidence for geochemical heterogeneity. Science 283, 1888–1891.

Kaneshima, S., Helffrich, G., 2003. Subparallel dipping heterogeneities in the mid-lower mantle. Journal of Geophysical Research 108, 2272.

Karato, S., Wu, P., 1993. Rheology of the upper mantle. Science 260, 771–778.

Katz, R., 2008. Magma dynamics with the Enthalpy Method: Benchmark solutions and magmatic focusing at mid-ocean ridges. Journal of Petrology 49, 2099–2121.

Katz, R., Knepley, M., Smith, B., Spiegelman, M., Coon, E., 2007. Numerical simulation of geodynamics processes with the Portable Extensible Toolkit for Scientific Computation. Physics of the Earth and Planetary Interiors 163, 52–68.

Katz, R., Rudge, J., 2011. The energetics of melting fertile heterogeneities within the depleted mantle. Geochemistry, Geophysics, Geosystems 12, Q0AC16.

Katz, R., Spiegelman, M., Carbotte, S., 2004. Ridge migration, asthenospheric flow and the origin of magmatic segmentation in the global mid-ocean ridge system. Geophysical Research Letters 31, L15605.

Katz, R., Spiegelman, M., Holtzman, B., 2006. The dynamics of melt and shear localization in partially molten aggregates. Nature 442, 676–679.

Katz, R., Spiegelman, M., Langmuir, C., 2003. A new parameterization of hydrous melting in the mantle. Geochemistry, Geophysics, Geosystems 4, 1073.

Katz, R., Weatherley, S., 2012. Consequences of mantle heterogeneity for melt extraction at mid-ocean ridges. Earth and Planetary Science Letters 335-336, 226–237.

Katz, R., Worster, M., 2008. Simulations of directional solidification, thermochemical convection, and chimney formation in a Hele-Shaw cell. Journal of Computational Physics 227, 9823–9840.

Katz, R.F., 2010. Porosity–driven convection and asymmetry beneath mid–ocean ridges. Geochemistry, Geophysics, Geosystems 11, Q0AC07.

Kelemen, P., 1990. Reaction between ultramafic rock and fractionating basaltic magma I. Phase relations, the origin of calc-alkaline magma series, and the formation of discordant dunite. Journal of Petrology 31, 51–98.

Kelemen, P., Aharonov, E., 1998. Periodic formation of magma fractures and generation of layered gabbro in the lower crust beneath oceanic spreading ridges, in: Buck, W., DElaney, T., Karson, A., Lagabrielle, Y. (Eds.), Faulting and magmatism at mid-ocean ridges. AGU, Washington. Volume 106 of *Geophysical Monograph Series*, pp. 267–289.

Kelemen, P., Braun, M., Hirth, G., 2000. Spatial distribution of melt conduits in the mantle beneath spreading ridges: Observations from the Ingalls and Oman ophiolites. Geochemistry, Geophysics, Geosystems 1, 1999GC000012.

Kelemen, P., Dick, H., 1995. Focused melt flow and localized deformatin in the upper mantle: Juxtaposition of replacive dunite and ductile shear zones in the Josephine peridotite, SW Oregon. Journal of Geophysical Research 100, 423–438.

Kelemen, P., Dick, H., Quick, J., 1992. Formation of harzburgite by pervasive melt rock reaction in the upper mantle. Nature 358, 635–641.

Kelemen, P., Hirth, G., Shimizu, N., Spiegelman, M., Dick, H., 1997. A review of melt migration processes in the adiabatically upwelling mantle beneath oceanic spreading ridges. Philosophical Transactions of the Royal Society A 355, 283–318.

Kelemen, P., Shimizu, N., Salters, V., 1995a. Extraction of mid-ocean ridge basalt from the upwelling mantle by focused flow of melt in dunite channels. Nature 375, 747–753.

Kelemen, P., Whitehead, J., Aharonov, E., Joordahl, K., 1995b. Experiments on flow focusing in soluble porous media, with applications to melt extraction from the mantle. Journal of Geophysical Research 100, 475–496.

Kellogg, L., Turcotte, D., 1990. Mixing and the distribution of heterogeneities in a chaotically convecting mantle. Journal of Geophysical Research 95, 421–432.

Kent, G., Singh, S., Harding, A., Sinha, M., Orcutt, J., Barton, P., White, R., Bazin, S., Hobbs, R., Tong, C., Pye, J., 2000. Evidence from three-dimensional seismic reflectivity images for enhanced melt supply beneath mid-ocean ridge discontinuities. Nature 406, 614–618.

King, D., Zimmerman, M., Kohlstedt, D., 2010. Stress-driven melt segregation in partially molten olivine-rich rocks deformed in torsion. Journal of Petrology 51, 21–42.

Kinzler, R., Grove, T., 1992. Primary magmas of mid-ocean ridge basalts 2. Applications. Journal of Geophysical Research 97, 6907–6926.

Klein, E., Langmuir, C., 1987. Global corelations of ocean ridge basalt chemistry with axial depth and crustal thickness. Journal of Geophyscial Research 92, 8089–8115.

Knepley, M., Katz, R., Smith, B., 2006. Developing a geodynamics simulator with PETSc, in: Bruaset, A., Tveito, A. (Eds.), Numerical Solution of Partial Differential Equations on Parallel Computers. Springer, Berlin. Volume 51 of *Lecture Notes in Computer Science and Engineering*, pp. 413–438.

Kogiso, T., Hirschmann, M., Pertermann, M., 2004. High pressure partial melting of mafic lithologies in the mantle. Journal of Petrology 45, 2407–2422.

Kogiso, T., Hirschmann, M.M.and Reiners, P., 2004. Length scales of mantle heterogeneities and their relationship to ocean island basalt geochemistry. Geochimica et Cosmochimica Acta 68, 345–360.

Kohlstedt, D., Holtzman, B., 2009. Shearing melt out of the Earth: An experimentalist's perspective on the influence of deformation on melt extraction. Annual Reviews of Earth and Planetary Science 37, 561–593.

Kojitani, H., Akaogi, M., 1997. Melting enthalpies of mantle peridotite: calorimetric determinations in the system CaO-MgO-Al_2O_3-SiO_2 and application to magma generation. Earth and Planetary Science Letters 153, 209–222.

Kokfelt, T., Hoernle, K., Hauff, F., Fiebig, J., Werner, R., Garbe-Schoenberg, D., 2006. Combined trace element and Pb-Nd-Sr-O isotope evidence for recycled oceanic crust (upper and lower) in the Iceland mantle plume. Journal of Petrology 47, 1705–1749.

Korenga, J., Kelemen, P., 1997. Origin of gabbro sills in the Moho transition zone of the Oman ophiolite: Implications for magma transport in the oceanic lower crust. Journal of Geophysical Research 102, 27729–27749.

Kuo, B., Forsyth, D., 1988. Gravity anomalies of the ridge-transform system in the South Atlantic between 31°S and 34.5°S—Upwelling centres and variations in crustal thickness. Marine Geophysics Research 10, 205–232.

Langmuir, C., Bender, J., 1984. The geochemistry of basalts in the vicinity of transform faults — Observations and implications. Earth and Planetary Science Letters 69, 107–127.

Langmuir, C., Bender, J., Batiza, R., 1986. Petrological and tectonic segmentation of the East Pacific Rise 5°30'-14°30'N. Nature 322, 422–429.

Langmuir, C., Bender, J., Bence, A., Hanson, G., Taylor, S.R., 1977. Petrogenesis of basalts from the Famous Area - Mid-Atlantic Ridge. Earth and Planetary Science Letters 36, 133–156.

Langmuir, C., Klein, E., Plank, T., 1992. Petrological systematics of mid-ocean ridge basalts: Constraints on melt generation beneath ocean ridges. Mantle Flow and Melt Generation at Mid-Ocean Ridges, Geophysical Monograph 71, 183–280.

Lassiter, J., Hauri, E., 1998. Osmium-isotope variations in Hawaiian lavas: evidence for recycled oceanic lithosphere in the Hawaiian plume. Earth and Planetary Science Letters 164, 483–496.

Liang, Y., Guo, Y., 2003. Reactive dissolution instability driven by chemical diffusion with applications to harzburgite reactive dissolution. Geophysical Research Letters 30, 1722.

Liang, Y., Schiemenz, A., Hesse, M., Parmentier, E., 2011. Waves, channels, and the preservation of chemical heterogeneities during melt migration in the mantle. Geophysical Research Letters 38, L20308.

Liang, Y., Schiemenz, A., Hesse, M., Parmentier, E., Hesthaven, J., 2010. High-porosity channels for melt migration: Top is the dunite and bottom is the harzburgite and lherzolite. Geophysical Research Letters 37, L15306.

Lin, J., Phipps Morgan, J., 1992. The spreading rate dependence of three-dimensional mid-ocean ridge gravity structure. Geophysical Research Letters 19, 13–16.

Lin, J., Purdy, G., Schouten, H., Sempere, J., Zervas, C., 1990. Evidence from gravity data for focused magmatic accretion along the Mid-Atlantic ridge. Nature 344, 627–632.

Lizarralde, D., Gaherty, J., Collins, J., Hirth, G., Kim, S., 2004. Spreading-rate dependence of melt extraction at mid-ocean ridges from mantle seismic refraction data. Nature 432, 744–747.

Lundstrom, C., 2000. Models of U-series disequilibria generation in MORB: the effects of two scales of porosity. Physics of earth and Planetary Interiors 121, 189–204.

Lundstrom, C., 2003. Uranium-series disequilibria in mid-ocean ridge basalts: observations and models of basalt genesis, in: Bourdon, B., Henderson, G., Lundstrom, C., Turner, S. (Eds.), Uranium-series Geochemistry. Volume 52 of *Reviews in Mineralogy and Geochemistry*, pp. 175–214.

Lundstrom, C., Chaussidon, M., Hsui, A., Kelemen, P., Zimmerman, M., 2005. Observations of Li isotopic variations in the Trinity Ophiolite: Evidence for isotopic fractionation by diffusion during mantle melting. Geochimica et Cosmochimica Acta 69, 735–751.

Lundstrom, C., Gill, J., Williams, Q., Hanan, B., 1998. Investigating solid mantle upwelling beneath mid-ocean ridges using U-series disequilibria: II. A local study at 33 degrees mid-Atlantic ridge. Earth and Planetary Science Letters 157, 167–181.

Lundstrom, C., Gill, J., Williams, Q., Perfit, M., 1995. Mantle melting and basalt extraction by equilibrium porous flow. Science 270, 1958–1961.

Lundstrom, C., Smpson, D., Perfit, M., Gill, J., Williams, Q., 1999. Insights into mid-ocean ridge basalt petrogenesis: U-series disequilibria from the Siqueiros Transfrom, Lamont Seamounts and East Pacific Rise. Journal of Geophysical Research 104, 13035–13048.

Maalœ, S., 2003. Melt dynamics of a partially molten mantle with randomly oriented veins. Journal of Petrology 44, 1193–1210.

Macdonald, K., Fox, P., Perram, L., Eisen, M., Haymon, R., Miller, S., Carbotte, S., Cormier, M., Shor, A., 1988. A new view of the mid-ocean ridge from the behaviour of ridge-axis discontinuities. Nature 335, 217–225.

Maclennan, J., 2008. Lead isotope variability in olivine-hosted melt inclusions from Iceland. Geochimica et Cosmochimica Acta 72, 4159–4176.

Maclennan, J., Jull, M., McKenzie, D., Slater, L., Grönvold, K., 2002. The link between volcanism and deglaciation in Iceland. Geochemistry, Geophysics, Geosystems 3, 1062.

Maclennan, J., McKenzie, D., Grönvold, K., Shimizu, N., Eiler, J., Kitchen, N., 2003. Melt mixing and crystallization under Theistareykir, northeast Iceland. Geochemistry, Geophysics, Geosystems 4, 8642.

MacLeod, C., Lissenberg, C., Bibby, L., Pearce, J., Goodenough, K., Styles, M., Condon, D., 2012. Geodynamics setting and origin of the Oman/UAE ophiolite, in: International Conference on the Geology of the Arabian Plate and the Oman Mountains, Sultan Qaboos University, Muscat, Sultanate of Oman. pp. 138–139.

Magde, L., Barclay, A., Toomey, D., R., D., Collins, J., 2000. Crustal magma plumbing within a segment of the Mid-Atlantic Ridge, 35°N. Earth and Planetary Science Letters 175, 55–67.

Magde, L., Sparks, D., 1997. Three-dimensional mantle upwelling, melt generation, and melt migration beneath segmented slow spreading ridges. Journal of Geophysical Research 102, 20571–20583.

Magde, L., Sparks, D., Detrick, R., 1997. The relationship between buoyant mantle flow, melt migration and gravity bull's eyes at the Mid-Atlantic Ridge between 33°N and 35°N. Earth and Planetary Science Letters 148, 59–67.

Matsuno, T., Evans, R., Nobukazu, S., Chave, A., 2012. Electromagnetic constraints on a melt region beneath the central Mariana back-arc spreading ridge. Geochemistry, Geophysics, Geosystems 13, Q10017.

McKenzie, D., 1984. The generation and compaction of partially molten rock. Journal of Petrology 25, 713–765.

McKenzie, D., 1985. ^{230}Th-^{238}U disequilibrium and the melting processes beneath ridge axes. Earth and Planetary Science Letters 72, 149–157.

McKenzie, D., O'Nions, R., 1991. Partial melt distributions from inversion of rare earth element concentrations. Journal of Petrology 32, 1020–1091.

McNutt, M., 1979. Compensation of oceanic topography: An application of the response function technique to the Surveyor area. Journal of Geophysical Research 84, 7589.

Morency, C., Doin, M., Dumoulin, C., 2005. Three-dimensional numerical simulations of mantle flow beneath mid-ocean ridges. Journal of Geophysical Research 110, B11407.

Morgan, Z., Liang, Y., 2003. An experimental and numerical study of the kinetics of harzburgite reactive dissolution with applications to dunite dike formation. Earth and Planetary Science Letters 214, 59–74.

Nedimovic, M., Carbotte, S., Harding, A., 2005. Frozen magma lenses below the oceanic crust. Nature 436, 1149–1152.

Nettles, M., Dziewonski, A., 2008. Radially anisotropic shear velocity structure of the upper mantle globally and beneath North America. Journal of Geophysical Research 113, B02303.

Nicolas, A., 1986. A melt extraction model based on structural studies in mantle peridotites. Journal of Petrology 27, 999–1022.

Nicolas, A., 1989. Structures of ophiolites and dynamics of the oceanic lithosphere. Volume 4 of *Petrology and Structural Geology*. Springer.

Niu, Y., 1997. Mantle melting and melt extraction processes beneath ocean ridges: Evidence from abyssal peridotites. Journal of Petrology 38, 1047–1074.

Niu, Y., Batiza, R., 1991. An empirical method for calculating melt compositions produced beneath midocean ridges: Application for axis and off-axis (seamounts) melting. Journal of Geophysical Research 96, 21753–21777.

Nowacki, A., Kendall, J., Wookey, J., 2012. Mantle anisotropy beneath the Earth's mid-ocean ridges. Earth and Planetary Science Letters 317-318, 56–67.

O'Hara, M., 1965. Primary magmas and the origin of basalts. Scottish Journal of Geology 1, 19–40.

Ortoleva, P., Chadam, J., Merino, E., Sen, A., 1987. Geochemical self-organisation II: The reactive-infiltration instability. American Journal of Science 287, 1008–1040.

Pallister, J., Knight, R., 1981. Rare–earth element geochemistry of the Samail ophiolite near Ibra, Oman. Journal of Geophysical Research 86, 2673–2697.

Panza, G., Doglioni, C., Levshin, A., 2010. Asymmetric ocean basins. Geology 38, 59–62.

Pearce, J., Alabaster, T., Shelton, A., Searle, M., 1981. The Oman ophiolite as a Cretaceous arc–basin complex: Evidence and implications. Philosophical Transactions of the Royal Society of London Series A 300, 299–317.

Pertermann, M., Hirschmann, M., 2003. Partial melting experiments on a MORB-like pyroxenite between 2 and 3 GPa: Constraints on the presence of pyroxenite in basalt source regions from solidus location and melting rate. Journal of Geophysical Research 108, 2125.

Phipps Morgan, J., Morgan, J., 1999. Two-stage melting and the geochemical evolution of the mantle: a recipe for mantle plum-pudding. Earth and Planetary Science Letters 170, 215–239.

Planert, L., Flueh, E., Reston, T., 2009. Along– and across–axis variations in crustal thickness and structure at the Mid-Atlantic Ridge at 5°S obtained from wide–angle seismic tomography: Implications for ridge segmentation. Journal of Geophysical Research 114, B09102.

Prinzhofer, A., Lewin, E., Allègre, C., 1989. Stochastic melting of the marble cake mantle: evidence from local study of the East Pacific Rise at 12 50'N. Earth and Planetary Science Letters 92, 189–206.

Prytulak, J., Elliott, T., 2007. TiO2 enrichment in ocean island basalts. Earth and Planetary Science Letters 263, 388–403.

Prytulak, J., Elliott, T., 2009. Determining melt productivity of mantle sources from ^{238}U–^{230}Th and ^{235}U–^{231}Pa disequilibria; an example from Pico Island, Azores. Geochimica et Cosmochimica Acta 73, 2103–2122.

Putirka, K., Perfit, M., Ryerson, F., Jackson, M., 2007. Ambient and excess mantle temperatures, olivine thermometry, and active vs. passive upwelling. Chemical Geology 241, 177–206.

Qin, Z., 1993. Dynamics of melt generation beneath mid-ocean ridge axes: Theoretical analysis based on ^{238}U–^{230}Th–^{226}Ra and ^{235}U–^{231}Pa disequilibria. Geochimica et Cosmochimica Acta 57, 1629–1634.

Quick, J., 1981. The origin and significance of large, tabular dunite bodies in the

Trinity peridotite, Northern California. Contributions to Mineralogy and Petrology 78, 413–422.

Reisberg, L., Allègre, C., Luck, J.M., 1991. The Re-Os systematics of the Ronda ultramafic complex of southern Spain. Earth and Planetary Science Letters 105, 196–213.

Renna, M., Tribuzio, R., 2011. Olivine-rich Troctolites from Ligurian ophiolites (Italy): Evidence for impregnation of replacive mantle conduits by MORB-type melts. Journal of Petrology 52, 1763–1790.

Reynolds, J., Langmuir, C., 1997. Petrological systematics of the Mid-Atlantic Ridge south of Kane: Implications for ocean crust formation. Journal of Geophysical Research 102, 14915–14946.

Ribe, N., 1985. The deformation and compaction of partial molten zones. Geophysical Journal of the Royal Astronomical Society 83, 497–501.

Richards, M., Morris, S., Busse, F., Lendardic, A., 2003. Towards a physical understanding of the effects of depth–dependent rheology on mantle convection, in: Eos Transactions, AGU Fall Meeting Supplements, AGU, San Francisco. pp. Abstract S11G–06.

Richardson, C., McKenzie, D., 1994. Radioactive disequilibria from 2D models of melt generation by plumes and ridges. Earth and Planetary Science Letters 128, 425–437.

Richter, F., Daly, S., 1989. Dynamical and chemical effects of melting a heterogeneous source. Journal of Geophysical Research 94, 12499–12510.

Riley Jr., G., Kohlstedt, D., 1991. Kinetics of melt migration in upper mantle-type rocks. Earth and Planetary Science Letters 105, 500–521.

Ringwood, A., 1982. Phase transformations and differentiation in subducted lithosphere: Implications for mantle dynamics, basalt petrogenesis, and crustal evolution. Journal of Geology 90, 611–643.

Roe, P., 1985. Some contributions to the modelling of discontinuous flows, in: Engquist, B., Osher, S., Somerville, R. (Eds.), Large-Scale Computations in Fluid Mechanics, pp. 163–193.

Ross, K., Elthon, D., 1997. Extreme incompatible trace-elements depletion of diopside in residual mantle from south of the Kane fracture zone, in: Karson, J., Cannat, M., Miller, J., Elthon, D. (Eds.), Mid-Atlantic Ridge Sites 920-924. Volume 153 of *Proceedings of the Ocean Drilling Program*, pp. 227–284.

Rubin, K., Sinton, J., Maclennan, J., Hellebrand, E., 2009. Magmatic filtering of mantle compositions at mid–ocean ridge volcanoes. Nature Geoscience 2, 321–328.

Rubin, K., van der Zander, I., Smith, M., Bermmanis, E., 2005. Minimum speed limit for ocean ridge magmatism from ^{210}Pb–^{226}Ra–^{230}Th disequilibria. Nature 437, 534–538.

Saal, A., Van Orman, J., 2004. The ^{226}Ra enrichment in oceanic basalt: Evidence for diffusive interaction processes within the crust-mantle transition zone. Geochemistry, Geophysics, Geosystems 5, Q02008.

Salevieva, G., Sobolev, A., Batanova, V., Suslov, P., Bruhmann, G., 2008. The structure of melt transport mantle channels. Geotectonics 42, 430–447.

Salters, V., Dick, H., 2002. Mineralogy of the mid-ocean-ridge basalt source from neodymium isotopic composition of abyssal peridotites. Nature 418, 68–72.

Salters, V., Longhi, J., 1999. Trace element partitioning during the initial stages of melting beneath mid-ocean ridges. Earth and Planetary Science Letters 166, 15–30.

Salters, V., Longhi, J., Bizimis, M., 2002. Near mantle solidus trace element partitioning at pressures up to 3.4 GPa. Geochemistry, Geophysics, Geosystems 3, 6.

Salters, V., Mallick, S., Hart, S., Langmuir, C., Stracke, A., 2011. Domains of depleted mantle: New evidence from hafnium and neodymium isotopes. Geochemistry, Geophysics, Geosystems 12, Q08001.

Salters, V., Stracke, A., 2004. Composition of the depleted mantle. Geochemistry, Geophysics, Geosystems 5, Q05004.

Savelieva, G., Sobolev, A., Batanova, V., Suslov, P., Brügmann, G., 2008. Structure of melt flow channels in the mantle. Geotectonics 42, 430–447.

Schemling, H., 2000. Partial melting and melt segregation in a convecting mantle, in: Bagdassarov, N., Laporte, D., Thompson, A., Bruce, A. (Eds.), Physics and Chemistry of Partially Molten Rocks. Springer. Volume 11 of *Petrology and Structural Geology*, pp. 141–178.

Schiemenz, A., Liang, L., Parmentier, E., 2011. A high–order numerical study of reactive dissolution in an upwelling heterogeneous mantle–I. Channelization, channel lithology and channel geometry. Geophysical Journal International 186, 641–664.

Schilling, J., 1973. Iceland mantle plume: geochemical evidence along Reykjanes Ridge. Nature 252, 565–571.

Schouten, H., Dick, H., Klitgord, K., 1987. Migration of mid-ocean ridge volcanic segments. Nature 326, 835–839.

Scott, D., Stevenson, D., 1986. Magma ascent by porous flow. Journal of Geophysical Research 91, 9283–9296.

Searle, M., Cox, J., 1999. Tectonic setting, origin, and obduction of the Oman ophiolite. Geological Society of America Bulletin 111, 104–122.

Seyler, M., Brunelli, D., Toplis, M., Mével, C., 2011. Multiscale chemical heterogeneities beneath the eastern Southwest Indian Ridge (52 °E–68 °E): Trace element compositions of along-axis dredged peridotites. Geochemistry Geophysics Geosystems 12, Q0AC15.

Seyler, M., Lorand, J., Dick, H., Drouin, M., 2007. Pervasive melt percolation reactions in ultra-depleted refractory harzburgites at the Mid-Atlantic Ridge 15°20'N: ODP Hole 1274A. Contributions to Mineralogy and Petrology 153, 303–319.

Seyler, M., Toplis, M., Lorand, J.P., Luget, A., Cannat, M., 2001. Clinopyroxene microtextures reveal incompletely extracted melts in abyssal peridotites. Geology 29, 155–158.

Shorttle, O., Maclennan, J., 2011. Compositional trends of Icelandic basalts: Implications for short-length scale lithological heterogeneity in mantle plumes. Geochemistry, Geophysics, Geosystems 12, Q11008.

Simpson, G., Spiegelman, M., Weinstein, M., 2010. A multiscale model of partial melts: 1. Effective equations. Journal of Geophysical Research 115, B04410.

Sims, K., Goldstein, S., Blichert-Toft, J., Perfit, M., Kelemen, P., Fornari, D., Michael, P., Murrel, M., Hart, S., DePaolo, D., Layne, G., Ball, L., Jull, M., Bender, J., 2002. Chemical and isotopic constraints on the generation and transport of magma beneath the East Pacific Rise. Geochimica et Cosmochimica Acta 66, 3481–3504.

Singh, S., Crawford, W., Carton, H., Seher, T., Combier, V., Cannat, M., Canales, J., Düsünür, D., Escartin, J., Miranda, J., 2006a. Discovery of a magma chamber and faults beneath a Mid-Atlantic Ridge hydrothermal field. Nature 442, 1029–1032.

Singh, S., Harding, A., Kent, G., Sinha, M., Combier, V., Bazin, S., Tong, C., Pye, J., Barton, P., Hobbs, R., White, R., Orcutt, J., 2006b. Seismic reflection images of the Moho underlying melt sills at the East Pacific Rise. Nature 442, 287–290.

Sleep, N., 1974. Segregation of magma must from a mostly crystalline mush. Geological Society of America Bulletin 85, 1125–1232.

Sleep, N., 1975. Formation of oceanic crust: Some thermal constraints. Journal of Geophysical Research 80, 4037–4042.

Sleep, N., 1988. Tapping of melt by veins and dykes. Journal of Geophysical Research 93, 10255–10272.

Small, C., Danyushevsky, L., 2003. Plate-kinematic explanation for mid-oceanic-ridge depth discontinuities. Geology 31, 399–402.

Sobolev, A., 1996. Melt inclusions in minerals as a source of principle petrological information. Petrology 4, 228–239.

Sobolev, A., Hofmann, A., Brügmann, G., Batanova, V., Kuzmin, D., 2008. A quantitative link between recycling and osmium isotopes. Science 321, 536.

Sobolev, A., Hofmann, A., Kuzmin, D., Yaxley, G., Arndt, N., Chung, S.L., Danyushevsky, L., Elliott, T., Frey, F., 2007. The amount of recycled crust in sources of mantle-derived melts. Science 316, 412–417.

Sobolev, A., Shimizu, N., 1993. Ultra–depleted primary melt included in an olivine from the Mid-Atlantic Ridge. Nature 363, 151–154.

Sobolev, S., Hofmann, A., Sobolev, S., Nikogoslan, I., 2005. An olivine–free mantle source of Hawaiian shield basalts. Nature 434, 590–597.

Sparks, D., Parmentier, E., 1991. Melt extraction from the mantle beneath spreading centres. Earth and Planetary Science Letters 105, 386–377.

Sparks, D., Parmentier, E., Phipps Morgan, J., 1993. Three-dimensional mantle convection beneath a segmented spreading center: Implications for along–axis variations in crustal thickness and gravity. Journal of Geophysical Research 98, 21977–21995.

Spiegelman, M., 1993a. Flow in deformable porous media 1. Simple analysis. Journal of Fluid Mechanics 247, 17–38.

Spiegelman, M., 1993b. Flow in deformable porous media 2. Numerical analysis - the relationship between shock waves and solitary waves. Journal of Fluid Mechanics 247, 39–63.

Spiegelman, M., 1993c. Physics of melt extraction: theory, implications and applications. Philosophical Transactions of the Royal Society A 342, 23–41.

Spiegelman, M., 2003. Linear analysis of melt band formation by simple shear. Geochemistry, Geophysics, Geosystems 4, 8615.

Spiegelman, M., Elliott, T., 1993. Consequences of melt transport for uranium series disequilibrium in young lavas. Earth and Planetary Science Letters 118, 1–20.

Spiegelman, M., Kelemen, P., 2003. Extreme chemical variability as a consequence of channelized melt transport. Geochemistry, Geophysics, Geosystems 4, 1055.

Spiegelman, M., Kelemen, P., Aharonov, E., 2001. Causes and consequences of flow organization during melt transport: the reaction infiltration instability in compactible media. Journal of Geophysical Research 106, 2061–2077.

Spiegelman, M., Kenyon, P., 1992. The requirements for chemical disequilibrium during magma migration. Earth and Planetary Science Letters 109, 611–620.

Spiegelman, M., McKenzie, D., 1987. Simple 2D models for melt extraction at mid-ocean ridges and island arcs. Earth and Planetary Science Letters 83, 137–152.

Stevenson, D., 1989. Spontaneous small-scale melt segregation in partial melts undergoing deformation. Geophysical Research Letters 16, 1067–1070.

Stolper, E., 1980. A phase diagram for mid–ocean ridge basalts: Preliminary results and implications for petrogenesis. Contributions to Mineralogy and Petrology 74, 13–27.

Stracke, A., Bourdon, B., 2009. The importance of melt extraction for tracing mantle heterogeneity. Geochimica et Cosmochimica Acta 73, 218–238.

Stracke, A., Bourdon, B., McKenzie, D., 2006. Melt extraction in the Earth's mantle: Constraints from U–Pa–Ra studies in oceanic basalts. Earth and Planetary Science Letters 244, 97–112.

Stracke, A., Hofmann, A., Hart, S., 2005. FOZO, HIMU, and the rest of the mantle zoo. Geochemistry, Geophysics, Geosystems 6, Q05007.

Stracke, A., Zindler, A., Salters, V., Mckenzie, D., Blichert-Toft, J., Albarède, F., Grönvold, K., 2003. Theistareykir revisited. Geochemistry Geophysics Geosystems 4, 8507.

Suhr, G., 1992. Upper mantle peridotites in the Bay of Islands Ophiolite, Newfoundland — formation during the final stages of a spreading centre. Tectonophyics 206, 31–53.

Suhr, G., 1999. Melt migration under oceanic ridges: Inferences from reactive transport modelling of upper mantle hosted dunites. Journal of Petrology 40, 575–599.

Suhr, G., Hellebrand, E., Snow, J., Seck, H., Hofmann, A., 2003. Significance of large, refractory dunite bodies in the upper mantle of the Bay of Islands Ophiolite. Geochemistry, Geophysics, Geosystems 4, 8605.

Sun, S., McDonough, W., 1989. Chemical and isotopic systematics of oceanic basalts: implications for mantle composition and processes, in: Saunders, A., Norry, M. (Eds.), Magmatism in Ocean Basins. Geological Society of London. Volume 42 of *Geological Society, London, Special Publications*, pp. 313–345.

Sundberg, M., Hirth, G., Kelemen, P., 2010. Trapped melt in the Josephene Peridotite: Implications for permeability and melt extraction in the upper mantle. Journal of Petrology 51, 185–200.

Sweby, P., 1984. High resolution schemes using flux limiters for hyperbolic conservation laws. SIAM Journal of Numerical Analysis 21, 995–1011.

Takahashi, E., Nakajima, K., Wright, T., 1998. Origin of the Columbia River basalts: melting model of a heterogeneous plume head. Earth and Planetary Science Letters 162, 63–80.

Takahashi, N., 1992. Evidence for melt segregation towards fractures in the Horoman mantle peridotite complex. Nature 359, 52–55.

Takei, Y., 2010. Stress-induced anisotropy of partially molten rock analogue deformed under quasi-static loading test. Journal of Geophysical Research 115, B03204.

Takei, Y., Holtzman, B., 2009a. Viscous constitutive relations of solid-liquid composites in terms of grain boundary contiguity: 1. Grain boundary diffusion control model. Journal of Geophysical Research 114, B06205.

Takei, Y., Holtzman, B., 2009b. Viscous constitutive relations of solid-liquid composites in terms of grain boundary contiguity: 2. Composite model for small melt fractions. Journal of Geophysical Research 114, B06206.

Takei, Y., Holtzman, B., 2009c. Viscous constitutive relations of solid-liquid composites in terms of grain boundary contiguity: 3. Causes and consequences of viscous anisotropy. Journal of Geophysical Research 114, B06207.

The MELT Seismic Team, 1998. Imaging the deep seismic structure beneath a mid-ocean ridge: the MELT experiment. Science 280, 1215–1218.

Tilton, G., Hopson, C., Wright, J., 1981. Uranium-lead isotopic ages of the Samail ophiolite, Oman, with applications to Tethyan ocean ridge tectonics. Journal of Geophysical Research 91, 9261–9276.

Tirone, M., Sen, G., Morgan, J., 2012. Petrological geodynamic modeling of mid-ocean ridges. Physics of The Earth and Planetary Interiors 190-191, 51–70.

Tolstoy, M., Harding, A., Orcutt, J., 1993. Crustal thickness on the Mid-Atlantic Ridge—Bulls-eye gravity anomalies and focused accretion. Science 262, 726–729.

Toomey, D., 2002. Asymmetric mantle dynamics in the MELT regions of the East Pacific Rise. Earth and Planetary Science Letters 200, 287–295.

Toomey, D., Wilcock, W., Solomon, S., Hammond, W., Orcutt, J., 1998. Mantle seismic structure beneath the MELT region of the East Pacific Rise from P and S wave tomography. Science 280, 1224–1227.

Turcotte, D., Ahern, J., 1978. A porous flow model for magma migration in the asthenosphere. Journal of Geophysical Research 83, 767–772.

Turcotte, D., Schubert, G., 2002. Geodynamics. Cambridge University Press, Cambridge.

Turner, S., Bourdon, B., 2011. Melt transport from the mantle to the crust – Uranium-series isotopes, in: Dosseto, A., Turner, S., Van Orman, J. (Eds.), Timescales of magmatic processes: From core to atmosphere. Wiley-Blackwell.

Van der Wal, D., Bodinier, J., 1996. Origin of the recrystallization front in the Ronda peridotite by km-scale pervasive porous melt flow. Contributions to Mineralogy and Petrology 122, 387–405.

van Keken, P., Zhong, S., 1999. Mixing in a 3D spherical model of present-day mantle convection. Earth and Planetary Science Letters 171, 533–547.

Van Orman, J., Saal, A., 2009. Influence of crustal cumulates on ^{210}Pb disequilibria in basalts. Earth and Planetary Science Letters 284, 284–291.

Van Orman, J., Saal, A., Bourdon, M., Hauri, E., 2006. Diffusive fractionation of U-series nuclides during mantle melting and shallow level melt-cumulate interaction. Geochimica et Cosmochimica Acta 70, 4797–4812.

Vaughan, P., Kohlstedt, D., 1982. Distribution of the glass phase in hot-pressed, olivine-basalt aggregates: An electron microscopy study. Contributions to Mineralogy and Petrology 81, 253–261.

Vera, E., Mutter, J., Buhl, P., Orcutt, J., Hardong, A., Kappus, M., Detrick, R., Brocher, T., 1990. The structure of 0–0.2 m.y. old oceanic crust at 9°N on the East Pacific Rise from Expanded Spread Profiles. Journal of Geophysical Research 95, 15529–15556.

Volpe, A., Goldstein, S., 1993. ^{226}Ra–^{230}Th disequilibrium in axial and off-axis mid-ocean ridge basalts. Geochimica et Cosmochimica Acta 57, 1233–1241.

von Bargen, N., Waff, H., 1986. Permeabilities, interfacial areas and curvatures of partially molten systems: results of numerical computations of equilibrium microstructures. Journal of Geophysical Research 91, 9261–9276.

Waff, H., Bulau, J., 1979. Equilibrium fluid distribution in an ultramafic partial melt under hydrostatic stress conditions. Journal of Geophysical Research 84, 6109–6114.

Walter, M., 1998. Melting of garnet peridotite and the origin of komatiite and depleted lithosphere. Journal of Petrology 39, 29–60.

Wang, X., Cochran, J., G.A., B., 1996. Gravity anomalies, crustal thickness, and the pattern of mantle flow at the fast spreading East Pacific Rise, 9°N-10°N: Evidence for three-dimensional upwelling. Journal of Geophysical Research 101, 17927–17940.

Wark, D., 2003. Reassessment of pore shapes in microstructurally equilibrated rocks, with implications for permeability of the upper mantle. Journal of Geophysical Research 108, 2050.

Wark, D., Watson, B., 1998. Grain-scale permeabilities of texturally equilibrated, monomineralic rocks. Earth and Planetary Science Letters 164, 591–605.

Warren, J., Shimizu, N., 2010. Cryptic variations in abyssal peridotite compositions: Evidence for shallow-level melt infiltration in the oceanic lithosphere. Journal of Petrology 51, 1–29.

Watts, A., 2001. Isostasy and Flexure of the Lithosphere. Cambridge University Press, Cambridge, U.K.

Watts, A., 2007. An overview, in: Schubert, G. (Ed.), Crustal and Lithosphere Dynamics. Elsevier, Amsterdam. Volume 6 of *Treatise on Geophysics*, pp. 1–48.

Weatherley, S., Katz, R., 2010. Plate-driven mantle dynamics and global patterns of mid-ocean ridge bathymetry. Geochemistry, Geophysics, Geosystems 11, Q10003.

Weatherley, S., Katz, R., 2012. Melting and channelized magmatic flow in heterogeneous, upwelling mantle. Geochemistry, Geophysics, Geosystems 13, Q0AC18.

Williams, R., Gill, J., 1989. Effects of partial melting on the uranium decay series. Geochimica et Cosmochimica Acta 53, 1607–1619.

Wood, D., 1979. A variably veined suboceanic upper mantle–genetic significance for mid-ocean ridge basalts from geochemical evidence. Geology 7, 499–503.

Yasuda, A., Fujii, T., Kurita, K., 1994. Melting and phase relations of an anhydrous mid-ocean ridge basalt from 3 to 20 GPa: Implications for the behaviour of subducted oceanic crust in the mantle. Journal of Geophysical Research 99, 9401–9414.

Yaxley, G., 2000. Experimental study of the phase and melting relations of homogenous basalt + peridotite mixtures and implications for the petrogenesis of flood basalts. Contributions to Mineralogy and Petrology 139, 326–338.

Yaxley, G., Green, D., 1998. Reactions between eclogite and peridotite: mantle refertilisation by subduction of oceanic crust. Schweizerische mineralogische und petrographische Mitteilungen 78, 243–255.

Yinting, L., Meissner, R., Theilen, R., Xue, E., 1991. Melt extraction from partially molten regions beneath mid-ocean ridges. Earth and Planetary Science Letters 103, 69–78.

Zhu, W., Gaetani, G., Fusseis, F., Montesi, J., De Carlo, F., 2011. Microtomography of partially molten rocks: Three-dimensional melt distribution in mantle peridotite. Science 332, 88–91.

Zimmerman, M., 2004. Rheological properties of partially molten lherzolite. Journal of Petrology 45, 275–298.

Zimmerman, M., Zhang, S., Kohlstedt, D., Karato, S., 1999. Melt distribution in mantle rocks deformed in shear. Journal of Geophysical Research 26, 1505–1508.

Zindler, A., Hart, S., Frey, F., Jakobsson, S., 1979. Nd and sr isotope ratios and rare earth element abundances in reykjanes peninsula basalts evidence for mantle heterogeneity beneath iceland. Earth and Planetary Science Letters 45, 249–262.